



HAL
open science

Vortex dynamics in ion irradiated YBCO superconducting nanowires : toward single photon detection

Paul Amari

► **To cite this version:**

Paul Amari. Vortex dynamics in ion irradiated YBCO superconducting nanowires : toward single photon detection. Materials Science [cond-mat.mtrl-sci]. Sorbonne Université, 2020. English. NNT : 2020SORUS262 . tel-03462798

HAL Id: tel-03462798

<https://theses.hal.science/tel-03462798>

Submitted on 2 Dec 2021

HAL is a multi-disciplinary open access archive for the deposit and dissemination of scientific research documents, whether they are published or not. The documents may come from teaching and research institutions in France or abroad, or from public or private research centers.

L'archive ouverte pluridisciplinaire **HAL**, est destinée au dépôt et à la diffusion de documents scientifiques de niveau recherche, publiés ou non, émanant des établissements d'enseignement et de recherche français ou étrangers, des laboratoires publics ou privés.



PHD THESIS
SORBONNE UNIVERSITÉ

Specialization: Physics

École doctorale n°564: Physique en Île-de-France

achieved in the

Laboratoire de Physique et d'Étude des Matériaux

supervised by Jérôme LESUEUR and Cheryl FEUILLET-PALMA

by

Paul AMARI

Dissertation submitted in application for the degree of:

DOCTOR OF PHILOSOPHY IN PHYSICS SORBONNE UNIVERSITÉ

Thesis subject:

**Dynamique des vortex dans des nanofils supraconducteurs
d'YBCO irradiés : vers la détection de photon unique**

Manuscript defended on March 6th, 2020

Doctoral committee:

Mr. Olivier BOURGEOIS	Referee
Mr. Claude CHAPELIER	Referee
Ms. Floriana LOMBARDI	Examiner
Mr. Félix BUSSIÈRES	Examiner
Mr. Bernard PLAÇAIS	President
Mr. Jérôme LESUEUR	Supervisor
Ms. Cheryl FEUILLET-PALMA	Supervisor
Ms. Rose-Marie SAUVAGE	Invited

Laboratoire de Physique
et d'Étude des Matériaux
ESPCI Paris
10 rue Vauquelin
75 005 Paris

École Doctorale
Physique en Île de France
Sorbonne Université
4 place Jussieu
75 005 Paris

*“Stay not where the lowlands are! Climb not into the sky!
The world looks best by far when viewed from halfway high.”*
— Friedrich Nietzsche, *The Gay Science*

Remerciements

Après une dizaine d'année universitaire, le doctorat clôt pour moi la fin d'un cycle. Loin d'être un accomplissement individuel, ce doctorat n'aurait pu se faire sans le soutien et la confiance qui m'ont été accordé par de nombreuses personnes et institutions, que ce soit durant ces trois années de recherche, mais aussi tout au long de mon parcours universitaire que j'ai effectué jusqu'ici. À travers ces quelques paragraphes, je souhaiterai témoigner de ma reconnaissance et de ma gratitude envers celles et ceux qui m'ont permis de réaliser mon doctorat.

Je tiens tout d'abord à remercier l'École Doctorale de Physique en Île-de-France et l'Agence de l'Innovation de Défense (AID) qui ont accepté de financer conjointement mes travaux de thèse. J'en profite pour remercier ma tutrice référente à l'AID Rose-Marie Sauvage. Son suivi tout au long de ma thèse m'a permis de mettre en relief mes travaux et d'avoir une vue d'ensemble sur ma thèse. Je remercie aussi Maria Luisa Della Rocca et Sergio Vlaic d'avoir accepté de faire parti de mon comité de thèse. Je leur suis reconnaissant d'avoir accordé de leur temps et de me donner un point de vue extérieur sur l'avancée de mes travaux.

Je tiens à remercier Olivier Bourgeois et Claude Chapelier d'avoir accepté d'évaluer mon travail en tant que rapporteurs, mais aussi Floriana Lombardi, Félix Bussièrès et Bernard Plaçais d'avoir participer à mon jury de thèse. Grâce à chacune de leur participation, j'ai eu l'honneur et le plaisir d'avoir eu une discussion scientifique riche et animée lors de la soutenance.

Maintenant, je souhaiterai remercier chaleureusement les membres permanents de l'équipe PHASME avec qui j'ai eu le plaisir de travailler durant ma thèse : Cheryl Feuillet-Palma, Nicolas Bergeal et Jérôme Lesueur. Vous formez une belle équipe d'enseignants chercheurs complémentaires au sein de laquelle il est agréable de travailler et d'apprendre. J'ai beaucoup appris de vos nombreuses expertises scientifiques et techniques, que ce soit pour se servir de sa matière grise ou de ses dix doigts. Celles-ci m'ont permis d'égayer ma curiosité en travaillant sur un projet varié depuis la conception de circuits supraconducteurs à la modélisation de données. Outre vos qualités professionnelles, j'ai aussi été conquis par vos qualités humaines. Cheryl, je te remercie grandement pour ton dynamisme et ta bonne humeur sans failles au quotidien : ils créent une atmosphère où il fait bon travailler. Jérôme, j'ai beaucoup apprécié ton recul et ton sens de l'écoute, ils m'ont permis de prendre de la hauteur durant ma thèse et de relativiser. Du début de la thèse jusqu'à la soutenance vous m'avez soutenu et encouragé, dans les moments délicats comme dans les heureuses découvertes. J'ai partagé mon quotidien avec les membres de l'équipe PHASME, mes camarades de bureau et les étudiants de passage pour quelques mois. Un grand merci va tout d'abord à François avec qui j'ai partagé presque trois années. C'était très agréable de travailler avec toi : sérieux quand il faut, blagueur à tes heures et prêt à refaire le monde par la pensée. J'espère que l'on ne manquera pas de le refaire à nouveau. J'ai aussi beaucoup apprécié la présence de Guilhem, toujours prêt à philosopher; de Zoé pour me faire découvrir le patin à glace par la pensée; ou encore Eliana et ses multiples disciplines sportives. Enfin, ce fût fort enrichissant de partager mes derniers mois de thèse

avec Sergeï. Je te souhaite un bon courage pour ta thèse, malgré des débuts chahutés par l'actualité je suis certain qu'elle se déroulera bien. En conclusion, toutes ces rencontres m'ont permis d'avoir des discussions variées avec des personnes brillantes et enthousiastes. Chacune d'entre elle a comblé une part de mon ignorance, alors merci pour ce partage.

Mes remerciements vont aussi aux personnes qui m'ont apporté leur aide durant ma thèse. Pour commencer, je souhaite remercier Javier Briatico de l'UMR CNRS-Thalès d'avoir répondu favorablement à nos demandes de films minces en YBCO. Javier, j'ai beaucoup apprécié ta motivation et ton écoute face à nos demandes complexes. Malgré toutes les contraintes que nous imposions pour pouvoir réaliser nos dispositifs tu as su mettre ton expertise en action. Les derniers résultats obtenus avec tes films sont très prometteurs. J'espère que les futurs travaux permettront de concrétiser le temps investi à adapter les technologies de croissance et de fabrication. Mes remerciements vont aussi à Christian Ulysse qui nous a accordé de son temps. En pleine période de déménagement du LPN vers le C2N, nous avons eu la chance d'utiliser le tout nouveau FIB Helium. Malgré la complexité de la machine, nos nombreux étonnements et interrogations durant la fabrication, je garde un bon souvenir de ces journées passées en salle blanche. Cela a été un plaisir de travailler avec toi Christian, malgré la difficulté nous avons su garder la tête froide. Je remercie évidemment Yann Legall d'avoir réaliser les nombreuses irradiations. Les levers matinaux pour aller à Strasbourg étaient toujours un peu difficile, mais le personnel du laboratoire ICUBE, en particulier Yann, m'ont toujours accueilli avec le sourire et la bonne humeur. Grâce à toi Yann, j'ai beaucoup appris sur les implanteurs mais aussi sur tout un tas de sujets et de bricolage. Ces voyages alsaciens m'ont permis de découvrir plus en détails un autre laboratoire, ses membres et son organisation. En bref, outre l'expérience ionique, c'était aussi une expérience humaine que j'ai beaucoup apprécié.

De retour dans le 5^{ème} arrondissement de Paris, de nombreuses personnes m'ont apporté leur soutien que ce soit à l'ESPCI, au LPEM ou dans les organismes voisins. Même si les remerciements ne seront probablement pas exhaustifs, je remercie toutes ces personnes par anticipation. Je remercie tout d'abord Sophie Demonchaux et Marie-Claude Theme pour leur support administratif. Elles ont toujours répondu à mes demandes et su m'aiguiller pour cheminer à travers les méandres de l'administration. Je suis également reconnaissant du service informatique du CNRS, de l'ESPCI, et aussi celui du laboratoire en la personne de Francis. Ils ont mis en place plusieurs outils qui ont facilité grandement la gestion des données dans mon travail de recherche mais pas seulement. De plus ils m'ont aidé à percer certains mystères de l'informatique. Tant qu'on est dans les technologies numériques, le réseau internet mondial m'a aussi été d'une grande utilité. Je souhaite remercier ici tous les anonymes qui contribuent au partage de la connaissances à travers les sites, les forums et les logiciels libres. Nombreux de mes petits problèmes quotidiens ont été résolu grâce à eux, que ce soit pour corriger un code, apprendre un nouveau langage ou découvrir de nouveaux outils numériques. Je dois aussi un grand merci aux membres de l'atelier mécanique, en particulier Ludovic. Ils ont toujours été de bons conseils et d'une grande aide pour réaliser nos pièces mécaniques, malgré nos besoins farfelus et complexes. Pour ce qui est de la nanofabrication, je suis redevable du personnel des salles blanches de l'ENS : Michael Rosticher et José Palomo, et de l'Université Paris Diderot : Pascal Filloux et Stéphan Suffit. Grâce à eux, j'ai pu réaliser mes nanofils dans de bonnes conditions et optimiser les différents procédés de nanofabrication. Sans cela, la thèse n'aurait pas pu aboutir à de si bons dispositifs. Je remercie à nouveau Michael Rosticher de nous avoir prêté du matériel optique assortis de conseils avisés. Ceux-ci nous ont permis de nous lancer dans la caractérisation optique de nos nanofils en YBCO.

Durant mes trois années de thèse, j'ai eu l'occasion d'enseigner l'électronique en L2 à l'UFR de Physique de Sorbonne Université grâce à Tristan Briant qui m'a fait confiance

trois fois de suite. Je suis tout simplement impressionné par sa pédagogie et sa motivation sans limites. L'application hydro-électrique "Pipeline" développée par ses soins en est un bel exemple. Réussir à donner le goût de l'électronique, des porte logiques et des transistors n'est pas une chose facile. Grâce au contenu de l'UE et sa célèbre compétition de robots, l'apprentissage et l'intérêt porté par les étudiants fonctionnent. J'ai pu voir, au fil des semaines les étudiants s'intéressaient et progressaient : c'était très stimulant. Cette expérience m'a permis de rendre accessible mes connaissances en des termes et des phrases claires. Cet enseignement était une réelle bouffée d'air durant ma thèse, alors merci à Tristan et à l'UFR de Physique pour cela.

Ensuite, j'aimerais mettre en perspective ma thèse avec ma formation universitaire. Je tiens d'abord à remercier la France de proposer un enseignement scientifique de qualité à moindres frais pour tous. La France m'a permis de réaliser de longues études et de m'épanouir par la connaissance. Durant mon parcours j'ai eu la chance de lier de nombreuses amitiés et de faire d'heureuses rencontres. Elles m'ont aidé à maintenir le cap jusqu'à l'achèvement de ma thèse. Je pense notamment à Antoine Comby et toute sa famille, je leur témoigne ici de ma gratitude pour m'avoir accueilli à Boubou city durant ma dernière année de prépa. J'en profite aussi pour remercier les professeurs de PC* du lycée Michel de Montaigne de Bordeaux. A la fois humains et rigoureux, ils m'ont soutenu pour atteindre mes objectifs universitaires, que ce soit pour intégrer l'ESPCI Paris mais aussi la Fondation Georges Besse. Arrivé à Paris, cette dernière m'a permis de mener à bien mes études avec une sérénité financière et morale. Je suis éternellement reconnaissant envers tous les membres qui constitue la Fondation Georges Besse et qui pérennise son action. J'ai trouvé une nouvelle famille au sein de l'Amicale des lauréats de la Fondation Georges Besse. Enfin, l'ESPCI Paris m'a permis de découvrir de nombreux aspects des sciences naturelles et d'aiguiser mon sens critique. Je remercie donc tous ceux qui font la qualité et la richesse de la formation de l'école.

Enfin, je souhaite adresser des remerciements plus personnels. En premier lieu, je suis reconnaissant envers ma famille qui m'a toujours encouragée dans mes choix, sans pression ni obligation. Cela m'a permis d'acquérir une autonomie dans la pensée et dans l'action, ainsi que la confiance nécessaire pour avancer face aux aléas de la vie. Je remercie ici évidemment ma mère, mais aussi mes oncles, mes grands-parents et ma seconde famille à Barbezières. Vous m'avez tous apporté beaucoup. Je souhaite aussi témoigner de la fierté que j'éprouve pour mes deux petits frères qui tracent chacun leur propre route avec volonté et persévérance.

Mes remerciements vont aussi à tous mes amis avec qui nous avons pu partagés des tranches de vies durant ma thèse : ceux de l'ESPCI, de prépa et d'autres encore. Avec mes amis doctorants, nous avons pu partagés les hauts et les bas de la vie de docteur; et les autres m'ont permis de relativiser tout ça. Un grand merci vont à mes compagnons d'aventures : Guillaume, Antoine, et aussi Nelo. Vous avez toujours répondu présents pour accomplir des idées saugrenues, peu importe la météo : qu'il vente, qu'il pleuve, qu'il neige, ou que le tonnerre gronde. Je pense notamment aux séances de manucures au viaduc, aux pyramides en plein milieu des avalanches de Montsouris, ou bien l'enchaînement de côtes en fractionné à 6h du matin. Je suis sûr que chacun se reconnaîtra dans ces activités aussi absurdes qu'elles soient. Toutes ces aventures m'ont permis de m'évader et ainsi reposer mon esprit.

Pour clôturer mes propos je terminerai par remercier Aude du fond du cœur. Ton soutien m'a permis de traverser mes phases de doutes profonds et de profiter de la vie avec simplicité. Tu es la personne qui rend ma vie plus douce et agréable.

Résumé de thèse

Introduction

Les détecteurs de photons uniques supraconducteurs (SSPD) offrent aujourd'hui les meilleures performances pour détecter des photons uniques, en particulier pour la lumière visible et le proche infrarouge. Ils présentent une grande efficacité de détection intrinsèque, un taux de comptage important, un taux de comptage noir faible et une gigue temporelle réduite. Les SSPDs surpassent, à bien des égards, leurs homologues semi-conducteurs telles que les diodes à avalanche à photon unique. Ainsi, ils s'imposent comme une technologie de premier plan pour un grand nombre d'applications dont la cryptographie quantique ou l'imagerie à faible intensité lumineuse. Ce type de détecteur, réalisé à partir de supraconducteurs à basse température, offre les meilleures performances à 1 K. Cette technologie nécessite donc le recours à une cryogénie lourde et énergivore pour fonctionner, ce qui en limite son développement à grande échelle.

Afin de permettre une utilisation plus large des SSPD, la thèse présentée ici a eu pour ambition d'étudier la possibilité de développer des SSPDs en $\text{YBa}_2\text{Cu}_3\text{O}_{7-x}$ (YBCO), une céramique supraconductrice en dessous de 90 K. Une telle température permet d'envisager le fonctionnement du détecteur à une température plus raisonnable, ce qui nécessiterait alors un système cryogénique simplifié, plus compact et moins onéreux. De plus, le temps d'interaction électron-phonon est particulièrement court dans ce matériau. Or ce temps fixe la limite intrinsèque du temps de réinitialisation du détecteur, nous pouvons donc espérer atteindre un taux de comptage d'autant plus rapide avec des détecteurs en YBCO. Néanmoins, l'YBCO est un matériau délicat à nano-structurer. En effet, ses propriétés supraconductrices sont très sensibles à la fois au désordre dans la structure cristalline, mais aussi au dopage en oxygène x . Par conséquent la structuration des films minces d'YBCO endommagent souvent leurs propriétés supraconductrices si des précautions suffisantes ne sont pas appliquées. L'utilisation de l'YBCO pour en faire des SSPDs est donc un défi de nanofabrication : à la fois pour la croissance des couches minces mais aussi pour y réaliser des nanofils tout en gardant de très bonnes propriétés supraconductrices homogènes le long du fil.

L'élément constitutif d'un SSPD est un long méandre de plusieurs centaines de microns de long avec une largeur d'environ 50 nm. Ils sont réalisés à partir de films supraconducteurs ultra minces (habituellement un supraconducteur à basse température critique comme Nb, NbN...) de quelques nanomètres d'épaisseur. Afin de détecter un photon unique, le nanofil est refroidi dans son état supraconducteur et polarisé en courant : la tension à ses bornes est nulle. Lorsqu'un photon unique est absorbé par le nanofil, une zone normale appelée point chaud se forme localement au sein du fil. Ce dernier s'étend jusqu'à couvrir toute une section du fil générant ainsi un court pulse de tension : c'est la signature de la détection d'un photon. De nombreux modèles théoriques ont été développés pour tenter de décrire l'ensemble des observations expérimentales associée au phénomène de détection dans les SSPDs. Les dernières recherches à ce sujet montrent l'importance des vortex supraconducteurs dans la création du pulse de tension, sans parvenir à un con-

sensus. A ce jour, il n'existe pas encore de mécanisme microscopique qui englobe toutes les expériences.

Par ailleurs, l'YBCO présente plusieurs particularités par rapport aux matériaux supraconducteurs conventionnels tels qu'un paramètre d'ordre de symétrie d et un temps de diffusion électron-phonon court. Ces paramètres spécifiques de l'YBCO pourraient changer drastiquement le mécanisme de détection d'un photon unique dans ce matériau. De plus, la compréhension théorique de la supraconductivité dans ce matériau reste un des défis majeurs de la matière condensée à ce jour. Il n'est donc pas possible de prédire théoriquement si l'YBCO peut ou non, détecter un photon unique. Pour contrecarrer cet écueil, la thèse présentée ici consiste à fabriquer et caractériser des nanofils en YBCO avec pour objectif de détecter des photons uniques.

Détection de photons uniques

Le chapitre 1 présente la détection de photons uniques dans son ensemble, depuis les applications jusqu'aux technologies utilisées. Nous donnons en premier lieu les applications principales de la détection de photons uniques. Parmi celles-ci, nous détaillons brièvement son intérêt pour l'information quantique et l'imagerie LIDAR (light detection and ranging). Ceci nous permet d'exposer simplement les enjeux de la détection de photons uniques d'un point de vue technologique. Par la suite, nous introduisons les différents paramètres qui caractérisent un détecteur de photons uniques, à savoir : l'efficacité de détection, le taux de comptage noir, le temps de réinitialisation, la gigue temporelle, la résolution du nombre de photons et sa gamme spectrale. Ces paramètres permettent de comparer des détecteurs afin de choisir le plus adapté selon l'application souhaitée.

Il existe déjà de nombreuses technologies pour détecter des photons uniques. Afin de mettre en perspective la technologie SSPD, nous présentons succinctement deux autres types de détecteurs semi-conducteurs largement utilisés aujourd'hui : le tube photomultiplicateur (PMT) et la diode à avalanche à photon unique (SPAD). Nous examinons rapidement le fonctionnement de chacun des détecteurs ainsi que leur degré de maturité. Les détecteurs PMT et SPAD ont été respectivement inventés en 1937 et 1964, à ce titre ce sont des technologies matures qui ont bénéficié d'importants efforts de développement. Enfin, nous présentons le mécanisme de détection d'un SSPD avec les dernières avancées technologiques réalisées pour en améliorer les performances. Notons que le premier SSPD a été développé en 2001 par Gol'tsman *et al.* [1, 2]. En deux décennies, les SSPDs se sont imposés comme les détecteurs présentant les meilleures performances tous paramètres confondus à l'exception de la température de fonctionnement. Afin de pallier à ce défaut, différents matériaux supraconducteurs de température critique plus élevées ont été envisagés tel que MgB2 [3] ou WSi [4]. Cependant, aucun d'entre eux n'a permis une augmentation drastique de la température de fonctionnement qui reste pour l'instant en dessous de 5 K.

Physique des nanofils supraconducteurs

Dans le chapitre 2, nous donnons les concepts physiques nécessaires à la compréhension des phénomènes mis en jeu dans les nanofils supraconducteurs. Le chapitre débute par un bref rappel de la supraconductivité. Il explicite les observations expérimentales au sein d'un matériau supraconducteur, à savoir une conductivité et un diamagnétisme parfaits. La première observation se manifeste par une résistivité nulle en dessous de la température critique T_c telle qu'observée par Kamerlingh Onnes en 1911 [5], alors que la seconde observation - aussi connu sous le nom d'effet Meissner - implique un flux magnétique nul

à l'intérieur du matériau supraconducteur. Ensuite, nous exposons les différentes théories - phénoménologiques et microscopiques - qui permettent d'expliquer en partie la supraconductivité : les équations de London [6, 7], la théorie Ginzburg-Landau [8] et la théorie Bardeen-Cooper-Schrieffer [9]. Enfin, nous présentons les propriétés supraconductrices particulières de la supraconductivité dans l'YBCO.

La fabrication de nanofils sont réalisées à partir de couches ultra minces. Il est important de noter que la température critique de l'YBCO est dégradée lorsque son épaisseur d est de plus en plus faible [10]. Il est difficile de réaliser des films minces avec des hautes T_c . Notons que les modèles théoriques présentés ci-dessus ne peuvent s'appliquer *stricto sensu* à l'YBCO. De plus, ils ne permettent pas d'élucider le mécanisme microscopique de la supraconductivité dans l'YBCO.

D'après les modèles théoriques, deux longueurs caractéristiques des supraconducteurs sont à considérer : la longueur de pénétration magnétique $\lambda(T)$ et la longueur de cohérence supraconductrice $\xi(T)$. Selon la valeur du paramètre de Ginzburg-Landau $\kappa = \lambda/\xi$, on peut classer les supraconducteurs dans deux catégories. Dans le cas où $\kappa > 1/\sqrt{2}$, cas de l'YBCO, le supraconducteur est dit de type II. En présence d'un champ magnétique dans de tels matériaux on observe l'apparition de vortex supraconducteurs [11]. Un vortex supraconducteur porte un quantum de flux magnétique $\Phi_0 = h/2e$ qui s'oppose au champ magnétique [12]. La présence de vortex dans les supraconducteurs de type II donnent lieu à de nombreux phénomènes. En particulier, les vortex sont à l'origine de certains mécanismes de détection de photons uniques dans les SSPD.

Par la suite, nous détaillons quelques phénomènes qui ont lieu dans les supraconducteurs lorsque certaines dimensions du système étudié sont réduites tels que l'effet Josephson [13–15], le glissement de phase [16, 17] et le mouvement des vortex [18, 19]. Chacun des phénomènes a des origines physiques bien distinctes, mais tous peuvent donner lieu à des signatures expérimentales similaires. En particulier, l'application d'ondes électromagnétiques radiofréquences (RF) génèrent des marches de courant à des tensions définies par la constante de Josephson. Dans le cadre des jonctions Josephson on les nomme marches de Shapiro [20] et elles sont dues aux relations Josephson qui lient les deux réservoirs supraconducteurs. Par contre, dans le cas de fil supraconducteur, les marches sont issues du mouvement cohérent de vortex synchronisé aux ondes RF. Ainsi, l'apparition de telles marches ne permet pas de conclure de manière univoque sur son origine. Il est donc nécessaire de réaliser des expériences *ad hoc* afin de déterminer cette dernière. Ces aspects permettent de définir les termes physiques nécessaires à l'interprétation des expériences qui seront exposés dans les chapitres suivants.

Pour terminer le chapitre, nous présentons les mécanismes de détection de photons uniques qui ont été proposé depuis la première réalisation d'un SSPD par Gol'tsman *et al.* [1] en 2001. Ces mécanismes prennent leur sources dans les travaux de Rothwarf et Taylor [21] ainsi que dans le modèle à deux températures appliqué aux supraconducteurs [22]. Tous deux sont présentés en premier lieu afin de mieux comprendre les interactions à considérer lorsqu'un supraconducteur absorbe un photon. Ensuite, nous détaillons les différentes observations expérimentales réalisées dans les SSPDs : l'évolution de l'efficacité de détection en fonction du courant critique, la relation entre le courant et l'énergie du photon ou encore la réponse du détecteur en présence d'un champ magnétique. Toutes ces observations permettent de valider ou rejeter un modèle théorique de détection de photons uniques. Les premiers modèles présentés dans les fig. 1(a-b) suggèrent l'apparition locale d'un point chaud normal au niveau de l'absorption du photon [23]. Le modèle initial (fig. 1(a)) ne permettant pas d'expliquer toutes les observations, il a été ensuite raffiné en y introduisant la diffusion des quasiparticules hors de la zone normale (fig. 1(b)) par Semenov *et al.* [24]. Malheureusement, même avec ces ajouts le modèle n'est pas complet puisqu'il ne permet pas d'expliquer que l'efficacité quantique de détection varie

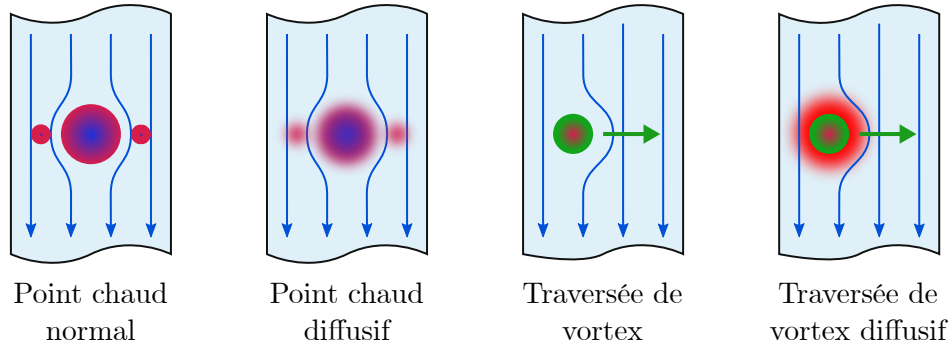


Figure 1 – Schémas de différents modèles de détection de photons uniques dans les SSPDs. Les figures (a) et (b) supposent la création d’un point chaud normal au niveau de l’absorption du photon, alors que les figures (c) et (d) considèrent que l’absorption d’un photon unique assiste le passage d’un vortex à travers le nanofil.

de manière exponentielle avec le courant I [25]. Afin de combler ces failles, plusieurs modèles ont inclus la présence de vortex dans le mécanisme de détection [26–31]. Dans cette interprétation, l’absorption d’un photon permet d’abaisser la barrière énergétique d’un vortex traversant le nanofil. Lors de sa traversée, le vortex dissipe de l’énergie et génère un pulse de tension comme présenté dans les fig. 1(c-d). Ces améliorations du modèle de point chaud sont pertinentes puisqu’elles permettent d’expliquer des observations expérimentales supplémentaires tel que l’effet du champ magnétique sur la détection. Cependant, ils n’arrivent pas à rendre compte de toutes les expériences. Par conséquent, la compréhension du mécanisme de détection de photons uniques dans les SSPDs restent encore incomplet à ce jour. Partant de ce constat, il n’est actuellement pas possible de faire des prévisions quantitatives raisonnables sur la réalisation de SSPD en YBCO. Pour pallier cet écueil, la thèse présentée dans ce manuscrit aborde la réalisation des SSPDs en YBCO d’un point de vue expérimental en fabriquant les nanofils puis en les caractérisant.

Fabrication de nanofils en YBCO par irradiation ionique

Le chapitre 3 s’attarde sur la fabrication de nanofils supraconducteurs sur des films minces d’YBCO. Malgré les nombreux procédés de fabrication développés dans différents groupes à travers le monde, la détection de photons uniques par des matériaux supraconducteurs à haute température n’a toujours pas été démontré. L’YBCO oppose deux difficultés majeures : le mécanisme de détection et les difficultés rencontrées lors de la fabrication de dispositifs ayant des dimensions suffisamment réduites. La difficulté d’une telle fabrication réside dans le fait que les propriétés supraconductrices du matériau sont très sensibles au dopage en oxygène x et au désordre dans la structure cristalline. Ceci devient encore plus crucial lorsqu’il s’agit de réaliser des nanostructures sur des films de faibles épaisseurs ayant également des largeurs réduites [32–34]. Le plus souvent les nanofils sont réalisés en gravant le film supraconducteur sous forme de fils. Pour limiter la dégradation des propriétés supraconductrices au sein du fil une couche supplémentaire est déposée sur le film d’YBCO [35–39]. Cette dernière permet de protéger les dispositifs afin de limiter les effets délétères lors de la gravure avec notamment la pénétration des ions Ar^+ .

Lors de cette thèse, nous avons développé une technique de nanofabrication basée sur l’irradiation par des ions oxygène de haute énergie présentée en fig. 2). Cette technique est utilisée depuis plus d’une quinzaine d’année afin de réaliser des jonctions Josephson (JJ) [40–42]. Ici, nous avons adapté et optimisé l’irradiation ionique pour réaliser des

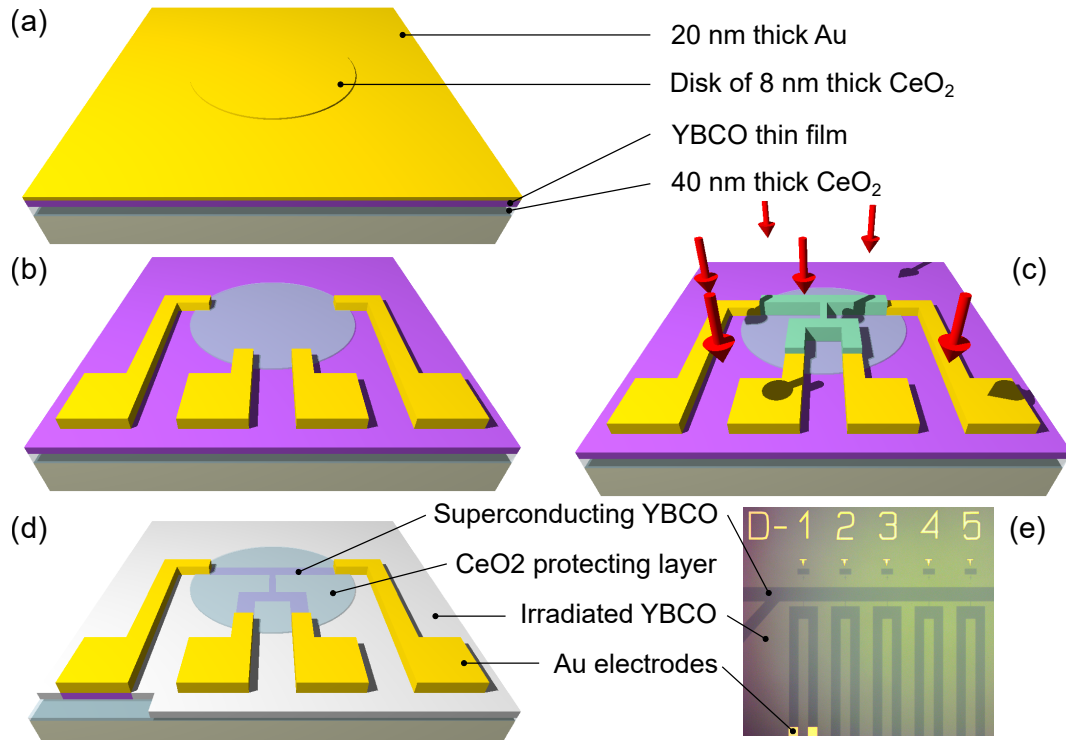


Figure 2 – (a) Composition type des films minces en YBCO utilisés dans cette thèse. Le film en YBCO est protégé en son centre par un disque d'une fine couche d'oxyde de cérium, le tout recouvert d'une couche d'or. (b) Après une première lithographie, les électrodes en or sont réalisées. (c) Une seconde lithographie permet de protéger certaines parties d'YBCO lors de l'irradiation ionique. On définit ainsi les électrodes supraconductrices et les nanofils en YBCO. (d) Une fois la fabrication terminée, les nanofils sont enterrés dans une matrice d'YBCO isolante en gris et un disque protecteur de CeO_2 . (e) Image optique de nanofils supraconducteurs connectés aux électrodes en or via des électrodes supraconductrices.

nanofils ayant une largeur pouvant descendre jusqu'à 100 nm sur des films minces d'YBCO ayant une épaisseur jusqu'à 12 nm. Comme annoncé précédemment, l'YBCO est sensible au désordre, à tel point qu'en introduisant des défauts dans la structure cristalline il est possible de passer la transition supraconducteur-isolant [43]. Ceci signifie que le matériau devient isolant lorsque le nombre de défauts par atomes (*dpa*) est suffisamment grand. L'irradiation ionique permet d'introduire de façon contrôlée de tels défauts dans la structure cristalline. Ainsi, en protégeant certaines parties du film supraconducteur puis en irradiant le tout par un faisceau d'ions à haute énergie, les zones protégées restent supraconductrices alors que celles exposées à l'irradiation deviennent isolantes. Ce procédé est fondamentalement différent de la gravure en ce qu'il ne retire pas la matière lors de l'irradiation, mais il introduit seulement des défauts dans la structure cristalline.

Nous avons mis au point une structure de film mince originale en partenariat avec nos fournisseurs de couches d'YBCO. Nous avons deux sources différentes de films minces d'YBCO. Les premiers sont réalisés par l'entreprise Ceraco GmbH qui propose une large gamme de films d'YBCO de différentes épaisseurs déposés sur différents substrats. Les seconds films sont réalisés par Javier Briatico au sein de l'UMR CNRS-Thales dans le cadre d'une collaboration académique. Javier et son équipe maîtrise le dépôt de couche mince d'YBCO jusqu'à des épaisseurs de quelques nanomètres tout en conservant des propriétés supraconductrices d'excellente qualité [44]. Ces derniers sont constitués d'une

couche mince d'YBCO protégée au centre par un disque d'oxyde de cérium (CeO_2) comme présentée sur la fig. 2. A la fin du procédé de nanofabrication les nanofils d'YBCO sont complètement encastrés dans une matrice isolante et ils ne sont jamais en contact avec l'air tout au long du procédé de fabrication. Sur les côtés l'YBCO est isolant et au dessus le dispositif est protégé par une couche de 8 nm d'oxyde de cérium (CeO_2) stœchiométrique et un dépôt d'or in-situ pour réaliser les contacts électriques. Par conséquent, les dispositifs sont protégés contre la diffusion d'oxygène - qu'elle soit latérale ou verticale - mais aussi de toute réaction avec l'environnement sachant que le CeO_2 est stœchiométrique.

Afin de réaliser l'irradiation ionique, il faut choisir les ions qui seront envoyés, leur énergie et la dose d'ions associée. Nous avons envisagé deux techniques pour irradier les films d'YBCO : un implantateur d'ions oxygène O^+ pleine plaque et un faisceau focalisé d'ions hélium He^+ . La première a l'avantage de ne pas introduire d'atomes différents de la composition du matériau supraconducteur. De plus, c'est une méthode qui a été largement éprouvée pour le dopage des semi-conducteurs puis la fabrication de JJs. Un large faisceau d'ions O^+ balaye la cible - dont certaines zones sont protégées - pour réaliser une irradiation homogène, ceci permet de réaliser de nombreux dispositifs sur un même film rapidement. A l'inverse, le faisceau focalisé d'ions He^+ envoie les ions localement pour irradier le film, il n'y a donc pas besoin de protéger certaines zones par de la résine. Ceci permet donc d'éviter une étape de lithographie électronique et de contrôler l'irradiation du faisceau au nanomètre près. Quelle que soit la méthode utilisée, la proportion d'ions introduite dans le matériau est négligeable. Afin d'optimiser l'irradiation - en particulier l'énergie et la dose des ions - nous utilisons le logiciel de simulation Monte-Carlo SRIM. Il permet de modéliser les trajectoires des ions de haute énergie envoyés dans un empilement de différents films déposés sur un substrat dont l'YBCO et le CeO_2 . Après une analyse numérique supplémentaire, nous pouvons estimer la proportion de défauts introduite dans le matériau dans l'espace selon le motif réalisé. Ainsi, nous pouvons estimer l'étendu de la zone d'YBCO qui est restée supraconductrice suite à l'irradiation ionique. Nous avons utilisé des ions O^+ et He^+ avec une énergie de 30 keV et des doses de quelques 10^{14} ions. cm^{-2} et 10^{15} ions. cm^{-2} respectivement. Nous verrons par la suite dans le chapitre 4 que l'irradiation pleine plaque avec des ions O^+ donnent les meilleurs résultats. Grâce à cette technique nous avons pu réaliser des nanofils robustes sur des films minces en YBCO avec d'excellentes propriétés supraconductrices.

A la fin du chapitre 3, nous présentons le procédé de nanofabrication dans sa globalité depuis la réception du film mince d'YBCO jusqu'à la réalisation des nanofils encapsulés dans la matrice isolante. Ensuite nous présentons les différents étapes et tests qui ont été mis en place pour obtenir les nanofils supraconducteurs. Grâce à ce procédé nous pouvons réaliser des nanofils de différentes formes, connectés en DC ou couplé à un guide d'onde coplanaire pour acheminer un signal RF.

Caractérisation électrique

Le chapitre 4 présente la caractérisation des dispositifs supraconducteurs une fois qu'ils sont fabriqués. Nous présentons les montages expérimentaux associés et les paramètres pertinents que l'on peut extraire de ces caractérisations. Une fois que les dispositifs sont placés sur le porte échantillon et connectés par le biais d'électrodes et de microsoudures, le tout est placé dans un cryostat où l'on peut contrôler la température, appliquer un courant et mesurer la tension.

Nous mesurons d'abord la résistance 4 points du nanofil en fonction de la température pour déterminer s'il y a une transition d'un état normal vers un état supraconducteur en dessous de la température critique T_c . La valeur de T_c comparée à la valeur mesurée

avant la nanofabrication permet de déterminer s'il y a eu un endommagement au cours de cette dernière. De plus la valeur de la résistivité à 100 K est un autre paramètre pertinent pour comparer la qualité des nanofils de différentes formes entre eux et ainsi s'affranchir des dimensions du dispositif. Pour chaque courbe résistance-température (RT) mesurée nous avons deux paramètres pour caractériser le dispositif : la température critique T_c et la résistivité à 100 K $\rho(100\text{ K})$. Pour des films de 30 nm, $T_c \approx 90\text{ K}$, plus la T_c d'un dispositif est proche de cette valeur, meilleur est le nanofil. En réalisant cette mesure sur les différents films et nanofils réalisés nous montrons que l'irradiation ionique par des ions O^+ fournit les meilleurs résultats par rapport au faisceau focalisé d'ions He^+ . En particulier, la reproductibilité est bien meilleure avec les ions O^+ . La seconde méthode propose des perspectives intéressantes mais requiert un travail d'optimisation pour en tirer les avantages. Outre les mesures quantitatives de paramètres, la forme de la transition nous donne aussi des informations précieuses sur la qualité du dispositif. Si la chute de résistance est droite en échelle logarithmique nous pouvons conclure que le nanofil possède une T_c homogène tout le long du fil. Au contraire, si un épaulement apparaît dans la transition c'est le signe que différentes T_c existent le long du fil. Selon l'importance de l'épaulement en terme de résistance par rapport à la résistance totale, tout le nanofil peut être endommagé, ou bien seulement une partie au niveau d'une inhomogénéité. Pour des nanofils de plus de 100 nm de large, nous avons montré que le procédé d'irradiation ionique par oxygène est viable et reproductible.

Si le nanofil présente une transition supraconductrice satisfaisante, nous mesurons les caractéristiques courant-tension (IV) associées à l'état supraconducteur dans une large gamme de température de 5 K jusqu'à la température critique. Ces données permettent de déterminer des propriétés supraconductrices supplémentaires du dispositif, en particulier les courants caractéristiques. Afin de s'affranchir des dimensions du nanofil nous convertissons le courant en densité de courant $j = I/wd$ où w et d sont respectivement la largeur et l'épaisseur du nanofil. Nous pouvons observer jusqu'à trois densités de courant caractéristiques dans la courbe densité de courant tension (jV) : la densité de courant critique j_c , la densité de courant d'échappement j_s et la densité de courant de retour j_r .

La densité de courant critique j_c correspond au courant à partir duquel une tension non nulle se développe aux bornes du nanofil. La densité de courant critique est limitée théoriquement par la densité de courant de brisure de paires dans la théorie de champ moyen de Ginzburg-Landau j_d . Celle-ci représente une valeur cible vers laquelle il faut tendre pour améliorer les propriétés du nanofil. Plus la densité de courant critique mesurée s'approche de cette valeur théorique, plus on peut polariser le nanofil avec un courant élevé et donc améliorer les conditions pour détecter un photon unique. Nous avons mesuré la densité de courant critique d'un grand nombre de nanofils supraconducteurs de différentes dimensions. Grâce à l'optimisation des procédés de nanofabrication, nous avons pu augmenter significativement sa valeur d'un ordre de grandeur, et ce, pour une largeur de nanofil jusqu'à 100 nm. Comme nous pouvons le voir dans la fig. 3(a), la densité de courant maximale atteinte pour une largeur donnée est sensiblement la même quelle que soit la largeur comprise entre 100 nm et 1 μm . Les dispositifs fabriqués atteignent une densité de courant critique d'environ 20% du courant de brisure de paire j_d .

Selon la valeur de j_c nous pouvons observer deux types de comportements dans la caractéristique jV . Si $j_c < 5 - 10\text{ MA.cm}^{-2}$ la tension augmente de manière continue lorsque le courant augmente jusqu'à atteindre un régime linéaire correspondant à l'état normal résistif du nanofil. Ce comportement est non hystérétique, il correspond à un pur régime de flux flow comme présentée dans la fig. 3(c). Au contraire, si $j_c > 5 - 10\text{ MA.cm}^{-2}$, lorsque le courant augmente nous observons pour une tension de l'ordre du millivolt un saut de tension abrupt vers un régime linéaire ohmique comme on peut l'observer sur la fig. 3(b). La densité de courant associée à ce saut correspond à la densité de courant

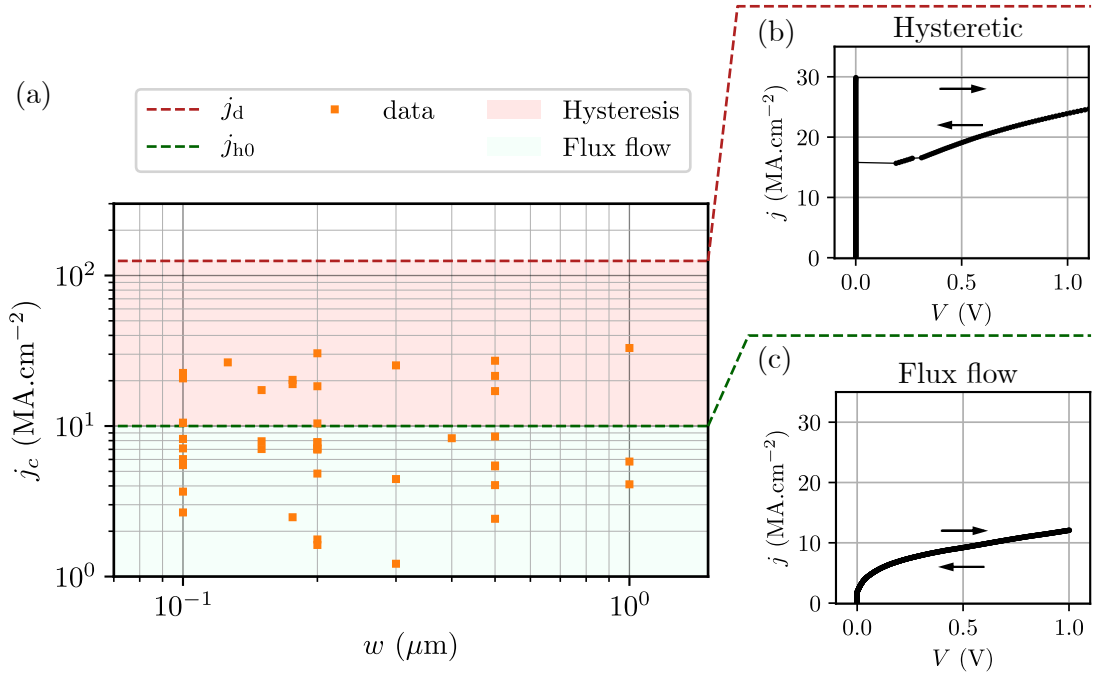


Figure 3 – (a) Évolution de la densité de courant critique j_c en fonction de la largeur du nanofil w à 5 K. Dans la zone verte, les fils ont un comportement de type flux flow comme on peut l’observer en (c), alors que dans la zone rouge les courbes IV sont fortement hystérétiques comme c’est le cas en (b). La ligne rouge en pointillé représente la limite théorique définie par la densité de courant de brisure de paires j_d . La ligne verte en pointillé représente la limite entre le régime de flux flow et l’apparition de l’hystérèse observée expérimentalement.

d’échappement j_s . Cette fois-ci, la courbe jV est hystérétique : lorsque le courant décroît le saut de tension apparaît pour une valeur de densité de courant plus faible que j_s , à la densité de courant de retour j_r . Plus le courant critique est important, plus l’étendue en courant de l’hystérèse est large.

Afin de mieux saisir ce comportement nous avons modélisé les données d’après le modèle thermique développé par Skocpol, Beasley et Tinkham [45]. Ce dernier permet d’estimer la densité de courant de retour à partir des propriétés thermiques du matériau. Lorsque le nanofil est dans l’état normal, la partie normale du nanofil génère de l’énergie thermique via l’effet Joule. Le nanofil peut dissiper cette énergie via le substrat et les réservoirs supraconducteurs, mais si la densité de courant est trop importante le nanofil reste dans l’état normal. Grâce à ce modèle nous pouvons modéliser l’évolution de la densité de courant de retour en fonction de la température depuis la température critique jusqu’à 30 K. Nous pouvons conclure que le courant de retour et l’apparition de l’hystérèse sont gouvernés par les propriétés thermiques du nanofils. Cependant, ce modèle ne nous donne pas d’information sur le saut de tension associé au courant d’échappement. Cet aspect sera étudié plus en détail dans le dernier chapitre.

Par ailleurs, plusieurs modèles décrivent l’évolution de j_c en fonction de la température. En modélisant les données, nous avons déduit que la densité de courant critique est limitée par le piégeage dûes aux fluctuations du libre parcours moyen (δl -pinning) d’après le modèle de Griessen *et al.* [46].

Le comportement d’un SSPD est caractérisé par sa réponse dynamique, elle-même déterminée par son inductance. L’inductance fixe le temps de réinitialisation effectif du SSPD après la détection d’un photon. La mesure de l’inductance du nanofil est donc d’une

importance majeure en vue de la détection. Nous avons caractérisé par des mesures de résonance radiofréquence des nanoméandres de plusieurs centaines de microns de long. Ces mesures permettent d'estimer l'inductance L du dispositif et sa longueur de pénétration magnétique λ_0 . En plus de cela, l'estimation de λ_0 permet d'évaluer la qualité du dispositif en comparant cette valeur à celle dans les films minces bruts. Pour l'expérience nous avons réalisé un circuit résonant RLC où le nanoméandre agit en tant qu'inductance. Cette dernière est constituée d'une inductance géométrique - fixée par les dimensions du dispositif - et d'une inductance cinétique qui provient de l'inertie des paires de Cooper dans l'état supraconducteur. La mesure du coefficient de réflexion Γ par un analyseur de réseau permet d'observer la résonance du système à une fréquence de l'ordre de 100 MHz. La mesure de la fréquence de résonance permet ainsi d'estimer l'inductance du nanofil. En répétant cette mesure en fonction de la température nous obtenons l'évolution de l'inductance totale en fonction de la température dans l'état supraconducteur. L'inductance géométrique ne dépend que de la géométrie du nanofil [47] alors que l'inductance cinétique varie fortement avec la température et diverge proche de T_c d'après le modèle phénoménologique de Gorter Casimir [48] adapté au cas de l'YBCO [41, 49–51]. L'évolution en température de l'inductance totale peut ainsi être modélisée pour estimer la contribution de chaque inductance. Sachant que l'inductance cinétique dépend de la longueur de pénétration magnétique [48], nous avons pu extraire λ_0 . Les valeurs mesurées sont cohérentes avec celles obtenues dans la littérature pour des films minces d'YBCO [49, 51]. Ces mesures prouvent une fois de plus que la technique d'irradiation ionique permet de réaliser des nanofils en YBCO tout en gardant de bonnes propriétés supraconductrices. Ceci est d'autant plus remarquable que les nanofils utilisés dans cette expérience ont des longueurs de plusieurs centaines de microns comparable à la longueur des nanofils utilisés dans les SSPD à base de supraconducteurs à basse température.

En conclusion, le chapitre 4 nous a permis de vérifier grâce à différentes caractérisations que les nanofils en YBCO fabriqués par irradiation ionique sont robustes et que le procédé est reproductible. Les fils les plus courts, de 500 nm de long, présentent les meilleures propriétés. En particulier, ils ont une densité de courant critique théorique d'environ 20% du courant de brisure de paires et un large saut de tension. Afin d'étudier plus en détail la possibilité de détecter un photon unique avec des nanofils en YBCO, la suite du manuscrit se focalise sur des fils courts de 500 nm de long.

Dynamique de vortex dans les nanofils en YBCO

Le chapitre 5 est consacré à l'étude détaillée de nanofils d'YBCO de 30 nm d'épaisseur et de 500 nm de long. D'après les derniers modèles théoriques présentés dans le chapitre 2, les vortex jouent un rôle prépondérant dans les SSPDs pour la détection de photons uniques et le comptage noir. Dans le chapitre 5, nous présentons la dynamique des vortex dans les différents régimes des caractéristiques IV et dans l'apparition de pulses de tension. La fig. 4 présente chacun des régimes dans les différents états du nanofil. Nous nous intéressons essentiellement aux régimes dans l'état mixte qui sont associés à la dynamique des vortex au sein du fil.

En premier lieu, nous étudions le régime de tension qui se développe après le courant critique. Cette branche dissipative est décrite par la théorie de flux creep initialement développée par Anderson et Kim [52], puis appliquée à des microponts en YBCO par Bernstein *et al.* [53]. Dans le cadre de ce modèle, les vortex sautent entre des sites de piégeage présents dans les nanofils grâce à l'action combinée de la force de Lorentz et de l'agitation thermique. En modélisant les courbes IV par ce modèle, nous obtenons un bon accord qualitatif de 5 K jusqu'à 40 K. Pour des températures plus élevées, un autre

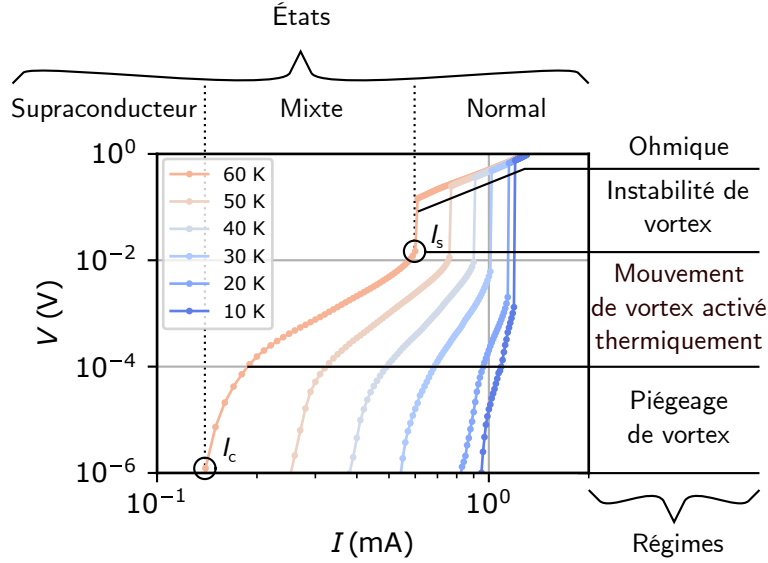


Figure 4 – Caractéristiques IV à différentes températures d'un nanofil d'YBCO de 500 nm de long 200 nm de large et 30 nm d'épaisseur. Différents régimes de dissipation existent dans la caractéristique IV selon la tension qui se développe aux bornes du nanofil listés dans la colonne de droite. Dans l'état supraconducteur, la tension est nulle. Dans l'état mixte, la tension est due au mouvement des vortex, tandis que dans l'état normal la tension suit un comportement ohmique.

mécanisme doit être prise en compte. L'évolution des paramètres du modèle en fonction de la température est cohérente avec celle observée dans la littérature [53, 54]. Cependant, la faible valeur de ces paramètres suggère que le piégeage des vortex est relativement faible dans nos nanofils. Ce modèle confirme que le comportement des nanofils en dessous de $T_c/2$ est gouverné par le piégeage de vortex.

Par la suite, nous étudions le comportement des caractéristiques IV lorsqu'un signal RF est envoyé sur le nanofil. Comme on peut le voir dans la 5(a), nous observons l'apparition de marches de courant aux tensions V_n déterminées par la fréquence du signal RF f et le quantum de flux magnétique $\Phi_0 = h/2e$ telles que :

$$V_n = n\Phi_0 f \quad (1)$$

où $n \in \mathbb{N}$. Ceci correspond à la même signature observée dans le cas de jonctions Josephson. En comparant nos résultats avec ceux obtenus dans le cas de jonctions Josephson en YBCO fabriquées par la technique d'irradiation ionique [55, 56] nous montrons que les causes sont bien distinctes. Dans le cas de nanofils supraconducteurs, l'apparition de marche n'est pas le résultat de l'effet Josephson [20] mais celui du mouvement cohérent de vortex synchronisé à la fréquence du signal RF [18, 57]. Nous observons les marches de courant pour différentes températures que ce soit proche de T_c ou à basse température à 6 K. L'observation des marches à différentes fréquences démontre que la fréquence détermine bien la tension à laquelle apparaît les marches. De plus, la modulation de la hauteur des marches en fonction de la puissance du signal RF nous donnent des arguments supplémentaires pour conclure que le phénomène observé n'est pas issue d'une jonction Josephson. Enfin, nous avons également observé l'apparition de marches fractionnaires où $n \in \mathbb{Q}$ tel que $n = k/q$ avec k et q deux nombres entiers. Ce phénomène est plus facilement perceptible en observant la résistance dynamique $R_d = \partial V / \partial I$ comme présentée sur la fig. 5(b), où les marches correspondent désormais à des zones telles que la résistance dynamique est nulle, hormis dans la branche supraconductrice. D'après Likharev [14],

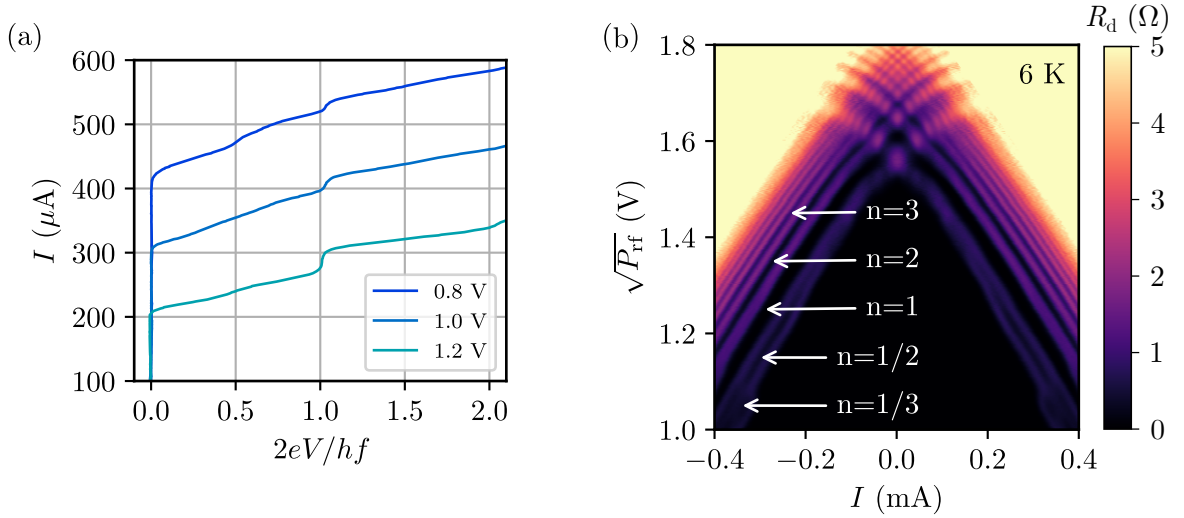


Figure 5 – (a) Caractéristique IV dans un nanofil en YBCO sous illumination RF à différentes puissances. (b) Évolution de la résistance dynamique R_d en fonction du courant et de la puissance RF à 6 K. Les flèches indiquent les marches entières et fractionnaires.

l'apparition de telles marches correspond à la synchronisation au mouvement de vortex de k lignes à la fréquence f_v , et ce, de façon synchronisé à des sous-harmoniques du signal RF f tel que : $f = qf_v$. Les différents arguments exposés dans cette partie montrent que l'interprétation en terme de mouvement cohérent de vortex est la plus pertinente dans le contexte des nanofils supraconducteurs en YBCO. Des simulations numériques basées sur les modèles de Likharev [18] et/ou d'Aslamazov [57] permettraient d'apporter un aspect quantitatif à l'analyse de nos résultats.

Dans une troisième partie, nous avons étudié le régime de tension au-delà du phénomène de flux creep avant l'apparition du saut de tension, *i.e.* toujours dans l'état mixte. Pour cela, nous avons étendu le modèle basé sur le mouvement de vortex thermiquement activé (TAVM) [58, 59] en introduisant l'interaction électromagnétique entre les vortex. Le modèle TAVM décrit la traversée d'un vortex perpendiculairement au courant au sein d'un fil supraconducteur dans un film mince. Dans le cadre de ce modèle, il est possible de calculer le profil énergétique du vortex dans la largeur du fil en présence d'un courant. En considérant que l'agitation thermique permet le passage de la barrière énergétique par le vortex, la tension peut s'exprimer en fonction du maximum du profil énergétique par une loi d'Arrhénius. Il est ainsi possible de simuler les courbes IV dans une gamme de tension intermédiaire. Un tel modèle ne permet pas de modéliser nos données avec des paramètres physiques cohérents. En particulier, la longueur de pénétration magnétique de Pearl est bien trop élevée par rapport à ce qu'elle devrait être. Afin d'obtenir une meilleure description quantitative des données nous avons introduits en supplément l'énergie d'interactions de vortex calculée par Kogan [60]. Grâce à cette modification nous pouvons décrire la tension avec des paramètres physiques cohérents et obtenir une distance inter vortex inférieure à la largeur du fil. D'après cette interprétation, comme dans le cas du flux creep, la traversée du vortex est encore une fois l'origine de la tension mais l'agitation thermique et la force de Lorentz étant plus importantes les vortex traversent de manière continue la largeur du fil sans ressentir les sites de piégeage.

La dernière partie du chapitre se concentre sur l'apparition de pulses de tension. Ils correspondent à des événements de détection liés à l'absorption de photons uniques ou bien à de faux événements de détection dus au passage d'un vortex. Pour observer ces événements, le nanofil est polarisé avec un courant proche mais en-dessous du courant

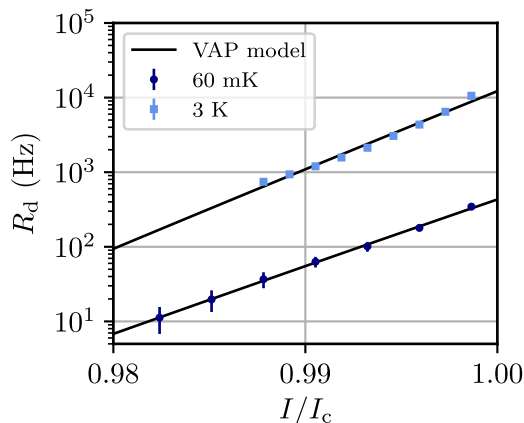


Figure 6 – Évolution du taux de comptage noir en fonction du courant de polarisation normalisé par le courant critique dans un nanofil d’YBCO à 60 mK et 3 K. Les Lignes noires représentent la modélisation des données d’après le modèle de brisure de paire VAP thermiquement activée.

critique tel que le fil soit dans l’état supraconducteur. Grâce à un système expérimental spécifique, le nanofil est polarisé avec un courant DC, tandis que le signal AC généré par le nanofil est collecté puis amplifié. Les pulses de tension sont contenus dans le signal AC. Ils peuvent être observés grâce à un oscilloscope, ou bien comptés à l’aide d’un compteur de pulses. Nous avons observé des pulses de tension dans les nanofils d’YBCO à 60 mK et 3 K en l’absence de lumière, ce sont donc de faux événements de détection. L’étude du taux de comptage de pulses en fonction du courant de polarisation permet d’étudier l’origine des coups d’obscurité. Plusieurs modèles théoriques ont été développés pour rendre compte de cette évolution dans les SSPDs [61–63]. Ejrnaes *et al.* [64] ont observé récemment des pulses de tension dans des nanofils d’YBCO à 4.9 K. Ils ont étudié le taux de comptage en fonction du courant d’après le modèle de brisure de paires vortex-antivortex activée thermiquement. Nous observons qualitativement et quantitativement la même dépendance dans nos dispositifs en YBCO à 3 K (cf fig. 6). Néanmoins, nous observons la même évolution en courant également à 60 mK alors que cette dépendance devrait varier d’un facteur 50 entre les deux températures. Le modèle de brisure de paires vortex-antivortex activée thermiquement est donc incompatible dans notre cas. Ainsi, pour expliquer cette évolution qui ne dépend pas de la température, l’interprétation devrait inclure la traversée de vortex par effet tunnel. Un travail de modélisation supplémentaire est nécessaire pour interpréter quantitativement nos résultats à l’aune de ce modèle. Par ailleurs, l’illumination du nanofil dans le rouge n’a montré aucun effet pour l’instant. Ceci pourrait être causé par une énergie de photons trop faible. Il serait donc particulièrement intéressant d’étudier les nanofils d’YBCO sous illumination UV, *i.e.* avec des photons d’énergie plus importante.

En résumé de ce chapitre, nous avons montré grâce à diverses expériences que les vortex supraconducteurs jouent un rôle prépondérant dans la génération d’une tension aux bornes de nanofils d’YBCO. En particulier, nous avons prouvé que la dynamique des vortex pouvait à la fois être activée thermiquement ou synchronisée par un signal RF. Les expériences de comptage démontrent l’apparition de pulses de tension lorsque le détecteur est dans l’obscurité. L’étude des faux événements de détection est très encourageante et constitue un pas décisif pour mettre en évidence la détection de photons uniques dans le futur. Les travaux présentés dans ce chapitre donne une compréhension générale des phénomènes physiques mis en jeu dans des nanofils d’YBCO de haute qualité fabriqués par irradiation ionique.

Saut de tension dans les nanofils d'YBCO

Dans le chapitre 4 nous avons évoqué l'apparition d'un saut de tension important dans la caractéristique IV sans donner d'interprétation physique. Au niveau du courant d'échappement I_s le nanofil transite de l'état mixte vers l'état normal de manière abrupte. Ce saut de tension est la signature d'un emballement du système électronique. Il est aussi observé dans les SSPDs fabriqués à partir de supraconducteurs à basse température tel que le NbN [65]. Dans ce dernier cas, le saut de tension a lieu depuis la branche supraconductrice - où la tension est nulle - vers l'état normal. Afin de comprendre l'origine physique du phénomène dans nos nanofils en YBCO, le chapitre 6 présente une étude approfondie du saut de tension en fonction de divers paramètres.

Les sauts de tensions sont observés dans divers dispositifs supraconducteurs tels que les jonctions Josephson [66–69], les nanofils supraconducteurs unidimensionnels¹ [70–72] et les fils supraconducteurs en YBCO [39, 73–75]. Dans les deux premiers cas - jonction Josephson et fil supraconducteur unidimensionnel - les fluctuations thermiques ou quantiques sont responsables de l'échappement depuis un état métastable. Ce phénomène est étudié grâce à une analyse statistique du courant d'échappement et des moments statistiques associés à ce dernier, lesquels sont décrits par la théorie de Kurkijärvi-Garg [66, 76]. Dans le cas des fils en YBCO, le plus pertinent pour notre étude, le saut de tension est causé par une accélération brutale des vortex suite à une chute de viscosité. Les vortex accélèrent de plus en plus, au fur et à mesure que le courant augmente. Ceci génère une instabilité dans la configuration dynamique des vortex engendrant un saut de tension. Ce modèle peut être vérifié en étudiant l'évolution des caractéristiques IV en présence d'un champ magnétique externe [73, 77–81]. La description statistique du courant d'échappement dans les deux premiers systèmes apporte une interprétation différente du mécanisme d'échappement. Afin de pouvoir comparer nos résultats avec les différentes théories, nous introduisons les mécanismes dans les trois systèmes.

Dans un second temps, nous définissons les méthodes statistiques qui permettent d'étudier le modèle de Kurkijärvi-Garg. En particulier, il est important d'estimer les moments statistiques suivants : la moyenne, l'écart type, le coefficient d'asymétrie (skewness) et le coefficient d'aplatissement (kurtosis). Leur évolution en fonction de la température donne des renseignements précieux quant à l'origine du mécanisme d'échappement : est-il déclenché par des fluctuations thermiques ou quantiques? Nous présentons ensuite le montage expérimental mis en place pour acquérir un grand nombre de caractéristiques IV , à chaque température, en un temps raisonnable à l'aide d'une rampe de courant et d'un oscilloscope. Cela nous permet d'obtenir deux échantillons de 10 000 courants d'échappement et 10 000 courants de retour afin d'estimer par la suite les moments statistiques associés. L'analyse statistique en fonction de la température du courant de retour nous a permis de valider notre méthode expérimentale. De plus, elle confirme à nouveau que le courant de retour est gouverné par les propriétés thermiques. En effet, les moments statistiques n'évoluent pas avec la température. En ce sens, ce courant est déterministe. A l'inverse, les moments statistiques associés au courant d'échappement évoluent largement en fonction de la température. Lorsque la température baisse en dessous de 50 K, l'écart type associé à I_s augmente jusqu'à atteindre un plateau en dessous de 20 K, alors que les moments statistiques d'ordre supérieurs (coefficients d'asymétrie et d'aplatissement) ont un comportement erratique. Le modèle de Kurkijärvi-Garg ne permet pas de donner une interprétation satisfaisante de ces résultats. Notamment les moments statistiques d'ordre supérieur ne sont pas universels comme cela devrait être le cas en théorie. L'étude des moments statistiques sur différents nanofils en YBCO fournissent les mêmes résultats et

¹Dans le cadre de la supraconductivité, un nanofil est dit unidimensionnel si sa largeur et son épaisseur sont tout deux plus petits que la longueur de cohérence supraconductrice ξ_0 .

confirment que le modèle de Kurkijärvi-Garg ne s'applique pas ici. Nous avons également étudié l'évolution des moments statistiques en fonction d'un champ magnétique extérieur et de la puissance d'un signal RF. Ces expériences suggèrent que la température n'est pas le paramètre physique pertinent pour l'étude du courant d'échappement. Nous avons trouvé que le courant auquel a lieu le saut de tension - *i.e.* le courant d'échappement - semblent être le paramètre qui contrôle l'écart type. Ainsi, cette partie confirme une fois de plus que les nanofils en YBCO présentés dans ce manuscrit n'ont pas le comportement attendu d'une jonction Josephson, ni d'un nanofil supraconducteur unidimensionnel.

Afin de donner une interprétation à nos résultats nous considérons plutôt les modèles basés sur l'instabilité de vortex. Ces modèles ont été initiés par les travaux de Larkin et Ovchinnikov [83] puis appliqués à des microponts en YBCO [73, 75, 84]. Ces travaux étudient l'évolution du courant et de la tension d'échappement en fonction d'un champ magnétique externe pour des températures proches de T_c . Comme le montre la fig. 7, nous avons réalisé ces mesures dans plusieurs de nos nanofils à 100 mK pour des champs magnétiques allant jusqu'à 6 T. Néanmoins l'évolution en champ magnétique n'est pas celle attendue. Nous avons réalisé nos mesures à basses températures, nous ne sommes donc plus dans le domaine de validité de ce modèle. Kunchur [82] a proposé un modèle permettant de décrire le phénomène d'échappement dans des microponts en YBCO en dessous de $T_c/2$. Grâce à ce modèle théorique, nous pouvons correctement modéliser les courbes IV aux différents champs magnétiques appliqués (fig. 7(a)), et nous obtenons une courbe maîtresse comme attendu par le modèle (fig. 7(b)). L'interprétation quantitative des paramètres physiques utilisés pour modéliser nos courbes nécessitent un travail de compréhension supplémentaire. Ceci étant dit, nous pouvons interpréter le saut de tension dans nos nanofils en YBCO comme gouverné par une instabilité de vortex.

Jusqu'à présent, nous avons seulement présenté les moments statistiques du courant d'échappement, c'est-à-dire une mesure globale. Afin d'avoir une vision statistique plus complète, nous étudions également les distributions de courant d'échappement dans nos nanofils dont certaines ont été représentées dans la fig. 8. Proche de la température critique, les distributions sont monomodales et très piquées, *i.e.* avec un écart type faible. Dès lors que la température diminue les distributions s'élargissent d'une part, et en dessous de 40 K, on observe l'apparition d'une distribution bimodale voire trimodale à 6 K. Ces

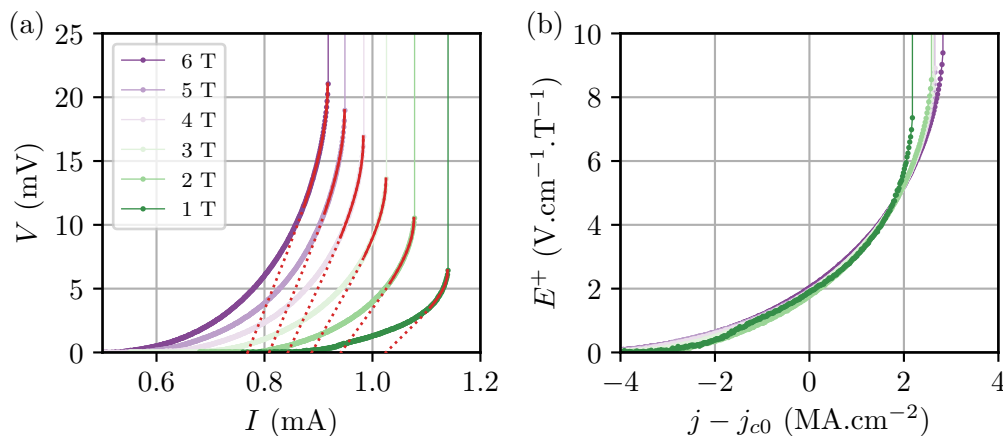


Figure 7 – (a) Courbes IV d'un nanofil d'YBCO sous différents champs magnétiques à 60 mK. Les lignes rouges représentent le modèle théorique développé par Kunchur [82]. (b) Courbe maîtresse obtenue en renormalisant la tension et le courant comme présenté par Kunchur [82].

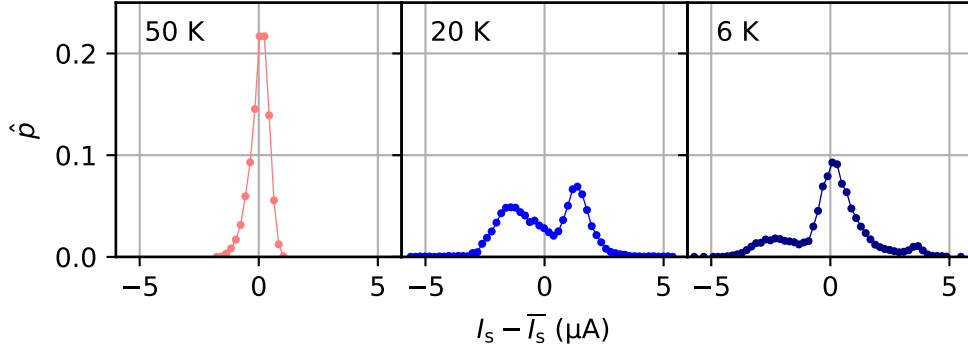


Figure 8 – Histogramme du courant d’échappement centré sur la moyenne du courant d’échappement d’un nanofil d’YBCO à différentes températures. Selon la température la distribution peut être unimodale, bimodale, voire trimodale.

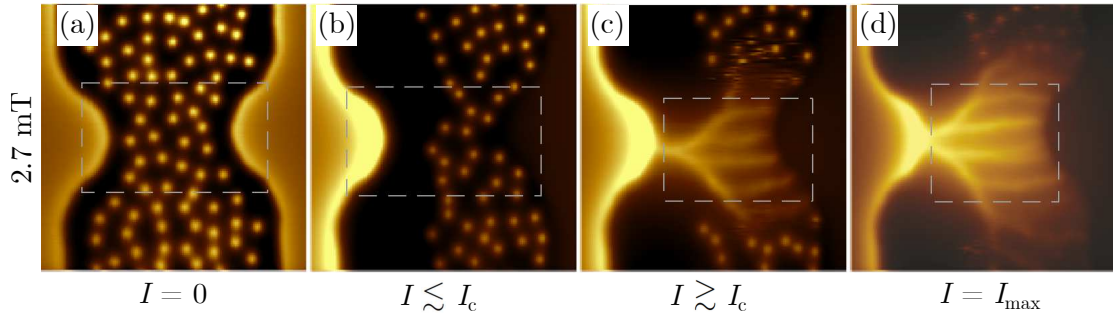


Figure 9 – Imagerie magnétique d’un micropont de Pb sous un champ magnétique de 2.7 mT à 4,2 K. Le micropont est polarisé en courant comme décrit sous chaque image. Selon la valeur du courant de polarisation, les vortex forment différentes configurations qui peuvent être statiques (a-b) ou dynamiques (c-d). Dans les images, chaque point jaune correspond à un vortex. Lorsque les vortex se déplacent, nous observons alors le chemin qu’ils parcourent dans la configuration dynamique. Figure adaptée de Embon *et al.* [85].

deux observations combinées reflètent le fait que l’écart type du courant d’échappement augmente lorsque la température diminue comme nous l’avons observés auparavant. Nous pouvons comprendre physiquement ce phénomène comme suit. D’après le chapitre 5, nous avons vu que les vortex pouvaient former plusieurs lignes pour traverser la largeur du nanofil grâce à la synchronisation RF. De plus, le saut de tension est décrit par une instabilité de vortex. Ainsi, dans l’état mixte avant le saut de tension, les vortex se trouvent dans une configuration dynamique complexe où ils peuvent suivre différents chemins en interagissant avec leurs voisins comme l’imagerie magnétique de vortex en mouvement présentée dans la fig. 9 en témoigne. Selon la configuration de vortex qui se forme au fur et à mesure que le courant augmente, la distribution des lignes de courant au sein du nanofil peut varier tout comme le courant d’échappement associé. A haute température, l’agitation thermique peut permettre de passer d’une configuration de vortex à une autre rapidement de telle sorte que le saut de tension apparaisse toujours avec le même courant d’échappement. Cependant lorsque la température baisse, une fois qu’une configuration de vortex est déterminée, il est moins probable de passer à une autre configuration, ce qui peut générer un saut de tension à un courant d’échappement bien différent. Afin d’approfondir cette interprétation, il serait pertinent d’étudier les échantillons de courant d’échappement pour savoir s’ils ont plutôt un caractère stochastique ou chaotique grâce à

des méthodes mathématiques adaptées [86, 87].

Conclusion

Les travaux de recherche présentés dans ce manuscrit ont eu pour but d'étudier la possibilité de détecter des photons uniques avec des nanofils supraconducteurs en YBCO à des températures plus élevées que les SSPDs actuels qui fonctionnent aux alentours du kelvin. Actuellement, aucune théorie ne permet de prédire si un SSPD en YBCO est réalisable ou non. Afin d'aborder cette problématique, nous avons réalisé un travail essentiellement expérimental consistant à fabriquer, caractériser puis étudier des nanofils en YBCO.

Nous avons développé et optimisé un procédé de fabrication originale basée sur l'irradiation ionique afin de fabriquer les nanofils. A la fin du procédé, les nanofils sont enterrés dans une matrice isolante qui permet d'éviter la dégradation des propriétés supraconductrices via la diffusion d'oxygène. Cette technique offre donc l'avantage de protéger les dispositifs supraconducteurs tout au long de la fabrication et au-delà. Nous avons ainsi fabriqué des nanofils robustes sur des films minces en YBCO de 30 nm d'épaisseur de manière reproductible. Ces nanofils peuvent avoir une longueur allant de 500 nm jusqu'à plusieurs centaines de microns pour une largeur minimale de 100 nm.

Par la suite, nous avons caractérisé les propriétés électriques de nombreux nanofils afin de déterminer les mécanismes physiques qui gouvernent l'apparition d'une tension. En se basant sur plusieurs modèles théoriques dans les différents régimes des caractéristiques IV étudiées nous avons démontré que la dynamique des vortex supraconducteurs jouent un rôle prépondérant. Même si la détection de photons uniques dans les nanofils n'a pas encore été démontré, les recherches présentées dans ce manuscrit donnent une vue d'ensemble sur les phénomènes physiques en jeu dans des nanofils d'YBCO de haute qualité.

Par ailleurs, nous avons également fabriqué des nanofils sur des films en YBCO de plus faible épaisseur par irradiation ionique grâce à une collaboration avec Javier Briatico. La réduction de l'épaisseur du film d'YBCO est un élément clé pour la détection de photons uniques. Elle permet de réduire la section du fil et donc d'augmenter les chances de créer un point chaud lors de l'absorption d'un photon unique. Les premiers résultats obtenus sur des nanofils de 12 nm d'épaisseur sont prometteurs. En effet, les dispositifs étudiés ont d'excellentes propriétés supraconductrices. Ces résultats constituent une avancée majeure qui valide le procédé de nanofabrication basée sur l'irradiation ionique pour des films très minces. L'étude de ces nanofils permettra de poursuivre les recherches sur la détection de photons uniques dans l'YBCO.

Contents

Résumé de thèse	i
Introduction	5
1 Single photon detection	7
1.1 Applications	8
1.1.1 An overview	8
1.1.2 Quantum information	9
1.1.3 Light detection and ranging imaging	10
1.2 Key metrics of a single photon detector	12
1.2.1 Detection efficiency	12
1.2.2 Dark count	13
1.2.3 Reset time	13
1.2.4 Timing jitter	13
1.2.5 Photon number and energy resolution	14
1.2.6 Spectral range	15
1.2.7 Properties of an ideal single photon detector	16
1.3 Single photon detection technologies	16
1.3.1 Photomultiplier tubes	16
1.3.2 Single photon avalanche diode	17
1.3.3 Superconducting single photon detector	19
1.3.4 Summary	21
1.3.5 YBCO as a superconducting single photon detector	24
2 Physics of superconducting nanowires	27
2.1 Superconductivity in a nutshell	29
2.1.1 Experimental observations	29
2.1.2 London equations	30
2.1.3 Ginzburg-Landau mean-field approach	31
2.1.4 Bardeen-Schrieffer-Cooper microscopic theory	31
2.1.5 Superconducting length scales	32
2.1.5.1 Clean and dirty limit of superconductors	32
2.1.5.2 Superconducting types	33
2.1.6 High temperature superconductivity in YBCO	34
2.2 Superconductivity at low dimensions	36
2.2.1 The Josephson junction	36
2.2.2 Phase slip in one-dimensional wire	39
2.2.2.1 Little phase slip	39
2.2.2.2 Phase slip center	40
2.2.3 Vortex motion in reduced dimension	41
2.2.3.1 Coherent vortex motion	41

2.2.3.2	Kinematic vortices and phase slip lines	42
2.2.3.3	Conclusion	43
2.3	Superconducting single photon detection mechanism	43
2.3.1	Photoresponse in superconductors	43
2.3.1.1	Rothwarf-Taylor model	43
2.3.1.2	The two-temperature model	45
2.3.2	Experimental observations	46
2.3.2.1	Detection efficiency versus bias current	47
2.3.2.2	Energy - bias current relationship	48
2.3.2.3	Detector response versus magnetic field	48
2.3.3	Hotspot models	49
2.3.3.1	Normal hotspot model	49
2.3.3.2	Diffusive hotspot model	50
2.3.4	Vortex based models	51
2.3.4.1	Vortex-entry model	51
2.3.4.2	Diffusive vortex-entry model	52
2.3.4.3	Normal core vortex model	54
2.3.5	Conclusion	55
3	Ion irradiated YBCO nanowires	57
3.1	Fabrication locks	58
3.2	Ion implantation	59
3.2.1	Effect of disorder	59
3.2.2	Ion implanter	60
3.2.3	He ⁺ focused ion beam	61
3.3	Simulation of irradiated devices	62
3.3.1	Simulations of the stopping and range of ions in matter	62
3.3.2	Influence of the ions	64
3.3.3	O ⁺ irradiation through a mask	65
3.3.4	He ⁺ focused ion beam patterning	68
3.4	Fabrication workflow	70
3.4.1	Standard irradiated devices	70
3.4.2	Special irradiated devices	72
3.4.3	He ⁺ focused ion beam process	73
3.4.4	Characterization tests	74
4	Transport measurements	77
4.1	Experimental setup	78
4.2	Resistance-temperature evolution	79
4.2.1	Experimental setup	79
4.2.2	Resistance-temperature curve analysis	81
4.2.3	Influence of the ion irradiation process	83
4.2.3.1	He ⁺ focused ion beam patterning	83
4.2.3.2	O ⁺ irradiation	85
4.2.4	Origin of the chip	86
4.3	Current voltage characteristics	89
4.3.1	General description	89
4.3.2	Hysteresis and flux flow behaviors	91
4.3.3	Influence of temperature	96
4.3.3.1	Retrapping current evolution	96
4.3.3.2	Critical current evolution	98

4.4	Resonant radio frequency measurement	101
4.4.1	Probing the dynamical properties	101
4.4.2	Experimental setup	102
4.4.3	Behavior at resonance	103
4.4.4	Temperature dependence of the kinetic inductance	104
4.5	Conclusion	106
5	Vortex dynamics in YBCO nanowires	109
5.1	Introduction	110
5.2	The flux creep regime	112
5.2.1	Theory	112
5.2.2	Current-voltage curve fitting	112
5.2.3	Temperature evolution of the pinning parameters	114
5.3	Radiofrequency synchronized vortex motion	116
5.3.1	Observation of Shapiro-like steps	116
5.3.2	Temperature dependence	118
5.3.3	Current steps height modulation	120
5.3.4	Non-integer fractional steps	123
5.4	Thermally activated vortex motion	125
5.4.1	Voltage-current power law regime	125
5.4.2	Current-voltage curve fitting with the original model	128
5.4.3	Including the vortex-vortex interaction	129
5.4.4	Current-voltage curve fitting with vortex-vortex interaction	131
5.5	Voltage pulse detection	133
5.5.1	Experimental setup	133
5.5.2	Voltage pulse observation	134
5.5.3	Count rate measurement	137
5.5.3.1	Discriminator level dependence of the dark count rate	137
5.5.3.2	Bias current dependence of the dark count rate	138
5.5.3.3	Count rate in presence of laser illumination	142
5.6	Conclusion	143
6	Voltage switch in YBCO nanowires	145
6.1	Switching mechanisms in superconducting devices	146
6.1.1	Vortex instability in superconducting wires	147
6.1.2	Phase dynamics in Josephson junctions	150
6.1.3	Phase slip in one dimensional superconducting wires	151
6.1.4	The Fulton-Dunkelberger transformation	153
6.2	Statistical moments	154
6.2.1	Definition	155
6.2.2	The Kurkijärvi-Garg model	156
6.2.3	Universality of the high order moments	159
6.3	Acquisition of the current distributions	160
6.3.1	Fast current-voltage curve measurement	160
6.3.2	Numerical analysis	162
6.3.3	Dealing with outliers	164
6.4	Estimate of the statistical moments	166
6.4.1	Evolution with temperature	166
6.4.2	Comparison with other devices	168
6.4.3	Evolution with external parameters	170
6.5	Voltage switch triggered by a vortex instability	171

6.5.1	Fingerprint of the Larkin-Ovchinnikov instability	171
6.5.2	The alternative model of Kunchur	173
6.5.3	Concluding remarks	176
6.6	Switching current distributions	177
6.6.1	Observation of multimodal distribution	177
6.6.2	Modelling of the histograms	179
6.6.3	Relation with the vortex instability	180
6.7	Conclusion	181
Conclusion		183
A Fabrication recipes of irradiated YBCO nanowires		185
A.1	Step 1: PMMA resist	186
A.1.1	Spin-coating	186
A.1.2	Electronic beam lithography	186
A.1.3	Development	187
A.2	Step 1: S1805B resist	187
A.2.1	Spin-coating	187
A.2.2	Laser lithography	188
A.2.3	Development	188
A.3	Step 2: Ar ⁺ ion beam etching	188
A.4	Step 3: Au deposition	188
A.5	Step 4: ma-N2405 resist	189
A.5.1	Spin-coating	189
A.5.2	Electronic beam lithography	189
A.5.3	Development	190
A.5.4	Lift-off	191
B Sample characteristics		193
C Estimate of the Shapiro-like current steps height		195
Bibliography		197

Introduction

Superconducting single photon detectors (SSPD) at visible and telecommunication wavelengths show unrivalled performances, including high intrinsic efficiency, high count rate, low dark count rate, and fast timing jitter. They outperform their semiconducting counterparts, such as photomultiplier or single photon avalanche diodes. Thus, SSPDs are particularly suitable for quantum information and low-light level imaging applications among others. SSPDs have been widely studied and developed using low-temperature superconducting (LTS) thin films, such as Nb or NbN, and thus they operate about 1 K. This represents one main drawback that limits their technological applications, since it requires complex and energy consuming cryogenics.

On the contrary, SSPDs based on high-temperature superconducting (HTS) thin films have not been realized yet. Among the HTS, $\text{YBa}_2\text{Cu}_3\text{O}_{7-x}$ (YBCO) thin films are commercially available and remain superconducting up to 90 K. Thus, SSPDs based on YBCO may potentially lead to higher operating temperature than the one in LTS SSPD making the technology easier to use and more affordable. In addition, we may expect higher detection rate due to the short electron-phonon interaction time in YBCO in comparison to LTS. Despite those appealing properties, YBCO has been set apart due to the challenging task of patterning ultra thin film at nanoscale. The patterning often results in damaging the superconducting properties because of oxygen diffusion and defects.

The key-element of the SSPD is a nano-meander of about 50 nm in width and 500 μm in length, patterned on a superconducting ultra thin film about a few nanometer thick. In terms of physics, the single photon detection arises from a hotspot creation triggered by a single photon arrival. Nevertheless, a complete microscopic description of the mechanism involved does not exist yet. On the contrary, several theoretical models have been developed to account for the different experimental observations. Furthermore, YBCO exhibits some peculiarities such as a d -wave order-parameter and a fast electron-phonon scattering time. They may change drastically the intrinsic single photon detection mechanism in comparison to the one in LTS. Since both YBCO superconductivity and SSPD mechanisms are not fully understood theoretically, we slip out of the controversies by addressing the problem experimentally. The research work presented in this manuscript studies the feasibility of detecting single photon with a high-temperature superconducting nanowire.

At first, chapter 1 will present the single photon detection with a view to applications in science and technology. It will present the main single photon detectors along with their key metrics, with a special emphasis on the use of YBCO as an SSPD. Then, chapter 2 will dive into the principal concepts of superconductivity, including a focus at low dimensions at which new physical phenomena arise. In order to provide further details of the SSPD mechanism, we will present the experimental observations on SSPDs along with the theoretical models which account for them. Especially, we will see that vortices play an important role in the detection mechanism, either when a photon is absorbed or as false counts. In this framework, we will discuss theoretically the possibility of detect single photon with YBCO.

Only then, we will go into the experimental side. First of all, chapter 3 will describe the

fabrication workflow that we have developed for patterning superconducting nanowires on YBCO thin films using ion irradiation technique, either with a He^+ focused ion beam or an O^+ ion implanter. Throughout the process, the YBCO superconducting thin films are protected by a thin insulating cerium oxide layer which prevents both oxygen diffusion and damaging. Thus, the YBCO circuitry containing the wires and the electrodes is completely enclosed: laterally by an insulating matrix, and on top by an insulating layer. Accordingly, it is not possible to observe directly the superconducting nanowires, neither the effect of the ion irradiation on their dimensions. In order to solve this issue and optimize the design, we perform Monte-Carlo simulations using SRIM software and complementary analyses.

Chapter 4 will present the transport measurements in direct and alternative current of numerous YBCO superconducting nanowires. They will give access to superconducting parameters such as the critical temperature, the resistivity, the characteristic current densities, and the magnetic penetration depth among others. In addition, it will allow us to check the integrity of the superconducting properties with respect to the pristine thin films and in general to the YBCO devices reported in the literature. We will also use theoretical models to account for the temperature dependence of the important parameters such as the critical current, the returning current, or the kinetic inductance. Having characterized the superconducting YBCO nanowires, we have been able to select the best devices for further investigations of the vortex dynamics and the single photon detection. Especially, we will be interested in superconducting nanowires with high critical current density which present a hysteretic current voltage (IV) characteristic and a large voltage switch.

Chapter 5 will look into the details of the vortex dynamics by studying the appearance of a voltage dissipation in the IV curve. Depending on temperature, bias current, and incident radiofrequency (RF) power, several scenarios may explain the voltage drop along the superconducting nanowires. Starting from the low voltage branch, we will use the flux creep theory to model the IV curves at various temperatures. On a similar voltage range, we will study the effect of an incident RF power on the IV characteristics. This gives rise to Shapiro-like current steps. Then, at higher voltages, a different vortex behavior arises, it will be modelled as a thermally activated vortex motion in presence of vortex interactions. Finally, we will investigate the dark and photon count rates of voltage pulses generated by the devices. It constitutes the corner stone to probe experimentally the single photon detection by superconducting YBCO nanowires.

Lastly, chapter 6 will focus on the voltage switch observed in superconducting YBCO nanowires. The switching current statistics have been widely studied in superconducting devices such as Josephson junctions (JJ) and one-dimensional (1D) superconducting nanowires. For such devices, the mechanism at the origin of the voltage switch is well established in the framework of the generalized Kurkijärvi-Garg model. It is activated either by thermal or quantum fluctuations. It results in the appearance of a crossover temperature between those two regimes such that at low temperatures a macroscopic quantum tunneling process occurs. On the contrary, only a few recent articles have reported this statistics in YBCO nanowires, and accordingly little is known on the theoretical side. Here, we will present an extensive study of the switching current statistics of superconducting YBCO nanowires measured as a function of temperature, magnetic field, and incident RF power. We will compare the existing models for JJs and 1D superconducting nanowires with our system to gain further insights of the switching mechanism. Theoretical models ascribe voltage switch of YBCO nanowires to a vortex instability. Due to non linearities, the system becomes chaotic and triggers the switch. By studying the effect of an external magnetic field, we will test the validity of such a model in the nanowires. Having gathered numerous experiments and theoretical models, we will propose physical interpretations of the switching current statistics in the framework of the vortex instability.

Chapter 1

Single photon detection

Contents

1.1 Applications	8
1.1.1 An overview	8
1.1.2 Quantum information	9
1.1.3 Light detection and ranging imaging	10
1.2 Key metrics of a single photon detector	12
1.2.1 Detection efficiency	12
1.2.2 Dark count	13
1.2.3 Reset time	13
1.2.4 Timing jitter	13
1.2.5 Photon number and energy resolution	14
1.2.6 Spectral range	15
1.2.7 Properties of an ideal single photon detector	16
1.3 Single photon detection technologies	16
1.3.1 Photomultiplier tubes	16
1.3.2 Single photon avalanche diode	17
1.3.3 Superconducting single photon detector	19
1.3.4 Summary	21
1.3.5 YBCO as a superconducting single photon detector	24

Since the beginning of modern science, the nature of light has been investigated thoroughly. It was first interpreted as moving particles by Descartes during the 17th century. Only then, the Huygens-Fresnel law tackled the original idea of Descartes by replacing it by a wave packet interpretation. In the early 20th century, Einstein postulated the existence of discrete light quanta, later on referred as photons, with both wave and particle aspects in order to account for the photoelectric effect. This discovery gave birth to two major breakthroughs in science and technology. In terms of scientific knowledge, it led De Broglie to extend the wave-particle duality initially developed for photon to all kind of particles. The wave particle duality had a major impact on the foundations of quantum mechanics that have been further investigated in the next years. Besides, in the applicative view, the photomultiplier tube (PMT) has been developed using the photoelectric effect. It constitutes the first single photon detector (SPD) that converts a light flux into an electrical signal. Thereupon, the use of PMTs spreads widely in scientific research, from particle Physics to medicine, but also in applicative domains such as for ionization survey or spectrophotometry. Beyond the specific scientific domain, the photoelectric effect provides an illustrative example on how Science and Technology are strongly interconnected together. But, as Bacon wrote "[the] mechanical arts have an ambiguous or double use, and serve as well to produce as to prevent mischief and destruction" [88]. Since then, several philosophers and scientists reminded us that we should always bear in mind this aspect in the research and development process.

Hereafter, the main focus is on the single photon detection whether to serve scientific research domains or applicative areas. In order to understand the impact of single photon detection we will briefly present some potential applications, while some have been successfully completed, others are envisioned with serious efforts. We will define next how a SPD is characterized by presenting its key metrics. Then, we will give an overview of the main SPD technologies available to this day from near-ultraviolet through visible to the near-infrared spectral range. By combining the preceding sections, we will summarize the different SPD technologies according to their performances to compare them with each other. Lastly, we will develop how the study of YBCO superconducting nanowires fits within this context.

1.1 Applications

1.1.1 An overview

In the field of single photon detection, and more generally of light detection, several applications have been completed successfully while others are envisioned with strong interests. At first, numerous efforts have been realized in two fundamental scientific areas: high-energy physics and astronomy, in other simple words the infinitely small and the infinitely large nature of the universe. They helped to detect both particles and photons in order to investigate the fundamental interactions at small scales, but also to survey celestial bodies and electromagnetic radiations generally. In the case of astronomy, the electrical photon detectors have been used to replace the photographic techniques. As an example, in 1956 Hanbury Brown and Twiss made use of two PMTs to measure the angular size of the Sirius star with an interferometer technique [89]. The Hanbury Brown-Twiss experiment did not only provide an excellent resolution as an interferometer, but has also generated many benefits to the physics community such as in particle physics with the discovery of ρ^0 resonance by Goldhaber *et al.* [90].

More recently, the SPD technologies have attracted a lot of interest in quantum mechanics and modern physics: to study the single photon sources, interferences, or indistinguishability [91, 92]; to detect dark matter [93]; to develop the quantum technolo-

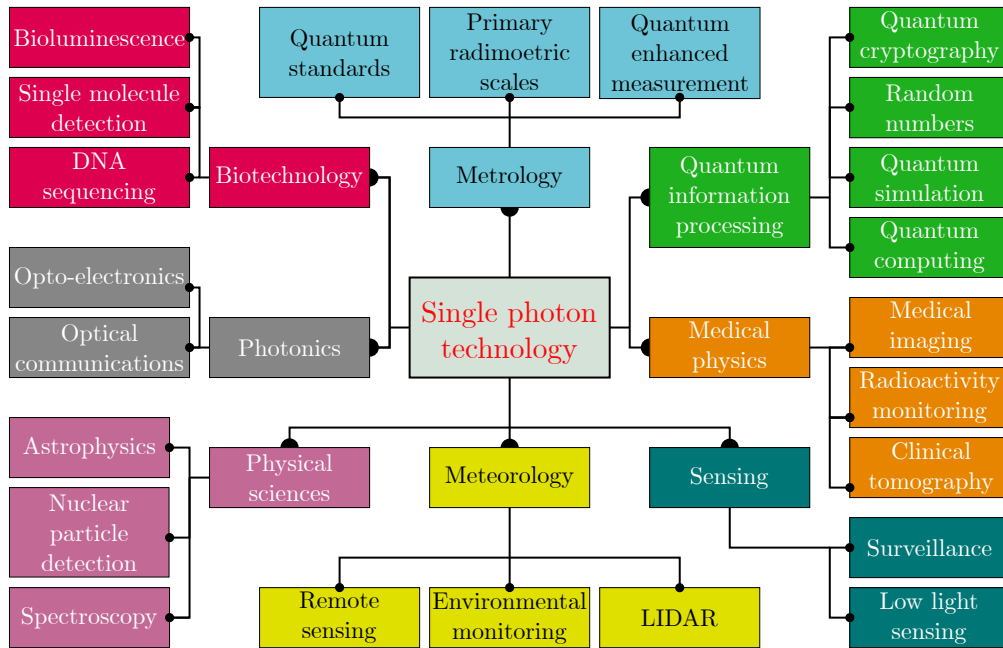


Figure 1.1 – Overview of the main applications of single photon generation and detection. Adapted from Chunnillal *et al.* [92].

gies [94, 95], the long range and low light level imaging [96–98], the atmospheric remote sensing, or the space communications [99]. Figure 1.1 schematizes the main use of the single photon technology in different domains. In the following, we provide two concrete examples in quantum information and low light imaging in order to gain insights into the potential impacts of SPD applications.

1.1.2 Quantum information

In the field of quantum information, the SPD is a key-element to perform a quantum key distribution (QKD). Actually, communications are encrypted in a classical way based on the Rivest-Shamir-Adleman (RSA) algorithm proposed in 1977. It relies on the fact that it is practically difficult to factorize the product of two large prime numbers. The standard key length contains 2048-bits, that is the decryption requires factoring a 617-digit number. If classical computer based algorithm are used, it would take more than $6 \cdot 10^{15}$ years, which is equivalent to half a million of the age of the universe.¹ Less than two decades later in 1994, Shor proposed a quantum computer based algorithm to factorize integers [100]. In comparison to the most efficient classical algorithm, the Shor’s algorithm is almost exponentially faster. Provided that enough quantum bits (qubit) can be operated, the RSA encryption can be potentially broken. In practice, Gidney and Ekerå have reported recently that it would require 20 millions qubits to decrypt a 2048-bits in 8 hours [101]. As the maximum qubits number operating together is less than 100 for now², the quantum decryption of standard 2048-bit RSA is not imminent, but if it exists one day organizations should be worried about it.

Meanwhile, different quantum cryptographic systems have been proposed to counteract the eventuality of quantum decryption. The QKD is one of them in which the public key

¹For the detailed calculation see "The math behind estimation to break a 2048-bit certificate".

²We openly omitted the quantum computers developed by D-wave as it substantially differs from the standard quantum computers in its architecture which limits its capabilities as explained by Van Der Walt. Here, we rather refer to the quantum computers developed by Google or IBM which respectively claimed 72-qubit and 53-qubit systems.

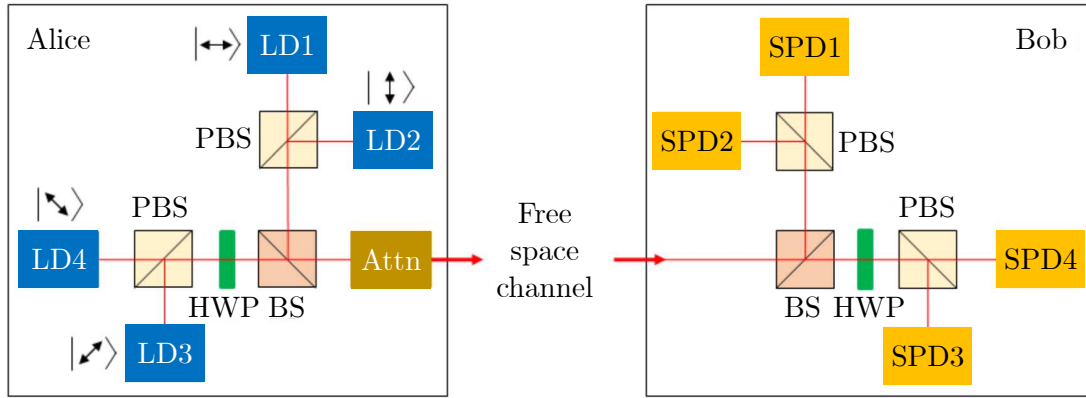


Figure 1.2 – Schematic of an optical assembly for a QKD communication using the BB84 quantum protocol. The laser diodes (LD) generate light that goes into a set of optical pieces - polarization beam splitters (PBS), half wave plates (HWP), attenuator (Attn), and beam splitters (BS) - to handle the photon quantum states. Once the photons are prepared in the Alice side, they are sent *via* a channel to the Bob side that manipulate them and read them using single photon detectors (SPD). Adapted from Ko *et al.* [103].

is now quantum, that is the information is encoded in the photon quantum states rather than the standard parity bits. For instance, it was originally proposed to use the photon polarization for the BB84 protocol [102] as depicted by the optical assembly in fig. 1.2. But any other conjugate paired states can also be used as a quantum state. In QKD, any eavesdropping attempts will destroy the quantum states in such a way that the sender and the receiver will be warned as a consequence of the uncertainty principle. It results that the quantum protocols used in QKD make the communication unconditionally secure.

Whatever the specific quantum state and the quantum protocol used, as information is encoded in a single photon quantum state the physical implementation impose some constraints. It is mandatory to generate a single photon, to prepare the quantum state as desired, to send the photon *via* a communication channel - whether *via* free space such as in fig. 1.2 or *via* optical fibers - and eventually to read the photon quantum states using SPDs. Each function needs to be optimized in such a way that the QKD is fast across long distances involving that the light absorption is low through the communication channel and that there are as low errors as possible. In order to comply those requirements, the QKD targets the standard telecommunication wavelength at 1550 nm to limit losses in the optical fibers. In the detection side, it requires that the SPDs are fast, have precise timing of the photon arrival, and detect most of the photons at telecommunication wavelength. The QKD is a concrete example that represents a major breakthrough in communication technology in which the new SPD technologies must fulfil high detection performances criteria. That being said, as presented in fig. 1.1 there are plenty of other applications of SPDs in quantum information such as the quantum random number generator or the quantum tomography. At last, it is worth noting that the SPDs are not restricted to quantum information but they may also benefit to low light power communication in general as for deep space communication [104].

1.1.3 Light detection and ranging imaging

In classical imaging area, the SPDs emerge as strong candidates for high-speed and precise light detection and ranging imaging referred as LIDAR imaging. The LIDAR technology allows one to make high-resolution three dimensional (3D) mapping for a large set of applications in atmospheric research, autonomous cars, geography, meteorology, forestry,

surveying, or astronomy. Viewing all this applicative domains, we see that it can be used on the ground, in the air, or within the space. The LIDAR inherits from the radio detection and ranging (RADAR) technology invented during the world war II and have the same working principle though. The main difference is that LIDAR uses near visible wavelengths (200 nm - 10 μm) while RADAR operates with radio electromagnetic wavelengths (1 mm - 100 m).

The LIDAR principle arises from the time-of-flight measurement as presented in fig. 1.3. In a simplistic way, a light source emits light short pulses onto an object located at a distance d . A very few number of photons are reflected back to the photon detector that generate an electrical pulse. The detected pulse is delayed with respect to the emitted pulse by the time-of-flight τ . Knowing that the speed of light into the air is approximately the one into the vacuum c , the distance between the LIDAR transceiver and the object simply writes:

$$d = \frac{c\tau}{2} \quad (1.1)$$

for d significantly longer than the separation length between the light source and the photon detector. Then, by measuring the delay τ for various direction of the light pulses, it is possible to reconstruct a cloud of data points representing the 3D object. Equation (1.1) sets the acquisition speed between two data points, *i.e.* the analog of a pixel in a two dimensional (2D) picture, and the distance resolution. For an object at 3 m distance of the transceiver at maximum, the longest delay will be 20 ns, thus the acquisition frequency is about 50 MHz. In practice, such a frequency is lower due to the pulse analog processing that lengthen the acquisition rate, but the photon detector requires to be fast if live imaging is required. In terms of precision, to obtain d at 1 cm resolution, the timing precision should be about 70 ps that requires state-of-the-art photon detectors. In comparison to RADAR, LIDAR imaging provides a better lateral resolution thanks to its wavelength about 1 μm . It allows one to image smaller objects such as cloud particles or aerosols. However, the RADAR can operate in presence of clouds that are transparent to the radio wavelengths, while the LIDAR imaging is limited to clear atmospheric conditions. In addition, for a given LIDAR transceiver, the longer is light distance, stronger the absorption. High sensitive detectors are thus required in order to correctly operate in such a low light intensity conditions. As a conclusion, the ability to detect single photon is not mandatory for LIDAR technology, since it works in the classical limit, but the photon detection needs to be fast, efficient, and at weak light power to be widely used. This is exactly the requirements met by the SPDs technologies. On the other side, if the intended application

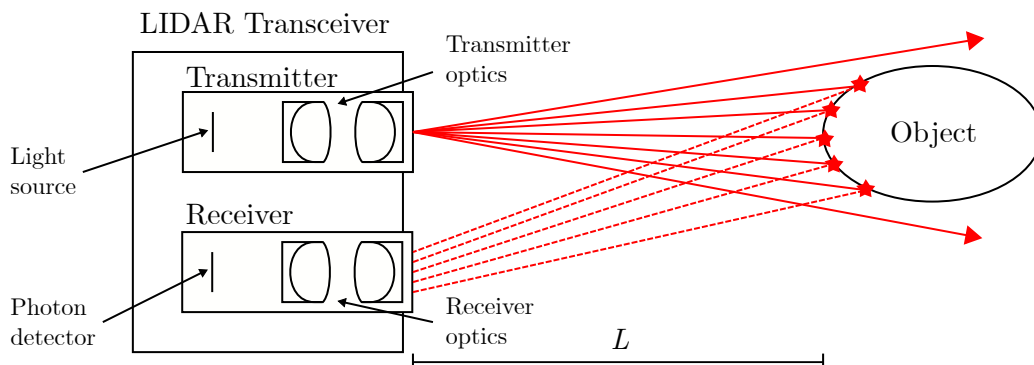


Figure 1.3 – LIDAR operation scheme, a light source sends light onto an object located at a distance d that reflects back to the photon detectors. By measuring the time-of-flight τ given by eq. (1.1), the object is mapped in three dimensions. Adapted from Eckhardt Optics.

is in motion - whether a car, an aircraft, or a satellite - the payload of the SPD system has to be taken into account. Thus, it needs to be light and energy efficient and also fit in a small volume.

In comparison to quantum information, the LIDAR imaging is already well established in a large range of applications. The LIDAR is still extending its scope due to the fact that it becomes more and more accessible. Depending on the specific needs, it is implemented with different photon detectors and various analog and digital systems. The LIDAR technique is powerful to the extent that it can map a large 3D area with high precision at long distances in a reasonable time. For instance, in the recent years WWF launches a large survey using LIDAR for ecology and conservation in order to provide high precision data on the 3D structures of forests. Nevertheless, it does not involve SPDs. On the opposite, as part of the earth observing system mission, the NASA has launched two Ice, Cloud, and land Elevation Satellites (ICESat) in 2003 and 2018 embedding SPDs in the LIDAR system. They are both dedicated to measure the changing of the Earth height let it be glaciers, ice sheets, forests, but also the cloud properties. Going back on earth, the SPD LIDAR is also emerging in 3D live imaging [98] and 3D long-range imaging [97, 105]. In summary, the SPDs outperform the standard photon detectors - such as the charged-coupled device (CCD) used in cameras - to image a target whether it is located at a long-distance or in a low light environment.

1.2 Key metrics of a single photon detector

A single photon detector (SPD) collects the incident photons and convert them into an output signal. The latter signal is generally a voltage pulse that has been filtered and amplified with an electronic setup. The electronic signal is then used for later experiments as photon counting or photon energy measurements. The performances of SPDs are characterized considering a various set of parameters. In this section, we briefly introduce the key metrics of an SPD. It will enable us to review the different SPD technologies in the light of the metrics and compare them with each other in the next section.

1.2.1 Detection efficiency

The detection efficiency η_d is the most valuable parameter to consider. It corresponds to the probability that a single photon triggers a detection event in the detector and generates an output signal. If we introduce the total detection rate as R_t and the incident photon rate as R_i , the detection efficiency writes:

$$\eta_d = \frac{R_t}{R_i} \quad (1.2)$$

An ideal SPD will count every single photon impinging the detector resulting in $\eta_d = 1$. In practice, several limitations lower the detection efficiency. Following Natarajan *et al.* [106], the detection efficiency can be decomposed in three distinct parts. At first, the extrinsic parameters may cause a loss of photons before they reach the detector, it affects the coupling efficiency η_c . Then, depending on the geometry and the material of the device, the impinging photons have a specific probability to be absorbed: it sets the absorption efficiency η_a . Once the photon is absorbed, the detector may eventually generate an output signal with an intrinsic detection efficiency η_i . This latter efficiency is also reported as quantum efficiency in the literature, not to be confused with quantum efficiency defined in solar cell technology. Finally, the total detection efficiency η_d is written as:

$$\eta_d = \eta_c \eta_a \eta_i \quad (1.3)$$

In that respect, it is possible to optimize the detection efficiency at different levels requiring distinct technical expertise. While η_c and η_a need specific knowledge in photonics and material science respectively, η_i is set by the physical phenomena involved in the detection process. For some SPD technology, the latter may approach unity efficiency with specific parameters. But, for almost all SPDs, the detection efficiency will depend on the illumination wavelength. Usually, lower the wavelength, higher the energy, and thus higher the detection efficiency.

1.2.2 Dark count

In practice, a detector may register an event while there is no incident photon. It is a false positive known as the dark count that is undistinguishable from a photon count event. The corresponding dark count rate R_d is the average number of detection events without illumination in a given time window. It is mostly due to the fluctuations, whether thermal or electrical, but it may also be affected by unwanted radiation such as the black body radiation. Depending on the technology, the detector may exhibit more or less dark count events.

Whatever the SPD, the main requirement is that during a specific detection time window the detector registers sufficient true photon counts with respect to the counting noise. In practice, it is possible to remove the background dark count rate from the measurement, but the fluctuations will limit this technique. Thus it becomes easier to perform an experiment when the photon detection rate is higher than the dark count rate. For any application, the dark count rate has to be minimum. In the case of quantum communication, this becomes even more important to reduce the errors as much as possible and make the communication secure.

1.2.3 Reset time

After registering a photon, device is unable to detect efficiently a new photon. The detector resets itself going back to its initial state after a time delay known as the recovery time or dead time. It roughly sets the maximum theoretical count rate of a SPD. In practice, other factors may limit the count rate such as the electronic setup. In general, if the incident photon rate bypasses the maximum count rate, the SPD risks to saturate. While the coupling and absorption efficiency are not affected, the intrinsic efficiency drops during the recovery time. Therefore the photon count rate will not correspond to the incident photon rate.

1.2.4 Timing jitter

The timing jitter is the uncertainty that a photon is detected at a given time. In terms of statistics, if we measure the time delay between the photon arrival and the output detector signal several times, the timing jitter corresponds to the standard deviation of the time delay. It may also be estimated as the full-width half maximum (FWHM) of the detector instrument response. Among the astronomy and detection community, the instrument response function corresponds to a mapping that links the incident photons with the detected events.³ Thus the timing jitter characterizes how precise is the SPD timing with respect to the photon arrival. If it is necessary to observe a phenomenon with a specific time resolution, it becomes necessary to obtain a timing jitter lower than the expected time resolution. If this condition is not satisfied, the measurement will blur the signal of interest.

³An illustrative example can be found on the Cherenkov Telescope Array science analysis software site.

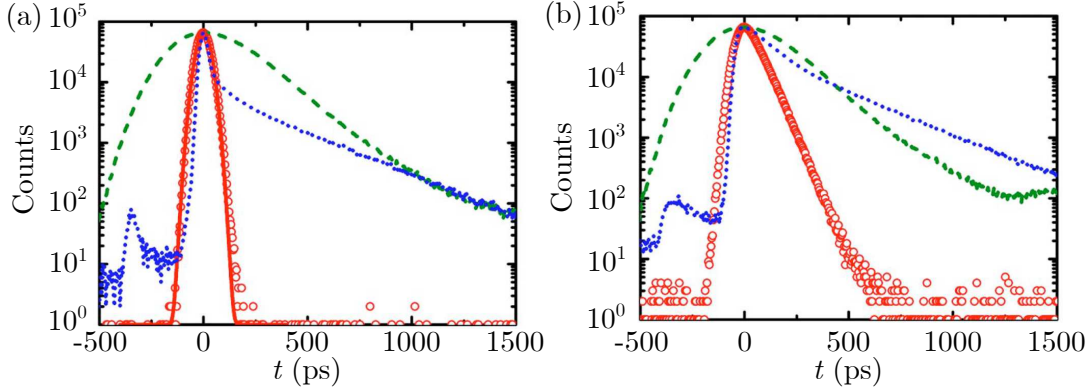


Figure 1.4 – (a) Instrument response for three different SPDs: a conventional Si single photon avalanche photodiode (dashed green curve), a fast Si single photon avalanche photodiode (dotted blue line), and a superconducting single photon detector (red open circles). (b) Lifetime measurement of the emitted light at 935 nm from a quantum well with the three detectors presented in (a). Adapted from Stevens *et al.* [107]

Figure 1.4 shows the typical instrument response of three different SPDs: two Si single photon avalanche photodiode (SPAD) and one superconducting single photon detector (SSPD). In fig. 1.4(a), we observe that the timing delay distribution of the SPADs have long tails and are highly asymmetric. By contrast, the timing delay of the SSPD is almost a Gaussian distribution. Thus, by taking the FWHM we estimate a jitter about 50 ps for the fast SPAD and the SSPD, while the conventional SPAD exhibits a 400 ps jitter. The three SPDs are used to measure the recombination lifetime of a semiconducting quantum well emitting source. The resulting signal depicted in fig. 1.4(b) corresponds to the convolution of the instrument response with the lifetime measurement signal. Therefore, the conventional SPAD does not provide any information since its jitter is too long. On the contrary, the two other detector captures the relevant parameter that is the count decay with a better signal for the SSPD. We clearly see that the timing jitter is a key metric to consider when the timing resolution is crucial. It becomes particularly relevant for time-correlated single photon counting and quantum communication applications like the QKD.

Generally speaking, the overall SPD timing jitter σ has different origins. If we assume that the origins are statistically independent with respect to each other, it follows that σ writes:

$$\sigma^2 = \sigma_{\text{noise}}^2 + \sigma_{\text{setup}}^2 + \sigma_{\text{intrinsic}}^2 \quad (1.4)$$

where σ_{noise} is the jitter arising from the noise, σ_{setup} is the jitter associated to the electronic setup, and $\sigma_{\text{intrinsic}}$ is the jitter due to the intrinsic properties of the SPD. As in the case of the detection efficiency, several options are available to minimize the jitter. In contrast to the detection efficiency, the main jitter source has to be identified and optimized first since the timing jitters add together (eq. (1.4)) while the detection efficiencies are multiplied (eq. (1.3)).

1.2.5 Photon number and energy resolution

The photon number resolution characterizes the ability to distinguish the photons number in an incident pulse arriving onto the detector. Since most of the SPDs are based on the conversion of the incident photon into a high voltage requiring an avalanche process their electronic response is intrinsically non linear with respect to the photon numbers. It results that they only discriminate between zero photon and some incident photons,

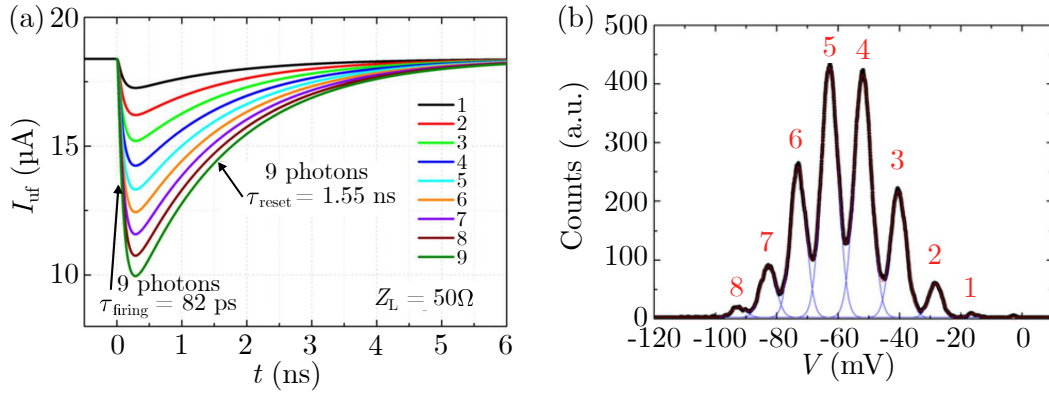


Figure 1.5 – (a) Current flowing through a series of 10 SSPDs with $50\ \Omega$ load resistances in parallel after absorption of different photon numbers. (b) Evolution of the photon counts as a function of the output voltage at a fixed light power. Adapted from Mattioli *et al.* [109].

that is an 'off' state and an 'on' state respectively. The photon number resolution goes generally hand in hand with the photon energy resolution as it is difficult to make a clear distinction between them. Especially, as one SPD converts the overall photon energy into an electronic signal, it will not make the difference between one photon at energy $h\nu$ and two photons at energy $h\nu/2$.

Nonetheless, some SPDs have the energy sensitivity such as the transition edge sensor (TES). Even for the one who does not intrinsically exhibit the energy resolution, several approaches have been proposed to implement this ability [108–110]. In the case of the SSPDs, the photon generates an output voltage pulse determined by the load resistance and the kinetic inductance of the superconducting wire. Thus, for a given nanowire geometry and load resistance the response is the same. As it is, an SSPD does not resolve the photons number. But Mattioli *et al.* have implemented space multiplexing by placing several nanowires in series and adding one resistance in parallel for each nanowire. Then, the output signal corresponding to the sum of all the individual voltage pulse depends on the number of individual SSPD that has been triggered. Figure 1.5 shows typical photon number resolution results obtained by Mattioli *et al.*. In fig. 1.5(a) we clearly see that depending on the average photon number per unit of time, the voltage pulse response is varying. Now, if the voltage pulses are counted in function of their output level for a constant light power, we observe that the counts oscillate in fig. 1.5(b). Each maximum represents the mean output level corresponding to a specific detected photons number. Therefore, it is possible to achieve photon number resolution by tweaking the electrical design. Here we presented an approach using space multiplexing, but an alternative based on time multiplexing which introduce time delay has also been largely used [111, 112].

1.2.6 Spectral range

A detector works over a given spectral range whose choice depends strongly on the application. For standard telecommunication, the SPDs are optimized to work at 1550 nm for minimizing the optical fiber losses. As SPD is an encouraging technology for quantum communication, in the long run they must operate at such a wavelength. On the contrary, the particle physics community is more interested for SPDs at shorter wavelength for measuring high energy particles such as the double beta decay for instance.

Generally speaking, for a given detector it will be easier to achieve detection at higher energies. Some detectors, as SSPDs, exhibit a saturated detection efficiency in photon

energy. It results that above a given threshold energy, η_d reaches its maximum constant value. In this case, raising the photon energy will not affect the intrinsic detection efficiency.

1.2.7 Properties of an ideal single photon detector

The ideal SPD has to fulfill various requirements. It has to resolve both photon number and photon energy with unity intrinsic detection efficiency in a broad spectral range from UV to near-IR with a dark count rate as low as possible. The ideal SPD should operate at high speed with more than GHz count rate and low timing jitter below 1 ps. In addition, it has to be easy to use, scalable, reliable, affordable, and compact. In practice, one given SPD only satisfies some of the requirements because it is difficult to comply all these requirements altogether. Depending on the intended application, a particular focus will be placed on some metrics to better address the application needs.

1.3 Single photon detection technologies

There are already a myriad of SPD technologies available that are used in specific applications. Hereafter, we only focus on the SPDs operating in the visible and near-IR spectral range as they are the targeted wavelengths for the SSPDs. Before describing the mechanism of an SSPD, we first introduce the commonly used the photomultiplier tubes (PMT) and the single photon avalanche diode (SPAD).

1.3.1 Photomultiplier tubes

The photomultiplier tube (PMT) is the first SPD developed during the year 1934. In this respect, the PMT benefits from more than 80 years of research and development. The PMT is based on both the photoelectric effect and the secondary emission phenomena. Figure 1.6 shows a PMT device and the working principle of the PMT in the left and right panel respectively. The PMT consists of a vacuum tube containing a photocathode, several dynodes and one anode. As depicted in fig. 1.6(b), when an incident photon is absorbed by the photocathode, a photoelectron is generated due to the photoelectric effect. This occurs only if the photon energy is higher than the work function of the material in photocathode. In this respect, the photocathode is made of alkali materials presenting a low work function. The emitted photoelectron is focused thanks to the focusing electrodes onto the electron multiplier. The latter is made of several secondary electron emission surfaces, referred as dynodes. Each dynode generates subsequent electrons *via* the secondary

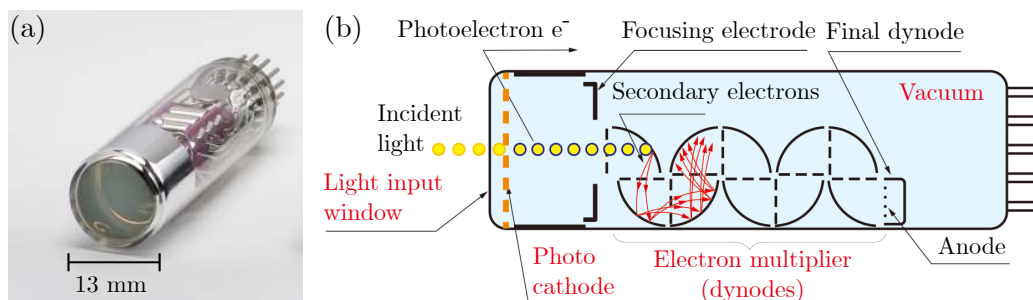


Figure 1.6 – (a) A 13 mm diameter photomultiplier tube of the R12421 series developed by Hamamatsu Photonics K.K. Adapted from Hamamatsu [113]. (b) Working principle of a photomultiplier tube. Adapted from Hamamatsu [114].

emission. As this step is repeated several times on each dynode, it amplifies significantly the electron total number up to several millions with respect to the initial photon electron. Eventually, the anode collects the electrons and a current spike is detected.

The PMT has a high amplification gain allowing to detect single photon, especially at high energy. As an avalanche process it is not possible to resolve the photon number intrinsically with this type of detector. However, they have a large sensitive area about $1 - 10^4 \text{ cm}^2$. Depending on the desired spectral range, different photocathode materials may be used to optimize the quantum efficiency. The photocathode material usually sets the upper wavelength cutoff. For a given PMT, as the photon energy lowers the quantum efficiency drops exponentially with respect to the wavelength.⁴ Most of the PMTs are limited to the visible wavelength about 700 nm. Nonetheless, some progress has been made to develop PMT at telecommunication wavelength using semiconducting material [115], but the quantum efficiency is limited to a few % which is less attractive in comparison to other SPDs introduced later on in this section. On the other hand, the lower wavelength cutoff is due to the window transmittance that is less stringent than the upper wavelength cutoff. In particular, if the photon energy is too high, it is possible to couple a scintillator with the PMT. The incident photon is absorbed and subsequent photons at visible wavelength are generated. This specific scheme has opened up the possibility to detect ionising radiation such as X-rays and gamma rays.

As a conclusion, the PMT detector is a mature technology which has proven its worth. From more than 80 years, the PMTs have been used in a wide range of applications from high-energy particle physics to medical equipment including ionising radiation measurement, astronomy and spectrophotometer. Nevertheless, the PMT is a bulky vacuum based device that limits its reliability and the possibility to design an array. Since its invention, other SPD alternative technologies have been developed to better suit specific requirements and by now they outperform the PMTs.

1.3.2 Single photon avalanche diode

Since the transistor discovery in 1947 by Bardeen and Brattain, the semiconducting industry had a rapid growth driven by the market oriented Moore's law. Following the advent of semiconducting technologies, new types of SPD based on semiconductors have been developed. In particular, the avalanche photodiode (APD) is the semiconducting counterpart of the PMT. As the PMT, the working principle of the APD also arises from the photoelectric effect but it consists of a $p-n$ junction. For the purpose of single photon detection, the single photon avalanche diode (SPAD) has been developed.

⁴See figure 34 in [113] as an example Hamamatsu

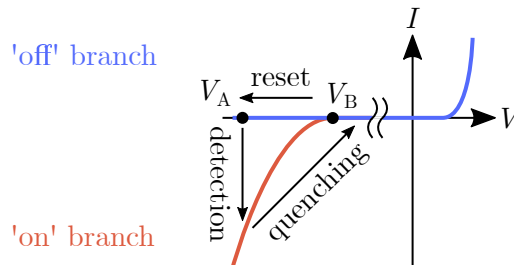


Figure 1.7 – Current-voltage characteristic of a diode showing the detection mechanism of a SPAD. The device operates in the breakdown regime at V_A in the blue 'off' branch. Upon photon detection, an avalanche process triggers the SPAD to the red 'on' branch. The device needs to be quench above V_B and reset back to its initial state.

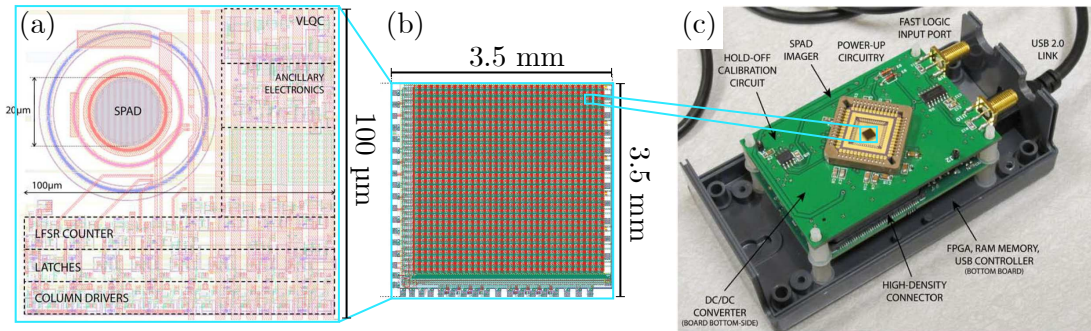


Figure 1.8 – (a) Layout of a SPAD pixel including CMOS circuits including a variable load quenching circuit (VLQC) and a linear feedback shift register (LFSR). (b) SPAD imager chip layout with a $100\ \mu\text{m}$ pitch. (c) SPAD camera boards embedded in a casing connected *via* an USB link. Adapted from Guerrieri *et al.* [119]. .

The SPAD operates at high negative voltage V_A in the breakdown regime, in which a single absorbed photon may trigger a significant current pulse. Figure 1.7 shows a typical IV curve of a SPAD to illustrate the mechanism involved. At equilibrium, the voltage is maintained below the breakdown voltage V_B while no current is flowing. The detector lies in the 'off' branch state (blue branch) with a voltage V_A . Upon photon absorption, a photoelectron is produced. The high electric field accelerates the photoelectron that generates electron-hole pairs *via* ionization. It triggers a self-sustained avalanche process in which the number of charge carriers is significantly amplified. The current flow exponentially raises until the voltage reaches a constant value in the 'on' branch state (red branch). During the avalanche process, the detector is insensitive to the incident photons. The SPAD current switch corresponds to the photon detection event. In order to detect a successive photon, the device needs to be quenched by an adequate electronic circuit. The voltage is raised above V_B , and reset back to the 'off' branch state, ready to detect another photon. Various techniques are used to reset the SPAD such as active gating technique that allows one to improve both the signal-to-noise ratio and the detection efficiency.

The key parameter in SPAD technology is the excess bias voltage defined as $V_E = V_A - V_B$ [116, 117]. Typically, with V_B lying between -10 V to -500 V, $|V_E|$ is about 1 V to 50 V. The excess bias voltage mainly sets the photon detection efficiency and the dark count rate. At higher $|V_E|$ the avalanche triggering probability is increased due to a higher electric field and accordingly a larger electron acceleration. It has been demonstrated that raising the excess bias voltage enhances the detection efficiency that eventually saturates at high V_E [118]. The downside is that the dark counts arising from the thermally generated carriers also increases in this case. In addition, the SPAD suffers from an after pulsing. After an avalanche process, a few carriers may be trapped at intermediate energy levels. They may be eventually released after the quench and trigger another avalanche process before that the SPAD resets. This drawback extends the recovery time of the detector and the timing jitter, as can be seen in fig. 1.4 for the instrument response function of the SPADS. In SPAD, the semiconducting material band gap sets the photon energy that can be detected. While the Si based SPADs are designed for visible light, the InGaAs based SPADs cover the near infrared wavelengths at a cost of a higher dark count rate.

Despite those specificities, the SPAD technology has tremendous performances. It exhibits relatively high intrinsic detection efficiency from 10 to 50% even at telecom wavelength, a short timing jitter, and a low dark count rate. In addition, it is worth noting that the SPAD benefits from all the complementary metal oxide semiconductor (CMOS) technology inherited from the semiconducting industry. Thus, it is possible to integrate

all the electronic circuitry onto the same chip to reset the device, shape the output pulse, and count them as depicted in fig. 1.8(a). It allows one to design SPADs array onto a few mm size chip, as presented in fig. 1.8(b). For a size pixel of $100 \times 100 \mu\text{m}^2$, a $3.5 \times 3.5 \text{ mm}^2$ chip holds a 32×32 pixels array. This is easily embedded in a small package to design a camera, as depicted in fig. 1.8(c).

Since the invention of the avalanche photodiode by Nishizawa in 1952, the SPAD has become a mature technology which is commercially available. Driven by the semiconducting industry, the use of SPADs has raised significantly and has supplanted the PMT as a general purpose, scalable, and reliable SPD. It is widely used in a large number of area such as in biophotonics [120], or for QKD network [121, 122]. Nevertheless, alternative semiconducting SPDs are currently under development such as the visible light photon counter (VLPC), the solid state photomultiplier, or the quantum dot (QD) based devices [123, 124]. They may be relevant for applications that require specific detection performances such as the photon number resolution. Typically VLPC and QD field effect transistor have intrinsically the capacity to resolve photon number at a cost of an operating temperature of about a few kelvins.

1.3.3 Superconducting single photon detector

Apart from semiconducting technologies, various alternative detectors based on superconducting material have emerged in the early '90s. Since superconductivity occurs well below the room temperature, a cryogenic system is mandatory to operate the superconducting detectors. Thus the thermal fluctuations generating dark counts are attenuated *de facto*. The superconducting detectors make use of different physical aspects of superconductivity. Nonetheless, it needs only a few concepts to grasp their basic principles of operation. While the temperature decreases below the critical temperature T_c , a superconducting material exhibits a normal to superconducting transition in which its resistivity drops suddenly toward zero.⁵ In the same vein, for $T < T_c$, a superconductor goes back to the normal state if the current flowing into the device reaches the critical current I_c . While in the superconducting state, the electrons are paired together with a binding energy: they form Cooper pairs. An excitation with an energy higher than the binding energy, also called the superconducting gap, unbind the Cooper pairs and generate excited quasiparticles. After long enough time, the quasiparticles go back to equilibrium in the form of Cooper pair. Those three concepts are sufficient to understand the main superconducting detector mechanisms such as the transition edge sensor (TES), the superconducting tunnel junction, or the superconducting single photon detector (SSPD). Hereafter, we only introduce the SSPD technology that outperforms the SPAD capability for almost every metrics.⁶

The SSPD has been initially proposed in 2001 by Gol'tsman *et al.* [1, 2] to detect single photons. At present, there is still no consensus of the microscopic mechanism involved in the detection process. It remains an active research area that requires additional experimental and theoretical work. For the moment, we only present the early simplified picture of the detection principle developed by Semenov *et al.* [23], as depicted in fig. 1.9. We will cover in more details the fundamental aspects of the microscopic understanding of the SSPDs in chapter 2. The device consists of a nanowire with extremely reduced cross-section patterned on an ultra thin superconducting film in a meander shape to increase the detection area. It is usually made of a Nb based superconductor such as NbN

⁵The term normal referred to a normal resistive metal in comparison to the superconducting state which has no resistance.

⁶The reader interested in further details of other superconducting detectors may refer to the literature about photon detection such as the book of Migdall *et al.* [124].

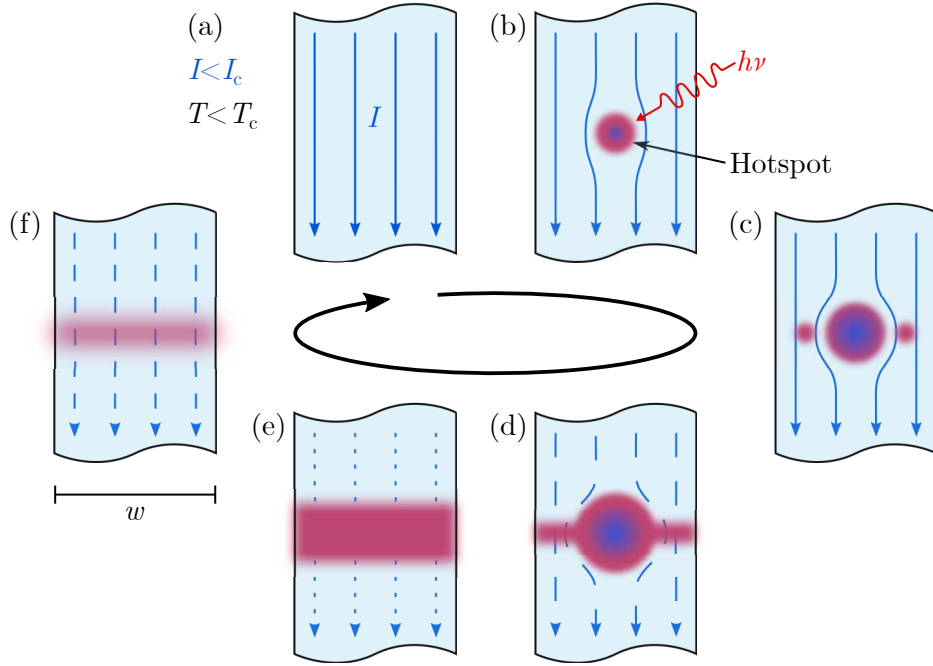


Figure 1.9 – SSPD operating mechanism. (a) A superconducting nanowire of width w and thickness d is cooled below T_c while a bias current I flows. (b) Upon photon absorption with a photon energy higher than the gap a hotspot nucleates inside the nanowire. (c) The superconducting current flow is redirected apart from the hotspot and reaches the critical current. (d-e) The hotspot grows and eventually covers a whole cross-section. A voltage pulse is generated, and the device goes back to its initial state thanks to an adequate electronic circuit. .

or NbTiN, or more seldomly of a Si based superconductor as MoSi or WSi. The typical SSPDs are 100 nm wide, a few nanometers thick, and about 100 μm long. It is cooled below the critical temperature T_c about a few kelvins. A current bias I flows into the nanowire such that I is close, but lower than the critical current I_c . Under such a configuration, the device is still superconducting: there is no voltage drop across the device and only a few number of Cooper pairs remain. When the SSPD absorbs a photon with energy higher than the binding energy, Cooper pairs are broken and form quasiparticles. If the quasiparticles have sufficient energy, they may generate additional quasiparticles *via* the electron-electron interaction. Meanwhile, the quasiparticles also recombine themselves into Cooper pairs and release their excess energy through the electron-phonon interaction. As the superconductivity is suppressed locally in the nanowire, an out of equilibrium normal state forms: it is referred as the hotspot. The current flow is diverted around the hotspot, and as a result the critical current is overpassed. Therefore, a complete cross-section becomes normal resulting in a voltage output pulse across the device. In order to be reset, the current flow is deviated thanks to a passive electronic circuit such that the hotspot vanishes and the SSPD is ready to detect a new photon arrival.

While the SSPD has been invented less than two decades ago, they combine a high intrinsic detection efficiency, a low dark count, a short timing jitter, and a high count rate from the visible to the IR wavelengths. More than six companies are already commercializing SSPDs for various applications. For instance, the QKD has been demonstrated with SSPDs over a few 100 km length of channel communication [125–127]. There are also numerous examples in quantum information protocol such as the big bell test [94], the quantum teleportation with independent source [95], or the quantum random num-

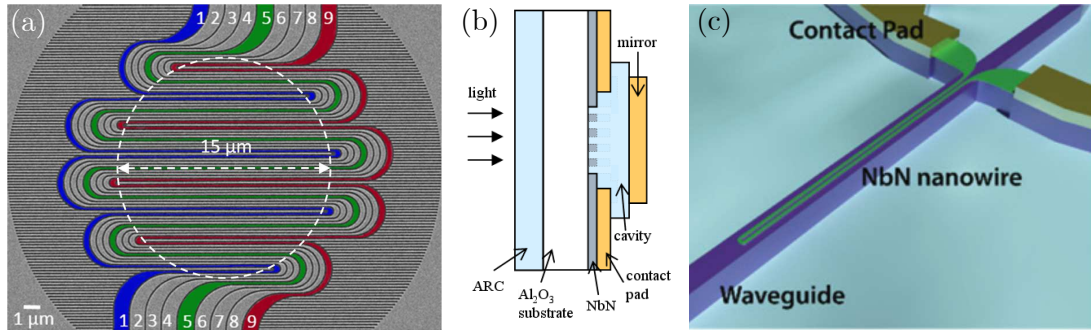


Figure 1.10 – (a) SEM picture of a 15 μm diameter SSPD array composed of nine interlaced superconducting nanowires. Adapted from Huang *et al.* [132]. (b) Schematic of an SSPD embedded in an optical cavity with an anti reflection coating (ARC). Adapted from Rosfjord *et al.* [133]. (c) SSPD integrated in a waveguide. Adapted from Ferrari *et al.* [135].

ber generation [128]. But the SSPD breakthrough does not stop to the quantum world. They have been also used in space communication for the lunar laser communications demonstration performed by NASA [129] and for the deep-space optical communication at NICT, in LIDAR [96], and in time-of-flight imaging [130, 131]. In summary, the SSPDs exhibit tremendous performances in terms of detection aspects, but these results need to be contrasted.

The SSPDs have a small detection area that make the light coupling difficult, but several research work are providing new technological solutions, as shown in fig. 1.10. One approach consists of patterning several SSPDs closely pack together [132]. Another alternatives is to couple the light more efficiently by using optical cavity [133] or integrated waveguides [134, 135]. For the moment it remains a big challenge to build large SSPD arrays with homogeneous properties. Finally, the SSPD operating temperature is typically below 3 K. It is an important limiting factor in a view of applications. It requires cryogenic systems that are cumbersome, expensive, and energy consuming. We stress that the SSPD technology is in its early stage, thus there is still a lot of improvements to expect in the future, as evidenced by the significant research activity among the SSPD community. Nonetheless, if an application needs the high performances of SSPDs while the drawbacks are not an obstacle, the SSPD technology is definitely the detector to use.

1.3.4 Summary

Finally, to gain an overall view, we summarized in table 1.1 some of the different SPD technologies along with their corresponding key metrics. We have included the material used and also the year since they have been developed to emphasize on the detector maturity. Generally speaking, a lot of progresses have been made in the single photon detection since the PMT invention. All the detection performances have been improved through time *via* new SPDs technologies at a cost of a lower operating temperature. The SPAD technology has proven its worth for a good balance between detection metrics with a reasonable intrinsic detection efficiency in comparison to the PMT at 1550 nm, a small jitter about 50 ps, a high maximum count rate about 100 MHz, but a high dark count about 10 kHz. The other main advantages of SPAD in terms of applications is the ease of use thanks to a reasonable operating temperature and the possible integration with the CMOS technology. By contrast the SSPD works about 1 K, but it provides better detection properties with up to 93% intrinsic detection efficiency at telecom wavelength, about 10 Hz of dark count rate, about 100 MHz maximum count rate, and a similar timing

jitter of 50 ps. In addition, we stress that other NbN SSPDs may even exhibit lower timing jitter [136, 137] down to a few ps, but it goes with a decline of the other characteristics. The PMT, the SPAD and the SSPD do not resolve photon number intrinsically but it is made

Table 1.1 – Comparison of SPDs inspired from different reviews [138–140].

Detector	Developed since	Material	Operating temperature	Intrinsic detection efficiency	Dark count rate	Maximum count rate	Jitter	Photon number resolution	Reference
PMT	1937 [141]	Classic	300 K	40% @ 580 nm	100 Hz	10 MHz	300 ps	No	Hamamatsu
PMT	1972 [142]	InP/InGaAs	200 K	2% @ 1550 nm	200 kHz	10 MHz	300 ps	No	Hamamatsu
SPAD	1964 [143]	Si	250 K	49% @ 550 nm	25 Hz	10 MHz	35 ps	No	MPD
SPAD	1984 [144]	InGaAs	250 K	10% @ 1550 nm	10 kHz	100 MHz	50 ps	No	[145]
VLPC	1999 [146]	Si	7 K	88% @ 694 nm	20 kHz	10 MHz	40 ns	Yes	[146]
TES	1995 [147]	W	0.1 K	95% @ 1556 nm	negligible	100 kHz	100 ns	Yes	[148]
TES	2007 [149]	Ti	0.1 K	98% @ 850 nm	negligible	1 MHz	30 ns	Yes	[150]
SSPD	2001 [1]	NbN	2 K	67% @ 1064 nm	30 Hz	40 MHz	200 ps	Some	[151]
SSPD	2008 [152]	NbTiN	2.5 K	92% @ 1310 nm	130 Hz	150 MHz	50 ps	No	[153]
SSPD	2010 [3]	MgB ₂	3 K	0.4% @ 405 nm	-	-	-	No	[3]
SSPD	2011 [154]	WSi	2 K	93% @ 1554 nm	1 kHz	20 MHz	150 ps	No	[4]
SSPD	2014 [155]	MoSi	0.8 K	80% @ 1550 nm	1 kHz	-	26 ps	No	[156]

possible thanks to specific architectures. On the contrary, the VLPC and the TES resolve the photon number naturally due to their physical mechanism. Additionally, the TES technology is outperforming all the SPDs in terms of the intrinsic detection efficiency and the dark count that is negligible in this technology, but it has poor jitter of about 10-100 ns and it operates about 0.1 K.

1.3.5 YBCO as a superconducting single photon detector

One of the main factor limiting the impact and the use of the SSPDs is the low temperature required to operate them properly. This is mainly due to the fact that only low-temperature superconductors (LTS) with $T_c \approx 10$ K are used to fabricate SSPDs as shown in table 1.2. By contrast, the high-temperature superconductors (HTS), especially the cuprate family discovered in the late '80s, exhibit high critical temperature: in the case of $\text{YBa}_2\text{Cu}_3\text{O}_{7-x}$ (YBCO), $T_c \approx 90$ K. At such a temperature, it is possible to cool down the detector at 50 K using only a volume about 0.001 m^3 with a 50 W dry cryocooler [157], as depicted in fig. 1.11(a). In comparison, a dry cryostat with its compressor occupies a volume of about 0.1 m^3 and it consumes a power about 1.5 kW.⁷ We also stress that the cryostats are dictated by Carnot's law that limits the possibility to lower the volume of the cryogenic fluid to complete the cooling closed-cycles. Therefore, there is no reason to hope for a drastic downsizing of the cryostats as the thermodynamic laws are well established.

In such a context, the main goal of the present thesis is to study the feasibility of an SSPD made of YBCO to enable superconducting single photon detection at more accessible temperature. Table 1.2 sums up some relevant parameters in order to support the opportunity of making a YBCO based SSPD. Especially, we introduce the electronic thermalisation time τ_T and the electron-phonon interaction time τ_{e-ph} . The latter ruled how the electrons release their excess energy to the phonons. Roughly speaking, the intrinsic bottleneck process to recover superconductivity is mainly set by τ_{e-ph} . Therefore, we may expect that the YBCO device returns back to equilibrium faster than the NbN SSPD, in other words that the YBCO SSPD has a shorter reset time. This assertion needs to be emphasized since the measurements on YBCO are performed on film thicker by one order of magnitude with respect to NbN. The characteristic times may evolve as the superconducting properties may change for thinner films. Usually, in SSPDs, the readout electronics set the maximum count rate. But the reset time could potentially be lowered using innovative readout architectures to reach the intrinsic device reset time. The counterpart for SSPD based on YBCO is that for a given cross-section and temperature, it may be more difficult to trigger a hotspot in comparison to NbN since the energy is released faster in YBCO. Moreover, the superconducting gap Δ is higher by one order of magnitude in YBCO with respect to NbN. It results in a smaller number of quasiparticles generated upon photon absorption. However, it is worth noting that MgB_2 , a conventional superconductor with intermediate critical temperature of about 40 K, has a superconducting gap similar to YBCO. Although, and yet the single photon detection has been reported by Shibata *et al.* in MgB_2 [3]. Once again, we stress that neither the SSPD detection mechanism nor the superconductivity in YBCO are fully understood. Thus, it is hard to forecast the SSPD made of YBCO since quantitative predictions are not completely reliable.

Besides the application aspects, there is also a significant scientific interest in studying the potential of the HTS SSPDs. The superconductivity arising in cuprates has been subject of an intensive research activity for three decades in both bulk and micron size devices. Even though, the complete microscopic understanding of the HTS materials have not been reached yet. The fabrication technologies are still being improved nowadays to fabricate

⁷For further details see the technical specification of the single photon detection system proposed by Scotel.)

Table 1.2 – Summary of some superconducting parameters relevant for SSPD application.

Material	d (nm)	T_c (K)	Δ (meV)	τ_{e-ph} (ps)	τ_T (ps)	Ref
Nb	7.5	9	1	370	63	[160]
NbN	3.5	16	1	60	6.5	[161]
MgB ₂	50	40	10	-	60	[162, 163]
YBCO	100	89	17	1	0.56	[164, 165]

nanometric size devices made of HTS materials. It enables to study physical phenomena that specifically emerge because the device dimensions become smaller than the characteristic scales of superconductivity. We also briefly mentioned that the detection mechanism is not fully understood in SSPDs. Thus, the investigation of the potential of new superconducting materials is relevant to gain further insights of the microscopic mechanism of single photon detection. The research on the nanometric scale HTS devices remains a highly promising area of research. The following chapter will go into more details on the physics of superconducting YBCO nanowires. It will provide the theoretical background to better understand the physical mechanisms arising from nanoscale superconductivity.

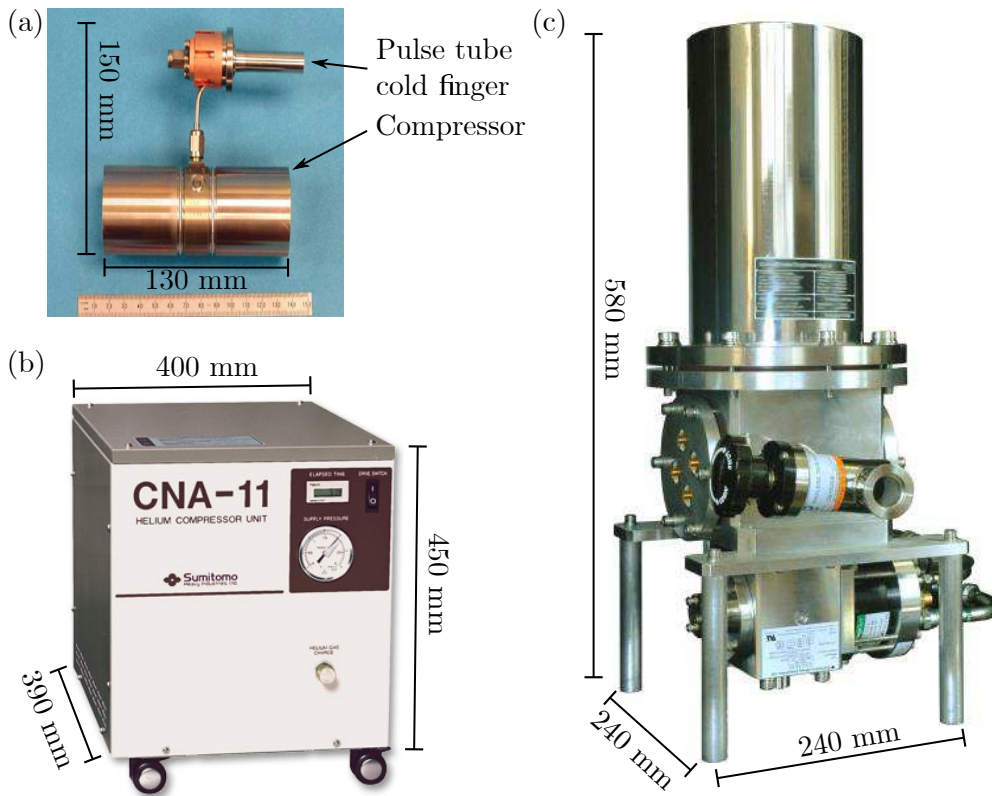


Figure 1.11 – Pictures of different cryostats and compressors along with their dimensions. (a) A space micro pulse tube cooler operating at a minimum base temperature of 50 K. Adapted from Nguyen *et al.* [157]. (b) An indoor air-cooled compressor (adapted from CNA-11 Sumitomo [158]) typically used to operate (c) a helium-free closed-cycle cryostat system for LTS SSPD at 2.2 K (adapted from SCONTEL [159]). The payloads of the systems presented in panel (a), (b), and (c) are respectively about 1 kg, 42 kg, and 25 kg.

Chapter 2

Physics of superconducting nanowires

Contents

2.1 Superconductivity in a nutshell	29
2.1.1 Experimental observations	29
2.1.2 London equations	30
2.1.3 Ginzburg-Landau mean-field approach	31
2.1.4 Bardeen-Schrieffer-Cooper microscopic theory	31
2.1.5 Superconducting length scales	32
2.1.5.1 Clean and dirty limit of superconductors	32
2.1.5.2 Superconducting types	33
2.1.6 High temperature superconductivity in YBCO	34
2.2 Superconductivity at low dimensions	36
2.2.1 The Josephson junction	36
2.2.2 Phase slip in one-dimensional wire	39
2.2.2.1 Little phase slip	39
2.2.2.2 Phase slip center	40
2.2.3 Vortex motion in reduced dimension	41
2.2.3.1 Coherent vortex motion	41
2.2.3.2 Kinematic vortices and phase slip lines	42
2.2.3.3 Conclusion	43
2.3 Superconducting single photon detection mechanism	43
2.3.1 Photoresponse in superconductors	43
2.3.1.1 Rothwarf-Taylor model	43
2.3.1.2 The two-temperature model	45
2.3.2 Experimental observations	46
2.3.2.1 Detection efficiency versus bias current	47
2.3.2.2 Energy - bias current relationship	48
2.3.2.3 Detector response versus magnetic field	48
2.3.3 Hotspot models	49
2.3.3.1 Normal hotspot model	49
2.3.3.2 Diffusive hotspot model	50
2.3.4 Vortex based models	51
2.3.4.1 Vortex-entry model	51

2.3.4.2	Diffusive vortex-entry model	52
2.3.4.3	Normal core vortex model	54
2.3.5	Conclusion	55

Superconductivity is a macroscopic manifestation of a quantum state. This condensed matter research field encompasses both a wide range of intriguing phenomena and several state-of-the-art technologies. For over a century, it has been investigated both theoretically and experimentally, and it still presents fundamental and technical challenges.

Research work presented in this thesis requires concepts underlying the physics of superconducting nanowires for the implementation of YBCO as a new material for SSPD. In this context, section 2.1 introduces the general superconducting theories, the key superconducting parameters, and a brief overview of the specific superconductivity in YBCO. Section 2.2 focuses on the physics of superconducting wire when the dimensions become smaller than the characteristic superconducting length scales. The working principle of SSPD is then described in section 2.3. Beginning with a rapid description of the experimental observations, we introduce the main models presented in the literature to explain the single photon detection mechanism in superconducting nanowires.

2.1 Superconductivity in a nutshell

2.1.1 Experimental observations

The superconductivity was first discovered in 1911 when Kamerlingh Onnes reported that mercury cooled below 4 K has no resistance [5]. From this date, the race for room temperature superconductors began. In seventy years, superconductivity was found in many other metals and alloys such as Al, Pb, Nb, NbTi, *etc.* Despite the intense efforts of the scientific community, the temperature below which the superconductivity is observed raised very slowly. In 1973, Nb₃Ge is discovered by Gavaler with a critical temperature $T_c = 22.3$ K at ambient pressure, the highest T_c at this time [166].

A decade later, in 1986, a new class of compound came into play: the cuprates. Among them the discovery of YBCO in 1987 by Wu *et al.* was a tremendous breakthrough in the field [167]. With reported critical temperature up to 93 K for YBCO, the commercialization of superconducting devices became more feasible thanks to affordable nitrogen cryogenic systems. Since that day, several applications of superconducting materials have emerged such as superconducting quantum interference devices, superconducting quantum interference filters, superconducting electromagnets, low-loss power cables, or superconducting detectors such as SSPD.

The perfect conductivity below T_c was the first experimental observation of superconductivity, but this effect is not sufficient to explain the phenomenon. Besides, in 1933, Meissner and Ochsenfeld discovered perfect diamagnetism in tin, today known as the Meissner effect [168]. In the presence of an external magnetic field \mathbf{H} the total magnetic flux density \mathbf{B} inside the material writes:¹

$$\mathbf{B} = \mu_0 (\mathbf{H} + \mathbf{M}) \tag{2.1}$$

where \mathbf{M} is the material magnetization and μ_0 is the vacuum permeability. When an external magnetic field \mathbf{H} is applied to a superconductor below its critical temperature, the material expels all the magnetic field. To do so, the magnetization \mathbf{M} cancels out the external magnetic field \mathbf{H} , thus the magnetic field inside the superconducting material becomes zero.

As soon as the temperature of the material exceeds the critical temperature T_c , the Meissner effect and the zero resistivity do no longer exist. The material goes to a normal metallic state.

Different theoretical approaches have been considered to explain the superconductivity: the London phenomenological model, the Ginzburg-Landau (GL) mean-field approach [8],

¹With such an equation, \mathbf{B} is in T, while \mathbf{H} and \mathbf{M} are in A.m⁻¹.

and the Bardeen–Cooper–Schrieffer (BCS) microscopic theory [9]. In the following sections, we give physical concepts of interest and main characteristic features of such superconducting theories.

2.1.2 London equations

In 1935, the London brothers proposed a phenomenological theory [6, 7] to explain the two experimental observations of superconductivity: the perfect diamagnetism and the perfect conductivity. They based their model on a two-fluid concept previously developed to describe superfluid helium. In the case of superconductivity, the electrons are either in the superconducting phase or in the normal phase, while the two phases do not interact with each other. They introduced the superfluid and normal fluid densities as n_S and n_N respectively, with their corresponding velocities \mathbf{v}_S and \mathbf{v}_N . They described the electromagnetic properties of the superfluid and normal fluid made up of electrons with different behaviors. Let be n the average electron density, it follows that $n = n_S + n_N$. In this framework, superfluid current density $\mathbf{J}_S = -en_S\mathbf{v}_S$, and normal current density $\mathbf{J}_N = -en_N\mathbf{v}_N$ satisfy respectively the Drude’s model and the Ohm’s law:

$$\frac{\partial \mathbf{J}_S}{\partial t} = \frac{n_S e^2}{m} \mathbf{E} \quad (2.2a)$$

$$\mathbf{J}_N = \sigma_N \mathbf{E} \quad (2.2b)$$

where m is the electron mass, and σ_N is the normal electron conductivity. In the presence of an electric field, the superconducting electrons accelerate, whereas normal electrons sustain their velocity. It explains that the perfect conductivity arises from the superconducting electrons of the superfluid.

Additionally, using the Maxwell equations, the relation between the total flux density \mathbf{B} and the supercurrent \mathbf{J}_S is given by:

$$\nabla \times \mathbf{J}_S = -\frac{n_S e^2}{mc} \mathbf{B} \quad (2.3)$$

Using the Maxwell-Ampere’s law with the latter equation, the total magnetic field obeys the following differential equation:

$$\nabla^2 \mathbf{B} = \frac{1}{\lambda_L^2} \mathbf{B} \quad (2.4)$$

where λ_L is the London magnetic penetration length written as follow:

$$\lambda_L(T) = \sqrt{\frac{mc^2}{4\pi n_S(T)e^2}} \quad (2.5)$$

By considering a normal-superconducting interface at position $x = 0$, we show from eq. (2.4) that $B(x) = B(0) \exp(-x/\lambda_L)$. Hence, the magnetic field decays exponentially inside the superconductor on a length scale λ_L which explains the Meissner effect. The external magnetic field \mathbf{H} still penetrates into the surface of the superconductor on a few λ_L , in which the supercurrent induce a magnetic field \mathbf{M} in the opposite direction of the external magnetic field. The temperature dependence of λ_L is set by n_S , the only temperature dependent parameter. In the framework of the phenomenological two-fluid theory of Gorter and Casimir, the London penetration length writes:

$$\lambda_L(t) = \frac{\lambda_0}{\sqrt{1 - t^4}} \quad (2.6)$$

where $t = T/T_c$ is the reduced temperature and λ_0 is the magnetic penetration depth at zero temperature.

The London phenomenological approach successfully describes the two main experimental observations, and eq. (2.6) nicely accounts for the experiments. Nonetheless there are no microscopic details of superconductivity, the electrons are treated macroscopically as a whole phase.

2.1.3 Ginzburg-Landau mean-field approach

In the spirit of the second order phase transition theory developed by Landau in 1938, Ginzburg and Landau proposed that the free energy density f can be expressed as a function of a spatial complex order parameter $\Psi(\mathbf{r})$. The latter is introduced as:

$$\Psi(\mathbf{r}) = |\Psi(\mathbf{r})|e^{i\varphi(\mathbf{r})} \quad (2.7)$$

where $|\Psi(\mathbf{r})|$ and $\varphi(\mathbf{r})$ are respectively the amplitude and the phase of the order parameter.

As a phase transition theory, the model is valid near T_c where $|\Psi(\mathbf{r})|$ is small enough and varies slowly in space. Nevertheless, there are some cases in which the theory holds in a wider temperature range.² Under a volumetric external magnetic field h , the free energy density of a superconductor expresses in series of Ψ as follows:

$$f = f_{n0} + \alpha|\Psi|^2 + \frac{\beta}{2}|\Psi|^4 + \frac{1}{4m} \left[\left(\frac{\hbar}{i}\nabla + \frac{2e}{c}\mathbf{A} \right) \cdot \Psi \right]^2 + \frac{h^2}{8\pi} \quad (2.8)$$

Here above f_{n0} corresponds to the free energy density in the normal state without magnetic field while α and β are temperature dependent phenomenological parameters. In addition, m and e are the mass and the charge of an electron respectively, and \mathbf{A} is the magnetic vector potential. By deriving the order parameter, two temperature dependent characteristic lengths arise: ξ and λ_{GL} . The latter corresponds to the magnetic penetration depth previously defined. But in the framework of the GL theory, for temperatures close to T_c , it is shown that:

$$\lambda_{GL}(t) = \frac{\lambda_0}{\sqrt{1-t}} \quad (2.9)$$

where t is the reduced temperature. The GL coherence length ξ represents the typical distance over which the order parameter varies. In the vicinity of T_c , $\xi \propto 1/\sqrt{1-t}$.

The model can be more refined with the time dependent Ginzburg-Landau (TDGL) theory. It allows one to solve the time evolution of the superconducting order parameter. This approach is particularly useful when the characteristic time scales involved are smaller than the recovery time of the superconducting order parameter τ_Δ . Depending on the material, τ_Δ might vary from a few nanoseconds to less than a picosecond. In SSPD, the time scales are of the order of the picoseconds, making TDGL model a powerful tool to describe the physics as we will see in section 2.3.4.3.

The phenomenological model developed by Landau and Ginzburg makes possible to explain superconductivity in terms of symmetry breaking of an order parameter. While the GL theory does not account for the microscopic mechanism behind superconductivity, it is a powerful technique as it can deal with inhomogeneities in space and non-constant band gap. Hence it is a universal model describing any superconducting material.

2.1.4 Bardeen-Schrieffer-Cooper microscopic theory

Although the two previous models account for experimental observations, the microscopic picture behind superconductivity remained mysterious until 1957 when Bardeen, Cooper

²See discussion at p.78-79 in [169] for further details.

and Schrieffer proposed a theoretical framework along with a physical interpretation. The theory is based on a weak interaction between the electrons mediated by the phonons. When the attractive interaction overrides the repulsive screened Coulomb interaction, the total net interaction gives rise to superconductivity.

They consider two electrons at position \mathbf{r}_1 and \mathbf{r}_2 , with their complex wave function $\psi(\mathbf{r}_1, \mathbf{r}_2)$ and with an isotropic attractive coupling in momentum space. The analytic derivation shows that the pairing interaction only takes place for electrons of opposite wave vector \mathbf{k} and $-\mathbf{k}$, and opposite spins. These two electrons form a Cooper pair which extends on the BCS coherence length scale ξ_0 . In such a configuration, paired electrons populate states below the Fermi sea, with energy smaller than the Fermi energy E_F . The depopulation of the Fermi surface opens an energy gap $2\Delta_0 = 3.52k_B T_c$ at zero temperature. It represents the minimum excitation energy required to break a Cooper pair, which is typically of about 1 meV. As long as the thermal fluctuations become larger than the energy gap, the Cooper pairs break and superconductivity disappears.

The results presented above concern the analytic solution of BCS model for an isotropic coupling. When the coupling becomes anisotropic, like in the cuprate case, the equations are not solvable analytically, though a numerical approach is used. The materials well described by the BCS theory, with an isotropic coupling in momentum space, are referred as conventional superconductors in contrast with the unconventional superconductors.

In conventional superconductors, ξ_0 is close to the GL coherence length at $T = 0$ K. Within BCS theory, the zero temperature coherence length ξ_0 writes:

$$\xi_0 = \frac{\hbar v_F}{\pi \Delta_0} = \frac{\hbar v_F}{\pi \Delta_0} \quad (2.10)$$

where v_F is the Fermi velocity, and Δ_0 is the gap energy at zero temperature. Later on, Gor'kov [170] demonstrated that GL theory gives the same results than BCS theory for conventional superconductors only. In this case, the Cooper pair wave function identifies with the superconducting order parameter introduced by Ginzburg and Landau. For unconventional superconductors, it is not the case as the two complex quantities do not describe the same variations even though their phases are the same.

2.1.5 Superconducting length scales

Two characteristic lengths arise from the theory of superconductivity: the coherence length and the magnetic penetration depth. Depending on the material and the temperature range, the latter dimension is better described by GL theory or London theory. The magnetic penetration at zero temperature is always the same, but the temperature dependence varies. For the sake of simplicity, hereafter we drop the subscripts of the magnetic penetration depth: "L" for London and "GL" for Ginzburg-Landau. When necessary, we will explicit the theory used to describe the temperature dependence of the magnetic penetration depth. Depending on their respective values, compared to the device dimensions and the electronic mean free path l_0 , different physical behaviors are predicted.

2.1.5.1 Clean and dirty limit of superconductors

The GL coherence length corresponds to the length over which the order parameter Ψ varies spatially in a pure material. It is valid as long as $l_0 \gg \xi_0$, referred as the pure or clean limit. Within such limit, in the GL model using some BCS results, it is possible to show that the GL coherence length writes [48]:

$$\xi(t) = 0.74 \frac{\xi_0}{(1-t)^{1/2}}, \quad (l_0 \gg \xi_0) \quad (2.11)$$

As soon as $l_0 \ll \xi_0$, the superconductor is in the dirty limit. In this diffusive limit, the coherence length ξ_0 has to be corrected and writes: $\xi'_0 = \sqrt{l_0 \xi_0}$. The impurities have to be considered to define the effective coherence length. In the GL model using some BCS results, ξ_0 is given near T_c , *i.e.* $t = 1$, by:

$$\xi(t) = 0.86 \frac{\sqrt{\xi_0 l_0}}{(1-t)^{1/2}} \quad (l_0 \ll \xi_0) \quad (2.12)$$

Depending on the superconducting material, the coherence length might be of about a few nanometers, like for YBCO, to $1 \mu\text{m}$ for conventional superconductor such as Al. In the YBCO case, $l_0 \approx 15 \text{ nm}$ [171–173], hence YBCO is in the pure limit.

2.1.5.2 Superconducting types

Superconductors can be classified in two types depending on the GL parameter κ defined as:

$$\kappa = \frac{\lambda}{\xi} \quad (2.13)$$

The materials with $\kappa < 1/\sqrt{2}$ are called type-I superconductor. In this case, when an external magnetic field is applied, the superconductor becomes normal when all the superconducting electrons are involved in the screening currents. Above the critical field H_c the external magnetic field is no longer screened thanks to the Meissner effect. The material switches to its normal state following a first order phase transition. The critical field writes [48, 169]:

$$H_c(T) = \frac{\Phi_0}{2\sqrt{2}\pi\mu_0\lambda(T)\xi(T)} \quad (2.14)$$

where $\Phi_0 = h/2e$ is the magnetic flux quantum.

Shubnikov *et al.* [11] have shown experimentally in 1937 that some superconducting materials exhibit two distinct critical fields, they correspond to type-II superconductors. Prior to the first critical field, the material is completely superconducting. For magnetic field higher than the first critical field, the material lies in an intermediate state with both superconducting and normal state. At the second critical field higher than the first

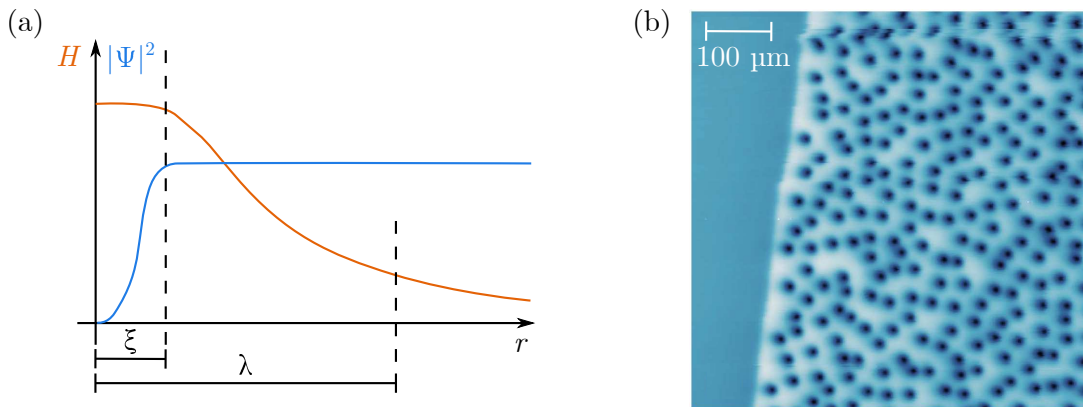


Figure 2.1 – (a) Spatial evolution of the order parameter, Ψ , and of the external magnetic field, H , in presence of a vortex inside an infinite superconductor, R being the distance from the vortex center. The vortex consists of a normal zone at the left side of the vertical dashed line with surrounding supercurrents. Adapted from Mourachkine [169]. (b) Scanning SQUID microscopy picture of vortices in 200 nm thick YBCO film at 4 K with an external field of $6.93 \mu\text{T}$. Adapted from Wells *et al.* [174].

one, the type-II superconductors undergo a second order transition. Only then in 1957, Abrikosov [12] have accounted theoretically for such experiments in type-II superconductor. For $\kappa > 1/\sqrt{2}$, the magnetic field partially penetrates thanks to the appearance of Abrikosov vortices. They consist of a normal core of size ξ surrounded by supercurrents which decay exponentially on a distance λ_L as illustrated in fig. 2.1(a). The supercurrents induce a magnetic field opposite to \mathbf{H} . Each vortex carries a flux quantum Φ_0 defined as:

$$\Phi_0 = \frac{h}{2e} \approx 2.067 \times 10^{-15} \text{T.m}^2 \quad (2.15)$$

Upon appearance, Abrikosov vortices tend to form a static triangular lattice. Figure 2.1(b) shows an experimental observation of a static vortex configuration under the application of an external magnetic field using scanning SQUID microscopy imaging. In this picture, the usual vortex triangular lattice is significantly disrupted due to the impurities in the superconductor.

The presence of vortices in the material has several physical implications in our context. Type-II superconductors exhibit two different critical magnetic fields such that $H_{c1} < H_{c2}$. The lower critical field, H_{c1} , corresponds to the appearance of the first vortex. In other words superconductor exhibits a transition between a superconducting state and a mixture of superconducting and normal state: the mixed state. In the limit in which $\kappa \gg 1$ it writes:

$$H_{c1}(T) = \frac{\Phi_0}{4\pi\mu_0\lambda^2(T)} (\ln(\kappa) - 0.18) \quad (2.16)$$

As the magnetic field increases above H_{c1} , more vortices penetrate, and their edges are getting closer. Vortices begin to interact with each other electromagnetically at a maximum distance of λ . When the upper critical field H_{c2} is reached, all the vortex normal cores overlap. All the superconducting material is paved by vortices spaced by the effective vortex radius of about ξ . H_{c2} sets the limit between the mixed state and the normal state where Cooper pairs do no longer exist. In the GL framework, it writes:

$$H_{c2}(T) = \sqrt{2}\kappa H_c = \frac{\Phi_0}{2\pi\mu_0\xi^2(T)} \quad (2.17)$$

Vortices may also nucleate in a type-II superconducting bridge from the edges or defects of size ξ under a current bias. At sufficiently high current, the induced magnetic field lowers the vortex-entry energy barrier which previously prevents the vortex from entering at zero bias. Once created, vortices tend to move under the Lorentz force perpendicularly to the current direction which generates dissipation. In this respect, current induced vortex nucleation is different, since a dynamical vortex state is established.

When the thickness of a superconducting sample d is smaller than λ , the external magnetic field completely penetrates in depth. Pearl [175] has shown that to balance this effect and preserve superconductivity, the vortex electromagnetic extension grows in the plane perpendicular to the depth. The Abrikosov vortices become Pearl vortices, with a penetration length renormalized into the Pearl length as:

$$\Lambda = \frac{2\lambda^2}{d} \quad (2.18)$$

Thus, vortices have a larger electromagnetic extension in thin films, so they interact together at a longer range.

2.1.6 High temperature superconductivity in YBCO

The discovery of the first cuprate material by Bednorz and Müller in 1986 was a real breakthrough in superconductivity with $T_c = 35$ K for $\text{LaBa}_2\text{Cu}_3\text{O}_7$ [176]. One year later,

Chu almost triples the record T_c with the discovery of the new cuprate $\text{YBa}_2\text{Cu}_3\text{O}_{7-x}$ with $T_c = 93$ K [167]. It is the first superconductor with a T_c above the boiling point of nitrogen. Since then, numerous other HTS materials have been synthesized such as $\text{Bi}_2\text{Sr}_2\text{CaCu}_2\text{O}_{8+x}$ or $\text{HgBa}_2\text{CuO}_4$.

The cuprates have all in common a perovskite structure with copper and oxygen atoms bonded together in CuO_2 planes, or ab -planes. Most of the HTS cuprate materials have a tetragonal crystalline structure. However, YBCO shows an orthorhombic structure as depicted in fig. 2.2(a) with the following lattice parameters: $a \approx 3.82$ Å, $b \approx 3.89$ Å, and $c \approx 11.7$ Å. The maximum critical temperature for $\text{YBa}_2\text{Cu}_3\text{O}_{7-x}$ is obtained for an optimal hole doping of $x \simeq 0.15$.

However, the energy gap is not isotropic unlike the conventional superconductors. After long debates, a consensus has been found in favor of a $d_{x^2-y^2}$ -symmetry for the order parameter (fig. 2.2(b)) illustrated by many experimental works. Historically, measurements of magnetic penetration length showed that low-energy excitation exists in HTS suggesting the existence of nodes in the gap [178]. Angle resolved photoemission spectrum (ARPES) measurements of $\text{Bi}_2\text{Sr}_2\text{CaCu}_2\text{O}_{8+x}$ confirmed the presence of nodes in the directions oriented at 45° of the crystallographic axis [179]. Finally, the SQUID experiments performed by Wollman and Van Harlingen [180], and the tricrystal experiment of Tsuei and Kirtley [181] definitely convince the community for a $d_{x^2-y^2}$ -symmetry. Both studies confirmed that a π -phase shift occurs between two adjacent lobes as observed in a $d_{x^2-y^2}$ -symmetry (fig. 2.2(b)). It consists of four lobes in perpendicular direction of the ab -planes. As a consequence, YBCO presents a pseudogap as quasiparticles may exist, even at 0 K, in the nodal lines tilted at 45° from the lobe direction. This specific symmetry indicates that the mechanism responsible for superconductivity in HTSs are different than the conventional BCS electron-phonon coupling. Today, understanding the HTS physics remains one of the major challenge of condensed matter.

Since YBCO has a $d_{x^2-y^2}$ -symmetry, the superconducting length scales are different in

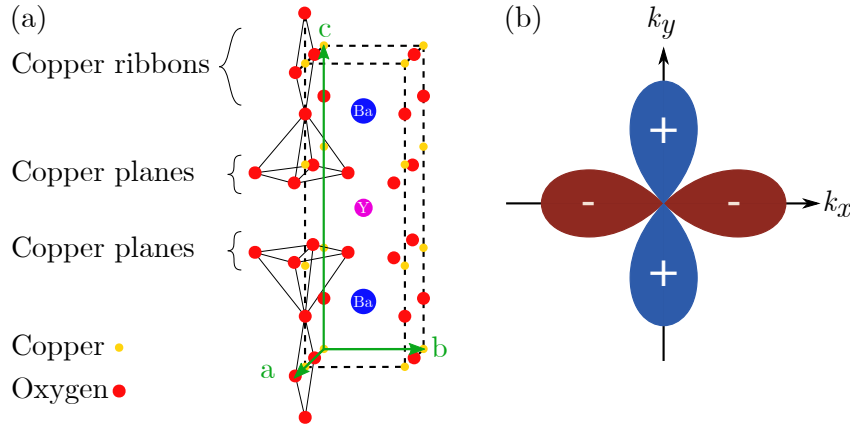


Figure 2.2 – (a) Crystalline structure of YBCO with copper planes and copper ribbons. (b) $d_{x^2-y^2}$ superconducting order parameter of YBCO in reciprocal space.

Table 2.1 – Superconducting properties for bulk YBCO depending on directions [169, 177].

Direction	ξ (nm)	λ_0 (nm)	κ	$\mu_0 H_{c2}$ (T)
ab -plane	1.5	150	100	120
c -axis	0.2	600	300	40

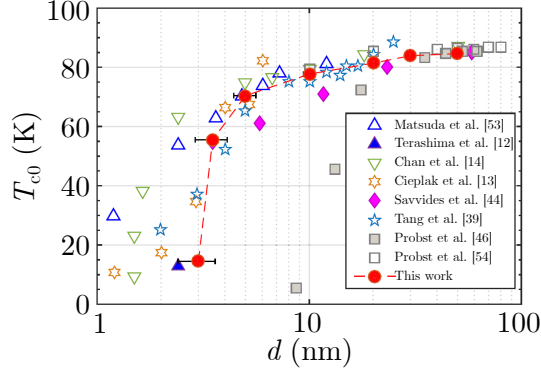


Figure 2.3 – Evolution of the critical temperature T_c as a function of the YBCO film thickness. Adapted from Arpaia *et al.* [10].

the ab -plane and along the c -axis. The superconducting characteristic lengths and critical fields are highly anisotropic in the two directions (see table 2.1). With $\kappa \gg 1/\sqrt{2}$ in both directions, YBCO is unambiguously a type-II superconductors in which the vortices play a crucial role.

The electronic mean free path in bulk YBCO, $l_0 \approx 15$ nm [171–173], is larger by one order of magnitude than the coherence length, as a consequence bulk YBCO is considered as a clean superconductor for bulk. When YBCO thickness becomes thinner than l_0 , the effective mean free path is partially renormalized with the thickness. The effective mean free path l_{eff} is mainly set by the thickness. In addition, T_c is largely damaged when thickness is reduced below 10 nm as shown by fig. 2.3, which can be interpreted as a loss of pairing energy. Hence, ξ becomes larger to balance this effect and to maintain superconductivity. Nevertheless the coherence length remains small: for 5 nm thick film $\xi(T = 0) \approx 3$ nm has been reported [182]. Combining these two effects, we expect that YBCO thin film should be in the dirty limit for thickness about 5 nm and below.

2.2 Superconductivity at low dimensions

When the lateral dimensions of a superconducting sample are reduced with respect to λ and ξ , new physical effects have to be considered such as Phase slip or kinematic vortex motion. Depending on the cross-section $S = wd$ of the superconducting wire of width w and thickness d , distinct scenarios have been predicted, as shown in fig. 2.4. Three different main phenomena are relevant in superconducting devices at low dimensions: the Josephson junction, the phase slip in one-dimensional wire, and the vortex motion.

2.2.1 The Josephson junction

In 1962, Josephson originally predicted the tunnelling of Cooper pairs through a thin normal barrier separating two superconducting leads [13], named Josephson Junction (JJ). It turns out that Josephson effect applies for any kind of weak-link separating two superconducting regions [14]. It means that the barrier could be either insulating or only weakly superconducting or even constituted by a wire whose width w is smaller than the coherence length [15]. The electric behavior of a JJ biased by a current I is governed by

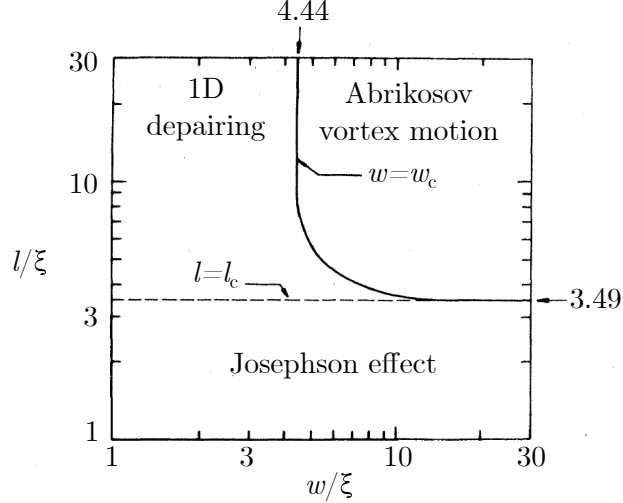


Figure 2.4 – Depending on the cross-section of a w -wide, l -long bridge, different physical phenomena arise that are all experimentally characterized by a Josephson effect signature. Adapted from Likharev *et al.* [14]

a set of two equations:

$$I = I_C \sin \phi \quad (2.19a)$$

$$\frac{\partial \Delta \phi}{\partial t} = \frac{2e}{\hbar} V \quad (2.19b)$$

where I_C is the critical current of the junction, ϕ is the pair wave function phase difference between the two superconducting regions, and V is the voltage drop across the junction. Equation (2.19a) is referred as the DC Josephson equation, while eq. (2.19b) corresponds to the AC Josephson equation. By setting I or V , it is possible to control the phase difference. Today, the current phase relation (CPR) is at the heart of fundamental studies and applications. For instance, it is used to define the standard value of Volt. When a JJ is illuminated by a radiofrequency (RF) signal at a frequency f , current steps appear in the Current-Voltage Characteristic (IVC), known as Shapiro steps [20] shown in fig. 2.5, at given voltages set by:

$$V_n = n \frac{\hbar f}{2e} = n \frac{f}{K_J} \quad (2.20)$$

where $n \in \mathbb{N}$, and $K_J = 2e/\hbar = 1/\Phi_0 = 0.484 \text{ GHz.V}^{-1}$ is the Josephson constant. As the RF power level increases, the current steps height grows, and successive steps at higher n values appear. The superconducting branch at zero voltage diminishes with increasing RF power, until it completely disappears while the current step width begins to decrease and are also suppressed finally. As the incident RF power increases further, both critical current and current steps height enlarge. They are both modulated with the incident RF power.

While Shapiro steps are a typical fingerprint of a JJ, it cannot be attributed unequivocally to JJ as Shapiro-like steps are also predicted [18, 57, 183] and observed [17, 184] in superconducting nanowires.

To account for the JJ IVC, McCumber [186] and Stewart [187] have proposed an electrical circuit modelling the JJ called the resistive capacitive shunted junction (RCSJ) equivalent circuit model, depicted in fig. 2.6. A shunt resistor R_N describes the quasiparticles current i_N . A shunt capacitance C corresponds to the charge imbalance between superconducting regions and contributes as a dissipative current i_D . They are both in

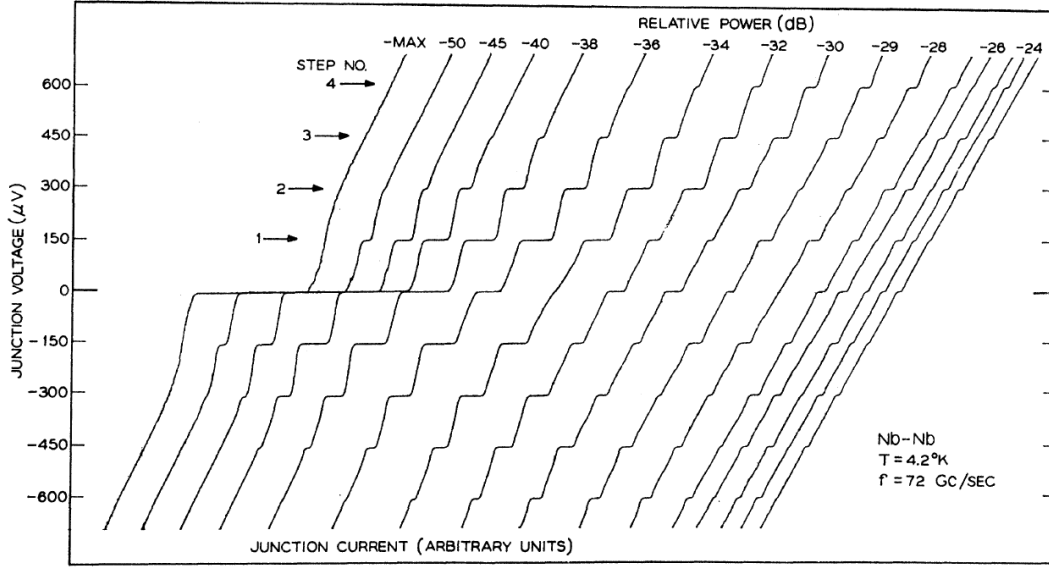


Figure 2.5 – Shapiro constant current steps observed in the Voltage-Current characteristics of a Nb-Nb point-contact Josephson junction illuminated by a 72 GHz RF signal at different power levels. Adapted from Grimes *et al.* [185].

parallel with a pure Josephson non dissipative element depicted as a cross in the electrical scheme with a supercurrent i_S .

Based on fig. 2.6, using the Kirchoff law and the Josephson equations eqs. (2.19a) and (2.19b), the RCSJ circuit equation writes:

$$I = \frac{\Phi_0}{2\pi} C \frac{\partial^2 \phi}{\partial t^2} + \frac{\Phi_0}{2\pi} \frac{1}{R} \frac{\partial \phi}{\partial t} + I_c \sin(\phi) \quad (2.21)$$

The formula describes the time evolution of the phase ϕ . It can be rewritten as:

$$\frac{\partial U}{\partial \phi} + \frac{1}{\omega_J^2} \frac{\partial^2 \phi}{\partial t^2} + \frac{1}{\omega_J Q} \frac{\Phi_0^2}{R} \frac{\partial \phi}{\partial t} = 0 \quad (2.22)$$

where U is the energy potential, ω_J is the Josephson pulsation, and Q is the JJ quality factor. The latter is also frequently considered in terms of the damping parameter as $\beta = Q^2$. They all depend on the JJ intrinsic parameters given by the following equations:

$$U = -\frac{\Phi_0 I_c}{2\pi} \left(\cos(\phi) + \frac{I}{I_c} \phi \right) \quad (2.23a)$$

$$\omega_J = \sqrt{\frac{2\pi I_c}{\Phi_0 C}} \quad (2.23b)$$

$$Q = \omega_J R C = R \sqrt{\frac{2\pi C I_c}{\Phi_0}} \quad (2.23c)$$

Only U depends on the bias current with $E_J = \Phi_0 I_c / 2\pi$ being the Josephson energy. It is equivalent to the dynamics of a particle in a tilted washboard potential in which C represents the mass while $1/R$ corresponds to the damping. Such an analogy is relevant to understand the physics of JJs, in particular its phase evolution. Figure 2.6 shows the corresponding tilted washboard potential of eq. (2.23a). It corresponds to a sum of a linear term and a periodic term as a function of the phase. It results in local minimum

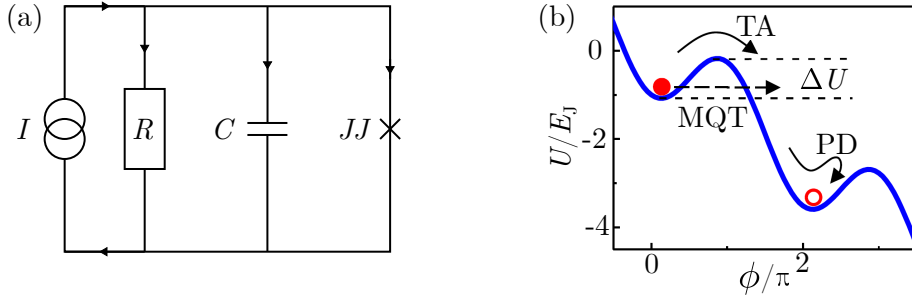


Figure 2.6 – (a) Resistive Capacitive Shunted Junction equivalent circuit describing the behavior of a Josephson junction. (b) Schematics of a phase particle (red dot) trapped in a washboard potential described by eq. (2.23). The phase particle may leave the local minima *via* thermal activation (TA) or macroscopic quantum tunnelling (MQT) to go in a lower energy state (red circle). Adapted from Lee *et al.* [188].

separated by 2π phase shift with amplitude controlled by I_c , with an additional negative global slope set by the bias current I . If we consider a phase particle trapped in one specific local minimum, fluctuations enable the particle to go in another lower energy state. It can be achieved either *via* thermal activation (TA) or macroscopic quantum tunnelling (MQT).

Naively, there is no direct link between supercurrent tunnelling and superconducting wires with reduced dimensions. If we postulate that a CPR exists for a superconducting nanowire, effects similar to Josephson effect arise. Even if the DC Josephson equation does not describe correctly the CPR of a superconducting nanowire, it is relevant to compare them in the light of the RCSJ to understand how they differ.

2.2.2 Phase slip in one-dimensional wire

2.2.2.1 Little phase slip

Following the discovery of Josephson, the study of a one-dimensional (1D) superconducting wire, whose cross-section dimension is smaller than the GL coherence length ξ , arose interest. Little studied in 1967 the suppression of the superconducting order parameter $\Psi(x, t)$ in a 1D superconducting loop [16]. In the framework of Ginzburg-Landau theory, he showed that a DC supercurrent can only decay thanks to fluctuations, whether quantum or thermal. They enable a phase slip between the wire ends, which causes a supercurrent reduction.

Figure 2.7 depicts in more details how current is reduced in a 1D superconducting wire of length l . The superconducting order parameter phase difference between the ends of the wire at $x = 0$ and $x = l > \xi$ is given by $\Delta\phi = n2\pi$ with $n \in \mathbb{N}$. In other words, n corresponds to the number of twists of the superconducting order parameter around the horizontal x -axis. In fig. 2.7 two configurations of $\Psi(x, t)$ belonging to the subsets $n = 0$ and $n = 1$ are represented. They only vary one from another locally near the point A, the latter $n = 1$ makes one revolution around the x -axis, while $n = 0$ subset has zero turn. In order to have a supercurrent reduction, $\Delta\phi$ has to be lowered, passing to a lower n subset: for instance from $n = 1$ to $n = 0$ as illustrated in fig. 2.7. It implies necessarily that $\Psi(x, t)$ crosses the x -axis, which generates a 2π -phase slip and leads to a zero amplitude order parameter locally in space and time. The process is known as the Little Phase Slip (LPS). For a 1D wire whose cross-section is smaller than ξ^2 , this is the only process by which the DC supercurrent might be diminished.

As $\Psi(x, t) = 0$ during a short time of the order of $\tau_\Delta = \Delta/\hbar$, a voltage spike is generated

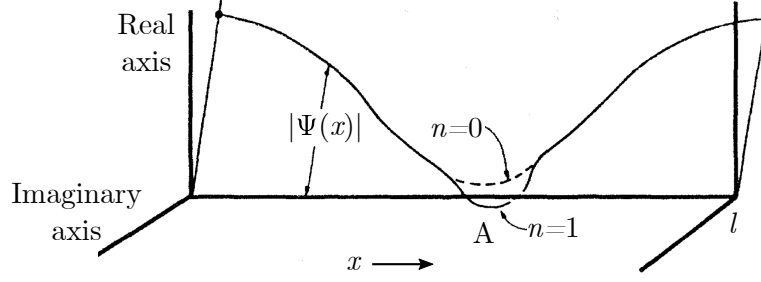


Figure 2.7 – Variation of the superconducting order parameter in the complex plane along a 1D superconducting wire. Two different configurations are presented in the subset $n = 0$ and $n = 1$, with n representing the number of twists around the horizontal axis. Therefore $n = 0$ and $n = 1$ correspond respectively to a 0 and 2π phase shift at the wire extremities. In order to go from one configuration to another, the superconducting order parameter necessarily crosses the horizontal axis. It results that the superconducting order parameter is locally suppressed during a short time. It forms a normal zone which dissipates heat. Such a process is referred as the Little phase slip (LPS). Adapted from Little [16].

due to the normal region produced on a length ξ . To create the normal zone, the system has to bypass an energetic barrier ΔF . Hence, the PS is generated thanks to fluctuations, whether thermal or quantum. For T about T_c , LPS might be so greatly generated by the thermal fluctuations that they result in a non-zero resistance contribution below T_c . It leads to a smoother transition in resistance-temperature curve due to the thermally activated phase slips (TAPS).

Two models have been developed to ascribe for the resistance contribution of TAPS: the Little expression [189, 190], and the Langer-Ambegaokar-McCumber-Halperin (LAMH) [191–193] model. These models have been widely used to account for the finite resistance below T_c in nanowire [189, 194, 195].

2.2.2.2 Phase slip center

Skocpol, Beasley, and Tinkham refined further the initial model of Little to explain the voltage steps appearing in bias current tin whisker crystals [17]. They consider a bridge of length l and cross-section $A \lesssim \xi^2$ as depicted in fig. 2.8(a). As current raises in the device, phase slips are more prone to be generated by the thermal fluctuations since the energy barrier is lowered. The fluctuations eventually create a phase slip center (PSC): a region of typical size 2ξ in which Ψ goes to zero and supercurrent is suppressed as shown in fig. 2.8(a). Since quasiparticles are generated in the PSC normal zone, they diffuse out from each side of the normal region on a length Λ_Q . The latter corresponds to the quasiparticle diffusion length given by:

$$\Lambda_Q = \sqrt{D_N \tau_Q} = \sqrt{\frac{1}{3} v_F l \tau_Q} \quad (2.24)$$

where D_N is the quasiparticles diffusion coefficient in normal state, τ_Q is the inelastic scattering time, and v_F is the Fermi velocity. After a long enough diffusion time, the supercurrent is re-established and another PSC might occur. It results in a self-sustained AC supercurrent, with an average value of approximately half the critical current.

Figure 2.8(b) points out the experimental observation of the PSC in IV characteristic of a tin whisker crystal. For each new PSC center created, a voltage step appears and the additional resistance is always the same. Another argument pointing toward a dynamical

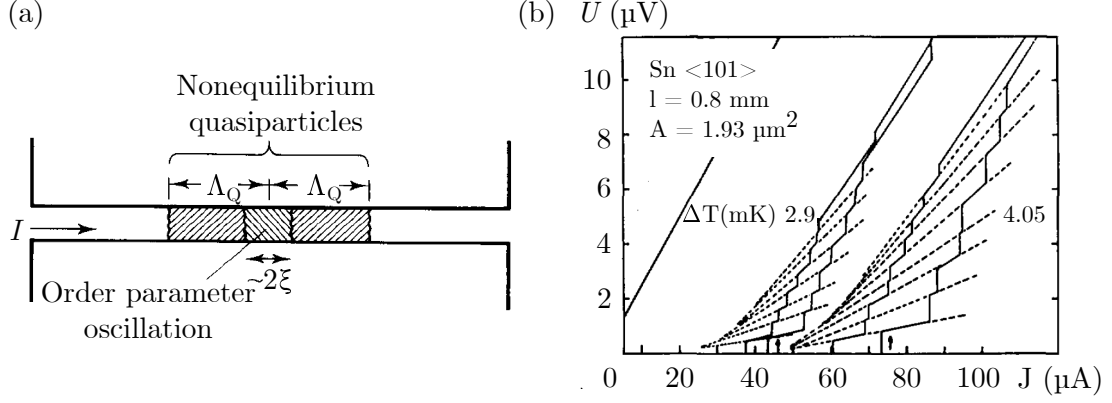


Figure 2.8 – (a) Schematic of a phase slip center created in a wire with cross-section $A \lesssim \xi^2$ and length $l > \xi$, biased with a current I . A normal core of a typical size 2ξ forms due to a phase slip. The generated quasiparticles diffuse out of this region in a length Λ_Q from both sides. Adapted from Tinkham [196]. (b) IV characteristic of a tin whisker crystal showing step-like behavior for each new phase slip center created. Adapted from Meyer PhD Thesis [197]

process is the appearance of Shapiro-like steps upon RF illumination as shown in fig. 2.5. It reveals that the formation of a PSC can be synchronized and allows one to eliminate the interpretation of a large sustained normal hotspot as presented in [45].

As a concluding remark, we stress that for the PSC model, like the LPS event, width and thickness are both lower than $w_c = 4.4\xi$, and $l > 3.49\xi$. According to Likharev [198], in such a limit, vortices do no longer exist since surrounding supercurrents cannot flow around the normal core which occupy the whole width.

2.2.3 Vortex motion in reduced dimension

On the contrary, if the width of the device of interest is higher than w_c , and the length is higher than $l_c = 3.49\xi$, the vortex motion comes into play in the form of Abrikosov or Pearl vortices. According to fig. 2.4, there is no longer any pure Josephson effect strictly speaking, neither 1D pair breaking.

2.2.3.1 Coherent vortex motion

Likharev [18] demonstrated theoretically that a behavior similar of a JJ appears for superconducting bridges which satisfy: $\xi \ll l \ll w \ll \lambda_{\text{eff}}$, with λ_{eff} being λ or Λ for $d > \lambda$ or $d < \lambda$ respectively. Under application of an external RF electromagnetic field, current steps should appear at constant voltage steps like the Shapiro steps described previously. Likharev stated that the vortex motion is synchronized by the external electromagnetic field. Aslamazov and Larkin [57] developed further the calculation in presence of an external RF field by introducing an alternating current source term oscillating at frequency f , and considering an AC Josephson relation across the bridge eq. (2.19b). One year later, in 1976, Gubankov *et al.* [184] showed experimentally the transition between the pure Josephson effect ($l < 3.49\xi$ in fig. 2.4) and the Abrikosov coherent vortex motion ($l > 3.49\xi$ and $w > 4.4\xi$ right up quadrant in fig. 2.4).

An oversimplified picture is that under a current bias, vortices nucleate at a constant rate fixed by the RF frequency f at one edge of the bridge. The Lorentz force drives them to the opposite edge, perpendicularly to the bridge, where they vanish. Another scenario is that two vortices of opposite polarity nucleate at the same time, one vortex

pointing toward $+\mathbf{e}_z$ parallel to the thickness, one anti-vortex pointing toward $-\mathbf{e}_z$. They are either located at the edges, or in the center of the bridge, and they collapse at the center or disappear at the edges respectively. In practical device, the first case is more relevant since any asymmetry of the bridge will tend to favour the vortex creation at one edge. Each vortex crossing generates a 2π -phase shift across the bridge at a rate f which leads to the relation $hf = 2eV$, with V the average voltage drop across the bridge. For a bridge, the CPR is usually much more complicated than the one given by eq. (2.19a) for a JJ.

2.2.3.2 Kinematic vortices and phase slip lines

A few years after the discovery of cuprates, Andronov *et al.* [19] studied the resistance appearance in a bridge whose width is $\xi \ll w \ll \lambda_{\text{eff}}$, within the framework of the TDGL equations. These conditions are easily satisfied in YBCO nanowires, making this case of particular interest. They studied the resistance appearance in a bias current superconducting bridge in the absence of an external magnetic field. Since $w \ll \lambda_{\text{eff}}$, the current across the width is homogeneous. In their work, they considered two cases: a homogeneous bridge and a bridge with a normal inhomogeneity at the wire edge. By solving the TDGL equations, they determined the superconducting order parameter and the current density for both cases.

In the homogeneous case, they distinguished two sub cases according to the normal state conductivity σ with respect to a critical state conductivity $\sigma_{\text{cr}}(w, j)$ set by the wire width w and the current density j . If $\sigma > \sigma_{\text{cr}}$, or equivalently for narrow enough width $w < w_{\text{cr}}$ where w_{cr} is the corresponding critical width, the normal state corresponds to a phase slip line (PSL) in which the order parameter is suppressed across the whole wire width. This is the two-dimensional analog of the PSC for a 1D wire presented before [17]. For $\sigma < \sigma_{\text{cr}}$, or equivalently $w > w_{\text{cr}}$, the vortex nucleation followed by the vortex motion across the wire generates a voltage drop, and thus a resistive state. As long as w or σ is approaching the PSL space phase, the vortices become more anisotropic and move faster. The transition occurs when vortices have an infinite velocity, namely a kinematic vortex, meaning that the superconducting order parameter is zero along a line crossing the wire.

In the case of a nonuniform bridge, Andronov *et al.* introduced a normal region at the edge shown in fig. 2.9. Under such conditions, strong anisotropic vortices nucleate at the normal inhomogeneity and run along the PSLs, even in the case of $\sigma > \sigma_{\text{cr}}$ in which the PSL contributes to the resistive state before.

Sivakov *et al.* [199] estimated a vortex velocity of about 10^5 m.s^{-1} , suggesting that they are faster than Abrikosov vortices by two orders of magnitude [78, 200]. It supports the idea of kinematic vortices with arbitrary high velocity, which cannot be considered as quasiparticles such as Abrikosov vortices. They can be viewed as fast running PSC, but they do not share the same origin. Nevertheless, both PSL and kinematic vortex motion

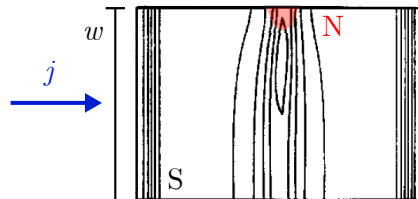


Figure 2.9 – Contour lines of $|\Psi|$ showing the nucleation of a kinematic vortex at a normal inhomogeneity located on an edge of a superconducting bridge under a biasing current density j . Adapted from Andronov *et al.* [19].

produce a phase slippage between two superconducting reservoirs, which translates into a Josephson behavior with voltage step appearance under RF radiation [199]. The main difficulty of discriminating between physical origins lies in the fact that the Josephson behavior is often probed indirectly.

2.2.3.3 Conclusion

In conclusion, it is not an easy task to experimentally distinguish LPS, PSC, or pure Josephson effect signatures in a superconducting nanowire. Golubov *et al.* [201] pointed out that multivalued CPR exists in 1D wires [198, 202] and wires governed by vortex motion [14]. Such a relation leads to similar effect than JJ previously presented, such as the appearance of Shapiro steps along with TAPS behavior [203]. The direct measurement of the CPR is usually performed using SQUIDS allowing to control the current and the phase independently [67, 204, 205]. This type of measurement could resolve the ambiguity. Especially, it enables to see the crossing between the pure Josephson effect and the depairing effect in 1D wire.

2.3 Superconducting single photon detection mechanism

A quick overview of the SSPD detection mechanism has been presented in section 1.3.3. Here, we expose in details the different models describing light-matter interaction in superconductors relevant for SSPD, from the photon absorption to the return at equilibrium state. As we shall see, several models have been proposed to account for the experimental observations in SSPD. For the time being, no consensus has been reached on the microscopic origin of the detection mechanism, thus space is left to test new material for single photon detection.

2.3.1 Photoresponse in superconductors

Prior to the single photon detection proposal in the early 2000s, theoretical models have been developed to understand the photoresponse of superconductors. It consists to study the quasiparticles thermalization back to equilibrium upon an electromagnetic absorption. For this purpose, we present briefly two models which explain the return at an equilibrium state after quasiparticles creation: the Rothwarf-Taylor model, and the two-temperature (2T) model. While they do not explain single photon detection mechanism, they have the merit to introduce general concepts relevant for energy transfer in superconductors and their corresponding time scales.

2.3.1.1 Rothwarf-Taylor model

Figure 2.10 depicts how quasiparticles in a superconductor thermalize and recombine into Cooper pairs. When the energy absorbed by the material is higher than the energy gap 2Δ , Cooper pairs are broken into excited electrons. The quasiparticles thermalize by releasing their energy through the electron-electron and the electron-phonon interactions (fig. 2.10(a)) generating other quasiparticles and phonons respectively. During these processes, other Cooper pairs might be broken either by electron-electron scattering or emitted phonons. The excited electrons accumulate at the gap, and recombine together into pairs in a time τ_R while releasing recombination phonon (fig. 2.10(b)). The latter phonon, either breaks Cooper pairs (fig. 2.10(c)), creating two low-energy quasiparticles, or diffuses through the substrate *via* anharmonic decay in low-energy phonon with the characteristic time τ_{es} (fig. 2.10(d)). The balance between phonon pair-breaking and pairs recombina-

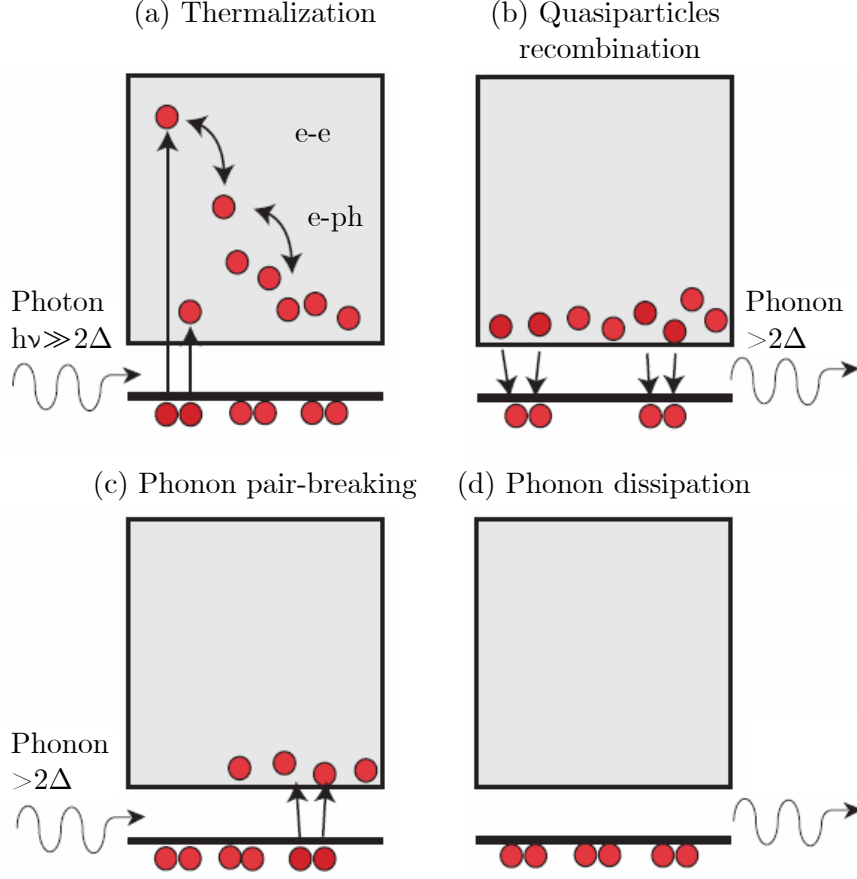


Figure 2.10 – Schematics of the quasiparticles dynamics in a superconductor under illumination. (a) A photon absorbed by the material with an energy higher than the energy gap 2Δ breaks Cooper pairs. The quasiparticles thermalize by releasing their energy through the electron-electron and the electron-phonon interactions generating other quasiparticles and phonons respectively. (b) The excited electrons accumulate at the gap and recombine together into pairs in a time τ_R while releasing recombination phonon. (c) The latter phonon breaks Cooper pairs, creating low-energy quasiparticles; (d) Or it diffuses through the substrate *via* anharmonic decay in a low-energy phonon with the characteristic time τ_{es} . Adapted from Kadin *et al.* [206].

tion is the so-called phonon bottleneck. It is the limiting process to recover equilibrium which continues until all phonons come back to the equilibrium state.

The Rothwarf-Taylor (RT) model [21], developed in 1967, is the first to describe correctly the recombination rate of quasiparticles. For $T \ll T_c$, the pairs density is much more important than the quasiparticles density. The evolution of the quasiparticles density N_{qp} and the phonon density N_ω with energy higher than 2Δ , are governed by two coupled non-linear differential equations given as:

$$\frac{dN_{qp}}{dt} = I_0 + \beta N_\omega - RN_{qp}^2 \quad (2.25a)$$

$$\frac{dN_\omega}{dt} = \frac{RN_{qp}^2}{2} - \beta \frac{N_\omega}{2} - (N_\omega - N_{\omega T})\tau_\gamma^{-1} \quad (2.25b)$$

where I_0 is the number of quasiparticles created, β is the transition probability for pair-breaking by a phonon, R is the recombination coefficient, and τ_γ^{-1} is the net transition probability for a phonon to release its energy. The model successfully described the photoexcitation and the relaxation processes in superconducting state. But, as temperature

approaches T_c and the superconductor is biased near its critical current the pairs density varies a lot. The initial hypothesis is not verified and another approach has to be considered.

2.3.1.2 The two-temperature model

After the discovery of cuprates and the development of femtosecond pulsed laser in the 80's, a revival of superconducting photoresponse occurred driven by the idea of fast and sensitive detectors [207]. Semenov *et al.* [22] used the two temperatures ($2T$) model to quantitatively explain the photoresponse of different superconductors. The samples were current biased in the resistive state, close to the transition, at a temperature T . Under uniform illumination by a short laser pulse, the hot electrons create a hotspot. The strength of the model is to consider two subsystems with their own temperature: one for the electrons at the temperature T_e , and one for the phonons at the temperature T_{ph} . This approach holds as long as the thermalization in the two subsystems is fast compare to the other processes. With such an assumption, the only interactions to be considered are the one between the two subsystems and the one between phonons and substrate as shown in fig. 2.11(a).

Following the notation of Lindgren *et al.* [165], the temperatures are described by a set of coupled time-dependent heat balance equations in each subsystem:

$$\begin{aligned} C_e \frac{dT_e}{dt} &= \frac{\alpha P_{in}(t)}{V} - \frac{C_e}{\tau_{e-ph}} (T_e - T_{ph}) \\ C_{ph} \frac{dT_{ph}}{dt} &= \frac{C_{ph}}{\tau_{ph-e}} (T_e - T_{ph}) - \frac{C_{ph}}{\tau_{es}} (T_{ph} - T_b) \end{aligned} \quad (2.26)$$

where C_e and C_{ph} are the electron and the phonon specific heats respectively, α is the radiation absorption coefficient, $P_{in}(t)$ is the time dependent absorbed optical power, τ_{e-ph} is the electron-phonon scattering time and τ_{ph-e} is the phonon-electron interaction time. At equilibrium, the set of equations eq. (2.26) becomes $\tau_{e-ph}C_{ph} = \tau_{ph-e}C_e$.

In practice, a picosecond voltage pulse is measured in response to an optical pulse excitation shorter than 100 fs. The photon energy increases T_e and put the system out of equilibrium (fig. 2.11(b)). Experimental data are fitted with eq. (2.26) in relative good agreement [22, 161, 165] by including the gaussian optical pulse shape and the readout

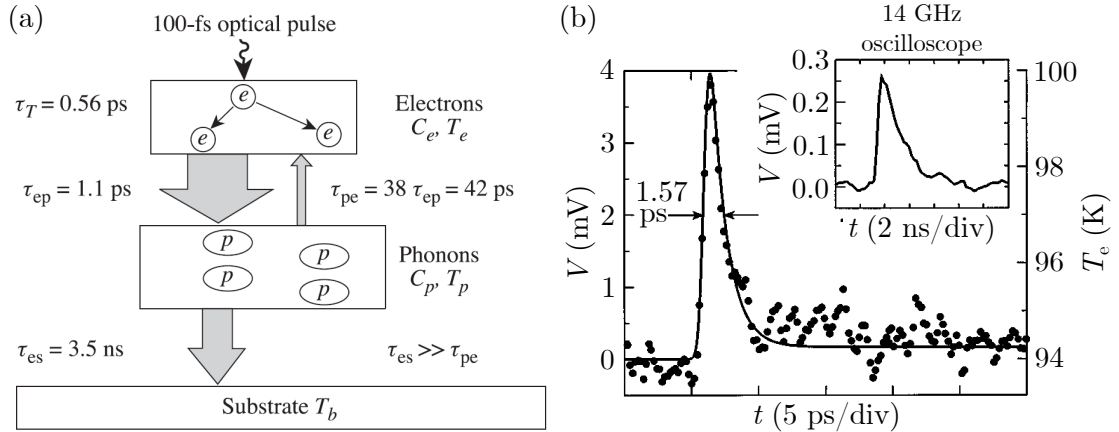


Figure 2.11 – (a) Diagram of the energy transfers under light illumination within the $2T$ model. Adapted from Semenov *et al.* [208]. (b) Voltage pulse measured in the resistive hotspot state, dots are data points, while solid line is a fit according to $2T$ model. The inset shows the bolometric photoresponse. Adapted from Lindgren *et al.* [165].

electronics effect. Schematically, the rising edge of the voltage peak is governed by electron thermalization time τ_T , while the falling edge give τ_{e-ph} and τ_{es} . Using the equation at equilibrium, and knowing the specific heats, the value of τ_{ph-e} is extracted.

The $2T$ model has been extensively used to extract characteristic times involved in the voltage pulse creation [22, 161, 165, 209, 210]. The parameters of the analysis for both NbN and YBCO films are summarized in table 2.2. It is worth noting that the retrieved parameters are quantitatively similar whatever the experimental data for both materials. The values of τ_T show that the electrons thermalization is faster than other characteristic time scales, in agreement with the starting assumption.

Table 2.2 – Parameters extracted using $2T$ model, along with the experimental conditions.

	NbN	NbN	YBCO	YBCO	YBCO
Reference	[22]	[161]	[22, 209]	[22, 210]	[165]
Thickness, d (nm)	20	3.5	40	45	100
C_e ($\text{J}\cdot\text{cm}^{-3}\cdot\text{K}^{-1}$)	1.3×10^{-3}	1.7×10^{-3}	0.022	0.022	–
C_{ph} ($\text{J}\cdot\text{K}^{-1}$)	5.0×10^{-3}	0.011	0.9	0.9	–
T_b (K)	8.1	10.5	85	77	80
T_c (K)	8.2	10.6	85	75	> 89
Pulse duration (ps)	0.1	0.1	0.3	40	≈ 0.1
τ_T (ps)	–	6.5	–	–	0.56
τ_{e-ph} (ps)	17	10	1.5	3.5	1.1
τ_{ph-e} (ps)	65	65	61	123	42
τ_{es} (ns)	0.16	0.038	2.0	3.9	3.5

The time response of the voltage peak is set by the electron-phonon interaction. τ_{e-ph} is the intrinsic limiting time of the resetting dynamics. The relatively fast electron-phonon interaction time measured in YBCO promises a fast thermalization. It is an argument in favor of a rapid intrinsic reset time for YBCO based detectors, but at the same time, the thermal release might be so quick that photon could not trigger a voltage pulse in SSPD.

As a concluding remark, RT model and $2T$ model describe the energy relaxation of a uniformly illuminated superconductor far from T_c , and close to T_c respectively. They estimate the characteristic times involved in the thermalization process by describing the different energy transfer mechanisms inside a superconductor. However, the models do not explain the physics of single photon detection in which individual photon absorption is localized in space.

2.3.2 Experimental observations

Before going into the details of single photon detection mechanisms, we provide a brief overview of some experimental observations on SSPD that need to be explained for a good SSPD model. For greater details on SSPD mechanism, the reader should refer to the complete and clear review of Engel *et al.* [211].

In single photon detection experiment, the device is illuminated either by a continuous wave or a pulsed laser source at a given wavelength, λ , with an incident power, P_i . The average photon number is $\mu = R_i\tau$, where τ is the time interval and R_i is the incident photon rate given by $R_i = P_i\lambda/hc$. If we consider a Poissonian light source, in the case of single photon detection events only, the total detection count rate R_t is proportional to μ . On one hand, this linear relationship between R_t and μ is the first experimental observation to verify that single photon triggers a single detection event. On the other hand, it does not tell us anything about the underlying detection mechanism. The detection efficiency

of the detector simply writes: $\eta_d = R_t/R_i$.

The device is biased at a current $I < I_c$ below its critical temperature T_c . In order to both characterize the detector and understand the physics of the SSPD, numerous experiments have been performed by varying different parameters. In particular, the detection efficiency is generally measured a function of the photon wavelength and the bias current as shown in fig. 2.12. One of the first observation is the appearance of a plateau in the measurement of the detection efficiency as a function of the photon wavelength. It could be done by increasing the photon energy above an energy E_{\min} at a fixed bias, in other words by reducing the wavelength below λ_{\max} such as in fig. 2.12(a). But it could be also reached by increasing I above I_{th} at a constant wavelength such as in fig. 2.12(b). Apart from the plateau the detection efficiency rapidly decreases below the sensitivity of the pulse counter. Thus the detector saturates for high energy photon, or large bias. Several optical simulations [4, 212] have shown that the optical coupling limits the detection efficiency. It suggests that the intrinsic detection efficiency (IDE), also named quantum efficiency (QE), might equal unity in the plateau, meaning that any absorbed photon by the nanowire triggers a counting event in this region.

2.3.2.1 Detection efficiency versus bias current

Figure 2.12(a) shows that a higher photon energy is required to reach the plateau for a lower threshold current, and reciprocally I_{th} decreases when photon energy is raised in fig. 2.12(b). It indicates that both quantities E_{\min} and I_{th} are intrinsically linked together for a given detector. The experimental study of the dependence of such quantities with respect to external parameters are precious information to determine the relevant detection model. In order to compare adequately measurements with theoretical models, it is worth noting that I_{th} has to be normalized with respect to the maximum theoretical current set by GL theory, *i.e.* the depairing critical current I_d . It allows one to eliminate the variations respect to the tested device.

In fig. 2.12(b) two operation temperatures have been set. When temperature is lessened, the detection curve shifts toward lower normalized bias current. It means that it becomes easier to trigger a photon detection event at colder temperature. Theoretical model should account for this counter-intuitive temperature dependence.

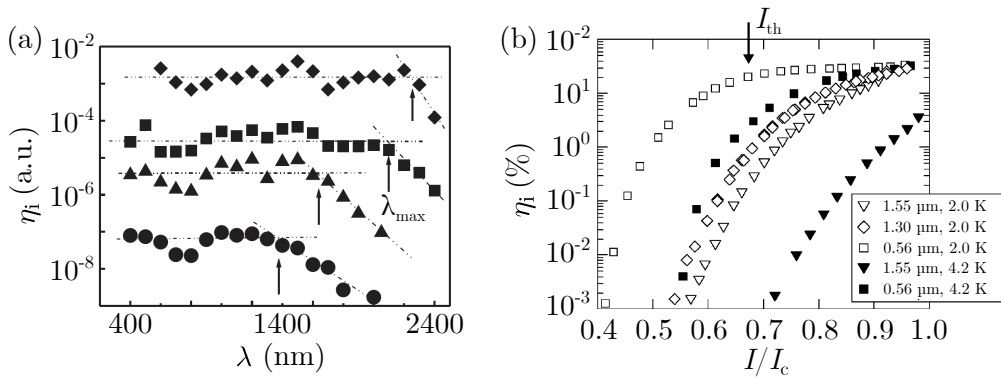


Figure 2.12 – (a) Evolution of the relative quantum efficiency of a NbN meander illuminated at different wavelengths cooled at 2 K with a bias current equals to $0.6I_c$, $0.77I_c$, $0.8I_c$ and $0.89I_c$ from bottom up. The data curves are shifted along the vertical axis for clarity. Arrows indicate the spectral cut-off on each curve. Adapted from Semenov *et al.* [24]. (b) Evolution of the quantum efficiency with normalized bias current I/I_c at different wavelengths and temperatures for a NbN meander. Adapted from Korneev *et al.* [213].

2.3.2.2 Energy - bias current relationship

Quantum tomography measurements on SSPD has been performed by Renema *et al.* [214] to test the detection mechanism. Renema *et al.* used the quantum tomography technique to study the detector response to different photons number. This method allows one to characterize separately the intrinsic response contribution from the extrinsic absorption contribution. By doing so, the accessible energy range was extended by almost a factor 4, going from 2.5 eV at maximum in the single photon regime, to 8.2 eV for multi-photon regime. Figure 2.13(a) displays the bias current required to obtain a 1% intrinsic detection probability upon absorption of n photons as a function of the overall absorbed energy. First of all, the data points coincidences for different photon numbers event suggest that only the total absorbed energy is relevant in the detection mechanism. Secondly, the relation between the bias current and the energy is linear over one order of magnitude in the energy range.

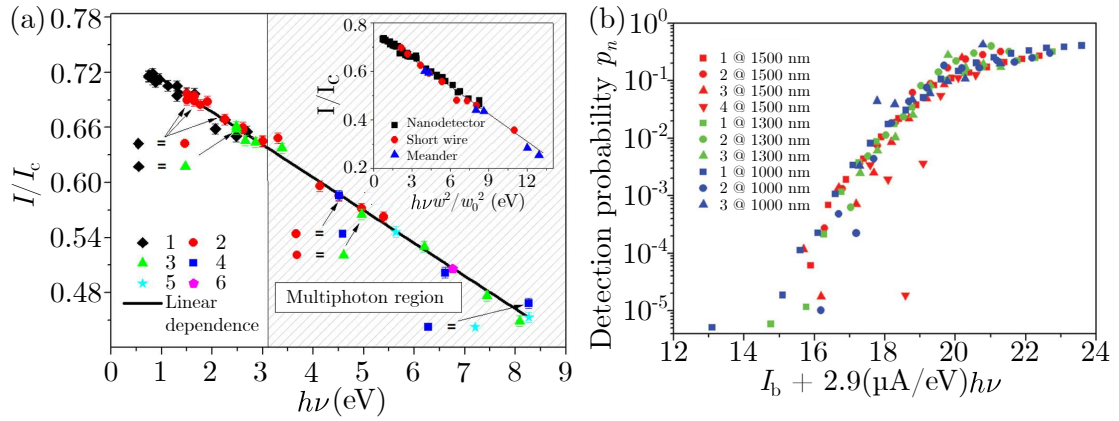


Figure 2.13 – (a) Linear evolution of the bias current picked at 1% probability of detection with the total photon energy for a 220 nm wide NbN bow-tie nanodetector. The coloured symbols represent different photons number involved in the detection event. Inset: the same evolution with different device geometries and energy normalized to the width of the nanodetector. The 220 nm wide nanodetector, the 150 nm wide short wire, and the 100 nm wide meander are all made of NbN. Adapted from Renema *et al.* [214]. (b) Universal curve obtained by renormalizing the bias current with eq. (2.27) for different wavelengths and photon numbers. Adapted from Renema *et al.* [215].

Another striking experimental observation based on detection tomography is the possibility to obtain a universal response curve for a given detector [215]. By renormalizing the bias current with a linear energy relationship according to:

$$p_n(E, I) = p_n(\gamma E + I) \quad (2.27)$$

all the measured detection probability curves collapse on a single curve as shown by fig. 2.13(b). It demonstrates that it is sufficient to obtain one data curve of detection efficiency varying with either λ or I presented in fig. 2.12 to characterize completely the device. By applying eq. (2.27), the behavior for a different set of energy and bias current can be inferred.

2.3.2.3 Detector response versus magnetic field

The presence of an external magnetic field is another parameter to vary for understanding the microscopic detection mechanism, in particular to test if the vortex dynamics comes into play. It helps to probe both photon detection mechanism, and the appearance of dark

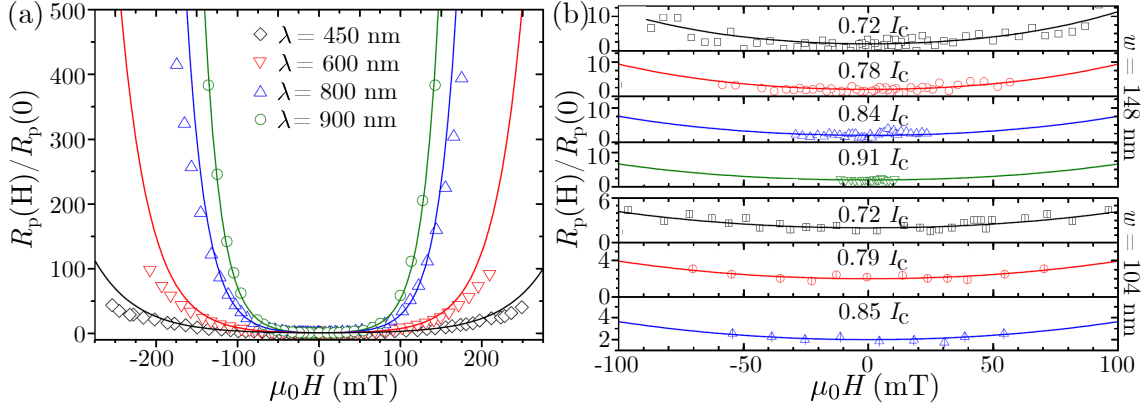


Figure 2.14 – (a) Normalized photon count rate evolution with magnetic field of a 148 nm wide NbN SSPD for different wavelengths at $I = 0.57I_C$. Adapted from Lusche *et al.* [216]. The solid lines represent fitting based on the vortex-entry model [28]. (b) Normalized dark count rate evolution with magnetic field of two NbN meanders with different width at different bias currents. Adapted from Lusche *et al.* [216].

counts, *i.e.* false positive count, in the device. Lusche *et al.* [216] measured the evolution of the photon count rate R_{PCR} , and the dark count rate R_{DCR} with magnetic field for NbN meander, as shown in fig. 2.14(a) and fig. 2.14(b). In fig. 2.14(a), we clearly see that the magnetic field enhances R_{PCR} , whatever the wavelength, with a stronger effect at the highest wavelength. In fig. 2.14(b), R_{DCR} increases for higher I than for R_{PCR} , but the rate is less affected.

In terms of device dimensions, experiments showed that the threshold energy has to be linear with both thickness d and width w [26, 212]:

$$E_{\min} \propto wd \quad (2.28)$$

Having summarized the main experimental observations performed on SSPD, we will now present in the following sections the different theoretical models.

2.3.3 Hotspot models

2.3.3.1 Normal hotspot model

In 1996, Kadin and Johnson [217] suggested a new mechanism of optical absorption to propose a new type of detector based on a single photon absorption creating a hotspot in ultra thin metallic films. A few years later, the model was extended to the case of ultra-thin superconducting films by Semenov *et al.* [23]. It is the first microscopic response mechanism for SSPD referred as the normal hotspot model. It combines the effect of quasiparticles diffusion with the supercurrent redistribution. In their model, they consider an ultra thin superconducting bridge biased near its critical current below T_c such that it remains in the superconducting state. Once a photon is absorbed in the film, Cooper pairs are broken and quasiparticles continue to be generated due to electron-electron and electron-phonon scattering. At some point, a normal spot forms where the superconductivity has been suppressed: it is the so-called hotspot. It spreads along the bridge due to diffusion of quasiparticles, with D_N being the normal state diffusivity of quasiparticles. As the thickness d is smaller than the thermal diffusion length $L_{th} = \sqrt{D_N \tau_T}$, the problem becomes two-dimensional. The hotspot covers the whole thickness upon the photon absorption with

an uniform quasiparticles density in a cylinder of diameter $\approx L_{\text{th}}$. While hotspot grows, the supercurrent density is redistributed around the hotspot and reaches its critical value. A complete cross-section of the bridge becomes resistive generating a voltage pulse. From NbN parameters used in [23] we estimate that $L_{\text{th}} = 17$ nm. It is thus expected that NbN thin films detect single photon.

The experiments performed a few months later by Gol'tsman *et al.* [1] confirmed the prediction while measuring voltage pulses upon photon absorption in NbN bridges. In particular, they reported a linear relation between the count rate and the average number of photon, proving the single photon response of their NbN nanowire.

Later on, Semenov *et al.* [218] observed a minimum threshold of photon energy below which the detection efficiency collapses: this is the spectral cutoff. When photon energy is too low, or equivalently wavelength is too high, the hotspot volume is not sufficiently large to result in a voltage pulse. According to the hotspot model with current conservation law, the current density redistribution writes:

$$jw = j(w - 2R) \quad (2.29)$$

where $2R$ is the normal core diameter, j is the biasing current density, j is the supercurrent density once the hotspot is created and w is the bridge width. To create voltage pulse, j has to bypass the critical current density j_c which leads to the criteria of the minimum hotspot radius:

$$2R_m \geq \left(1 - \frac{j}{j_c}\right) w \quad (2.30)$$

In order to estimate the threshold current density j_{th} above which detection is possible, eq. (2.30) re-writes in the following form:

$$\frac{j_{\text{th}}}{j_c} = \left(1 - \frac{2R_m}{w}\right) \quad (2.31)$$

It is shown that $R_m = A\sqrt{h\nu} \ln(1 + Bh\nu)$ with $h\nu$ the photon energy, A and B being material and temperature dependent parameters. It follows from eq. (2.31) that the threshold biasing current density above which detection occurs is given by:

$$j_{\text{th}} = j_c - A\sqrt{h\nu} \ln(1 + Bh\nu) \quad (2.32)$$

Using eq. (2.31), Semenov *et al.* argued that the intrinsic detection efficiency equals 1 above I_{th} at a given wavelength, it is referred as the detection plateau. Experimentally, the quantum efficiency does not drop to zero as energy is lowered, but it goes linearly to zero. It is interpreted as fluctuations triggering the detection event.

While this simple model succeeded in accounting for SSPD behavior, it failed to describe the linear current-energy relation observed experimentally in Nb and NbN thin films. Indeed, eq. (2.32) stipulates that j_{th} is non-linear with respect to the photon energy. The hotspot model fails to explain the linear dependence of the threshold current with photon energy. In addition, the estimate of the hotspot diameter leads to values smaller than the coherence length for wavelength higher than $1.2 \mu\text{m}$ [24]. It suggests that no photon should be detected above which is in contradiction with the experimental curves previously displayed in fig. 2.12(b) in which the detection plateau is almost reached for wavelength larger than $1.2 \mu\text{m}$.

2.3.3.2 Diffusive hotspot model

The previous model was refined a few years later into the diffusive hotspot model [24] to better describe the experiments. It is based on the quasiparticles diffusion outside

the normal core. The normal resistive cylinder of radius R_m is now surrounded by a quasiparticles cloud. It corresponds to a weakened superconductivity on the diffusion length L_e where electric field penetrates [91]. Starting from a superconducting bridge with a bias current I and a thickness $d < \xi$, a two dimensional diffusion model is applicable. They consider a slab of size greater than ξ such that a change of the Cooper pairs density n_S is noticeable. The reduction of n_S in the slab results in the acceleration of remaining Coopers pairs to maintain the same supercurrent. When the velocity of the condensate exceeds the depairing velocity, a normal zone nucleates and the slab goes to the normal state.

It is worth noting that a normal core is not required in the diffusion-based hotspot model. In this picture, most of the slab remains superconducting, but the evolution of n_S with current flow generates the voltage pulse. This model successfully describes the linear dependence of I_{th} with $h\nu$, and also the linear relation eq. (2.28) between w and E_{min} as observed in [26, 212]. It is also the only model predicting qualitatively the threshold temperature dependence presented in fig. 2.12. Unfortunately those two models do not take into account neither thermal nor quantum fluctuations that can result in a detection event. Models involving vortex creation and vortex motion were proposed later on to account for fluctuations.

As interest grew in Nb based SSPD, experimental data accumulate with different set of parameters and deeper characterization of the devices which undermined the two hotspot models for several reasons. The dark count is completely missing since detection is forbidden for photon with a too low energy. Experimentally, the quantum efficiency η_i grows exponentially with I [25], none of the two hotspot models describe this trend.

2.3.4 Vortex based models

2.3.4.1 Vortex-entry model

In their experimental study of SSPD, Hofherr *et al.* [26] assigned the vortex-entry crossing as the main contribution of dark counts. Following this idea, Bulaevskii *et al.* [27] theoretically developed three possible types of thermally activated fluctuations which could trigger a false positive: a 2π -phase slip, the single vortex crossing motion, and the vortex-antivortex pair (VAP) motion. By computing the attempt rate corresponding to each process, the single-vortex entry is predominant. The phase slip is involved in 1D superconducting nanowire which turns a portion of length ξ in its normal state (section 2.2.2). Since the phase slip energy barrier is high for wire's width higher than ξ , which is the usual case for SSPD, it is unlikely to occur. Considering an infinite long wire of finite width, the vortex crossing motion corresponds to a single vortex-entry on an edge that runs toward the opposite edge of the wire driven by the Lorentz force. The energy barrier being smaller by a factor w/ξ compare to the phase slip case, it is more likely to occur. The VAP motion mechanism is an unbinding of a VAP that are moving toward the edges, and the reverse process, with the creation of a vortex to one edge and an antivortex to the other edge, that annihilate in the middle of the bridge. The energy barrier is simply twice the single vortex crossing energy barrier. According to those energy barrier considerations, the single vortex-entry motion should be the main source of dark count.

The mechanism was further developed by Bulaevskii *et al.* [28] to theoretically study the single photon detection assisted by vortex through three different processes. If the absorbed photon has sufficient energy, it creates a normal spot. Else photon lowers the energy barrier and initiates the single vortex entry. As it moves toward the edge it creates quasiparticles, and generates a normal state belt all across the bridge. The model has also the merit to explain the appearance of dark counts due to single-vortex crossing either due to thermal or quantum fluctuations.

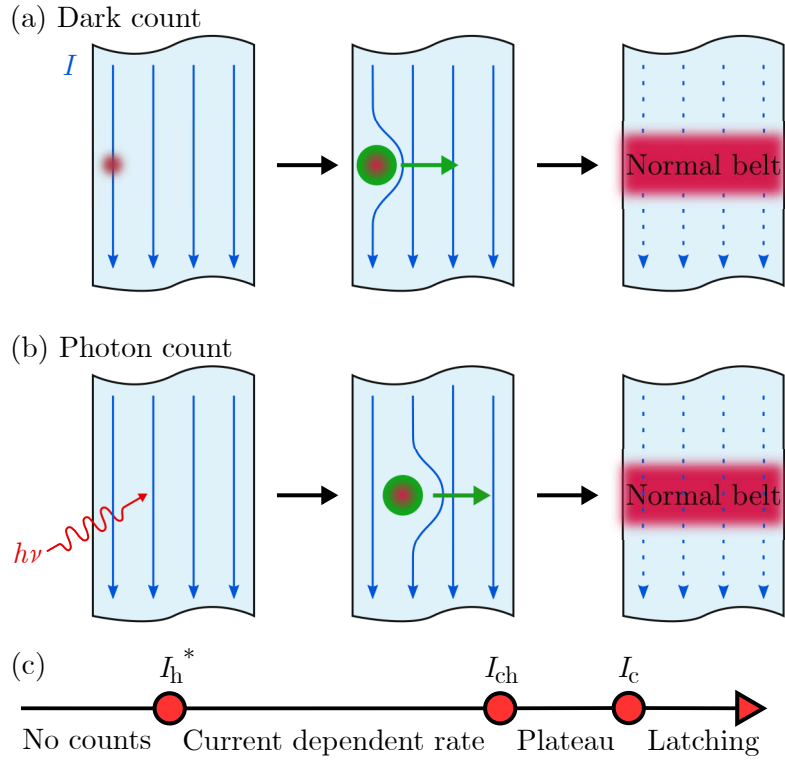


Figure 2.15 – Schematics of a vortex crossing a superconducting strip (a) without and (b) with photon absorption. (c) Depending on the bias current with respect to the current scales in the figure, the photon count rate has different behaviors. Herein, I_h is the threshold current, I_{ch} is the reduced critical current, and I_c is the critical current without magnetic field. Please note that the current ranges are not to scale. Adapted from Bulaevskii *et al.* [28].

In the vortex-entry model, the energy barriers are current dependent and magnetic field dependent. The vortex crossing rates are derived using the Fokker-Planck equations [28]. Depending on the bias current, they have predicted three different regimes exhibited in fig. 2.15(b). They successfully described the evolution of the detection efficiency η_d as current is raised progressively. At first, no count is registered below the threshold current I_h^* . As long as $I_h^* < I < I_{ch}$ photon count rate increases quickly with a power-law current dependency. Once $I_{ch} < I$, the saturation plateau is reached. Finally, if the critical current is overpassed $I > I_{ch}$, the SSPD latches to the normal state. All these features are observed experimentally. In addition, the analytical calculation of the magnetic field dependence of both the dark count rate and the photon count rate for a single vortex-crossing type detection mechanism accounts for the measurements presented in fig. 2.14. The magnetic field modifies the energy barrier of the vortex entry and the vortex crossing rate accordingly, while the hotspot formation is not affected. It is another experimental observation that supports this mechanism.

Nevertheless, the simple vortex-entry model does not catch several experimental behaviors. In particular it does not predict correctly the energy scale required for the photon detection neither the linear current energy relation.

2.3.4.2 Diffusive vortex-entry model

Engel and Schilling [29] later proposed a model using creation and diffusion of a quasiparticles cloud generated indirectly by the absorption of a photon and developed the diffusive

vortex-entry model.

As in the $2T$ model, thermalization time is assumed to be instantaneous compared to electron-phonon and phonon-phonon interaction time scales. They consider two electronic subsystems, one for the highly excited electrons upon the photon absorption of energy $h\nu$ and one for quasiparticles with energy Δ . The former electrons lose their energy E_e with an exponential decay: $E_e = h\nu \exp(-t/\tau_{\text{qp}})$ with τ_{qp} being the constant time scale. The latter originate from the pair-breaking by excited electrons through inelastic scattering processes. Each particle subsystem has its own diffusive equation with its own diffusion constant, denoted by D_e for the excited electrons at high energy and D_{qp} for the quasiparticles at the gap energy respectively. The coupled differential equations governing the density of excited electrons and quasiparticles time evolution are given by:

$$\frac{\partial C_e(\mathbf{r}, t)}{\partial t} = D_e \nabla^2 C_e(\mathbf{r}, t) \quad (2.33a)$$

$$\frac{\partial C_{\text{qp}}(\mathbf{r}, t)}{\partial t} = D_{\text{qp}} \nabla^2 C_{\text{qp}}(\mathbf{r}, t) - \frac{C_{\text{qp}}(\mathbf{r}, t)}{\tau_{\text{r}}} + \frac{\zeta h\nu}{\Delta \tau_{\text{qp}}} \exp\left(-\frac{t}{\tau_{\text{qp}}}\right) C_e(\mathbf{r}, t) \quad (2.33b)$$

where $C_e(\mathbf{r}, t)$ and $C_{\text{qp}}(\mathbf{r}, t)$ are the concentration of excited electrons and of quasiparticles respectively, τ_{R} is the Cooper pairs recombination time-scale and $\zeta \in [0, 1]$ is the conversion efficiency of quasiparticles during scattering events. In the right hand side of the quasiparticles diffusion equation, the second term describes the quasiparticles recombination, while the last term corresponds to the quasiparticles creation by the excited electron through diffusion event. No analytic solutions exist for $D_e \neq D_{\text{qp}}$, thus the system of eqs. (2.33a) and (2.33b) is solved numerically. It gives the evolution in space and time of $C_e(\mathbf{r}, t)$ and $C_{\text{qp}}(\mathbf{r}, t)$.

Three different microscopic mechanisms were regarded by Engel *et al.* as the origin of the detection event. They considered the diffusive hotspot model of Semenov *et al.* and the vortex-entry model proposed by Bulaevskii *et al.* previously presented in section 2.3.3.2 and section 2.3.4.1 respectively. The last one referred as the normal core vortex model was developed by Zotova and Vodolazov [219]. Similarly to the first scenario, they assume a hotspot with completely suppressed superconductivity. The order parameter in the surrounding area changes, and collapses locally in space and time if current is large enough. It results in the creation of a VAP which generates heat while vortex and anti-vortex move toward opposite edges due to the Lorentz force. As a result, a normal domain appears and gives raise to a voltage pulse. It will be explained in further details in the next section.

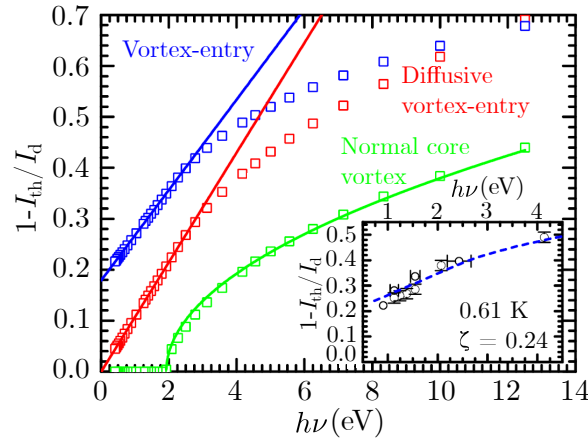


Figure 2.16 – Theoretical prediction of the threshold current expressed as $1 - I_{\text{th}}/I_{c,\text{dep}}$ as a function of the photon energy $h\nu$ for the three detection models. Adapted from Engel *et al.* [29].

Considering those three scenarios, it turns out that the vortex-entry mechanism gives the smallest threshold bias current to detect single photon at a given energy in fig. 2.16 which favor it compare to the others. In addition, it gives the linear $h\nu - I_{\text{th}}$ dependence unlike the hard-core model in fig. 2.16. The strength of the vortex-entry diffusive model is to consider the current-density and order parameter as inhomogeneous quantities due to the quasiparticles cloud, on the contrary to [28].

The diffusive vortex-entry model nicely gathers the ideas of the diffusive hotspot and the vortex-entry to understand the detection process involved in SSPD. Several experimental facts are explained quantitatively, but the model still lies on simplifications which limit its applicability. Especially, it fails to describe the temperature dependence of I_{th} , and it cannot account for the magnetic field dependence.

2.3.4.3 Normal core vortex model

The alternative approach proposed by Zotova and Vodolazov [219] in 2012 to explain the physics of SSPD has been refined several times [30, 31]. The so-called normal core vortex model relies on the evolution of the superconducting order parameter solved numerically.

A superconducting thin strip carrying a bias current is considered at equilibrium. Upon photon absorption, a hotspot with normal core nucleates through electron-electron interaction with a higher temperature with respect to the bath. The evolution of the quasiparticles temperature is ruled by the diffusion equation in two dimensions. Depending on the absorption position, a normal area forms either a cylinder in the middle of the strip or a semi-cylinder at one edge of the strip. Under the assumption that $T \lesssim T_c$, they use the TDGL equation to model the evolution of the superconducting parameter. In order to complete the model, they apply the current conservation. They also include the electrical scheme of SSPD with a kinetic inductance and a normal resistance to confront the simulation with the real experiments. With all these ingredients, the simulations fully describe the spatio-temporal evolution of the physical quantities such as the effective quasiparticles temperature and the order parameter.

At first, the temperature inside the hotspot decreases by means of diffusion and electron-phonon interaction while $|\Psi|$ collapses rapidly. For given dimensions, two situations are distinguished depending on the value of I with respect to the detecting threshold current I_{th} . If $I < I_{\text{th}}$, the energy is released quickly enough and the order parameter

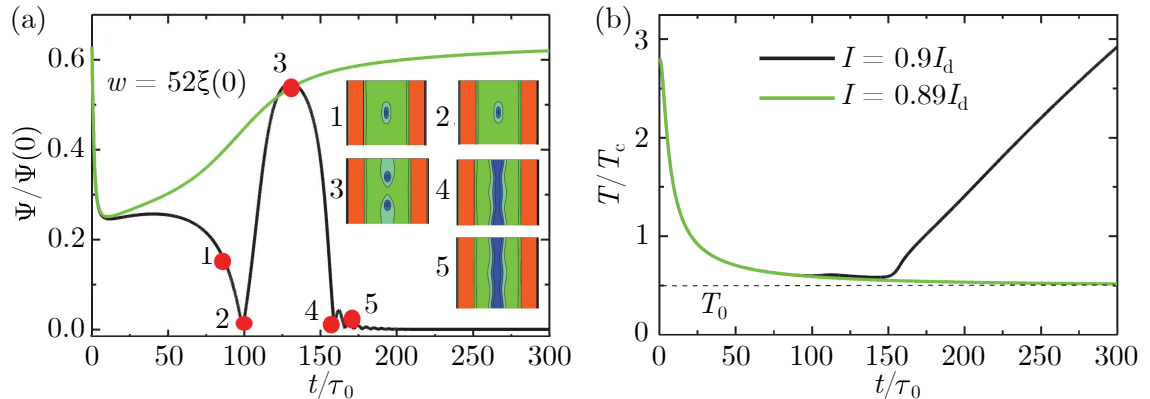


Figure 2.17 – Time evolution of the order parameter amplitude (a) and the temperature (b) in the middle of the hotspot for two bias currents. Inset: contour plots of the order parameter amplitude in the film at different times marked by the numbers on the black solid curves. In the figure, Δ corresponds to Ψ in the manuscript. Adapted from Zotova and Vodolazov [219].

recovers its equilibrium. In this case, no voltage pulse is observed. While in the opposite case $I > I_{\text{th}}$, at first $|\Psi|$ is completely cancelled out and then it oscillates through time. When $|\Psi|$ goes to zero a VAP is created inside the hotspot. Each one moves toward opposite direction and dissipates energy through their motion which increases locally the temperature. The resistive domain expands and covers the whole cross-section resulting in a voltage pulse.

In the original model [219], the threshold current is determined by the unbinding of a VAP in the middle of the strip, which is estimated to be lower than the threshold current due to the single vortex entry at the edge. This observation is in clear discrepancy with the diffusive vortex-entry model. By several improvements [30, 31] of the initial TDGL approach, the model successfully accounts for most of the experimental observations. As it can be seen in table 2.3, normal core vortex correctly predicts the magnetic field dependence and simulates nearly linear energy current dependence at high energy [214, 215]. Even if the validity of GL theory far from T_c is questionable, the approach is powerful thanks to the finite superconducting order parameter relaxation time.

2.3.5 Conclusion

The search for the detailed SSPD microscopic mechanism has been the source of many experimental and theoretical works over the past two decades. The different updated models gather numerous physical concepts, with their own assumptions and set of equations. Each model contributes to get a clearer physical picture as a whole. From this brief overview, it appears that diffusion of quasiparticles has a key-role. More unexpectedly, the vortex, either single or bound together with an antivortex, seems to play a dominant role in the photon detection event, and not only for the dark count event.

Table 2.3 summarizes the five different models presented here. The most complete mechanisms are the diffusive vortex-entry and the normal core vortex models. While both models are numerical, they solve the problem with their own hypothesis. They consider vortex entry at the edge and VAP unbinding, but they differ in the way they treat them. While normal core favours VAP, diffusive vortex-entry gives single vortex-entry an advantage over VAP. In terms of numerical results, both predict the linear dependence $E_{\text{min}} \propto I_{\text{th}}$ and $w \propto E_{\text{min}}$, but they fail to account for the temperature dependence of the relevant quantities. By contrast, the normal core model has the merit to explain the magnetic field dependence unlike the diffusive vortex-entry model.

Table 2.3 – Summary of the single photon detection models in the SSPD with their validity with respect to the experimental observations. ✓ attests that the model successfully describes the experiment, (✓) corresponds to a reasonable description at least qualitatively, ✗ means that the model fails to account for this experimental fact, and – means it cannot predict this behavior. Adapted from Engel *et al.* [211].

Model	Normal hotspot	Diffusive hotspot	Vortex-entry	Diffusive vortex-entry	normal core vortex
Reference	[23]	[24]	[27, 28]	[25, 29]	[30, 31, 220]
Solution	Analytic	Analytic	Analytic	Numeric	Numeric
$E_{\text{min}} \propto I_{\text{th}}$	✗	✓	✗	✓	✓
$w \propto E_{\text{min}}$	✗	✓	✗	(✓)	✓
T -dependence	–	(✓)	✗	✗	–
H -dependence	–	–	(✓)	–	✓
Universal curve	✗	✗	✗	✓	✓

Even if the two models do not predict exactly the same behavior, there is a chance that they might merge in the future to describe all the experimental observations. For now, theories have been mostly driven by the experimental data suggesting low- T_c superconducting materials with low superconducting density and low diffusion constant to build SSPD. Such ingredients help to generate a large number of quasiparticles limited to the photon absorption location due to a slow diffusion. Thus, a small number of quasiparticles is required to drive the device into a normal state.

A recent paper published by Vodolazov [221] studies the time evolution of the electronic and phononic population in dirty carrying superconductor upon photon absorption. In the frame of the BCS theory in the dirty limit, he expounded what physical quantities matter to achieve single photon detection. Reasoning with the normal hotspot model presented in section 2.3.3.1, and based on the experimental data on NbN, he showed in which extends HTSs could be used to create SSPD with an intrinsic detection efficiency about unity. Starting from the detection threshold set by the normal hotspot model (eq. (2.31)) with $\lambda = 1000$ nm for a superconductor with $T_c = 100$ K, and the same parameters than NbN, he estimates the hotspot radius to be: $R_m = 2.6$ nm. With such a radius, the achievement of $\eta_i \approx 1$ is possible with a critical current about half the GL depairing current I_d for really narrow wire $w = 10$ nm. In the case of high-quality film, with $I_c \approx 0.9I_d$, the constraint on the width is levered to reach unity IDE. The requirements on j_c is difficult to achieve experimentally in YBCO, this is especially true as the length of the wire is increased. But Papari *et al.* [35] demonstrated that such a technological feat is not far to be reached with measurements of critical current density about $0.4j_d$ for a 60 nm-wide YBCO nanowire. Their work is really enthusiastic on the fabrication point of view. Although, the normal hotspot approach estimates correctly I_{th} for conventional superconductors such as NbN, it is not obvious that it applies quantitatively to HTS material, especially as a complete theory of single photon detection mechanism does not exist yet. The specific $d_{x^2-y^2}$ -symmetry order parameter confined in ab -plane makes YBCO properties rather different from commonly used material in SSPD. In addition, the dirty superconductivity and the BCS theory do not apply for YBCO, even though they suggest the non-adequacy of YBCO to make a HTS SSPD. Even if the superconducting gap is higher by one order of magnitude for YBCO ($\Delta \approx 20$ meV) compare to NbN ($\Delta \approx 2$ meV), the presence of the $d_{x^2-y^2}$ -symmetry makes possible excitations at lower energy than the superconducting gap 2Δ in YBCO. Thus, quasiparticles generation might be improved in this case.

Beyond the controversy on the theoretical previsions of the HTS SSPD, there are two main reasons to look for single photon detection in YBCO nanowires. In terms of application, even though they do not become the best detectors for optical and telecommunication wavelengths, they could operate at a higher temperature or could be used for the detection of higher energy photon in the deep-UV or for high-energy physics. While we focus our work toward single photon detection, most of the achievements are transposable to other purposes concerning HTS electronics. On a scientific point of view, the HTS nanowire is a tool to probe both the underlying superconductivity and physical properties of interest at nanoscale.

Chapter 3

Ion irradiated YBCO nanowires

Contents

3.1	Fabrication locks	58
3.2	Ion implantation	59
3.2.1	Effect of disorder	59
3.2.2	Ion implanter	60
3.2.3	He ⁺ focused ion beam	61
3.3	Simulation of irradiated devices	62
3.3.1	Simulations of the stopping and range of ions in matter	62
3.3.2	Influence of the ions	64
3.3.3	O ⁺ irradiation through a mask	65
3.3.4	He ⁺ focused ion beam patterning	68
3.4	Fabrication workflow	70
3.4.1	Standard irradiated devices	70
3.4.2	Special irradiated devices	72
3.4.3	He ⁺ focused ion beam process	73
3.4.4	Characterization tests	74

The discovery of YBCO in 1987 aroused tremendous interests among the scientific community during the Woodstock of physics held in New York. Since then, a lot of research efforts have been devoted for both understanding high- T_c superconductivity and fabricating devices. After three decades, the knowledge and knowhow has definitely improved. In terms of fabrication, several groups succeeded to grow ultra thin films down to a few unit cells with a preserved superconductivity, but their critical temperature is largely reduced when the thickness becomes smaller than 10 nm [173].

The chapter is dedicated to the fabrication of ion irradiated nanostructures on YBCO thin films. Section 3.1 will introduce first the challenges of patterning devices with nanometric size out of thin films. The section 3.2 will lay out the ion irradiation technique used to fabricate the devices presented in this thesis. In section 3.3, we will describe the Monte Carlo simulations that support the ion irradiation process. Then, section 3.4 will resume the complete fabrication flow.

3.1 Fabrication locks

At present, no HTS SSPD has been realized yet while the development of HTS SSPDs - more generally of HTS nanometric size devices - is at the heart of an intense research worldwide. Only for the cuprate family, various superconductors are under investigation such as $\text{La}_{1.85}\text{Sr}_{0.15}\text{CuO}_4$ [222], $\text{Pr}_{2-x}\text{Ce}_x\text{CuO}_{4-\delta}$ [223], or YBCO [33, 36, 64, 80, 224–226]. In comparison to the LTSs, it remains a challenging task to grow ultra thin films and pattern nanometric size devices out of the HTS materials because it often results in degrading the superconducting properties.

For the YBCO case, the main reason is that it is a crystalline material whose superconducting properties are strongly deteriorated by the defects and the oxygen stoichiometry apart from the optimal oxygen doping. It generates two major issues which become crucial as the device dimensions lower in thickness and width [32–34]. At first, the standard Ar^+ etching process used to pattern a wire affects dramatically the superconducting transport properties. Thus, the etching parameters need to be finely and carefully tuned to avoid overheating and limit the interaction time with Ar^+ ions [227]. In addition, while exposed to the air, the bare YBCO films loses its optimal oxygen doping and its superconducting properties, and it becomes even worse for the ultra thin films.

In the light of the above remarks, the conclusions are twofold. Firstly, we should prevent that the YBCO thin film loses its oxygen vacancies. Secondly, we should limit the etching processes and more generally reduce the total number of fabrication steps as low as possible. By combining the two fabrication precepts above, it follows that the fabrication process letting the YBCO films bare must be avoided whenever possible or even prohibited. To counteract those problems various alternatives have been proposed. One approach consists of capping the YBCO film layer with a thin Au layer [35, 38, 39] or a 100 nm thick carbon mask [36, 37] in order to protect it during the Ar^+ etching. Those methods improve both the fabrication reliability and the superconducting properties homogeneity. Nonetheless, in the view of the photon detection, the protecting layer needs to be removed at the end, thus it requires an additional fabrication process which may damage the superconducting properties. An alternative approach to etching process is based on a Ga^{3+} focused ion beam milling which directly carve out the device into the film by implanting Ga^{3+} ions [39, 228, 229]. At first glance it represents an interesting alternative since the focused ion beam is more precise spatially than the usual lithography process. In addition, the ion doses are smaller than those of Ar^+ ions etching with similar energies limiting the introduction of disorder. In contrast, it has been reported in the literature that Ga^{3+} ions poison the YBCO and thus damage the superconducting properties by changing the

YBCO stoichiometry. Thus, it would be a better solution to choose more neutral ions which do not react with the YBCO thin films such as He^+ ions [230, 231].

3.2 Ion implantation

The ion irradiation, or implantation, process is widely used in the semiconductor industry to dope silicon with holes or electrons. In our case, we use the implantation technique to introduce disorder along the trajectories of the impinging ions and to destroy locally the superconducting properties of YBCO as we will present in section 3.2.1. With such a technique, the YBCO area which is not exposed to the ions source defines the superconducting circuit, *i.e.* the electrodes and the nanowires.

In this thesis, we have developed two nanofabrication processes either using an O^+ ion implanter or a He^+ focused ion beam (He^+ FIB) technology. The effect of the disorder on YBCO will be first presented in section 3.2.1. It will follow a description of the ion implanter in section 3.2.2 and the He^+ FIB machine in section 3.2.3.

3.2.1 Effect of disorder

As an HTS, YBCO is really sensitive to the defects, unlike most of the LTSs. The defects in the crystalline structure act as depairing centers for the Cooper pairs and destroy progressively the superconductivity in the material. As shown experimentally in fig. 3.1 with the high-energy He^+ ions, the material experiences a superconducting-to-insulating transition when the He^+ fluence increases. In order to quantify the density of disorder in the material, we introduce the displacement per atom, namely the dpa . It represents the fraction of atoms in the crystalline structure which has been displaced from their original sites. We will see in section 3.3 that the dpa is directly proportional to the ion dose.

Before going to an insulating state, it has been shown that T_c is gradually reduced when the dpa is raised as depicted in fig. 3.1. For a low dpa , *i.e.* $dpa \leq 0.02$, T_c decreases linearly, the material is still superconducting with a reduced T_c . As soon as $dpa \geq dpa_c \approx 0.042$, the superconducting properties are completely suppressed reducing T_c to 0 K [43]. While for $dpa \geq 0.05$, the material becomes rapidly insulating due to the poor conducting properties

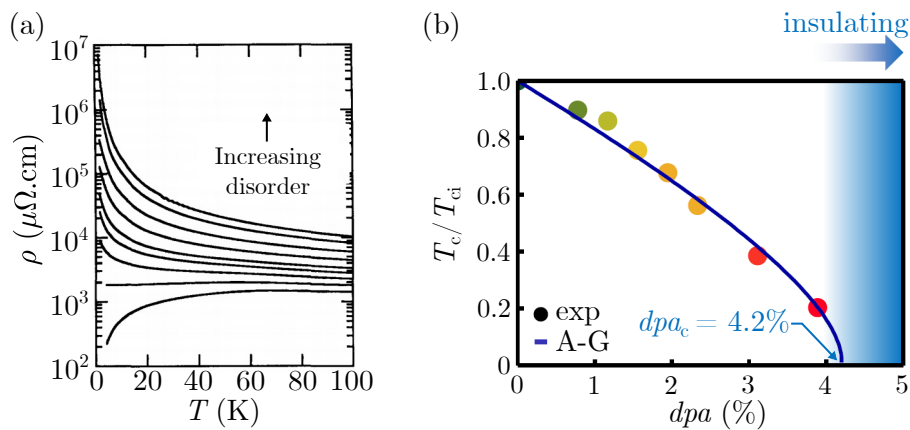


Figure 3.1 – (a) Resistivity as a function of the temperature for fluences in $10^{15} \text{He}^+ \cdot \text{cm}^{-2}$: 17.5; 20; 22; 24; 26; 29; 32; 35; 37. Adapted from Lesueur *et al.* [43]. (b) Evolution of T_c normalized with the initial critical temperature T_{ci} of the bare film as a function of the displacement per atom (dpa) due to the ion irradiation for different doses. The blue line represents a fit based on the Abrikosov-Gor'kov model. Adapted from Malnou PhD Thesis [232].

of YBCO in its normal state.

To account for the reported T_c reduction, it was first proposed that the disorder had an effect on Cu-O chains. Gupta *et al.* [233] showed theoretically that the charge transfer between the CuO_2 planes is blocked for the Cu-O chains which are completely disordered. In such a case, YBCO becomes insulating. Nevertheless, the required dpa to disorder all the CuO chains is higher than the dpa_c reported by Lesueur *et al.* [43] to suppress the superconducting state. Another mechanism has to be considered to explain such an important decrease of T_c for a low dpa .

A second model based on the Abrikosov-Gor'kov pair breaking mechanism [234] was proposed to get a better agreement with the experimental observations. For a s-wave superconductor, the magnetic impurities break Cooper pairs due to spin scattering. In a similar way, for a d-wave superconductor, when a Cooper pair scatters on a nonmagnetic crystalline impurity, the initial wave vector is kicked to another direction with a π phase shift. The Cooper pair is destroyed reducing at the same time Δ and T_c according to the dpa . Following the approach of Abrikosov and Gor'kov [234], Lesueur *et al.* have considered a finite lifetime for the Cooper pairs which gives the reduction of T_c as follows:

$$\ln\left(\frac{T_c}{T_{ci}}\right) = F\left(\frac{1}{2}\right) - F\left(\frac{1}{2} + 0.14 \frac{dpa}{dpa_c} \frac{T_{ci}}{T_c}\right) \quad (3.1)$$

where T_{ci} is the initial critical temperature of the film without implantation and F is the digamma function. Equation (3.1) established with this model is in a relative good agreement with the experimental measurements (fig. 3.1). The implantation technique in YBCO has been initially developed successfully to fabricate Josephson junctions [40–42]. In this thesis, we have push forward the ion irradiation technique to shape YBCO thin films into nanostructures by developing a new fabrication method with optimized fabrication steps.

3.2.2 Ion implanter

The ion irradiation process is mostly used in the semiconductor industry to introduce doping ions, usually doping atoms of silicon. The ions are expelled from the ion source and accelerated to reach an energy between 10 keV and 200 keV depending on the needs. This typical energy is sufficient to penetrate into 10 nm to 100 nm depth of material.

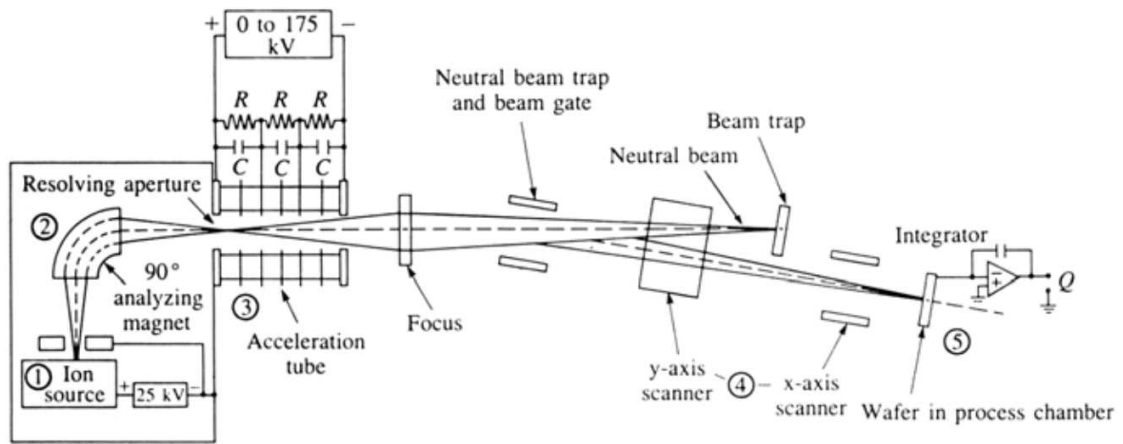


Figure 3.2 – Schematic drawing of a typical ion implanter showing (1) the ion source, (2) the mass spectrometer, (3) the high-voltage accelerator column, (4) the x -axis and the y -axis deflection system, and (5) the target chamber. Adapted from Jaeger *et al.* [235].

Figure 3.2 depicts the different elements of an ion implanter. It consists of an ion source, an analyzing magnet, an accelerator, and a neutral trap. The atoms are introduced in the vacuum arc chamber in the form of a gas, or liquid, depending on the atom chosen. For a sufficiently high arc voltage, a plasma appears into the chamber. An extraction voltage is applied to move the ions into the analyzing magnet. The latter selects the ions which satisfy a specific charge to mass ratio while the other ions collide the wall. The selected ions are then accelerated in the acceleration tube in order to increase their energy at a chosen value. Afterwards, the ion beam is focused and separated from the neutralized ions thanks to the neutral trap. Since the ion beam cross-section is about a few millimeters, the beam is scanned along the x -axis and y -axis to irradiate the whole target.

Once the specific ions have been chosen, two parameters remain to be set: the ion energy E_{ion} and the ion dose D usually expressed in ions.cm^{-2} . The energy goes from 10 keVs to 10 MeVs depending on the application. Each energy range has its own dedicated implanter. The dose D is determined precisely by choosing an implantation duration for a given current I through the target. Knowing the target area S and the implantation duration Δt , D is given by:

$$D = \frac{I\Delta t}{eS} \quad (3.2)$$

The ion dose value affects differently the material. For $D \approx 10^{14} \text{ ions.cm}^{-2}$, the implanted ions act only as dopants in the target, while for $D > 10^{17} \text{ ions.cm}^{-2}$, the target begins to be etched out. In our case, we use a 30 keV O^+ ions source with $D \approx 10^{14} \text{ ions.cm}^{-2}$ into the YBCO samples. Hence, we do not introduced foreign atoms in the superconducting material and the oxygen stoichiometry does not change.

3.2.3 He^+ focused ion beam

Following the acquisition of the ALIS corporation by ZEISS SMT in late 2006, the He^+ ion microscopy launch by ZEISS opens up important perspectives for nanotechnology. With its sub-nm diameter beam, the He^+ FIB offers numerous advantages over the scanning electron microscopy (SEM) in several scopes. It supplies a high-resolution and a better contrast for imaging applications. In addition, He^+ FIB competes with the best electron beam lithography (EBL) with a sensitivity enhanced by 1 – 2 orders of magnitude. It gives

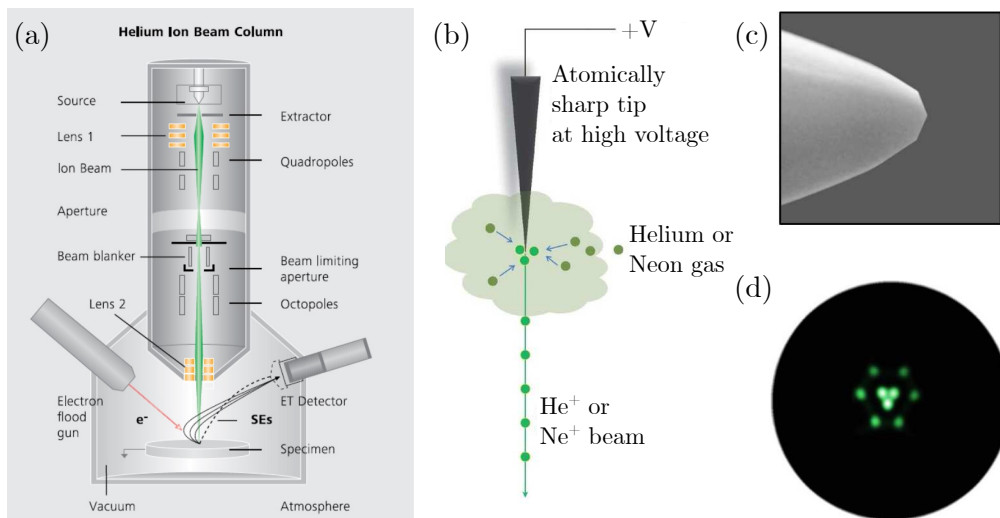


Figure 3.3 – (a) Schematic drawing of the He^+ FIB column. (b) Sketch of the source tip emitting the He^+ ions. (c) Apex of the tungsten tip. (d) Imaging of the He^+ trimer source. Adapted from the product information of the ZEISS ORION NanoFab He^+ FIB.

the opportunity to nanomanufacture a sample locally on request with etching and metal induced deposition. These achievements are possible due to the specific characteristics of the He^+ ions and their interaction with the materials.

The He^+ ion beam column is similar to the SEM technology except for the source, as shown by fig. 3.3(a). As can be seen in fig. 3.3(b-c), the source consists of a tungsten tip under a high voltage, with an apex faceted in a pyramidal shape containing only a few atoms at its very end (fig. 3.3(c)). The helium gas inserted near the end tip ionizes, then a trimer of He^+ ions is formed at the apex tip (fig. 3.3(d)), and finally only one emitting atom is selected as a source.

The source size has been estimated to be of 250 pm in diameter by simulations. It results in an almost ideal point source: small and bright. Thanks to this feature, the depth of field is more important for the He^+ FIB than for the EBL, and the focusing tolerance is enhanced for the manufacturing.

The ion energy is set by the extractor between 10 keV to 30 keV. Similarly to a SEM, the ion beam is focused thanks to a set of lenses and the stigmatism is corrected *via* magnetic poles. The aperture controls the beam size going to the sample and hence affects the current which is also tunable thanks to the helium vapor pressure.

Once the He^+ ions hit the sample, two additional effects broaden the beam. The elastic forward scattering of the He^+ ions with the material enlarges the beam size. The SRIM simulations show that for 30 keV He^+ ions into a titanium sample the divergence of the beam is only 0.1 nm at 5 nm penetration depth [236]. If the titanium is replaced by carbon, the beam divergence is below 1 nm [236]. In addition, the secondary electrons generated by the inelastic collisions of the He^+ ions deposit more energy per unit length compared with the EBL, and the proximity effect is negligible. As a consequence, for the lithography application the minimum feature size approaches 5 nm for densely packed structure without the need of corrections [237].

Another interesting aspects for the imaging and the manufacturing are the possibility to neutralize the trapped He^+ ions thanks to an electron flood gun (fig. 3.3(a)). It avoids the electrical charging of the sample and then it enhances the contrast while imaging.

In this thesis, we make use of the He^+ FIB to insert disorder into the YBCO film with He^+ ions to pattern the nanowires. In comparison to the ion implanter described in section 3.2.2, the He^+ FIB provides an extremely small ion beam. Furthermore, the He^+ ions have a smaller divergence than the O^+ ions. It opens up the possibility to design structures at nanoscale without the use of a protecting resist which limits the width of the wire to 100 nm.

3.3 Simulation of irradiated devices

In our case, we are interested in a secondary effect of the ion irradiation: the introduction of defects by the impinging ions rather than the doping. As the ions penetrate into the target, they shift atoms from their initial crystallographic positions which might successively displace another atom and so on and so forth. As a consequence the ion beam creates defects all along the implanted ion trajectories.

3.3.1 Simulations of the stopping and range of ions in matter

By considering the dose D , the thickness d , and the YBCO unit cell volume V_{cell} , we evaluate the number of ions introduced in the unit cell to be:

$$N_{\text{ions}} = \frac{DV_{\text{cell}}}{d} \quad (3.3)$$

For $D = 3.10^{14}$ ions.cm⁻² and a 30 nm thick film, 0.001 ions are introduced per unit cell. Even if eq. (3.3) considers that all the ions go into the superconducting layer - which over estimates the rate - the quantity of implanted ions is negligible compared with the total ions number in YBCO. Especially, it is really low compared with the characteristic stoichiometry needed to change YBCO properties with respect to the superconducting dome. Nevertheless, the total amount of implanted ions on a 3 inches target is still high, about 10^{16} ions.cm⁻². In this way, the defects distribution inside the material can be described using statistical methods.

We used the Monte Carlo simulation software developed in 1983 by Ziegler and Biersack called the stopping and range of ions in matter (SRIM) [238].¹ in order to predict the defect density created by the implanted ions and optimized the fabrication of the nanowires. The user sets the density and the chemical composition of the target layer by layer, along with the impinging ion and its energy.

Given the parameters, the SRIM software computes the trajectories of the ions into the matter which lose their energies as they interact with the electrons and collide with the nucleus of the target. For each collision the ion transfers a part of its energy to the atom. Each atom has its own displacement energy E_d representing the minimum amount of energy required to move it out of its lattice site, assuming that it will not fall back to its initial position. If the energy transfer is higher than the displacement energy of the collided atom, the latter is knocked out of its position creating a vacancy in the crystalline structure. The expelled atom will then produce a new collision sequence, by colliding other target nucleuses, while the ion will follow its own collision sequence. Altogether, the collision events create a collision cascade. It stops when the ion and all the ejected atoms transfer their energy to the phonons and the electrons of the target.

As a consequence, one ion creates numerous vacancies along its trajectory. The defects might be filled by the subsequent expelled atoms if they are of the same type. It is mentioned as a replacement event which does not contribute as a defect.

By looping the collision cascade process with a chosen number of impinging ions, denoted by N_{ions} , SRIM outputs a COLLISION.txt file. In the "Full Recoil Cascades" mode, the file output contains the atom number index involved in the collision cascade, the collision coordinates² (x, y, z) , and informs the user if it is a vacancy or a replacement.

Since we are interested in a statistical evaluation, the collision cascade is computed for large N_{ions} , typically 10^5 ions. One set of parameters bring us to approximately 10 Gb file with a large part of undesirable data. Henceforth, analyses are performed by a C# software to compute the three-dimensional (3D) matrix $dpa(x, y, z)$.

From the COLLISION.txt file, only the coordinates for the vacancy events are picked out and saved in a 1 Gb annexe file. We set an equally spaced mesh in 3D with δx , δy and δz being the elementary spacing in x , y , and z directions respectively. The largest x , y , and z collision event set the size of the matrix in the three different directions. Each collision event occurring at the position (x, y, z) in the elementary volume $\delta V = \delta x \delta y \delta z$ increments by one the 3D collision matrix $C(x, y, z)$ expressed in number of defects. After scanning all the collision cascade, each collision matrix element contains the total number of collisions which occurred in the volume δV .

We are interested in the dpa matrix of a beam dpa_B given by:

$$dpa_B(x, y, z) = \frac{C(x, y, z)D}{n\delta x N_{\text{ions}}} \quad (3.4)$$

¹We performed all the simulations using the SRIM - 2013 version.

²The x coordinate corresponds to the target depth, while the y and z coordinates are lateral in the film plane. Such a convention inherits from the SRIM software and is kept for all the SRIM simulations presented in the thesis.

where n_{material} is the material atomic density, with $n_{\text{YBCO}} = 7.53 \times 10 \text{ atoms.cm}^{-3}$. Looking at eq. (3.4), it is worth noting that dpa is directly proportional to the ion dose. Knowing that the ions go into the material from the origin of the coordinate system, the dpa matrix corresponds to the effect of a point-like ion source. In practice, it corresponds to a FIB such as the one described in section 3.2.3. If we need to simulate the effect of an ion implanter through a mask, or the design of a focused ion beam into a material, a scanning step is required. A two-dimensional (2D) boolean matrix $M(y_i, z_j)$ representing the designed pattern or the He^+ FIB design is convoluted with $dpa_{\text{B}}(x, y, z)$ to simulate the resulting dpa of the pattern:

$$dpa_{\text{P}}(x, y, z) = \sum_i^{N_x} \sum_j^{N_z} dpa_{\text{B}}(x, y - y_i, z - z_j) M(y_i, z_j) \quad (3.5)$$

In practice, it is uncomfortable to represent the dpa matrix in three dimensions. Thus, cuts of the dpa in different directions will be presented to gain clarity in further sections.

3.3.2 Influence of the ions

Three parameters are tunable by the user to optimize the defects distribution into the materials: the ions, their energy, and the dose. For our purpose, two types of atoms are considered: the O^+ ions and the He^+ ions. The former presents the advantage of not contaminating the material with foreign atoms, while the latter is advantageous for designing a structure with a FIB as we will see in section 3.2.3. The main features of the simulation are:

- The lateral standard deviation, or straggling, given by the lateral extension of the disorder at a given dpa reference.
- The longitudinal standard deviation given by the longitudinal extension of the disorder at a given dpa reference.

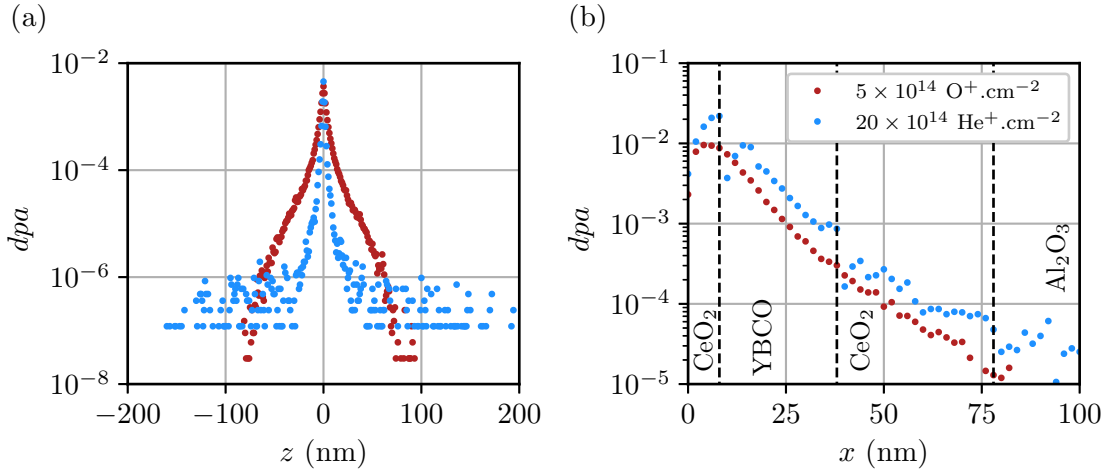


Figure 3.4 – Simulation of the dpa generated by the He^+ and the O^+ ion sources with 10^5 ions at an energy of 30 keV into a stack of CeO_2 (8 nm)/YBCO (30 nm)/ CeO_2 (40 nm)/ Al_2O_3 . (a) Average dpa along x in the YBCO layer at $y = 0$ as a function of the lateral dimension z . (b) dpa at $y = 0$ and $z = 0$ as a function of the depth x . The dose is adjusted such that the maximum dpa in (a) are equal for the He^+ ions and the O^+ ions. The black dashed lines separate the different material layers.

- The penetration depth, which is the depth given by the deeper defect.

Figure 3.4 presents the dpa generated by the two different ion sources. The doses have been set in such a way that the maximum of the dpa are similar for the two ion types.

The first feature to look at is the straggling in fig. 3.4(a). The dpa generated by the He^+ simulation has a sharp peak, it decreases by 99% within a 5 nm lateral extension, while for the O^+ case the extension is about 40 nm. Due to the light weight of the He^+ ions with respect to the O^+ ions, the defects are introduced far away from the impact point. The last collision event occurs at a lateral extension of 280 nm for the He^+ ions while it stops about 100 nm for the O^+ ions. The same could be said in terms of depth, when we look at fig. 3.4(b), the O^+ ions are stopped more rapidly in the target compared with the He^+ ions. At such an energy, the penetration depth of the O^+ ions is about 100 nm, while it reaches more than 300 nm with the He^+ ions. With respect to these information, we expect to create a more precise pattern with sharp edges using the He^+ ions rather than the O^+ ions. But we should keep in mind that the defects may be implanted far away from the impact. Thus, a special care has to be taken to choose an appropriate design with the He^+ FIB, as we will see in section 3.3.4.

3.3.3 O^+ irradiation through a mask

The SRIM simulation is a precious support to choose the appropriate protecting layer thickness and also to determine the T_c profiles of the ion irradiated devices. For O^+ implantation, the ion beam is about 1 mm, that is why the whole target is scanned in the lateral dimensions. In the simulation, we also perform a lateral scanning with a sufficient small step about 1 nm to simulate properly the effect of the ion irradiation. If the whole area is exposed to the beam, it is mentioned as a plain sheet irradiation. To fabricate the nanowires with such a technique, the superconducting areas are protected either by a ma-N resist layer or an Au layer. We determined the minimal thickness of each layer by estimating the penetration depth of the ions into each layer at a given energy with the plain sheet irradiation in a 800 nm side square area, as shown in fig. 3.5.

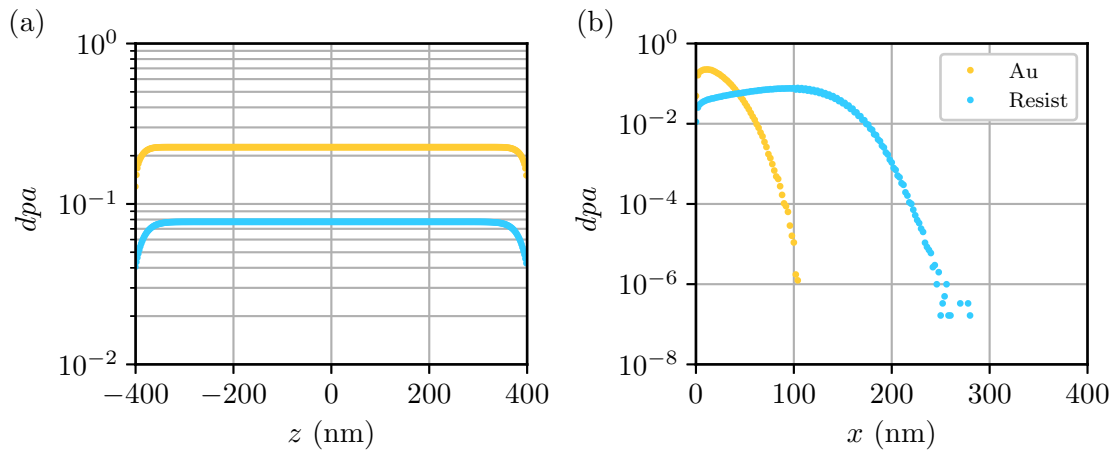


Figure 3.5 – Simulation of the dpa generated by a 30 keV O^+ plain sheet irradiation with $D = 1.10^{15}$ ions.cm $^{-2}$ into the protecting layers: a 500 nm thick ma-N2405 resist layer and a 150 nm thick Au layer. A square of 800 nm in side is scanned by the ion beam presented in fig. 3.4 with a 2 nm step size to simulate the effect of the ion implanter. (a) dpa along the lateral dimension z at $y = 0$ and $x = x_{\text{max}}$ such that the dpa is maximum. (b) $dpa(x, |y| < 2 \text{ nm}, |z| < 2 \text{ nm})$ as a function of the depth x .

The lateral dpa cut in fig. 3.5(a) is almost constant 100 nm apart from the center. It indicates that the exposed size is enough to consider the effect of a point-like ion source which extends over a 200 nm length for Au, and a 350 nm length for the resist. As a heavy metal, with $d_{Au} = 19.3 \text{ g.cm}^{-3}$, the Au layer stops more effectively the ions than the ma-N2405 resist layer with $d_{ma-N} = 0.95 \text{ g.cm}^{-3}$. We conclude that the dpa at the origin simulates correctly the effect of the ion implanter.

Figure 3.5(b) presents the dpa profile at $z = 0$. The two protecting layers are effective if the last defect event occurs before reaching the YBCO layer. The penetration depth for ma-N2405 resist and Au layers are respectively of 250 nm and 100 nm. By choosing a layer thickness higher than the penetration depth, we ensure that the ions do not penetrate into the YBCO superconducting layer whatever the dose. During the fabrication, we set an Au layer thickness above 150 nm and a ma-N2405 resist layer thickness above 300 nm at least.

Since the irradiated nanowires are completely buried by the insulating matrix and a capping layer, it is difficult to access the superconducting profile of the wire. In such a context, the simulation is a precious tool to estimate the T_c profile of the irradiated nanowires. Figure 3.6 represents the T_c reduction profile created by a 30 keV O^+ irradiation through a 100 nm wide resist mask into a 30 nm YBCO thin film protected by a 8 nm thick CeO_2 layer. For such a simulation, the area is exposed only if $|z| > 50$ nm in a 400 nm side square in the yz plane. A xz plane cut is performed at $y = 0$ to retrieve the homogeneous dpa .

The heatmap presented in fig. 3.6(a) shows the reduction of T_c in the xz plane by converting the dpa using eq. (3.1). The white contour shows the wire edges at $T = 0$ K which are bended because the ions introduce different amounts of disorder depending on the depth. The cuts along the z direction of the heatmap at different depths are represented in fig. 3.6(b). They clearly show that T_c is nonuniform along both the x direction and the z direction, but they do not vary drastically. To gain a more quantitative picture of the wire width, we evaluate it as a function of the depth for different temperatures in fig. 3.6(c). In other words, one point in fig. 3.6(c) corresponds to the lateral extension z of one curve in fig. 3.6(b) at a specific T_c . As the temperature raises, the wire edges become no longer superconducting, so they do no longer contribute to the wire width which shrinks down. At last, fig. 3.4(d) shows that the average width in depth slowly decreases up to half T_c and it goes rapidly to zero afterwards.

The simulations show that the wire width is reduced by 20 nm at the lower temperatures compared with the 100 nm set by the lithographic mask. But the temperature dependence is far from being simple.

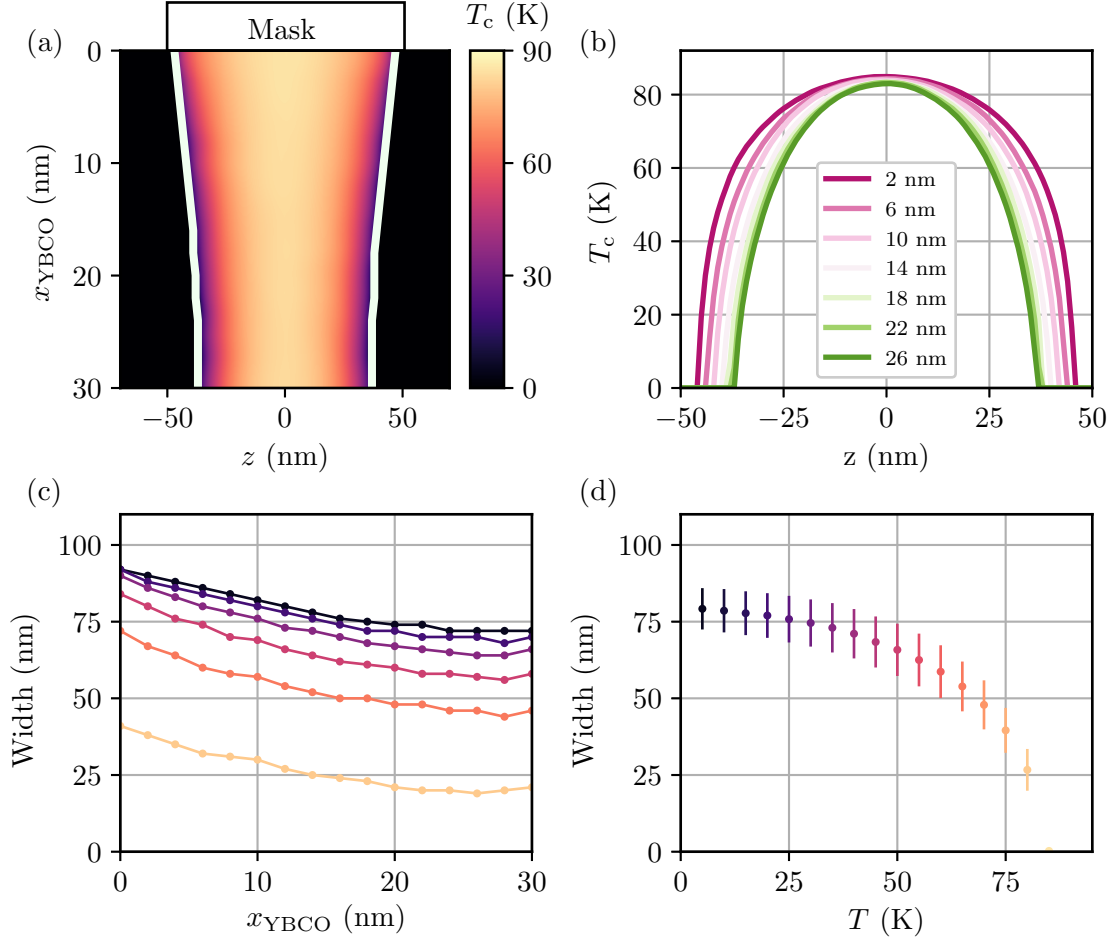


Figure 3.6 – Simulation of a 30 keV O^+ irradiation into a sample of a 30 nm thick YBCO thin film protected by a 100 nm wide 500 nm thick ma-N2405 resist with $D = 5 \times 10^{14}$ ions.cm $^{-2}$. The dpa have been converted to T_c using eq. (3.1) for a better understanding. (a) Heatmap of T_c in the xz plane in the YBCO layer. White contour is set for $T_c = 0$. Note that the resist thickness is not to scale. (b) Lateral variation of T_c at different depths x . (c) Variation in depth of the wire width extracted from (b) at different temperatures. (d) Evolution of the wire width with respect to the temperature. The color scale in (c) and (d) is the same that the colorbar in (a).

3.3.4 He⁺ focused ion beam patterning

Cybart *et al.* were the first to fabricate YBCO irradiated devices by means of the He⁺ FIB [239]. They successfully created Josephson junctions by writing a single line perpendicular to a superconducting bridge with $D \approx 5 \times 10^{16}$ ions.cm⁻².

Unlike the O⁺ implanter, the He⁺ FIB scans a specific design on the sample without requiring of a lithographic step before. In this case, the main interest of the simulation is to optimized the design of the nanowires with the He⁺ FIB structuring.

Starting from a YBCO microbridge of a few microns width, two different ways to carve out a nanowire are presented in fig. 3.7: the biline pattern and the multiline pattern. The former consist of two parallel lines of He⁺ FIB writing separated by a specific width defining a smaller nanowire, while the latter considers two sets of ten parallel lines separated by a 20 nm pitch on each side of the bridge. A trade-off in the dose has to be set wisely: it has to be high enough to avoid the Josephson effect and a short circuit through the YBCO isolated islands of fig. 3.7, at the same time it has to be low enough such that the dpa in the center of the wire remains negligible not to affect the superconductivity. For these reasons, the simulations of the two patterns have been carried out and the resulting dpa has been converted in terms of the reduction of T_c with respect to the initial T_c using eq. (3.1). Figure 3.8 and fig. 3.9 model the biline pattern in fig. 3.3(a) and the multiline pattern in fig. 3.3(b) respectively, for different nanowire widths.

For the biline pattern, the simulations show that only the 500 nm wide nanowire leaves T_c unchanged at the center of the wire, as depicted by fig. 3.8. As the width is reduced, the lateral straggling affects the central part with T_c reduction of 10% and 20% for the 200 nm and 100 nm wide nanowire respectively. The T_c reduction is not drastic for such a dose, but it turns out that the He⁺ FIB lines do not introduce enough disorder to completely isolate the nanowire from the YBCO isolated islands. The normal barrier separating the two superconducting parts is only 5 nm wide. As a consequence, the Josephson effect might contribute to the overall current. One solution to address this problem is to raise the He⁺ dose. If the dose is larger by one order of magnitude, the barrier width is of 30 nm, which suppresses the Josephson effect. Unfortunately, such a dose almost kills the superconductivity for a 100 nm wide nanowire. We suffer from the important lateral straggling of the He⁺ ions into the matter. As they introduce defects laterally in a long range due to their light weight, it is difficult to make a compromise while choosing the dose.

That is why we suggested the multiline pattern. From the simulations presented in fig. 3.9, we observe a significant reduction of T_c at the center of the nanowire of 50%

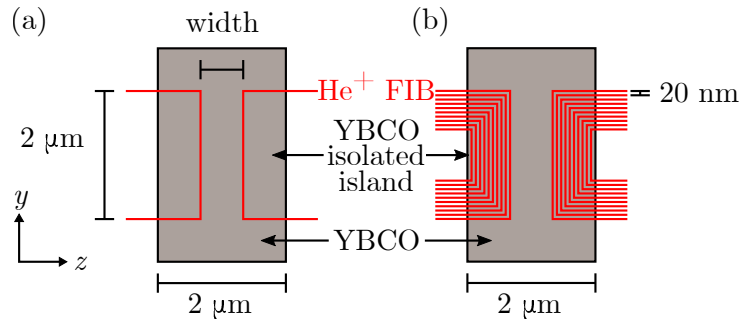


Figure 3.7 – He⁺ FIB patterns out of a YBCO microbridge to isolate electrically a nanowire from the lateral superconducting YBCO islands. (a) Biline pattern: two parallel written lines along the y direction separated by a specific width. (b) Multiline pattern: two groups of ten parallel lines along the y direction separated by a 20 nm pitch, on each side.

and 20% respectively for a 100 nm and 200 nm wide wire . In addition, T_c reduction profile is almost constant for the wires wider than 100 nm, but it varies about a factor 2 for the 100 nm wide wire, as shown by fig. 3.9(b). Nonetheless, the design limits the constraints on the high dose to electrically isolated the YBCO islands from the nanowire. An intermediate dose of 1×10^{17} s ions.cm⁻² is sufficient to completely decouples the YBCO nanowire.

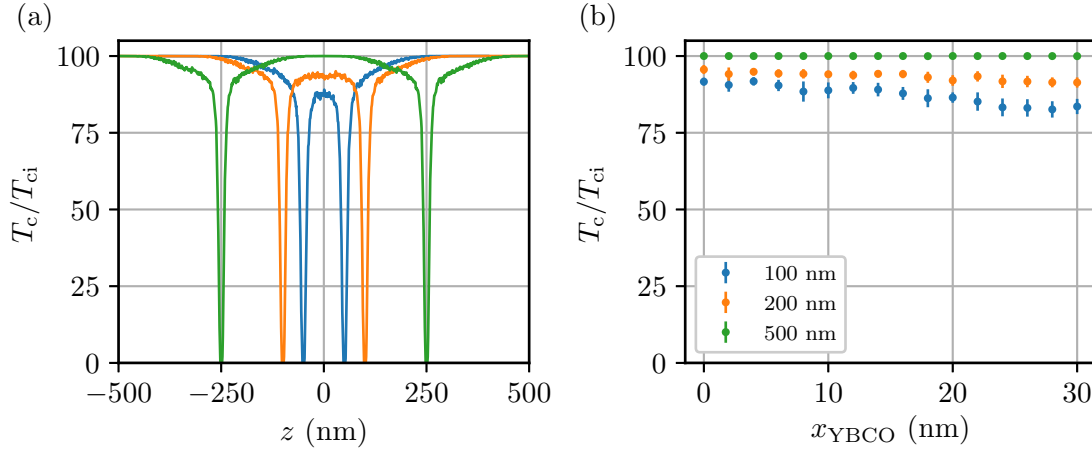


Figure 3.8 – Simulation of 30 keV He⁺ ions into a 30 nm thick YBCO thin film protected by a 8 nm thick CeO₂ capping layer corresponding to the pattern shown in fig. 3.7(a) with $D = 1.10^{17}$ ions.cm⁻². (a) Average lateral reduction of T_c with respect to T_{ci} over the depth. (b) Average reduction of T_c with respect to T_{ci} at $z = 0$ in function of the depth. The error bars correspond to the standard deviation along z .

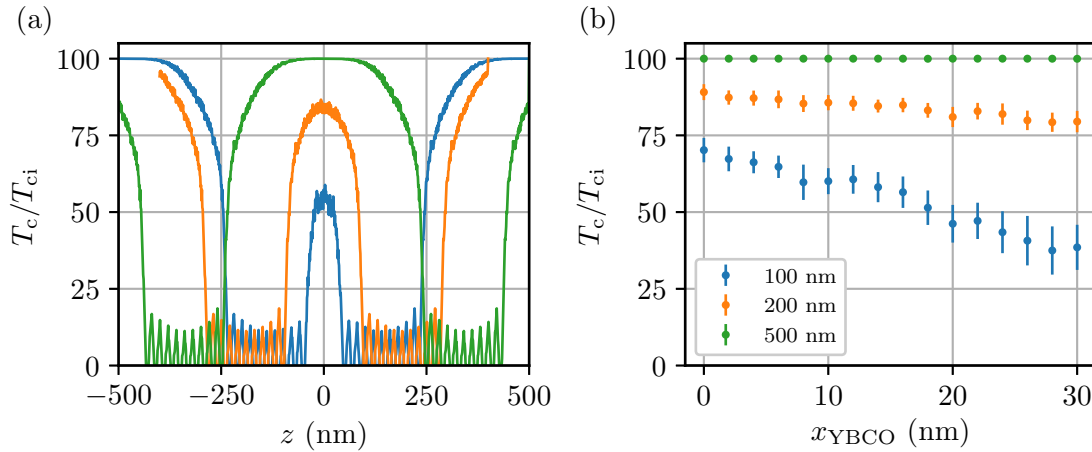


Figure 3.9 – Simulation of 30 keV He⁺ ions into a 30 nm thick YBCO thin film protected by a 8 nm thick CeO₂ capping layer corresponding to the pattern shown in fig. 3.7(b) with $D = 1.10^{17}$ ions.cm⁻². (a) Average lateral reduction of T_c with respect to T_{ci} over the depth. (b) Average reduction of T_c with respect to T_{ci} at $z = 0$ in function of the depth. The error bars correspond to the standard deviation along z .

3.4 Fabrication workflow

The nanofabrication workflow involves several processes performed in cleanroom facilities of Paris Centre. We have succeeded in developing a reproducible, robust, and versatile method to fabricate YBCO nanostructures using the laser beam lithography, the electronic beam lithography, and the ion irradiation. The methods are not specific to SSPDs, they might be also applied to every kind of nanodevices made of YBCO for many applications.

YBCO is a difficult material to pattern due to the specific optimal stoichiometry making it really sensitive to the atmosphere. The first attempt to fabricate YBCO nanowires with O^+ irradiation involved a YBCO thin film covered by an Au layer, with the superconducting layer exposed to the air at the end of the process. The nanowire quality and stability were compromised because they were electrostatically unstable, the optimal doping was lost, and the etching process introduced a small quantity of Ar^+ ions into the YBCO layer. It is well known that the oxygen atoms easily diffuse out of the YBCO layer, especially in the thin films. As a consequence, YBCO loses its optimal doping and the corresponding superconducting properties. In addition, numbers of devices burnt if not enough safety precautions were taken. Such a damaging behavior has been also reported by the Chalmers group when the device is not protected. To solve the problem, the devices have been capped by a thin Au layer [36] or LSMO layer [37]. But as far as the top layer is removed, the superconducting properties are damaged (fig 3.b [37]).

In our case, we protect the device by a thin insulating CeO_2 layer which has numerous advantages. Its fixed stoichiometry prevents the change of the YBCO stoichiometry. The material is already used and calibrated in the deposition chamber since it is the seed layer for YBCO growth.

The samples presented in the thesis have two different origins. The first one is commercially available from Ceraco GmbH. They propose a wide range of thicknesses and qualities of HTS deposited by chemical vapor deposition. The other source of samples arises from a collaboration with Javier Briatico at the UMR CNRS-Thales. He has a strong expertise on the growth of superconducting YBCO ultra thin films by pulsed laser deposition, with superconducting thicknesses down to 2 unit cells [44].

3.4.1 Standard irradiated devices

The following part describes the different nanofabrication steps summarized in fig. 3.10 for the O^+ irradiated devices completely covered by a CeO_2 layer. Specific details of the different steps are depicted in appendix appendix A.

Step 0: Bare sample (fig. 3.10(a))

The nanofabrication begins with YBCO thin films with a thickness ranging from 8 nm to 30 nm, grown on top of a 10 mm side square wafer with a 40 nm thick CeO_2 seed layer deposited for the lattice matching, and capped with a thin protecting oxide. In the figure, the seed layer is omitted for clarity.

Step 1: Au Electrodes lithography (fig. 3.10(b))

The first step consists of a lithography to design the electrodes. We use either an EBL at ESPCI Paris with a positive 500 nm thick poly(methyl methacrylate) (PMMA) resist, or a laser beam lithography with a positive 500 μm thick S1805B resist at Collège de France. As far as the smallest dimensions are larger than 10 μm both recipes presented in appendices A.1 and A.2 are suitable. During the lithography, the exposed areas will be developed and will define the Au layer.

Step 2: Ar^+ etching (fig. 3.10(c))

Prior to making the electrical contacts with the YBCO layer, we follow the recipe presented

in appendix A.3. We etch the protecting CeO_2 layer thanks to an Ar^+ ion beam etching (IBE) at 500 eV () to retrieve the YBCO layer.

Step 3: Ti-Au deposition (fig. 3.10(d-e))

In order to make the electrical contacts between the Au electrodes and the YBCO layer, we deposit 0.5 nm of Ti as an adhesive layer, followed by a 200 nm Au layer immediately after the step 2. The resist is then lifted off in a hot acetone bath with help of short time low powered ultrasound baths. The complete recipe is described in appendix A.4.

Step 4: YBCO electrodes and nanowires lithography (fig. 3.10(f))

The fourth step consists of a two steps EBL, detailed in appendix A.5, aiming at protecting the specific YBCO areas during the O^+ ion irradiation step. It defines both the superconducting electrodes and the superconducting nanowires. Afterwards, an EBL is performed with an SEM FEG-SEM Magellan FEI at ESPCI Paris to pattern the resist. As a negative electronic resist, the unexposed ma-N2405 resist is removed during the development while the other areas last to protect YBCO.

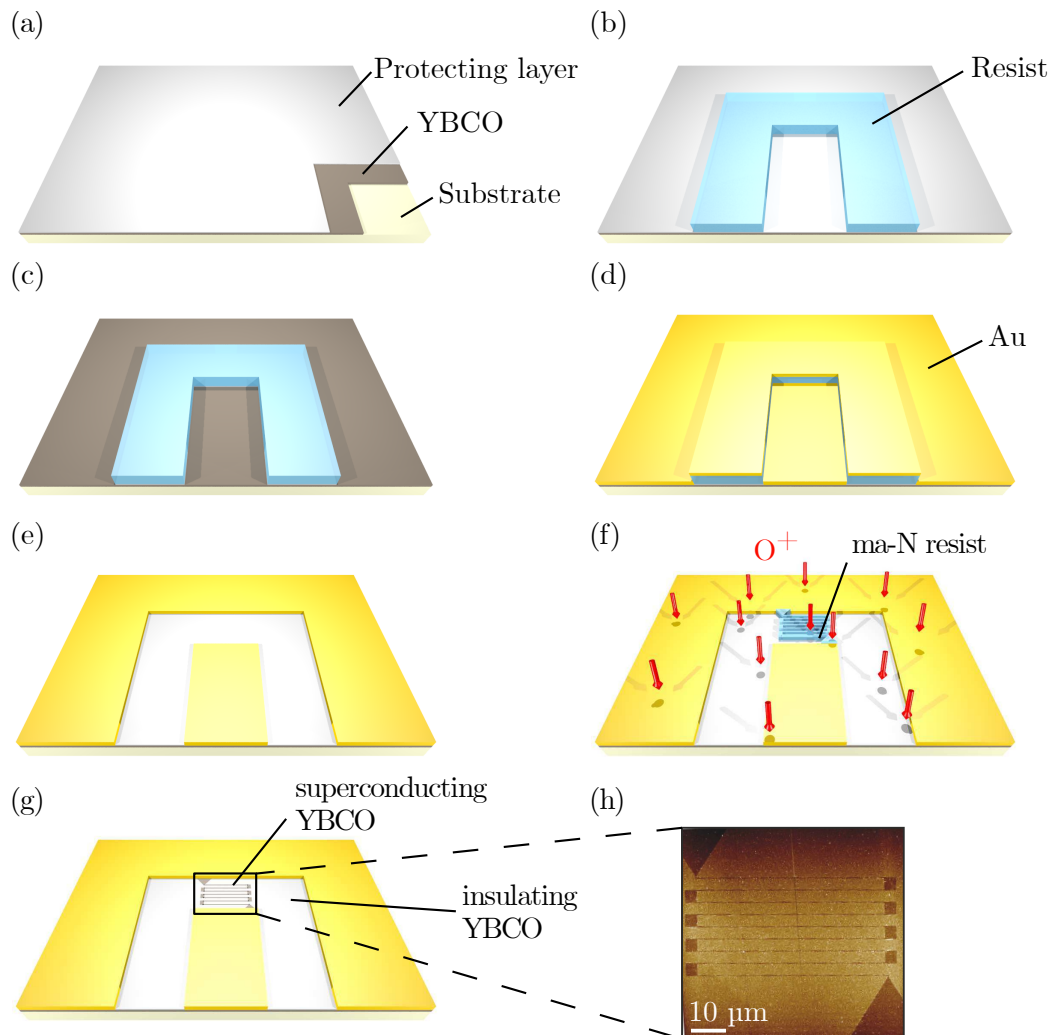


Figure 3.10 – (a-g) Fabrication workflow described in the text. (h) AFM picture of a 750 nm wide YBCO nanomeander. Adapted from Amari *et al.* [225].

Before the ion irradiation, a final control with a UV filtered microscope is made in the optical room. It aims to verify the alignment between the Au electrodes and the ma-N2405 resist mask, but also to check that the ma-N2405 nanowires are not broken.

Step 5: O⁺ irradiation (fig. 3.10(f-g))

The ion irradiation is the last step for the O⁺ irradiation performed at ICUBE laboratory in Strasbourg by Y. Legall. The batch of samples is prepared in a cleanroom environment to avoid a dust contamination. The samples are carbon taped in the center of a 3 inches diameter metallic target in order to thermalize the substrate during the ion irradiation. In addition, metallic clips are fixed on top of the sample in contact with the Au electrodes to evacuate the charges and avoid an electrical discharge which could damage the devices.

The common parameters used are an energy of 30 keV with $D = 3.10^{14}$ ions.cm⁻². The targets are placed in the vacuumed process chamber. Before the ion irradiation, the beam is set in a proper way such that the scanning is homogeneous along the sample dimensions. During the ion irradiation, we ensure that the current is set between 10 μ A and 15 μ A not to overheat the samples.

At the end, we need to remove completely the resist. It is particularly tedious since the irradiation hardens the resist on the surface. Prior to the lift-off, we perform an O⁺ plasma stripping with a Corial 200I ICP-RIE during 1 min. This process helps to tear the harden resists from the samples.

The normal fabrication workflow described in this subsection correspond to the N-type samples. The stack of layers of the different N-type samples that have been patterned are summarized in appendix B. Their thicknesses range from 30 nm down to 12 nm. We have later noticed that the contact resistances between YBCO and CeO₂ were not ohmic. The process resulted in k Ω contact resistances at best. Furthermore, as the YBCO films were thinner, the Ar⁺ etching required more precision and could damage significantly the YBCO layer.

3.4.2 Special irradiated devices

In order to get rid of the problem with the N-type samples, we have developed a special fabrication method on the Ceraco thin films mentioned as the CS-type samples. They consist of a 5 mm diameter 8 nm thick CeO₂ disc layer to protect the central YBCO thin film area, while the whole area is covered on top by a 20 nm thick Au layer. During the thin film deposition, a mechanical mask with a circular hole in its center is inserted in order to grow the CeO₂ capping layer. The mask is then removed to complete the deposition with the Au layer. With such a technique, we have obtained good electrical contacts outside the disc area, while the central area is always protected by the CeO₂ blue disc shown in fig. 3.11(a).

In order to include this modification, the fabrication workflow is marginally modified by inverting the Ar⁺ IBE (step 2) with the Au deposition (step 3), while the next steps remain exactly the same. Since the films are covered by an Au layer, the contact is easier to make during the Au deposition and we do no longer need to lay YBCO bare before depositing the Au layer. Once a 150 nm Au layer is deposited, the resist is lifted-off and the samples are placed again in the plassys to etch the 20 nm thick Au layer remaining on the sample to suppress the short circuit. The special process as described above have provided high-quality superconducting YBCO nanowires at the end of the nanofabrication with the samples from Ceraco GmbH called the CS-type samples.

Meanwhile, the collaboration with J. Briatico have continued. He initially masters the deposition of ultra thin YBCO films on STO substrate with PBCO as a seed and protecting layer. We succeeded in fabricating some nanowires using the standard fabrication process by adapting the etching rate. The corresponding samples are mentioned as the

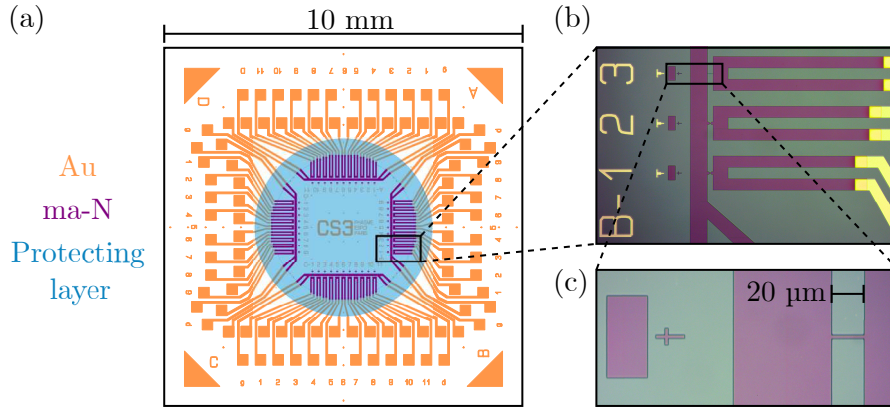


Figure 3.11 – Overview of Ceraco Special chip design. (a) Overall chip layout: the 5 mm-diameter blue disc shows the area protected on top by an oxide layer. (b) Optical microscope picture after the development of the second lithography. (c) Zoom of (b) containing the cross mark positioning for the He^+ FIB design.

T-type samples. He have also managed to adapt the special fabrication process to his own deposition chamber to fabricate the JS-type sample. As we will see in chapter 4, this sample gives the best superconducting properties, and it is similar to the best CS samples. Appendix appendix B summarizes the four different types of YBCO samples which have been fabricated and tested in the thesis.

3.4.3 He^+ focused ion beam process

During the thesis, we have fabricated YBCO nanowires using the He^+ FIB in the clean-room facility of C2N at Marcoussis under the supervision of C. Ulysse. In this case, the samples are patterned with the He^+ FIB at the very end of the fabrication workflow, once the ma-N2405 resist layer is completely removed. The first structures written with the He^+ FIB were Josephson junctions. The results are out of scope of the present thesis, but they helped to choose the first FIB parameters to design the nanowires. We have fabricated the different He^+ FIB patterns described in section 3.3.4. In addition, we have performed perpendicular cuts of the microbridges with the same line patterns with different doses. The latter devices are references to check that the dose is suitable to separate the central nanowire from the lateral YBCO islands.

Similarly to the step 4, the devices area have not to be scanned since the He^+ FIB damages the superconducting properties (section 3.3.2). It is more difficult to satisfy this requirement with the He^+ FIB, because there is no pattern generator which helps to locate the device with respect to the Everhart-Thornley detector (ETD) pictures unlike in the SEM. To meet the requirement, ma-N2405 resist rectangles and alignment crosses have been written during the step 4. Beginning from the sample center, we look for the numbered Au marks shown in fig. 3.11(b) defining the device name. We make the He^+ FIB patterning test on the rectangles in order to fine tune the ion beam column parameters on the superconducting YBCO layer, especially the focus and the stigmatism. When the He^+ FIB parameters are satisfying, we aligned the cross in the center of the picture and turn the He^+ FIB into the writing mode. From here, knowing the exact distance between the cross and the microbridge (fig. 3.11(c)), we shift blindly the sample such that the device of interest is in the write field, and we pattern it.

3.4.4 Characterization tests

The nanodevices patterning needs carefulness, clean-room facilities availability, and travel time between different processes. Overall, they are all time consuming and they become time wasting when the sample becomes no longer superconducting at one given step of the fabrication workflow. We perform several tests during the fabrication to discard the low-quality films and the samples with damaged superconductivity.

Once electrodes have been designed on a sample, the chip is tested with the Van der Paw measurement [240] in a cryostat at low temperatures. We check the bare T_c and the resistivity of the film. If the superconducting properties are damaged - large superconducting transition, high resistivity - or do not exist at all, we throw the sample out. Since the chips of one batch are grown together at the same time, if one sample is rejected at this step, the whole batch is incriminated. In this case, we check another sample from the batch prior to any fabrication step using a vibrating-sample magnetometer. If the superconducting transition is not present, the first fabrication steps are not responsible, but the films are not superconducting from the early beginning just after the deposition. Therefore, we put the whole batch aside.

The ma-N2405 lithography plays also a crucial part in the fabrication workflow. In order not to reassess the step 4 after the resist removal, additional ma-N2405 wires are patterned in the center of the chip. They serve as test devices to evaluate the width and the aspect using the SEM prior to the step 5. It will be too late after the resist removal and it could generate an electrical discharge if it is performed just after the ion irradiation since the YBCO matrix becomes insulating. The homogeneous aspect and the sharp edges of the resist observed in fig. 3.12(a) ensure that the ion irradiation will create a relatively homogeneous dpa along the wire.

In fig. 3.12(b), the nanowire presents a curved bow-tie shape to avoid current crowding effect. We measure its dimension and compare with what we expected to ensure the conformity of the lithographic process. It also helps to detect breakage which could happen when the resist pattern becomes too narrow and too long, as shown in fig. 3.12(c) in which the 150 nm wide nanowire mechanically collapses.

Due to the different substrates and stacked layers, it could happen that the doses are no longer suitable for a sample. If we detect too much problems during the SEM imaging, such as ma-N2405 resist inhomogeneity, broken devices, or non-compliance of

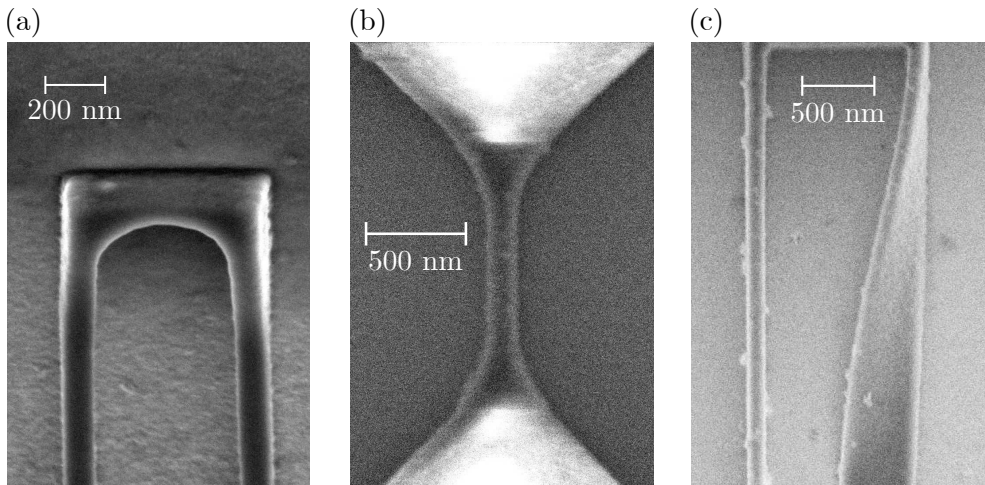


Figure 3.12 – SEM pictures of different devices. (a) 40° tilted angle picture of a meander. (b) 150 nm × 500 nm nanowire. (c) 100 nm wide meander with a broken part.

the dimensions, a ma-N2405 dose test is performed to go on again on good bases.

The last stage of verification is carried out during the ma-N2405 lift-off. Since the aim of the project is to detect photons, we want to be sure that the ma-N2405 resist is completely removed. In addition, if sample is dedicated to He⁺ FIB patterning we also need clean bridges. Thus, we first check with an optical dark-field microscope that the ma-N2405 resist is no longer visible as residue nearby the nanowires. Once we are satisfied, some devices are scanned with an atomic force microscope (AFM). The irradiated matrix slightly swells under irradiation, about 1 nm, depending on the YBCO thickness and substrate. The superconducting material may be subjected to a partial amorphization due to volumetric expansion of the material. The details of such a process in cuprates are still to be understood. If the superconducting YBCO layer is at same depth or below the one of the insulating YBCO matrix, the resist removal is finished.

Chapter 4

Transport measurements

Contents

4.1	Experimental setup	78
4.2	Resistance-temperature evolution	79
4.2.1	Experimental setup	79
4.2.2	Resistance-temperature curve analysis	81
4.2.3	Influence of the ion irradiation process	83
4.2.3.1	He ⁺ focused ion beam patterning	83
4.2.3.2	O ⁺ irradiation	85
4.2.4	Origin of the chip	86
4.3	Current voltage characteristics	89
4.3.1	General description	89
4.3.2	Hysteresis and flux flow behaviors	91
4.3.3	Influence of temperature	96
4.3.3.1	Retrapping current evolution	96
4.3.3.2	Critical current evolution	98
4.4	Resonant radio frequency measurement	101
4.4.1	Probing the dynamical properties	101
4.4.2	Experimental setup	102
4.4.3	Behavior at resonance	103
4.4.4	Temperature dependence of the kinetic inductance	104
4.5	Conclusion	106

Electrical tests are performed on raw thin films prior to the nanofabrication and on devices patterned by ion irradiation. We also measured the superconducting properties of the films during the fabrication process, they help to decide whether to carry on the fabrication or not. The electrical characterizations of the devices are more extensive, they tell us to what extent superconducting properties are preserved after the patterning. It usually begins with the measurement of the resistance temperature (RT) curve to observe the superconducting state to the normal state transition. The corresponding experimental methods to measure and extract parameters of interest are depicted in the beginning of section 4.2. Then, we present the results obtained for the various irradiation process and the different type of samples. If the quality of the transition is satisfying, we characterize further the device by measuring its current voltage (IV) characteristic at several temperatures, as presented in section 4.3. The measurements provide information on the superconducting properties, especially the critical current density, which gives good indication of the device quality and the possibility to detect single photon. Depending on j_c values, the IV curve displays different behavior, either hysteretic or flux flow like. SSPDs operate from picosecond to nanosecond time scales which is mainly set by the wire inductance. In section 4.4, a radio frequency (RF) resonant RLC circuit is probed thanks to a vector network analyzer (VNA) to estimate the inductance of hundreds microns long YBCO meanders.

4.1 Experimental setup

In order to perform electrical measurements at low temperature, the sample of interest is glued on a copper sample holder with silver paste to ensure good correct thermalisation. The Au electrodes on the sample are wirebonded to a homemade printed circuit board (PCB) as shown in fig. 4.1. They can be either connected to standard direct current (DC) electrodes or to a coplanar waveguide for RF measurements. Unless otherwise stated, all the measurements are performed on an OptiDry pulsed tube cryostat with a 3.4 K base plate temperature. An optical plate, slightly decoupled from the base plate, goes down to 3.7 K. It allows us to place the electronics and the sample holder at low temperature. The former is decoupled from the optical plate thanks to Duralumin pillars and reaches 4.5 K at best. A calibrated CX-1030 resistor measures temperature, while a Arcol HS10 100 Ω resistor heats up the sample. Both resistors are screwed on the backside of the sample holder. Temperature is set between 4.5 K and 200 K thanks to a Cryo.Con 24C temperature controller. The DC and SMA connectors of the sample holder are plugged inside the cryostat which has 3×12 twisted pairs of DC manganese wires and three calibrated coaxial cables. Both DC wires and RF lines are thermalised on each stage of

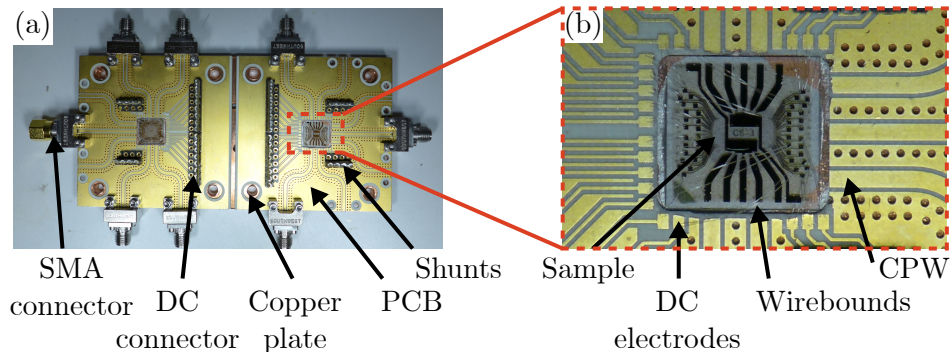


Figure 4.1 – Pictures of a sample holder ready to be plugged on the cryostat.

the cryocooler as they go into the cryostat to limit the thermal noise and the heat transfer. Only the DC ports are low-pass filtered at the entry of the cryostat.

The cryostat DC ports are connected to a measurement box in which a 1.8 k Ω protecting resistor has been placed in series with each connection. It allows us to either ground both the device and the resistor, or to connect them to the measuring port *via* a mechanical switch. The 1.8 k Ω resistor protects the device from the external environment to reduce possible electrostatic discharges. Devices are sensitive to voltage breakdown, especially in the superconducting state at low temperatures. Therefore, it is important not to let the device floating once it is wirebonded. For such a purpose, all the electrodes are shunted and the sample holder is connected to the ground during the wirebonding. Once wirebonding is done, connectors are then plugged to the cryostat while box is in grounded mode. Only then shunts on the sample holder are removed. In order to perform an experiment, the instruments are connected to the measurement box and all the switches are turned to the measuring mode to avoid shortcuts. When the cryostat is cold, this sample connection procedure is done about 120 K on the sample holder to avoid damaging the devices in the superconducting state. The method have made its proofs not to break the connected devices and it is performed for all type of DC measurements.

4.2 Resistance-temperature evolution

4.2.1 Experimental setup

Once a device is connected and cooled down into the cryostat, we first measure its RT curve. To this end, we perform four-terminal sensing to eliminate contact and lead resistance contribution. As shown in fig. 4.2, the current I flows from the common electrode, which is connected to several devices, to a specific electrode of the tested device. The voltage is measured between the upper right common electrode and the lower right specific electrode. The sketch is equivalent to the electrical circuit diagram shown in fig. 4.3(a) where R_{serie} represents all the resistance contributions from the measurement chain, such as the contact resistance, the Mn wires, and the 1.8 k Ω protecting resistance. With such

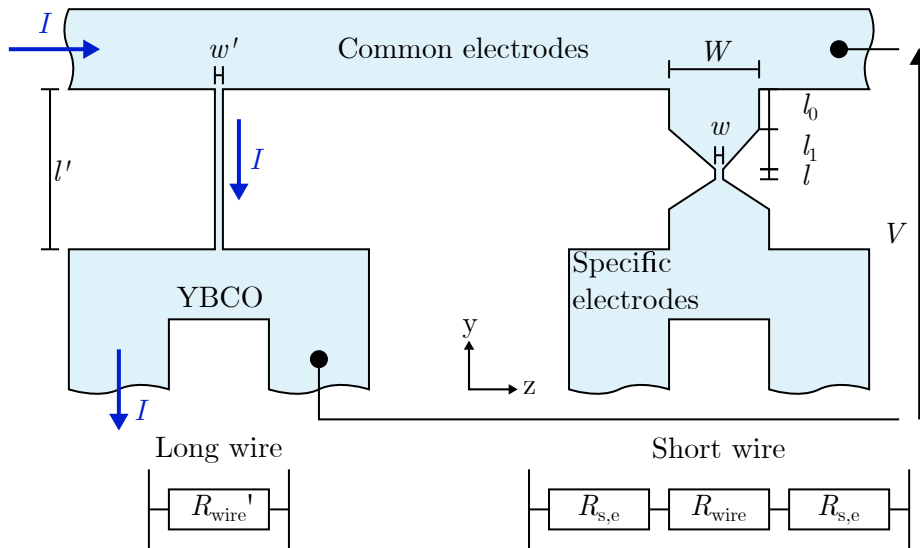


Figure 4.2 – Schematic of two superconducting wires connected to the common electrodes, and to their own specific electrodes. The left device is a micron long wire whose equivalent resistance is $R_{\text{wire}'}$. The right device consists of a nanometer short wire of resistance R_{wire} surrounded by two small superconducting electrodes of resistance $R_{\text{s,e}}$.

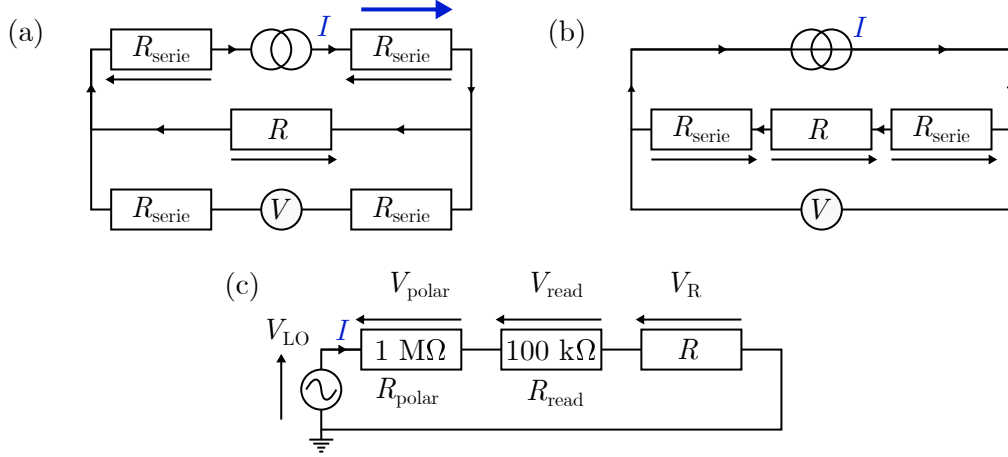


Figure 4.3 – (a) Four-probes DC resistance measurement. (b) Two-probes DC resistance measurement. (c) Low-frequency lock-in resistance measurement. R corresponds to the resistance to measure, while R_{serie} is the resistance in series corresponding to the sample electrodes, the wireboundings, the cables inside and outside the cryostat, and the $1.8 \text{ k}\Omega$ protecting resistance. For the sake of clarity purposes, R_{serie} and 4-probes have been omitted in (c), but they remain in measurements.

a scheme, we only measure the voltage drop across the device between the common and the specific electrodes since no current flows through electrodes on the right hand side.

Whenever possible, the four-terminal sensing configuration is preferred, but if the device is connected to a RF coaxial line, there is only two electrodes to measure the resistance: the ground and the core. In this case, the electrical circuit depicted in fig. 4.3(b) describes the two-terminal sensing scheme. A voltage drop develops along R and $2 R_{\text{serie}}$, we need to subtract the contribution of R_{serie} to the voltage to obtain the device resistance R .

In the two configurations exhibited, we use a Yokogawa GS200 DC current source, and a Keithley 2200 voltage multimeter. A DC current $I_{\text{DC}} = 100 \text{ nA}$ flows through the device and its polarity reverts every second. At the same time, the voltage is measured alternatively for the positive and the negative current flow denoted respectively by V_+ and V_- . Half of the voltage difference gives the voltage drop across the device without the voltage offset. The resistance is obtained simply using Ohm's law with:

$$R_{\text{DC}} = \frac{V_+ - V_-}{2I_{\text{DC}}} \quad (4.1)$$

While the RT DC measurement is easy to implement, its sensitivity is limited to a narrow voltage range, typically a few orders of magnitude. Since the resistance R goes from a value varying slowly above T_c to $0 \text{ }\Omega$ after the superconducting transition, it is preferable to use lock-in amplifiers to enhance the voltage sensitivity range. For this purpose, we realize a four-probes RT alternating current (AC) measurement with the electrical circuit depicted in fig. 4.3(c), in which we omitted the connection of the lock-in amplifier instrument for the sake of clarity. In this case, a local oscillator (LO) applies a fixed low frequency (13.79 Hz) alternating voltage across a set of resistors in series: the polarization resistance $R_{\text{polar}} = 1 \text{ M}\Omega$, the current reading resistance $R_{\text{read}} = 100 \text{ k}\Omega$, and the device resistance R . Each voltage drop along R_{read} and R are measured simultaneously with a Signal Recovery 7265 DSP lock-in amplifiers at the frequency of the LO. The complex voltages across R_{read}

and R are respectively noted $\underline{V}_{\text{read}}$, and \underline{V}_R . As a result, the device resistance is given by:

$$R = \frac{\Re(\underline{V}_R)}{\Re(\underline{V}_{\text{read}})} R_{\text{read}} \quad (4.2)$$

The dephasing between the two voltage drops tells us about the capacitive and the inductive effects in the device. In our system, the dephasing is generally interpreted as a bad quality of the electrical contacts dominated by the coupling between the gold electrodes and the superconducting thin film. The polarization resistance R_{polar} is chosen sufficiently high to set a resulting alternating current I_{polar} low enough not to affect the superconducting transition and in order to keep I_{polar} constant. To satisfy this requirement, R_{polar} has to be dominant with respect to R_{read} and R . The lock-in AC setup is a powerful setup to measure small voltage signals down to a few nanovolts.

Overall, we favour the four-terminals AC sensing with lock-in amplifiers since it offers the best voltage sensitivity. Another advantage is the ability to perform two lock-in measurements of distinct devices linked to the same common electrodes by setting two different LO frequencies for each setup. This specificity helps to measure two devices simultaneously. If the tested device presents a resistance too high or have bad contact resistance we use the four-terminals DC measurement. Nevertheless, the quality of the data in terms of signal to noise ratio is not as good as in the AC case. The two-terminals DC sensing is considered in the case of a device connected to a coaxial line or when one of the device electrode breaks down. At the end, the measured resistance is the same whatever the setup used, only the quality of the data in terms of signal to noise ratio changes.

In the following, we no longer differentiate the RT acquisition setups. Once devices are connected and instruments are measuring the corresponding resistances, the heat resistor ramps temperature up at $2 \text{ K}\cdot\text{min}^{-1}$. Such a rate is chosen sufficiently low with respect to the sampling time, about 1 s, and to the overall thermalisation time of the sample holder. The RT curves presented in the manuscript are always measured while ramping temperature up since thermalisation is better controlled than ramping down.

4.2.2 Resistance-temperature curve analysis

Figure 4.4 presents a typical RT curve of a short 500 nm long 200 nm wide nanowire patterned on a 30 nm thick film with its derivative with respect to temperature. We introduce T_{cm} as the onset critical temperature picked at the maximum value of the derivative dR/dT . It characterizes roughly the overall device when half of the normal resistance appears. At low temperature far below T_{cm} , only the voltage noise is measured since superconductor exhibits a zero resistance. In the case of DC measurement, resistance varies about zero due to the alternating of the current. In the lock-in setup, the voltage phase across the device is no longer fixed and evolves erratically. As temperature raises, a finite resistance appears when temperature becomes higher than the zero resistance critical temperature T_{c0} . The resistance rapidly increases in a small temperature range about a few kelvins: superconductivity disappears in the whole device. Depending on the wire dimensions and the superconducting material, the temperature evolution of the resistance might be explained by different physical models.

The two critical temperatures gives different information. For example, it happens that a large foot appears in the transition with a small resistance value. In this case, T_{c0} could be largely reduced from a few kelvins to ten kelvins, while T_{cm} remains unchanged compare to the raw thin film or other devices of the same chip. In these circumstances, we interpret it as a defect along the nanowire which could be intrinsic to the material, or created during the fabrication process. If the transition broadens continuously without

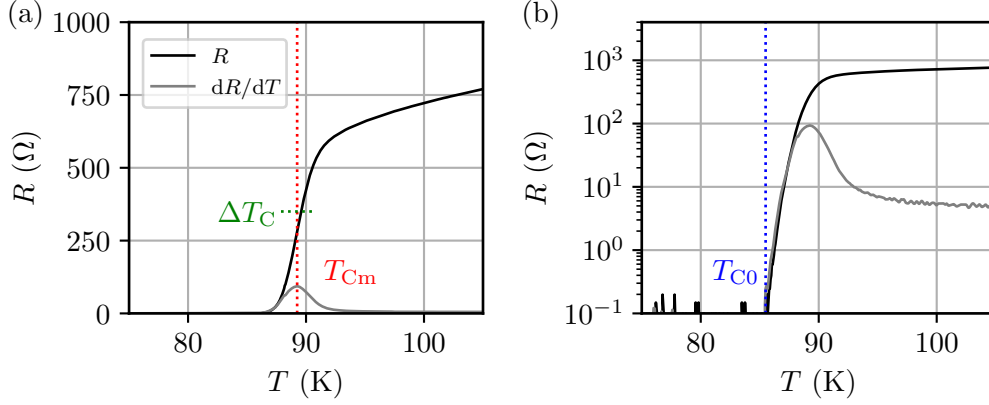


Figure 4.4 – Temperature evolution of the resistance and its derivative with respect to temperature of A7, a 30 nm thick 500 nm long 200 nm wide superconducting nanowire in linear (a) and log (b) scales respectively.

any kink in the RT curve, it is more likely that the whole device is damaged. Since we need preserved uniform superconducting properties all along the nanowire, T_{C0} is a more relevant parameter that gives information about inhomogeneities.

The other quantity of interest is the resistivity in the normal state near the transition at 100 K. It allows us to compare devices with different geometric properties. Its value enables a qualitative characterization of the damages. From the resistance measurement, we estimate the resistivity after taking into account the geometrical arguments. Fabricated nanowires belong to three distinct geometric classes: hundreds microns long meander, 20 μm long straight wire (left hand side wire in fig. 4.2), and 500 nm short bow tie (right hand side device in fig. 4.2). For the two former classes, as electrodes do not contribute to the resistivity ρ , it simply writes:

$$\rho = \frac{Rwd}{l} \quad (4.3)$$

where w is the width, d is the thickness, l the length, and R the measured resistance.

Conversely, the bow tie resistance has a contribution both from the wire R_{wire} and the two surrounding superconducting electrodes in a house shape $R_{\text{s,e}}$, as depicted in fig. 4.2. Following the notations on the figure and assuming that ρ is spatially uniform, $R_{\text{s,e}}$ is the sum of the resistance of a straight wire $\rho l_0/Wd$ using eq. (4.3) and the resistance of a truncated triangle. For the latter shape, in order to compute the corresponding resistance, we should integrate the resistivity contribution of each slab of length dy and of cross-section $A(y)$ given by:

$$A(y) = \left(w + \frac{W-w}{l_1} y \right) d \quad (4.4)$$

Applying eq. (4.3) for each slab of length dy , it follows that:

$$R_{\text{triangle}} = \int_0^{l_1} \rho \frac{dy}{A(y)} = \frac{\rho l_1}{d(W-w)} \ln \left(\frac{W}{w} \right) \approx \frac{\rho l_0}{dW} \ln \left(\frac{W}{w} \right) \quad (4.5)$$

The approximation in eq. (4.5) is valid as long as $W \gg w$. In our bow tie devices, $W = 10 \mu\text{m}$, while $w = 500 \text{ nm}$ at most such that the requirement is always verified. By summing the two contributions and setting $l_0 = l_1$, the superconducting electrode resistance writes:

$$R_{\text{s,e}} = R_{\text{triangle}} + \frac{\rho_0 l_0}{dW} \approx \frac{\rho_0 l_0}{dW} \left[1 + \ln \left(\frac{W}{w} \right) \right] \quad (4.6)$$

We conclude that the device resistivity can be estimated from the measured resistance as follows:

$$\rho \approx Rd \left(\frac{2l_0}{W} \left[1 + \ln \left(\frac{W}{w} \right) \right] + \frac{l}{w} \right)^{-1} \quad (4.7)$$

Thereafter, in order to estimate the resistivity for comparing different devices together, we apply eq. (4.7) for short nanowires, otherwise we use eq. (4.3).

As a last remark, d and l are dimensions estimated with higher precision and accuracy than the width w . The thickness is measured knowing the growing rate and controlled by X-ray diffraction. Assuming that all the YBCO layers are superconducting, we know the thickness with a few Å precision. The length is defined by the EBL with a few nanometers precision. As we saw in chapter 4, the width w is only estimated thanks to the SEM measurement of the protecting resist and the numerical simulation. w might vary about 20 nm, which represents 20% of the width for 100 nm wide wire. For simplicity, we always use the width measured with the SEM to compute ρ , thus overestimating the real value. Therefore, we should keep in mind that resistivity is not accurately estimated, especially for narrow wires.

Each RT curve provides a set of parameters. As an example, table 4.1 summarised the parameters retrieved from the RT curve of a 500 nm long bow tie wire shown in fig. 4.4. For this specific device, T_{c0} only decreases by 1 K with respect to the raw thin film. We obtain a typical value of 300 $\mu\Omega\cdot\text{cm}$ for the resistivity at 100 K and the midpoint critical point is higher than T_{c0} by almost 4 K. Such a device is of good quality since there is no foot in the transition, T_{c0} is almost unaffected and $\rho(100\text{K})$ is in the expected range.

The analysis procedure described in this subsection is applied to all the RT data curves, and helps to choose the appropriate devices for further investigations. We first apply this method to fabricated devices with both He^+ FIB patterning and O^+ irradiation technique.

Table 4.1 – Summary of the device dimensions and the parameters extracted from fig. 4.4

Thickness (nm)	Length (nm)	Width (nm)	T_{c0} (K)	T_{cm} (K)	ΔT_c (K)	$\rho(100\text{K})$ ($\mu\Omega\cdot\text{cm}$)
30	500	200	85.5	89.2	2.7	297

4.2.3 Influence of the ion irradiation process

4.2.3.1 He^+ focused ion beam patterning

Figure 4.5 shows the evolution of ρ with respect to temperature for three different wires patterned by He^+ FIB with the multiline method and a unpatterned bridge as a reference on the same chip. The corresponding parameters is summarised in table 4.2. Prior to the fabrication of the FIB nanowires, we perform He^+ dose tests by cutting 20 μm long 2 μm wide reference bridges perpendicularly to the length using the multiline method. We chose the dose of 1000 $\text{He}^+ \cdot \text{nm}^{-2}$ such that the bridge becomes completely insulating with a resulting resistance higher than 10 k Ω in the whole temperature range. As long as the wire resistance is lower than 10 k Ω , it is certain that we probe the constriction made by He^+ FIB and not the surrounding islands.

The reference allows us to check whether the sample is damaged or not by the preceding fabrication process: we look for a sharp transition and superconducting parameters similar to the ones presented in the first line of table 4.2. Hence, in the following only intact reference devices are kept. Thus, we exclusively study the effect of He^+ FIB in the deterioration of the devices. While the reference device is intact, the superconducting

transition is largely damaged by He^+ FIB patterning. As the FIB gap narrows, T_{c0} lessens and $\rho(100\text{K})$ increases significantly. For the gap of $1 \mu\text{m}$ and $0.5 \mu\text{m}$, T_{c0} is respectively reduced by 5 K and 26 K with respect to the reference bridge. But for the narrowest gap, there is no longer superconducting path established in the device even at 5 K. T_{cm} remains the same whatever the patterned gap. It is another indication that previous fabrication steps do not damaged the superconducting properties of the device.

If we examine more precisely the ρT curves, as temperature increases, the first resistivity appearance is only related to the resistivity increase in the FIB gap. The second sharp transition is the resistivity contribution of the superconducting electrodes adding to the previous one, thus resistivity increases only in the FIB gap. The resistivity range between the high temperature plateau and the subsequent kink at lower temperature is quantitatively the same for each devices. It demonstrates that the resistivity increasing is mainly due to the FIB gap contribution.

The He^+ FIB patterned devices are unsatisfactory and could not be exploited for further experiments. In relation to SRIM simulations presented in section 3.3.4, we interpret these results as a deterioration of the superconducting properties due to the proximity effect of the He^+ FIB. In the case of the resist lithography, He^+ FIB technique have a low proximity effect compared to the EBL. This is not the case for the ion irradiations and thus the defects introduction. As we saw in fig. 3.4, He^+ ions create lateral disorder at a longer distance than O^+ ions due to their lighter weight.

To counteract this side effect, additional experimental studies have to be performed. Especially, we can think of more sophisticated patterning methods, such as applying an ion dose gradient perpendicularly to the wire length. With such a process, less disorder will

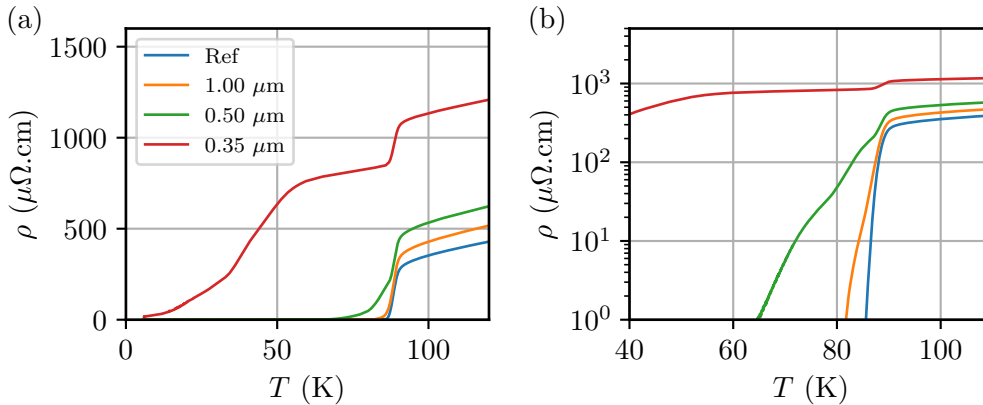


Figure 4.5 – Temperature evolution of the resistivity in (a) linear and (b) log scales. Blue curve represents an unpatterned $20 \mu\text{m}$ long $2 \mu\text{m}$ wide reference wire, while the others are $1 \mu\text{m}$ long constriction made by He^+ FIB on $20 \mu\text{m}$ long $2 \mu\text{m}$ wide wire with the multilines pattern presented in fig. 3.7(b) with $D = 1000 \text{He}^+.\text{nm}^{-2}$.

Table 4.2 – Summary of the device dimensions and the parameters extracted from fig. 4.5

FIB pattern	FIB gap (μm)	T_{c0} (K)	T_{cm} (K)	$\rho(100\text{K})$ ($\mu\Omega\cdot\text{cm}$)
none	-	84.1	88.4	353
$1 \mu\text{m}$ long	1	79.5	88.4	429
$1 \mu\text{m}$ long	0.5	58.1	88.7	534
$1 \mu\text{m}$ long	0.35	0	88.6	1135

be created in the middle of the constriction, while the rest of the superconducting isolated island will become insulating. Another method could consist of patterning a rectangle area instead of several parallel lines. In our case, such a method makes the patterning time too long with respect to the availability of the FIB equipment.

By using He⁺ FIB, Cho *et al.* [231, 241] have patterned JJs and 50 nm wide nanowires at lowest on YBCO thin films. They have successfully fabricated Josephson devices with good properties. On the contrary, they have not reported high-quality nanowires patterned with undamaged superconducting properties, with high T_{c0} and high j_c . Nevertheless, the He⁺ FIB technology is a powerful patterning tool. Further developments are required to perform high-quality YBCO nanowires with preserved superconducting properties.

4.2.3.2 O⁺ irradiation

We come up to the results obtained on O⁺ irradiated devices which will be carry on all along this thesis hereafter. Throughout the project, 47 distinct chips have been considered with varying thickness and origins as summarized in appendix B. Among them, slightly more than half of them, 29 chips exactly, have been irradiated to fabricate nanowires. The others have been rejected during the fabrication workflow due to their poor superconducting properties. One chip contains between 28 and 250 nanowires, depending on the EBL layout, with several widths, lengths, and geometries. In order to compare O⁺ irradiation with respect to He⁺ FIB processes, we present a subset of four devices fabricated on 30 nm thick YBCO films of CS type. The corresponding widths and lengths of the devices are synthesized in fig. 4.6. Table 4.3 summarised the parameters retrieved from fig. 4.6. We will go into the details of the different sample types in the next section.

At first sight, the three widest wires exhibit a sharp transition toward zero resistance,

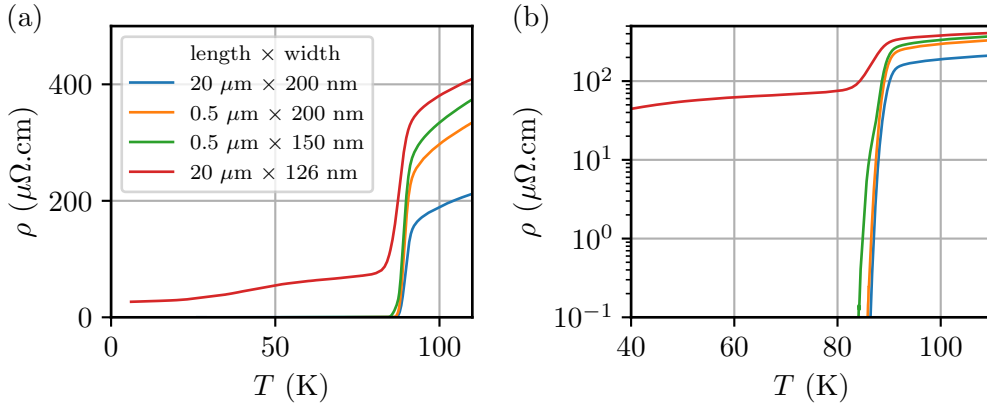


Figure 4.6 – Temperature evolution of the resistivity in (a) linear and (b) log scales, of superconducting nanowires patterned on 30 nm YBCO thick films with $D = 3 \text{ O}^+ \cdot \text{nm}^{-2}$.

Table 4.3 – Summary of the device dimensions and the parameters extracted from fig. 4.6.

Length (μm)	Width (nm)	T_{c0} (K)	T_{cm} (K)	$\rho(100\text{K})$ ($\mu\Omega \cdot \text{cm}$)
20	200	85.7	89.7	190
0.5	200	85.5	89.2	297
0.5	150	83.8	89.0	334
20	126	0	87.8	380

with a small kink for the 150 nm wide wire (green curve). It results for those three wires that T_{c0} and T_{cm} are almost unchanged with respect to the raw film. For the 126 nm wide wire, a large foot appears in the transition: there is no longer a complete superconducting path to obtain zero resistivity. The appearance of a foot in the transition is interpreted as a defect along the wire such as a grain boundary, a dislocation, or a crystal twin boundary. If the ion irradiation process was involved, as it is a 20 μm -long nanowire the effect of irradiation should be the same all along the wire. It would then result in a large RT transition with high resistivity, but this is not observed. We stress that there is no contribution of the superconducting electrodes to the resistance, but only that of the nanowire itself. Though, only one specific part of the device is deteriorated but not the whole nanowire. Typically, the width of 100 nm is the limit width that we have successfully patterned with preserved superconducting properties. Nevertheless, we have less chance to find undamaged superconducting wire at this narrowest width: the fabrication yield is reduced. At fixed width, assuming that defects are disseminated randomly onto the sample, the probability to encounter a defect along the wire linearly increases with the length. Therefore, the fabrication yield is improved by shortening the wire.

In the long-term perspective for detection application purposes, it is required that the superconducting nanowire extends along hundreds of micron length in a meander shape to raise the detection area. As we shall see in section 4.4, we successfully fabricated meandered shape nanowire down to 100 nm width on a 450 μm length. However, the narrowest long wires presented in fig. 4.6 has a foot in the RT transition which could extend from a few kelvins to 10 K. The foot appearance tells us that one part along the wire is damaged and it exhibits reduced superconducting properties or a normal behavior. As j_c is set by the smallest superconducting cross-section along the wire, the potential study of SSPD is restrained. Indeed, in order to operate properly an SSPD needs to be current biased near the critical current. If inhomogeneities are present along the nanowire, only a restricted part of the device will be current biased near j_c and could detect photons. Therefore, from the perspective of a proof of concept, we may expect better superconducting properties for a shorter nanowire. Especially, the critical current distribution in the wire has more chance to be homogeneous all along the wire. Hence, we have focused our research on 500 nm long nanowire to investigate the intrinsic physical properties of high-quality nanowires at a cost of a smaller detection area.

In conclusion, data presented in fig. 4.6 and table 4.3 are far more encouraging than He^+ FIB results. We obtain undamaged superconductivity with lateral dimension lower by one order of magnitude with respect to He^+ FIB patterned wires. Then we concentrate our efforts to the latter O^+ irradiation process which gives the narrowest superconducting nanowires.

4.2.4 Origin of the chip

In this section, we check the robustness of our fabrication workflow on different chips by studying the superconducting properties of the devices. As mentioned in chapter 3, the YBCO thin films originate from various deposition processes and layers stack. We recall that N and CS samples are both Ceraco thin films. The N type samples are fully capped by a CeO_2 layer, while the CS samples are protected by a CeO_2 disk on the center of the chip. T samples and JS samples are grown at the Unité Mixte de Physique CNRS/Thales (UMPhy) by J. Briatico: they are respectively fully capped by PBCO and protected by CeO_2 like CS samples (see appendix B for further details). N samples were the first to be fabricated, we upgraded them to the CS type samples. In parallel, we collaborated with J. Briatico to pattern YBCO devices on STO substrate with the T samples. When CeO_2 disk protection has proven its worth on Ceraco film, J. Briatico successfully adapted his

deposition equipment to master the CeO₂ disk protecting method on STO. In this section, we compare the superconducting properties extracted from ρT curves by gathering 155 devices of various widths, lengths, thicknesses, and protecting capping layer.

Figure 4.7 shows the estimate of $\rho(100\text{ K})$ as a function of the device width, while fig. 4.8 presents T_{c0} with respect to the width. Each class of data points presented may contain one or several chips.

If we look first at the left hand side panel representing the 30 nm thick samples, we notice an important dispersion of the N samples data points, both in terms of T_{c0} and resistivity at 100 K. The superconducting properties change significantly from a device to another. On top of that, T_{c0} is often reduced by a dozen of kelvins when approaching the 100 nm width limit. It is mainly due to the fact that we patterned meanders and 20 μm long wires which are more prone to be damaged in terms of T_{c0} due to defects. Many devices of the N samples could not be measured correctly due to poor contact resistance about 100 k Ω . We attributed it to the fabrication process of depositing Au layer *ex-situ*

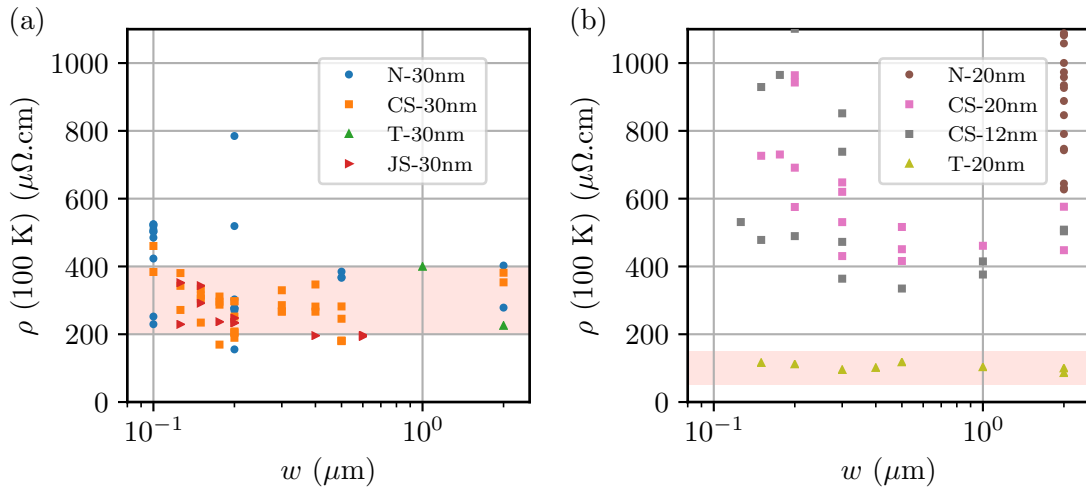


Figure 4.7 – Evolution of $\rho(100\text{K})$ with respect to the width of the device for 30 nm thick samples (a), and samples with thinner thicknesses (b).

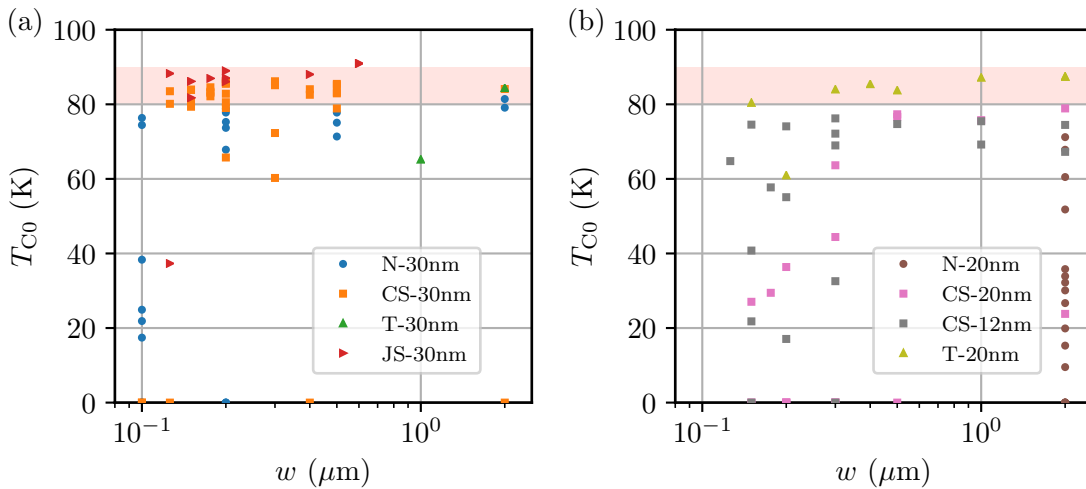


Figure 4.8 – Evolution of T_{c0} with respect to the width of the device for 30 nm thick samples (a), and samples with thinner thicknesses (b).

after the Ar^+ ion beam etching of the CeO_2 capping layer. This led us to the CS type samples.

The new protecting method involved in CS samples ensures ohmic contact resistances between YBCO and Au layers, thanks to the fact that the latter is deposited *in situ*, just after the CeO_2 protecting layer. While the dispersion in $\rho(100\text{K})$ still exists, it only spreads over $200 \mu\Omega\cdot\text{cm}$ in the orange area. It makes this technique more reliable than the N type process. We also stress that the narrowest superconducting wires have a T_{c0} lowered by only a few kelvin compared with the $2 \mu\text{m}$ wide devices, and most of the CS nanowires have a reasonable T_{c0} higher than 80 K. In addition, it is worth noting that three different CS chips, from two different batches, give the same results. We will see later in section 4.3 that it is not restricted to the ρT measurements. Their superconducting properties are also kept for months, and even for a year. These observations are strong arguments demonstrating the robustness of the YBCO films against oxygen diffusion and ageing. In conclusion, the reproducibility of high-quality nanowires with CeO_2 disk protection is mastered and sustainable with O^+ irradiation process on 30 nm thick YBCO films.

For the T type sample, the fabrication process damaged the superconducting properties when Ti/Au layers were deposited making this technique unreliable.

In contrast, the fabrication on 30 nm thick JS type samples is a clear success. As we see in the figures, the devices are competing with the best devices obtained on CS type samples in terms of resistivity and T_{c0} , which are globally better by a few kelvins. These results confirm that the ion irradiation technique combined with CeO_2 capping disk is suitable for different sample origins on distinct substrates. Finally, what really matters to obtain good YBCO superconducting nanowires is high-quality raw thin films stable with respect to the ageing.

In view of SSPD application, the wire cross-section is a key parameter to reduce as low as possible. It helps to confine the hotspot on a reduced volume such that a single photon absorbed by the device triggers a voltage pulse. For this purpose we also try to fabricate devices on chips whose thicknesses are lower than 30 nm. The right hand side panels of fig. 4.7 and fig. 4.8 show the same superconducting quantities, $\rho(100\text{K})$ and T_{c0} respectively, for thinner samples.

Unlike the width that we can control thanks to the EBL, we do not deposit YBCO thin films by ourself. Thus, we are completely dependent on our collaborators to reduce the YBCO thickness. Ceraco has made significant efforts to provide us sub 30 nm thick samples of thicknesses of 10 nm, 12 nm, 15 nm and 20 nm. The measurements of sub 30 nm thick N type samples are poorly engaging. Especially N-12 nm and N-15 nm are omitted in the figures because they have never presented any superconducting transition, whatever the fabrication steps. This means that most of the raw thin films have been damaged from the early beginning. Various explanations can be considered. As the thickness is reduced, we have less flexibility to etch the CeO_2 layer, the etching must be stopped at a precise depth prior to impacting the superconducting properties. This is a difficult task to do without fail. In addition, some of the raw thin films, which have never been processed in cleanroom facility, do not show any superconducting behavior. They seem to be really sensitive to environment. In conclusion, it is hard to tell whether the nanofabrication damages superconductivity, or the films are intrinsically unstable. It is probably a combination of both reasons.

Be that as it may, the CS protecting method was also used to grow batches of YBCO thin films of 20 nm and 12 nm thicknesses. In this case, superconducting transition is observed for both thicknesses, before and after the ion irradiation. The resistivity is twice higher than the 30 nm thick devices at best and it increases significantly as w is reduced. The corresponding T_{c0} are rather disappointing and drop dramatically when the wire becomes narrower. Here, the limiting width below which T_{c0} falls is about 500 nm. Even

if we divide the thickness by almost a factor 3 for the 12 nm thick wires, the minimum width is 5 times wider than the 30 nm thick films ones. We do not gain much in terms of the overall cross-section. If we only consider the devices whose width are equal or lower to 500 nm, the fabrication yield to preserve a superconducting path - meaning $T_{c0} > 0$ K - is about 63%. In addition for all the different widths, and especially for the narrowest nanowires ($w \leq 300$ nm), the critical temperatures are significantly dispersed. Nevertheless, we have successfully patterned nanowires down to a 150 nm in width on CS-12 nm samples with $T_{c0} \approx 75$ K. Such a device is reliable and can be used in subsequent experiments to study the physics of irradiated YBCO nanowires. To summarize, even if the patterning may affect T_{c0} , we will see in section 4.3 that the superconducting properties retrieved from the IV curves are encouraging. Therefore, we will explore the properties of the best devices of the CS-12 nm sample.

The measurements of T-20 nm sample is really encouraging. Here, all the measured wires are 20 μm long. Their corresponding resistivity at 100 K is about 100 $\mu\Omega\cdot\text{cm}$, which is the lowest values regardless of the thickness and it does not vary so much for smaller width. In addition, except for the pathologic 200 nm wide nanowire, T_{c0} is only reduced by a few kelvins with respect to $T_{c0}^{\text{raw}} = 88.9$ K of the raw film prior to clean room processes. These results allow us to serenely foresee the possibility to fabricate nanowires on thinner films with the collaboration of J. Briatico.

In this subsection, we gave a detailed overview of all the samples fabricated by O^+ irradiation through to the RT measurements. We demonstrated that nanowires on YBCO thin films present high-quality superconducting properties thanks to the CeO_2 disk protection. From now on, we focus our efforts to the promising devices whose T_{c0} is unchanged or slightly reduced. That being said, we discard the following samples: T-30nm, N-20nm, CS-20nm. In the next sections and chapters, we will explore in more details the physical properties of the high quality devices.

4.3 Current voltage characteristics

In the following section, we present the IV measurement performed on several nanowires of different types and dimensions. It is a complementary test to the RT measurement to assess the devices quality. Depending on the critical current density j_c , we classify the IV curves in two categories. For low j_c value, the voltage drops grows continuously to the ohmic state. When j_c is large enough, a hysteresis develops due to Joule heating. We then investigate the temperature evolution of specific current densities using different theoretical models.

4.3.1 General description

The current voltage (IV) curve is a standard way to characterize an electrical component. It provides precious information about the behavior and the potential of single photon detection of the superconducting nanowires. We employ the same electrical circuit presented in fig. 4.3(a) to measure IV curves. At fixed temperature, the current I is incremented by a current step δI each 100 ms and the corresponding voltage drop V is registered for each current value. δI might be either positive or negative, the resulting IV curves are mentioned as up and down respectively.

Regardless of the device geometry, the nanowire current density j is computed with respect to its superconducting cross-section $A = wd$ along its length as $j = I/(wd)$. In the whole dissertation, the width and the length are estimated from the EBL which overestimates them. When we discuss about current values, it is important to keep in mind that I is a measured value, whereas j is an estimate thanks to geometric parameters. The

latter are known with a precision about a few percent to dozens percent for the narrowest wire. As a consequence, j is estimated at 1% precision at best, but it is likely to be underestimated. The IV curves are converted into jV curves in order to compare the current density values all together and with respect to characteristic values such as j_d .

Figure 4.9 shows a set of typical current density voltage (jV) characteristics at 10 K measured up and down for two different 500 nm long 300 nm wide wires. Only the thickness of the YBCO thin films is varying: it has a thickness of 30 nm for the jV curves in green and red colors and only of 12 nm for the jV curves in blue and orange colors. The latter curves completely collapse together, no matter the δI sign. When I raises starting from 0 A, the nanowire is in the superconducting state: voltage drop remains zero. Then, the Cooper pairs density is progressively reduced until a voltage drop appears, the corresponding current density is called the critical current density j_c . Afterwards, V increases relatively quickly up to 1 mV, while the slope becomes gentler. The voltage range [0 mV, 1 mV] corresponds to the flux creep regime in which vortex motion is thermally activated. This phenomenon will be dealt with in greater details in chapter 5. For $V > 1$ mV, the nanowire is in the linear flux flow regime: the voltage is almost proportional to the current. By continuity it goes to the ohmic resistive state in which the voltage is also linear with respect to the current. The constant slope corresponds to a 5.0 k Ω dynamic resistance ($R_d = dV/dI$) comparable to the 6.6 k Ω normal resistance value measured at 100 K with RT measurement. We conclude that in the high voltage branch, the whole device is in the normal state with a simple ohmic behavior.

The other set of jV curves on 30 nm thick YBCO thin films is rather different. It exhibits a large hysteresis between the up and the down curves. For $V < 1$ mV, we observe the same behavior than the previous device, as depicted by fig. 4.9(b): a rapid increase of the voltage while current is slowly changing. When current increases, an abrupt large voltage switch appears, higher than 1 V. The corresponding current density and voltage are respectively the switching current density j_s and the switching voltage V_s . When j lowers, the curve presents an almost constant slope of 2.0 k Ω , which is three

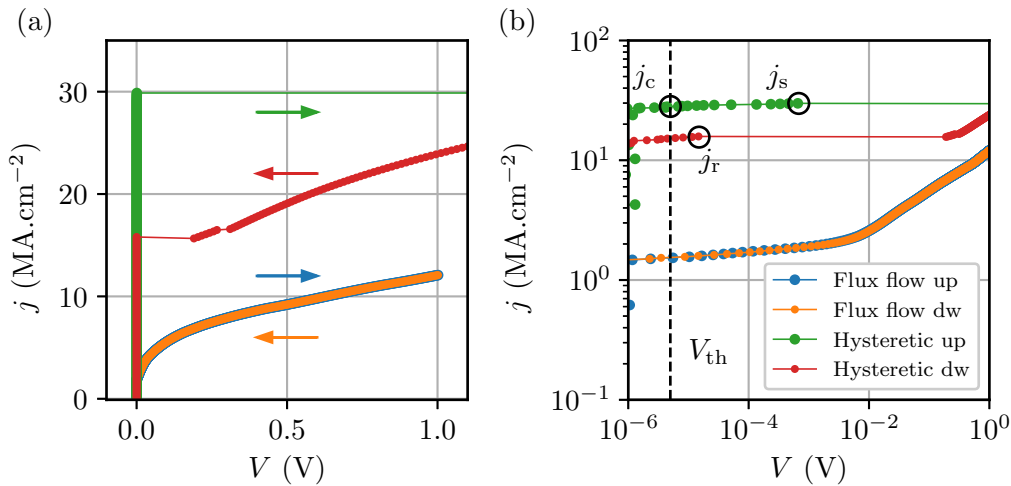


Figure 4.9 – jV curves measured at 10 K in linear scale (a), and log scale (b), with the up and down ramps for two 500 nm long wires. The blue ($\delta I > 0$) and orange ($\delta I < 0$) curves correspond to A7, a 300 nm wide nanowire patterned on a 12 nm thick film of CS types. It exhibits a linear flux flow regime at high voltage. The green ($\delta I > 0$) and red ($\delta I < 0$) curves correspond to a C8, a 200 nm wide nanowire patterned on a 30 nm thick film of CS types. It presents a large hysteresis.

times higher than the 0.73 k Ω resistance measured at 100 K in the RT curve. The Joule heating power in the high voltage branch is about 2 mW and located in the small volume of the YBCO nanowires. Thus, the temperature inside the nanowire might be rather hot resulting in a higher resistance value. Here, the nanowire cannot go back directly to the superconducting state due to the local Joule effect sustaining a large hot zone. An argument going to this direction is the fact that when the nanowire goes to the normal state, the temperature measured on the sample holder increases suddenly by 10 mK. For j low enough, the nanowire goes back to a steep slope regime, similar to the flux creep regime, with an abrupt voltage switch of hundreds millivolts. The related current density is denoted by j_r , as the return or retrapping current density equivalently. This result is the signature of a thermal runaway which drives rapidly the nanowire to the normal state as soon as a millivolt voltage drop develops.

Experimentally, we estimate j_c as the current density for which voltage overpasses a voltage threshold V_{th} . The threshold is chosen higher than the voltage noise in the superconducting state, which is about 5 μ V, as shown by the dashed line in fig. 4.9(b). We estimate numerically j_s and j_r by extracting the current density corresponding to the larger voltage difference dV for the up and down jV curves respectively. Table 4.4 summarizes different parameters extracted from the RT curve and the jV curve for both nanowires presented previously.

Table 4.4 – Parameters extracted from jV curves presented in fig. 4.9 at 10 K and the corresponding RT curves of the devices.

Device	d (nm)	$R_N(100\text{ K})$ (k Ω)	R_d (k Ω)	I_c (mA)	j_c (MA.cm $^{-2}$)	j_r (MA.cm $^{-2}$)	j_r (MA.cm $^{-2}$)
A7	12	6.7	5	0.037	1.6	-	-
C8	30	0.73	2	1.7	28	30	16

In the light of the estimate of $j_d \approx 125$ MA.cm $^{-2}$, the critical current density for 30 nm thick nanowire in table 4.4 represents 0.22 j_d . This experimental achievement is very encouraging toward the possibility of single photon detection with regard to the discussion in section 2.3.5. Nevertheless, the jV curve on its own does not tell much about the physical phenomenon involved in the voltage switch, neither whether single photon could be detected. In order to investigate those important aspects, we will present in chapter 6 a more extensive experimental study on the switching mechanism, while the single photon detection experiment will be presented within chapter 5.

4.3.2 Hysteresis and flux flow behaviors

In the previous section, we only inspected specific devices in order to get a brief overview of the physical phenomena involved in the superconducting YBCO nanowires. Figure 4.10 shows j_c values extracted from jV curves measured on 69 distinct devices at 5 K to adopt a global approach and to demonstrate the reliability of our fabrication process.¹ Like the superconducting properties extracted from RT data, the estimate of j_c is a precious parameter characterizing the quality of the device. It helps to chose devices of interest for further investigations, especially the ones with high critical current density. In addition, it allows us to validate the nanofabrication process on the thin films used in this thesis.

First of all, a high critical current goes along with preserved superconducting properties in the RT measurement as reported in section 4.2. The devices fabricated on CS-30nm,

¹For clarity, the pathological nanowires, those which are not superconducting or that present important damaged properties with respect to the pristine film, have been pulled out of the data set.

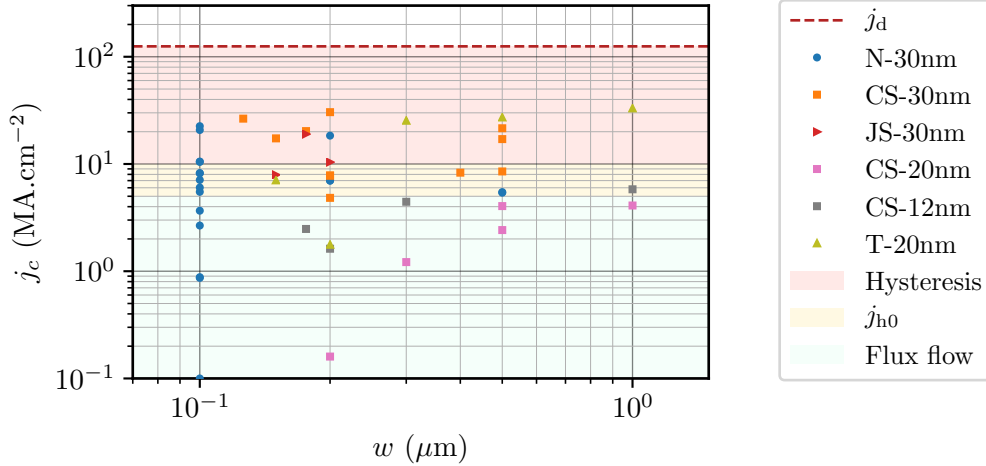


Figure 4.10 – Evolution of j_c extracted from jV curves at 5 K with respect to the nanowire width for different sample types and thicknesses. The red dashed line represents the theoretical depairing current density estimated to 126 MA.cm^{-2} . The yellow area is the healing current density $j_h \approx 5 - 10 \text{ MA.cm}^{-2}$ above which hysteresis appears.

JS-30nm and T-20nm samples have the best superconducting properties. The N-30nm samples have moderate j_c with some devices presenting a voltage switch in the millivolt range at 4 K. Finally, almost all the sub 30 nm thick CS samples exhibit a flux creep followed by a flux flow behavior at sufficiently high voltage. We have successfully fabricated several nanowires with a j_c higher than 10% of j_d , for widths down to 100 nm. The j_c values demonstrate the high quality of the patterned devices, even for the narrowest devices, but the limit width is reached about 100 nm.

Depending on the j_c values, we can separate out devices in two superconducting nanowires subclasses: devices which have flux flow behavior at large voltage in the mint green area, and devices with hysteretic IV curves in the red zone in fig. 4.10. Through the many different measured nanowires, we confirmed the experimental results observed by Arpaia *et al.* [10] that for $j_c < 5 - 10 \text{ MA.cm}^{-2}$, nanowires go smoothly to the normal state, while for $j_c > 5 - 10 \text{ MA.cm}^{-2}$, wires present a hysteretic IV curve with a voltage switch. We observe a similar distinction in our ion irradiated YBCO nanowires, for the same range of current densities. In addition, it is worth noting that similar hysteretic behavior has also been reported in under-doped YBCO nanowires by Andersson *et al.* [80].

We account for this crossover current density using the thermal model developed by Skocpol, Beasley, and Tinkham [45]. The Skocpol Beasley Tinkham (SBT) model [45] is widely used to model the self-heating of superconducting nanowires in both LTS [242–244] and HTS [223, 245] materials. In the original article [45], Skocpol, Beasley, and Tinkham have considered a 1D wire of thickness d , width w , and length l .² Figure 4.11 schematizes such a nanowire with a normal hot part of length $2y_0$ in the bridge center under a current flow I . Depending on the bridge thermal properties and the wire dimensions, the normal region is sustained by the Joule heating or dissipated thanks to the combination of the heat conduction *via* the superconducting thin film and the heat transfer through the substrate. According to the model, the temperature evolution $T(y)$ along the bridge writes:

²Here, the one-dimensional feature has to be considered in the sense of the thermal properties and not the superconducting properties. Both width and thickness are supposed to be smaller than the characteristic thermal length. In other words, it assumes that temperature is homogeneous in a complete cross-section at a given y position.

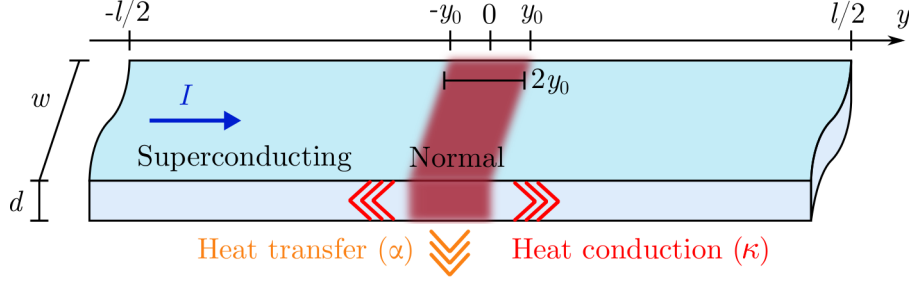


Figure 4.11 – Schematics of a bias current wire in the framework of the SBT thermal model. A normal hot region of length $2y_0$ along y -axis transfers thermal energy laterally to the superconducting wire *via* heat conduction κ , and through the substrate due to heat transfer α . Depending on the values of α and κ , the hot region either expands or self-heals.

$$-\kappa_n \frac{d^2 T}{dy^2} + \frac{\alpha}{d}(T - T_b) = \left(\frac{I}{wd}\right)^2 \rho \quad (|y| < y_0) \quad (4.8a)$$

$$-\kappa_s \frac{d^2 T}{dy^2} + \frac{\alpha}{d}(T - T_b) = 0 \quad (|y| > y_0) \quad (4.8b)$$

where κ_n and κ_s are the thermal conductivity in the normal and the superconducting state respectively, ρ is the film resistivity, T_b is the bath temperature, and α is the thermal conductance per unit area. For the normal region, the right hand side term of eq. (4.8a) is the Joule heating. In the left hand side of eqs. (4.8a) and (4.8b), the first term corresponds to the heat conduction through the normal and the superconducting part of the wire respectively, while the second term represents the heat transfer through the substrate. As a first approach, assuming that $\kappa = \kappa_s = \kappa_n$, the balance between those terms naturally brings the characteristic thermal length η_h , also called healing length, and given by:

$$\eta_h = \sqrt{\frac{\kappa d}{\alpha}} \quad (4.9)$$

For $l > \eta_h$, heat is mostly dissipated through the substrate and the normal zone is restricted to the bridge. In the case of $l < \eta_h$, the heat transport through the superconducting thin film dominates, thus the hotspot spreads in the superconducting leads. As a consequence, the solutions are different depending on the length l compare to η_h . Thus, it is of particular importance to estimate η_h . For YBCO thin film on sapphire substrate $\alpha \approx 1 \times 10^7 \text{ W.K}^{-1}.\text{m}^{-2}$ [246]. According to experimental measurements of the thermal conductivity, $\kappa_n \approx 3 \text{ W.K}^{-1}.\text{m}^{-1}$ for polycrystalline YBCO in optimal doping at 100 K [247]. In addition, the Wiedemann-Franz law separately estimates κ_n at a given temperature T thanks to the resistivity as follows:

$$\mathcal{L} = \frac{\kappa_n \rho}{T} = \frac{1}{3} \left(\frac{\pi k_B}{e} \right)^2 = 2.44 \times 10^{-8} \text{ W}.\Omega.\text{K}^{-2} \quad (4.10)$$

where \mathcal{L} is the Lorenz number. Using $\rho(100 \text{ K}) = 300 \mu\Omega.\text{cm}$, we estimate thanks to eq. (4.10) that $\kappa = 0.8 \text{ W.K}^{-1}.\text{m}^{-1}$. By using this two limit values for the thermal conductivity, according to eq. (4.9), the healing length in 30 nm thick YBCO film could be roughly estimated as $\eta_h \approx 50 - 100 \text{ nm}$. In our case, the nanowires are always longer than the estimated healing length while their width is of the same order of magnitude or larger than the healing length. For long bridges $l \gg \eta_h$, assuming that the temperatures at its ends equal the bath temperature and that T and $\kappa(dT/dy)$ are continuous at the

normal-superconducting interface, the current flow required to sustain a static hotspot writes [45]:

$$I_h(y_0) = \sqrt{\frac{\alpha w^2 d (T_c - T_b)}{\rho} \left[1 + \left(\frac{\kappa_s}{\kappa_n} \right) \coth \left(\frac{y_0}{\eta_N} \right) \coth \left(\frac{L}{2\eta_S} - \frac{y_0}{\eta_S} \right) \right]} \quad (4.11)$$

Using the Ohm's law, it follows that the corresponding voltage drop along the wire is simply:

$$V_h(y_0) = \frac{2y_0 \rho I_h(y_0)}{wd} \quad (4.12)$$

The parametric curve described by eqs. (4.11) and (4.12) corresponds to the healing curve. They are set by the thermal properties and the dimensions of the superconducting nanowire. For a given voltage, if the current lies below the healing current I_h , the working point in the IVC is stable because the hotspot vanishes thanks to the thermal exchange: the wire is self-healed. For current higher than I_h , the thermal exchange is not sufficient and the device rapidly self-heats. The device cannot relax back to the equilibrium state, it results that the hotspot remains. Therefore, the appearance of a hysteresis in the IVC is mainly set by the ability of maintaining a non zero voltage drop without creating a hotspot or not.

Figure 4.12 shows the $I_h V_h$ with the hysteretic IV curve at 66 K of C8 a 30 nm thick 500 nm long 200 nm wide wire. To simulate the $I_h V_h$ characteristic, we use the parameters extracted from the ρT curve: $\rho(100 \text{ K}) = 300 \mu\Omega \cdot \text{cm}$ and $T_{c0} = 86.1 \text{ K}$. We then adjust the surface heat transfer coefficient α and thermal conductivity κ such that the simulated curve crosses the retrapping and the switching data points. With such simulations, we estimate that $\alpha = 2.6 \times 10^7 \text{ W} \cdot \text{K}^{-1} \cdot \text{m}^{-2}$ and taking $\kappa = \kappa_s = \kappa_n$ for the sake of simplicity, we estimate $\kappa = 1.6 \text{ W} \cdot \text{K}^{-1} \cdot \text{m}^{-1}$. In this case we obtain a healing current density $j_{h0} \approx 11 \text{ MA} \cdot \text{cm}^{-2}$. At first it is worth noting that the estimated thermal parameters are within the same order of magnitude to the value given previously.

According to the SBT simulations presented in fig. 4.12, the low voltage branch diverges at zero voltage, while the high branch increases almost linearly. It follows that higher is

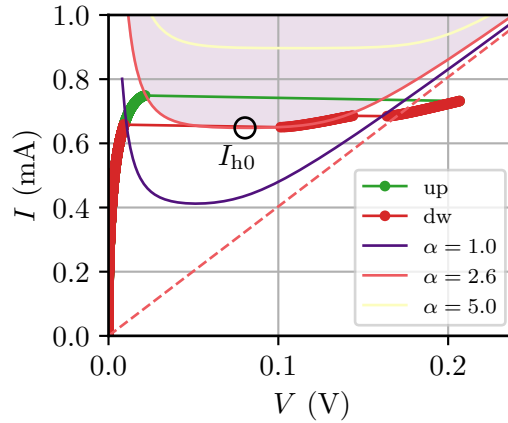


Figure 4.12 – IV curves of C8, a 30 nm thick 500 nm long 200 nm wide nanowire described by the SBT self-heating model in linear scale at 66 K. The solid lines are simulations of the $I_h V_h$ parametric curves given by eqs. (4.11) and (4.12). We set different values of α displayed in the legend in units of $10^7 \text{ W} \cdot \text{K}^{-1} \cdot \text{m}^{-2}$, and $\kappa = 1.6 \text{ W} \cdot \text{K}^{-1} \cdot \text{m}^{-1}$. The pink area defines the zone in which the device is thermally unstable for $\alpha = 2.6 \times 10^7 \text{ W} \cdot \text{K}^{-1} \cdot \text{m}^{-2}$, while the corresponding minimum healing current I_{h0} is highlighted by the black circle. The dashed line is the asymptote line of the ohmic state in the SBT simulation.

the j_c , larger the voltage switch V_s should be. The healing current density j_h is first set by the critical current density value, and then by the thermal properties when the voltage drop appears and reaches the unstable area in IV curve. Figure 4.12 illustrates that the healing curve varies with the thermal properties as α changes keeping κ constant.

Another supporting argument toward the SBT model lies in fig. 4.13. Several jV curves have been measured at various temperatures below T_c for C10, a nanowire whose j_c is approaching j_{h0} at 5 K. The nanowire presents a combination of flux creep followed by a flux flow behavior in the whole temperature range, except at 5 K, for which a small 0.6 mV voltage switch appears. As we will see in section 4.3.3, the healing current density has a different temperature dependence than the critical current density. Thus, the hysteresis appears at a lower temperature T_H as soon as $j_c > j_{h0}$. Following the same calculation in the framework of the SBT model for this specific device by taking $\rho = 852 \mu\Omega.\text{cm}$ and $T_{c0} = 68.0 \text{ K}$, we estimate $\eta_h \approx 30 - 60 \text{ nm} \ll w, l$ and $j_{h0} \approx 13 \text{ MA.cm}^{-2}$. In this case j_{h0} is overestimated by a factor 3, with respect to the j_c value in which voltage switch is appearing.

If we go back to fig. 4.12 Schematically, the self-heating $I_h V_h$ characteristic delimits the appearance of a hysteresis. When the current is ramped up such that $I(V) < I_h(V_h)$, the Joule heating is absorbed by the substrate and the superconducting thin film. Once $I(V) > I_h(V_h)$, *i.e.* the $I(V)$ points lie in the pink area, the hotspot spreads rapidly all along the wire and turns the wire to the normal state. In a voltage bias experiment, such as the one performed by Skoepol *et al.* [45], the IV curve would have follow the self-heating curve identified by the black line. When the current is ramped down, the device stays in the normal state due to the self-heating until the current becomes sufficiently small for the hotspot to dissipate excess heat. It then returns to the superconducting regime for I smaller than the minimal healing current I_{h0} . Here, I_{h0} corresponds to I_r in the IV measurement. The high voltage branch in the model coincides asymptotically to the normal ohmic state represented by a dashed line. In theory, the IV data should follow this branch while ramping up the current after the voltage switch. The quantitative mismatch for $V > 0.15 \text{ V}$ comes from the triangle shape electrodes connecting our nanowires, which adds a resistance contribution and thus a voltage drop in comparison with the SBT model. Nonetheless, the self-heating SBT simulation collapses with the returning voltage branch

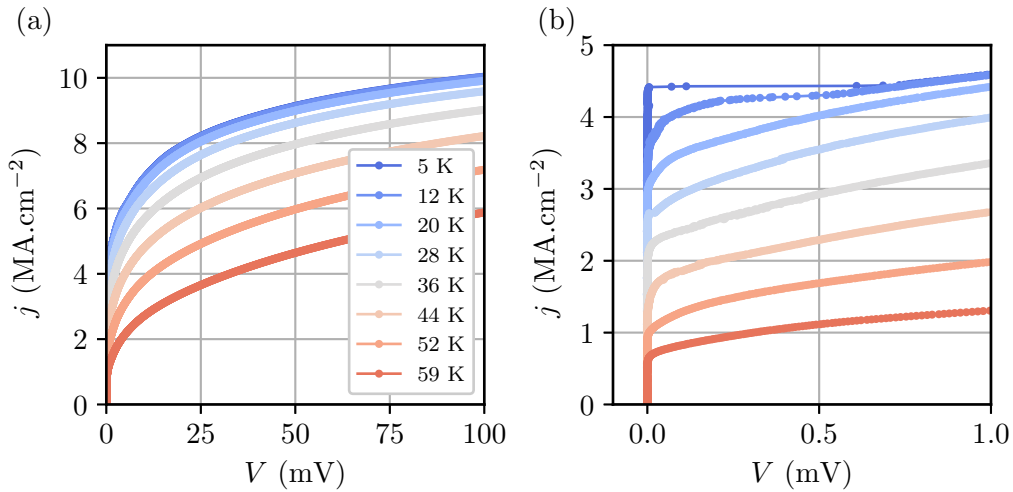


Figure 4.13 – jV curves of C10, a 12 nm thick 500 nm long 300 nm wide nanowire at different temperatures. (b) is a zoom of (a) which highlights the appearance of the voltage switch at 5 K.

for $V \in [0.1 \text{ V}, 0.15 \text{ V}]$ and allows us to estimate roughly the retrapping current I_r for the hotspot to vanish.

Despite the fact that the model does not predict exactly the j_c value limiting the two IV behaviors, it explains qualitatively well why a hysteresis appears in terms of thermal transfers. On the other hand, it does not give information about the mechanism driving the wire out of the superconducting state to the flux regime, neither the event which triggers the voltage switch. We will cover the latter aspect in chapter 6.

4.3.3 Influence of temperature

We are now interested in the influence of temperature on the characteristic current densities. Figure 4.14 shows the temperature evolution of the critical current density, the switching current density and the retrapping current density extracted from hysteretic IV curves of C8, a 500 nm long 200 nm wide 30 nm thick wire. We have also added the current density extension of the hysteresis loop defined as $\Delta j = j_s - j_r$. As temperature decreases below $T_{c0} = 86.1 \text{ K}$, the supercurrent appears and j_c raises monotonically down to low temperatures. Below $T_H = 78 \text{ K}$, the hysteresis loop starts, both j_s and j_r increase, and simultaneously Δj raises, *i.e.* the hysteresis progressively enlarges. For $T = 20 \text{ K}$, j_s and j_r are almost saturating and do not evolve significantly, while j_c is still increasing.

In the following we will study the different temperature dependencies of the current densities since they arise from different physical phenomena. The critical current evolution gives information about the physical mechanism that limits it. The switching current is due to instability that triggers the formation of a hotspot area and drives the nanowire to the normal state by a thermal runaway, as we will see in chapter 6. While the return current dependence provides information about the cooling of the system when the nanowire goes back to the superconducting state.

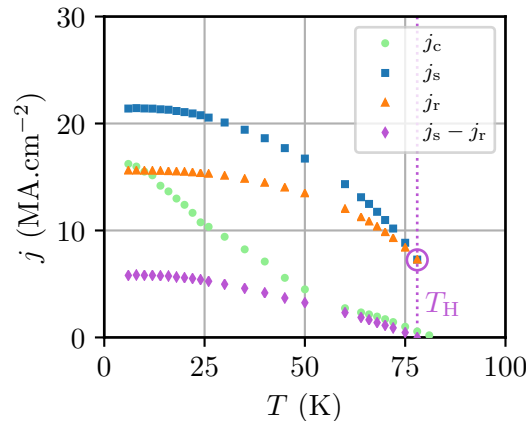


Figure 4.14 – Temperature evolution of four characteristic current densities: the critical current density j_c , the switching current density j_s , the returning current density j_r , and the current density extension of the hysteresis $\Delta j = j_s - j_r$ for C8, a 30 nm thick 500 nm long 200 nm wide nanowire. T_H highlights the hysteresis temperature T_H below which the hysteresis appears.

4.3.3.1 Retrapping current evolution

We first continue the analysis of the retrapping current temperature evolution using the self-heating SBT model [45] introduced in section 4.3.2 for C8, a 30 nm thick 500 nm long 200 nm wide nanowire. According to the model, j_r is interpreted as the minimum

healing current j_{h0} . We estimate j_{h0} numerically as the minimum current density using eq. (4.11) for y_0 ranging from 1 nm to 250 nm at several temperatures below T_{c0} . Once again, the resistivity and the critical temperature are taken from ρT curve which give $\rho(100\text{ K}) = 300\ \mu\Omega.\text{cm}$ and $T_{c0} = 86.1\text{ K}$ respectively. As in the previous section, we use $\kappa = \kappa_s = \kappa_n = 1.6\text{ W.K}^{-1}.\text{m}^{-1}$. Under such assumptions, $\eta_h = \eta_S = \eta_N = 67\text{ nm}$ is smaller than the total wire length of 500 nm such that the healing current expression in eq. (4.11) for long bridge is valid.

Figure 4.15(a) displays the evolution of j_r with temperature along with the thermal SBT simulation of j_{h0} for various values of the surface heat transfer coefficient. $\alpha = 1.10^7\text{ W.K}^{-1}.\text{m}^{-2}$ is taken from the literature [246], it underestimates the retrapping current, but the order of magnitude is in fair agreement with the data. We set $\alpha = 1.2 \times 10^7\text{ W.K}^{-1}.\text{m}^{-2}$ such that the simulation matches with the data at both temperature ends. In this case, the temperature evolution is not well described by the simulation. At last, we use $\alpha = 2.6 \times 10^7\text{ W.K}^{-1}.\text{m}^{-2}$, which is three times larger than the value in the literature. Obviously, the simulation matches the data from T_H down to 60 K including the data at 66 K presented previously in figure fig. 4.12. For lower temperatures, the model overestimates j_r by 50% at zero temperature.

In the simulation, we made the crude assumption that α and κ are constant on the whole temperature range. In practice, it is particularly erroneous. We refine the simulation by using a temperature dependent thermal conductance. The thermal conductance α is mostly set by the phonons, as temperature is lowered, the phonons wavelength enlarges resulting in an acoustic impedance mismatch at the interface [248, 249]. It implies that surface heat transfer is reduced at low temperature. For YBCO films grown on a sapphire substrate, Nahum *et al.* [247] estimate the thermal boundary resistance $R_b = 1/\alpha$ thanks to the acoustic mismatch model as follows:

$$R_b = A + \frac{B}{T^3} \quad (4.13)$$

where $A \approx 10^{-7}\text{ K.m}^2.\text{W}^{-1}$ and $B \approx 17 \times 10^{-4}\text{ K}^4.\text{m}^2.\text{W}^{-1}$ in their specific case. By equalizing the two terms in eq. (4.13) the crossover temperature $T_{\text{pm}} = \sqrt[3]{B/A}$ naturally arises. It delimits the temperature below which phonon mismatch has to be considered.

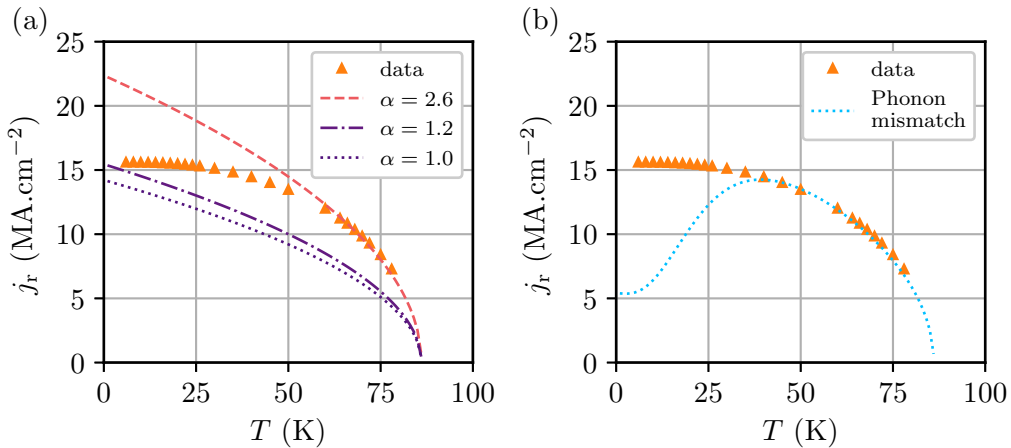


Figure 4.15 – Temperature evolution of the returning current density of C8, a 30 nm thick 500 nm long 200 nm wide nanowire presented in fig. 4.14. The lines in (a) and (b) correspond to simulations of the healing current density respectively for different values of the surface heat transfer α ($10^7\text{ W.K}^{-1}.\text{m}^{-2}$), and for a temperature dependent $\alpha(T)$ using the phonon mismatch model.

We try to adapt eq. (4.13) to our case. A represents $1/\alpha$ at high temperature, though we set $1/A = 2.6 \times 10^7 \text{ W.K}^{-1}$ and $B = 9 \times 10^{-4} \text{ K}^4.\text{m}^2.\text{W}^{-1}$ such that the model fit the data in a wider temperature range. The resulting curve is shown in fig. 4.15(b). Inserting the phonon mismatch temperature dependence of α helps to correctly describe the data down to 35 k. Below, the simulated healing current drops down to 5 MA.cm^{-2} at 0 K and does not match the j_r . The temperature evolution of α does not tell the whole story, but it allows us to limit the overestimation of j_r .

Now that α has been refined, κ is also likely to vary with temperature. Indeed, in optimally doped YBCO films, several experimental studies [250–252] reported the appearance of a thermal conductivity enhancement peaked about half T_c about 40-50 K. In the *ab*-plane of the YBCO crystalline structure, this κ value may vary by a factor 2-3 with respect to the value at 100 K. According to this effect, the heat transfer should be more important in the superconducting thin film, resulting in a higher j_r . If κ is higher and since α goes to zero at low temperature according to eq. (4.13), η_h enlarges drastically as temperature decreases. As η_h becomes higher than the wire length, the healing current formula does not longer hold. This consideration explains qualitatively the important discrepancy between the simulation and the results at low temperatures.

In conclusion, we interpreted the retrapping current measured in the *IV* curves as the minimum healing current in the framework of the SBT thermal model. We invoked a temperature dependent α to take account of the phonon impedance mismatch. Combined together, the models described quantitatively the temperature evolution of j_r from T_H down to 35 k. Below this temperature, the variation of the thermal properties broke the starting assumption of the SBT model $l \gg \eta_h$, making this estimate erroneous.

4.3.3.2 Critical current evolution

As discussed before, the voltage switch extent is mostly set by the value of j_c with respect to j_h , but the self-heating SBT model does not explain what limits the critical current density. We now investigate the temperature evolution of j_c to address this question. The data are fitted using four different expressions: the Bardeen formula eq. (4.14), the mean field Ginzburg-Landau model eq. (4.15), the δl pinning expression eq. (4.16), and the δT_c pinning formula eq. (4.17). Mathematically speaking, all the expressions have in common two fitting parameters, T_c and $j_c(0)$, representing the boundary on the abscissa and on the ordinate respectively. Figure 4.16 presents the simulations of the different theoretical models that will be developed hereinbelow. Either we set both parameters manually: $j_c(0)$ as the interpolation of j_c at zero temperature, and T_c as T_{cm} from *RT* measurement. Either we performed a least squares fitting of the data. The corresponding parameters are summarized in table 4.5.

The Bardeen formula is frequently used to describe the evolution of j_c with respect to temperature for LTS and also for HTS. It applies in the dirty limit $l \ll \xi_0$, provided that at least one dimension is smaller than the coherence length [253]. The critical current density is given by:

$$j_c(t) \simeq 3\sqrt{\frac{l}{\xi_0}} T_c (1 - t^2)^{3/2} \times 10^6 \text{ MA.cm}^{-2} \quad (4.14)$$

where $t = T/T_c$ is the reduced temperature. The mean free path in cuprate is $l_0 = 15 \text{ nm}$ [171–173], while the coherence length is $\xi_0 \simeq 2 \text{ nm}$. In the view of these elements, our devices are in the clean limit and all the dimensions are higher than ξ_0 . Thus, they cannot be described in the Bardeen framework as the basic assumptions are not satisfied. The Bardeen does not describe correctly the data and it would result in a critical current

density at low temperature about $j_c(0) = 578 \text{ MA.cm}^{-2}$ higher than the depairing current density $j_d = 120 \text{ MA.cm}^{-2}$.

The mean field Ginzburg-Landau model [8] corresponds to the depairing limit current when the normal cores of vortices overlap. In other words, all the superconducting material is paved by vortices spaced by the effective vortex radius approximated by ξ . Using the Ginzburg-Landau expression in the presence of a current, the order parameter is derived and then gives the theoretical depairing current density j_d . It corresponds to the maximum value of the supercurrent density expressed as $j_d(t) = (2/3)^{3/2} H_c(t)/\lambda(t)$. By replacing expression of $H_c(t)$ and $\lambda(t)$ in the Gorter-Casimir framework, it is shown that:³

$$j_d(t) = \frac{\Phi_0}{3\sqrt{3}\pi\mu_0\lambda_L(0)^2\xi_0} (1-t^2)^{3/2} (1+t^2)^{1/2} \quad (4.15)$$

where Φ_0 is the magnetic flux quantum. As a mean field approach, the formula should be only valid near T_c , and using physical parameters, as shown before, we estimate $j_d(0) = 120 \text{ MA.cm}^{-2}$. If we use such values, we clearly foresee that model will not describe correctly the data. As before, we try to model the curve with fixed parameters and with a least squares fitting method presented in fig. 4.16. The temperature evolution of j_c is even

³A complete demonstration could be found in the article written by Kunchur [254] or in Clem and Kogan article [255].

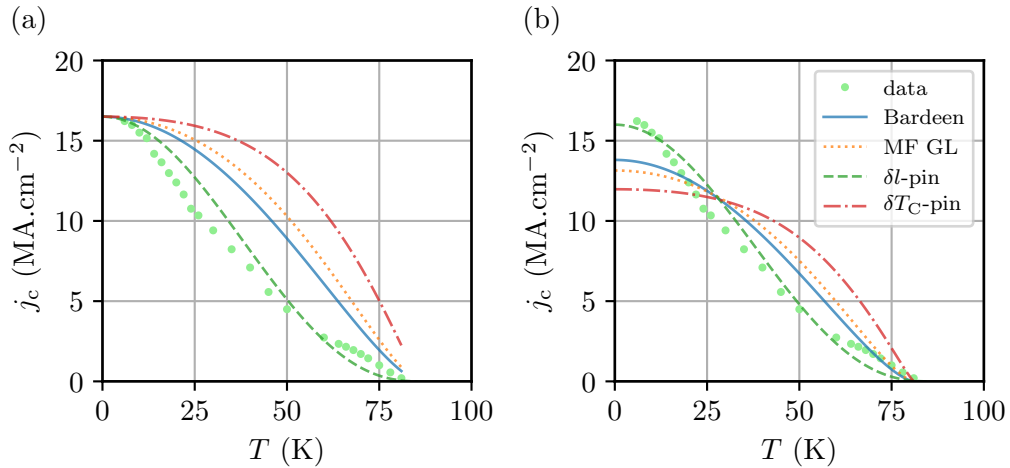


Figure 4.16 – Temperature evolution of j_c for C8, a 30 nm thick 500 nm long 200 nm wide nanowire presented in fig. 4.14 with four different models: Bardeen, Ginzburg-Landau, δl pinning, and δT_c pinning. (a) $j_c(0)$ and T_c are set by $j_c T$ and RT experimental curves respectively. (b) A least squares method fits the data curve. The parameters used for models are summarized in table 4.5.

Table 4.5 – Parameters for modelling $j_c T$ in fig. 4.16. T_c in (a) corresponds to T_{cm} .

Model	Method	$j_c(0)$ (MA.cm ⁻²)	T_c (K)
(b)	All	Fixed	16.5 86.1
(b)	Bardeen	Least squares	14.4 78.0
(b)	Mean-field GL	Least squares	13.8 78.0
(b)	δl pinning	Least squares	15.4 85.2
(b)	δT_c pinning	Least squares	12.7 78.0

worse than the one simulated by the Bardeen formula in this case compare to the data. Current density rapidly raises as temperature decreases, but it progressively decreases at lower temperature while the measured j_c values continue to raise. The MF-GL model does not describe correctly the global temperature evolution. Thus, vortex paving is not the limiting mechanism of j_c in the nanowire.

Vortex motion in type-II superconductors is sensitive to pinning centers which limit its dynamics. In order to be stuck, a vortex has to encounter a reduction of the order parameter on the length scale ξ . Since HTSs have small coherence length, vortices are more prone to be pinned in this material because it is easier to find small size defects. Two kinds of pinning are generally considered in HTSs, the fluctuations of electron mean free path, and the variations of the critical temperature, mentioned as δl pinning and δT_c pinning respectively. In the case of YBCO stoichiometric films, Griessen *et al.* [46] computed the expression of j_c for both pinnings using the general inversion scheme. They have evidenced a good agreement of the mean free path pinning relative to their data measured in different YBCO films. For δl pinning, j_c writes:

$$j_c(t) = j_c(0) \left(1 - t^2\right)^{5/2} \left(1 + t^2\right)^{-1/2} \quad (4.16)$$

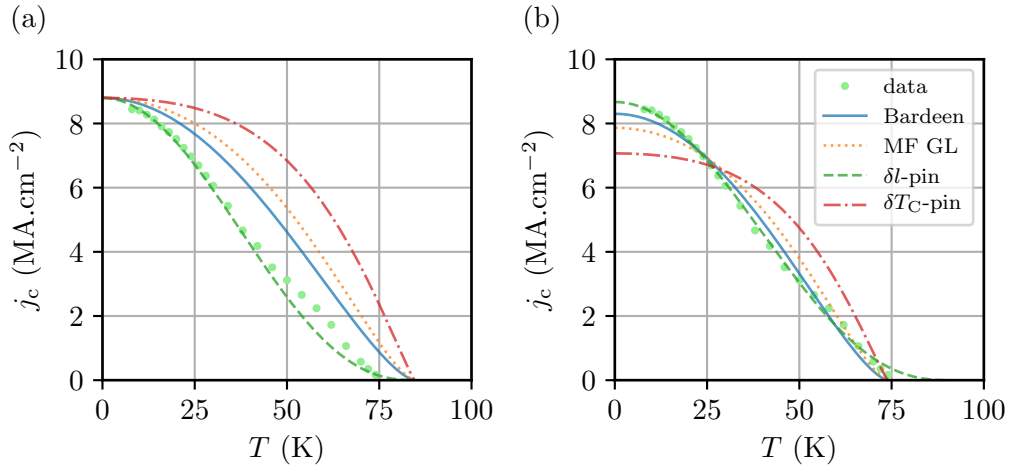


Figure 4.17 – Temperature evolution of j_c for D6, a 12 nm thick 500 nm long 200 nm wide nanowire with different models: Bardeen, Mean-field Ginzburg-Landau, δl pinning, and δT_c pinning. (a) $j_c(0)$ and T_c are set by $j_c T$ and RT experimental curves respectively. (b) A least squares method fits the data curve. The parameters of the models are summarized in table 4.6.

Table 4.6 – Parameters for modelling $j_c(T)$ in fig. 4.17. T_c in (a) corresponds to T_{cm} .

Panel	Model	Method	$j_c(0)$ (MA.cm ⁻²)	T_c (K)
(a)	All	Fixed	8.80	84.6
(b)	Bardeen	Least squares	8.30	74.0
(b)	Mean-field GL	Least squares	7.87	74.0
(b)	δl pinning	Least squares	8.67	90.3
(b)	δT_c pinning	Least squares	7.07	74.0

while for δT_c pinning, j_c is given by:

$$j_c(t) = j_c(0) \left(1 - t^2\right)^{7/6} \left(1 + t^2\right)^{5/6} \quad (4.17)$$

The current density at zero temperature depends on the nature of the pinning in the thin film, but it cannot be estimated easily using physical parameters. Thus, the current density is evaluated *via* a least squares fitting. Thus, it is highly sample dependent. The two models are presented in fig. 4.16, and the fitting parameters are summarized in table 4.5. T_c variation poorly describes the j_c data, while the electron mean free path fluctuations model gives the best fit among all the different models. Compare to other expression, the least squares method gives a reasonable value of T_c compare to T_{cm} , and an acceptable value of current density at low temperature. This result suggests that current density in our nanowires is limited by δl pinning rather than δT_c pinning or by the depairing current.

A further argument toward this conclusion lies in fig. 4.17. We have reproduced the same procedure of data fitting for a nanowire patterned on a 12 nm thick YBCO film, with the same geometry. With such a thinner thickness, it is expected that pinning becomes stronger. As we look at fig. 4.17, the model described even better the data in both panels than for the previous wire. In panel (b), the least squares fitting largely overestimates T_c by 6 K, while in panel (a) there is a deviation from data with respect to the model between 45 K and 70 K. It is likely that another mechanism is competing to set the current density at high temperatures. Here, Bardeen formula describes in a certain extent the temperature evolution, but as we discussed before there is no physical interpretation possible.

We conclude that the investigated YBCO nanowires in this section have their critical current mainly limited by the mean free path fluctuation. The pinning centers limit the vortex entrance into the films resulting in current density smaller by one order of magnitude with respect to the depairing limit current. We expect that reducing YBCO film thickness will enhance vortex pinning and thus increase the critical current density. In view of SSPD application, it will be of great interest.

4.4 Resonant radio frequency measurement

4.4.1 Probing the dynamical properties

Up to now, we only characterized the superconducting nanowires DC properties. In SSPD, the electronic dynamics is limited by the reset time τ_{reset} of the detector [256] given by:

$$\tau_{\text{reset}} = \frac{L}{Z_L} \quad (4.18)$$

where L is the total wire inductance, and Z_L is the circuit load impedance. In practice, low reset time is desired to measure high count rate which means low L and high Z_L . The latter is fixed by the amplifier and it generally equals 50 Ω . The wire inductance has two contributions: one is geometric and the other is kinetic arising from the Cooper pairs inertia.

For a wire in the form of a strip with length l , width w , and thickness d , the geometric inductance L_g in (nH) writes [47]:

$$L_g = 200l \left[\ln \left(\frac{2l}{d+w} \right) + 0.5 + \frac{d+w}{3l} \right] \quad (\text{nH}) \quad (4.19)$$

For $T < T_c$ in presence of an electromagnetic wave at frequency ν such that $h\nu \ll \Delta$, the kinetic inductance L_k writes [48]:

$$L_k(T) \simeq \frac{\mu_0 l \lambda^2(T)}{wd} \quad (4.20)$$

where λ is the magnetic penetration depth. In the case of YBCO, it has been suggested experimentally that the expression of λ is better described by the Gorter-Casimir (GC) phenomenological law [41, 49–51]. Instead of eqs. (2.6) and (2.9), in the framework of the GC model, the magnetic penetration depth for YBCO writes:

$$\lambda_{GC}(T) = \frac{\lambda_0}{\sqrt{1-t^2}} \quad (4.21)$$

where $t = T/T_c$ is the reduced temperature. In eq. (4.21), the magnetic penetration depth diverges more rapidly at high temperatures than the two-fluid expression expressed in eq. (2.6). As eq. (4.21) better accounts for the experiments in YBCO, we will use this formula throughout the rest of the manuscript, whenever the magnetic penetration depth is required. For these reasons, we also drop the subscript "GC" for the sake of clarity.

As T approaches T_c , L_k may take significant value with respect to L_g . For the case of a 30 nm thick YBCO thin film at zero temperature, and taking $\lambda_0 \approx 150$ nm, $w = 1$ μm and $l \in [1$ μm , 1 mm], $L_k(0) \approx L_g$ using eqs. (4.19) and (4.20). If the width is reduced, the inductance ratio raises: $L_k(0)/L_g \approx 10$ for $w = 50$ nm. As a consequence, at zero temperature the wire inductance is mostly fixed by the kinetic contribution for wire width smaller than 1 μm . In the case of damaged superconducting properties, the screening effect takes place on longer distances, resulting in a larger λ_L , hence in a higher kinetic inductance.

In the following sections, we describe a RF resonant experiment to measure the kinetic inductance. L_k is of importance since it is a key parameter setting the reset dynamics in SSPD. In addition, the measurement of the kinetic inductance gives access to the London penetration depth. It is another parameter assessing the quality of the fabricated devices and thus of the fabrication process.

4.4.2 Experimental setup

In order to probe the dynamical properties of O^+ irradiated YBCO devices, we measure the wire inductances thanks to a resonant RF method, and we retrieve the London penetration depth. For this purpose, three YBCO nanomeanders embedded in a coplanar waveguide (CPW) lines have been patterned on the same 30 nm thick YBCO film. Each meander, acting as an inductor below T_{c0} , forms a parallel resonant RLC circuit with surface mount devices (SMD) as shown in fig. 4.18. Two 12 pF capacitors, and two 100 Ω resistors from either side of the CPW line are placed on the sample holder, as close as possible to the chip to minimize the parasitic impedance contribution from the CPW transmission line of the PCB. It follows that the total SMD resistance is $R_0 = 50$ Ω , while the total SMD capacitor is $C_0 = 24$ pF. The CPW transmission line on the chip is wirebonded several times to the

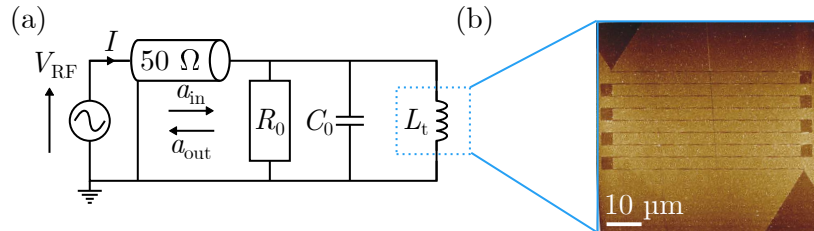


Figure 4.18 – (a) Picture of the RLC circuit formed by the surface mount resistors and capacitors on the sample holder in parallel with the YBCO meander embedded in a CPW on the chip. The sample holder and the chip are connected using Al wirebondings covered by a silver paste. (b) Equivalent RLC circuit connected to a vector network analyzer with a 50 Ω matched RF line.

sample holder as depicted in fig. 4.18(a), such that the inductive effect is limited and the impedance matching is enhanced. The sample holder is then placed on the optical plate of the cryostat to perform the measurement at low temperatures. Figure 4.18(b) shows the equivalent electronic circuit in which the total inductance is given by:

$$L_t = L_k(T) + L_g + L_p = L_k(T) + L_0 \quad (4.22)$$

where L_p is the parasitic inductance originating from the CPW transmission lines and the wireboundings, and $L_0 = L_g + L_p$ is the temperature independent inductance part.

The CPW parasitic impedance is summarised in a combination of a parallel capacitor with an inductance in series. The capacitive parasitic contribution from the CPW lines are estimated to be about 0.1 pF/mm. For 5 mm long CPW, it represents approximately 2% of C_0 . Since the parasitic capacitor is in parallel with the YBCO meander, by comparing their admittance it is possible to estimate the dominant element. The amplitude ratio between the wire inductance admittance $1/2\pi j f L$ and the parasitic capacitor admittance $2\pi j f C_0$ at $f = 1$ GHz is $1/(2\pi f)^2 L C_0 \approx 50$ for $L \approx 1$ nH. It means that the parasitic capacitor of the CPW transmission line in parallel with the nanowire inductance is negligible for frequencies lower than 1 GHz. Thus, it should be of concern at higher frequencies than 1 GHz. As the RF frequency lies below 1 GHz, we ignore the parasitic capacitive contribution from both CPW transmission lines. However, we keep the parasitic inductance L_p that contains the contribution in series of the CPWs and the wireboundings.

It follows that the impedance of the circuit presented in fig. 4.18(b) is expressed as:

$$Z = \frac{R_0}{1 + jQ \left(\frac{f_0}{f} - \frac{f}{f_0} \right)} \quad (4.23)$$

where $f_0 = 1/(2\pi\sqrt{L_t C_0})$ is the resonance frequency, while $Q = R\sqrt{C_0/L_t}$ is the quality factor. From eq. (4.22) it follows that:

$$f_0 = \frac{1}{2\pi\sqrt{L_t C_0}} = \frac{1}{2\pi\sqrt{(L_k(T) + L_0) C_0}} \quad (4.24)$$

From eq. (4.24) we see that, knowing f_0 and C_0 , it is possible to extract the total inductance, and thus the temperature dependent kinetic inductance. To do so a 50 Ω matched vector network analyzer (VNA) measures the scattering parameters S_{11} of the electronic circuit. In the configuration of fig. 4.18(b), VNA sends a RF signal with power a_{in} to the device under test (DUT) and receives the reflected RF signal with power a_{out} . The ratio between the two signal powers gives the complex reflection coefficient:

$$\Gamma = |\Gamma|e^{i\theta} = a_{out}/a_{in} \quad (4.25)$$

where θ and $|\Gamma|$ are respectively the argument and the module of Γ . For a DUT impedance Z and a load impedance $Z_L = 50 \Omega$, the reflection coefficient is expressed as follows:

$$\Gamma = \frac{Z - Z_L}{Z + Z_L} \quad (4.26)$$

4.4.3 Behavior at resonance

At resonance, *i.e.* $f = f_0$, the DUT impedance becomes real with $Z = R_0 = 50 \Omega$ from eq. (4.23), while θ shifts by π going from $f < f_0$ to $f > f_0$. Thus $Z = Z_L$, it follows from eq. (4.26) that Γ goes to zero. The DUT absorbs most of the RF power instead of reflecting due to the impedance matching. An absorption dip in the spectrum of $|\Gamma|$ is the signature of the resonance. Since L_t is of the order of 10 nH at low temperature and

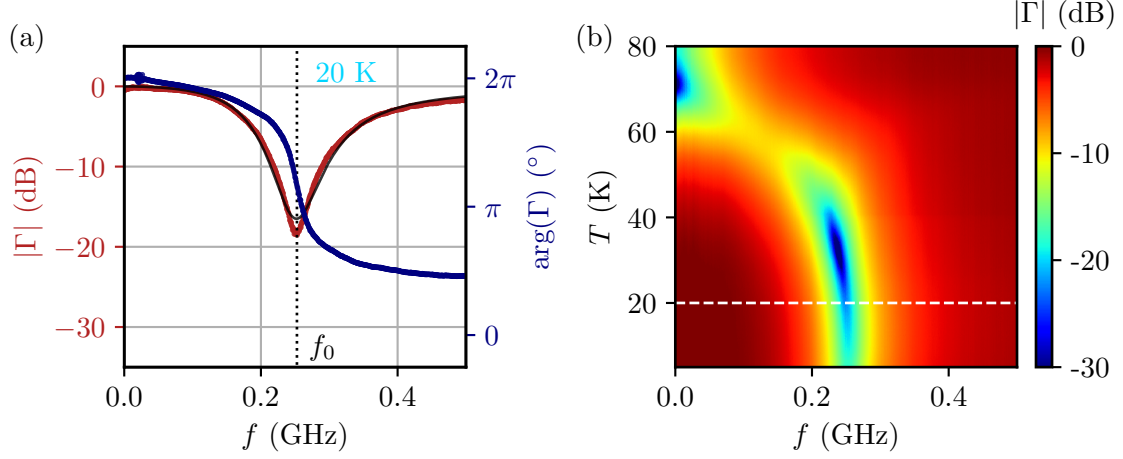


Figure 4.19 – VNA measurement of a M7', a 100 nm wide 450 μm long YBCO nanomeander. (a) RF spectrum at 20 K of the amplitude and the phase of Γ , in red and blue respectively. The solid black line is a least squares fitting of the amplitude of Γ , while the dotted black line highlights the resonant frequency. (b) Heat map of $|\Gamma|$ as a function of frequency and temperature up to T_c . The dashed white line highlights the cut of the heatmap at 20 K shown in (b).

$C_0 = 24$ pF, a rough estimate gives $f_0 \approx 0.3$ GHz. In this way, by measuring Γ with a VNA, a resonant dip should appear for $T < T_c$ about 0.3 GHz.

Figure 4.19(a) shows the VNA measurement of the spectrum of Γ in phase and in amplitude at 20 K on a 100 nm wide 450 μm long YBCO meander. The resonant dip appears in the spectrum with a $3\pi/2$ -phase shift about 0.25 GHz with 23 dB attenuation. By acquiring the spectrum of Γ at different temperature, we obtain the temperature evolution of L_k . The same experiment presented in fig. 4.19(a) is performed while temperature is varying up to T_c . Figure 4.19(b) displays the resulting colored heatmap of both temperature and frequency evolution of $|\Gamma|$. Starting from low temperature, the frequency resonance appears about 0.25 Hz. As temperature raises, the resonant frequency f_0 varies smoothly with respect to temperature. Once temperature approaches T_c resonance shifts quickly toward lower frequency. Such a behavior is expected, since $f_0 \propto (L_k + L_0)^{-1/2}$ and $L_k \propto \lambda_L^2 \propto (1 - (T/T_c)^2)^{-1}$ combining eq. (4.20) and eq. (4.21); the divergence of the kinetic inductance at T_c leads to small f_0 . For a temperature higher than T_c the resonance is poor because the meander is no longer superconducting but rather highly resistive. With such a resistive contribution of the YBCO nanomeander about 100 k Ω , the DUT is not impedance matched anymore. We are only interested in the temperature range below T_{c0} in which the absorption dip is well defined.

4.4.4 Temperature dependence of the kinetic inductance

We perform a least squares fitting of $|\Gamma|$ taking the amplitude of eq. (4.26) and using the expression of Z in eq. (4.23). Three parameters are varied: the quality factor Q , the load impedance Z_L , and the resonance frequency f_0 . Knowing C_0 , the total inductance is estimated thanks to eq. (4.24). We perform the resonant analysis procedure shown in fig. 4.20(a) for two different O⁺ ion irradiated meanders. They have different widths summarized in table 4.7. The resulting $L_t(T)$ data are fitted using eq. (4.21) and eq. (4.22) in which T_{c0} is set from RT measurement, while L_0 and λ_0 are free parameters to adjust. The parameters obtained to fit the data are summarized in table 4.7.

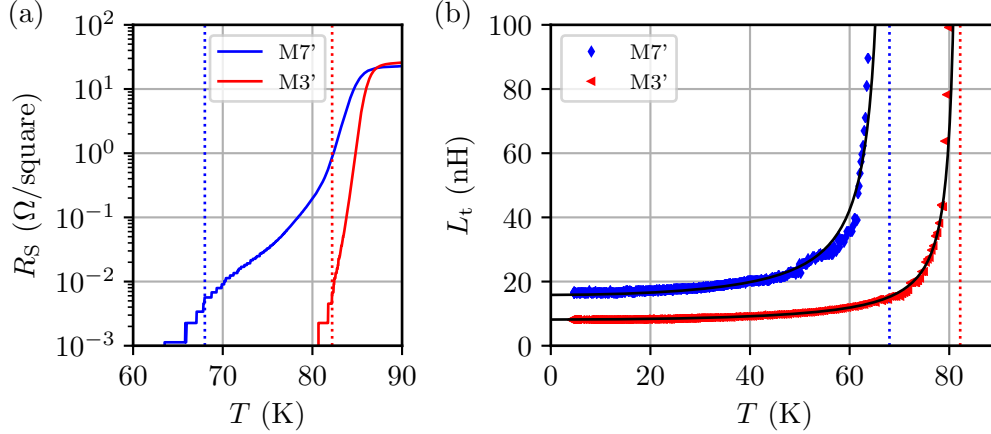


Figure 4.20 – (a) RT curve of two YBCO meanders. (b) Evolution of L_t with temperature for two 450 μm long nanomeanders pattern on a 30 nm YBCO thick film. Data points represent the total inductance extracted from VNA measurement and black plain lines are the corresponding best fit based on the two-fluid model. Dotted lines are located at T_{c0} .

Table 4.7 – Parameters for two different nanomeanders on a 30 nm thick YBCO film. T_{c0} and T_{cm} are extracted from RT curve, while the others are the best fit parameters of the temperature evolution of L_t .

Device	w (nm)	l (μm)	T_{cm} (K)	T_{c0} (K)	λ_0 (nm)	L_0 (nH)
M7'	100	450	85.8	68.0	200 ± 8	8.4 ± 1.1
M3'	200	450	86.2	82.2	186 ± 8	3.7 ± 0.5

Figure 4.20(a) shows that a low resistance foot develops in the 100 nm wide and 450 nm wide meander, while the 200 nm wide meander exhibits a rather sharp transition. For the narrowest 100 nm wide nanowire, the kink in the RT transition occurs for a resistance smaller than 0.1 Ω/square . Thus it does not question the irradiation process since T_{cm} is almost untouched with respect to $T_{cm} = 87$ K obtained in micron wide devices. For the reasons already mentioned in section 4.2, it is likely that a small portion of the nanowire has damaged superconducting properties due to the intrinsic defects or local degradation. Figure 4.20(b) shows the temperature evolution of L_t for the two meanders with their corresponding best fit curves. The total inductance is correctly described by the modified Gorter-Casimir model for YBCO case (eq. (4.21)) in the two devices with a divergence appearing at T_{c0} . The London penetration depth at 0 K extracted is substantially higher than the value of 125 nm for raw YBCO thin films [257], but it is consistent with the values reported in the literature for devices [49, 51]. It indicates that the whole wire length contributes to the kinetic inductance below T_{c0} . In the case of the 100 nm wide 450 μm long meander with $\lambda_0 = 200$ nm, we obtained $L_k = 7.5$ nH.

In the view of the application, the reset time of the meander τ_{reset} is fixed by the electronics. For the 100 nm wide nanomeander, we estimated thanks to eq. (4.18) that $\tau_{\text{reset}} = 0.15$ ns. It is possible that for thinner YBCO films, the magnetic penetration depth will be increased due to reduced superconducting properties. Nevertheless, the τ_{reset} value is encouraging toward a fast electronic reset time.

The RT curves along with the RF measurements validate once more that the ion irradiation process is a suitable fabrication technique to pattern YBCO thin films in a

meander shape, without damaging the superconducting properties of the wire. A superconducting transition appears above 65 K for all meanders, with a sharp transition for the 200 nm wide meander and a low resistive foot for the 100 nm wide meander. The London penetration depth is about 190 nm for the two different wires of various width. Overall, the meanders keep their global superconducting properties with respect to the thin film. Some inhomogeneities along the wire affect significantly the parameters, such as T_{c0} or j_c , fixed by the portion with the worst superconducting property. For this reason, both meanders have a critical current lower than 8 MA.cm^{-2} and thus do not present hysteresis neither photon detection.

4.5 Conclusion

In this chapter, we saw the general characterizations performed on different types and shapes of superconducting nanowires patterned with both the He^+ FIB patterning and the O^+ irradiation technique. Since the former process does not produced satisfying results in the RT measurements, the O^+ irradiation process has been chosen to fabricate most of the devices. Among the different sample types and thicknesses, we demonstrate thanks to RT and IV measurements that the O^+ ion irradiation process with a CeO_2 protecting layer is robust and reproducible. We successfully patterned high-quality superconducting nanowires on 30 nm thick samples down to 100 nm width and up to 450 μm length. Except the foot appearance in some RT curves, the onset critical temperature is almost unchanged with respect to the micron wide devices, even for 450 μm long meander. The critical current density achieved in long wires ($l \geq 10 \mu\text{m}$) are not suitable for the single detection at present. Nonetheless, 500 nm long wire reaches $j_{c0} \approx 0.2j_d$ with more than 1 V voltage switch in the best case. These achievements on YBCO thin films compete with the best results available in the literature.

While it is challenging to deposit high-quality YBCO thin film in itself, the results obtained on sub-30 nm thick samples are also encouraging. The fabrication yield of superconducting nanowires on such films is lower. But once a device is patterned on a sub-30 nm thick film with good superconducting properties, it is robust in external environment. We conclude that the fabrication workflow is also suitable for ultra thin YBCO films thanks to the protecting layer. It is worth noting that the results on devices patterned on J. Briatico YBCO thin films are also very promising. The nanofabrication process proves its worth for the 20 nm thick samples protected by $\text{PrBa}_2\text{Cu}_3\text{O}_{7-x}$ with a low resistivity at 100 K of $100 \mu\Omega.\text{cm}^{-1}$ attesting the high quality of the thin film. In addition, the 30 nm thick sample capped by CeO_2 layer is also very encouraging since its devices are slightly better than the best wires in Ceraco devices.

The RT measurements showed a superconducting transition in most of the devices. If the transition extends over a large temperature range, we interpret it as a distribution of superconducting properties over the length arising from damaged superconductivity in the overall device. In the case of a small resistive foot, it is likely that an inhomogeneity along the wire has a local damaged superconductivity.

We measured the IV curves of a large set of superconducting nanowires. We identified two distinct regimes depending on the value of the critical current density j with respect to the minimum healing current j_{h0} . If $j < j_{h0} \approx 10 \text{ MA.cm}^{-2}$, the voltage drop arises from flux creep followed by a flux flow behavior: the wire goes to the normal ohmic state continuously. In contrast, if $j > j_{h0} \approx 10 \text{ MA.cm}^{-2}$, a hysteresis develops due to Joule heating. A flux creep appears followed by a discontinuous voltage switch to the ohmic state. The voltage switch amplitude is mostly set by the value of the critical current with respect to j_{h0} according to the self-heating SBT model. The model provides a qualitative

interpretation of the hysteresis appearance and accounts for the temperature evolution of the retrapping current down to approximately 35 K. We concluded that once the thermal heat transfer is not sufficient, the wire goes directly to the normal state due to a thermal runaway. Nevertheless, it does not tell much about the voltage switch triggering event, we will address this question in chapter 6. We investigated the potential causes limiting the critical current in the 500 nm long nanowires using different theoretical models. The δl pinning model due to the electronic mean free path fluctuations is the most relevant scenario to consider in our case.

In order to probe the YBCO devices dynamics, we performed a RF resonant measurement with a RLC circuit made of 450 μm long YBCO meanders and along with SMDs. The experiment demonstrates that the fabrication is also suitable for meander shaped devices. For two meanders of distinct widths, we measured a London penetration depth about 200 nm similar to the value reported in the literature. It suggests that the reset time is less than 1 ns in our YBCO nanomeanders. Despite their good superconducting properties, they do not present voltage switches with hysteresis, neither photon detection. In the next chapter we focus our interest on the high quality nanowires - high critical temperatures and current densities above j_{h0} - in order to study the feasibility of single photon detection in YBCO superconducting nanowires. Henceforth, we will only consider 500 nm long bow tie in the following chapter to have better yield and superconducting properties, especially high j_c .

Chapter 5

Vortex dynamics in YBCO nanowires

Contents

5.1	Introduction	110
5.2	The flux creep regime	112
5.2.1	Theory	112
5.2.2	Current-voltage curve fitting	112
5.2.3	Temperature evolution of the pinning parameters	114
5.3	Radiofrequency synchronized vortex motion	116
5.3.1	Observation of Shapiro-like steps	116
5.3.2	Temperature dependence	118
5.3.3	Current steps height modulation	120
5.3.4	Non-integer fractional steps	123
5.4	Thermally activated vortex motion	125
5.4.1	Voltage-current power law regime	125
5.4.2	Current-voltage curve fitting with the original model	128
5.4.3	Including the vortex-vortex interaction	129
5.4.4	Current-voltage curve fitting with vortex-vortex interaction	131
5.5	Voltage pulse detection	133
5.5.1	Experimental setup	133
5.5.2	Voltage pulse observation	134
5.5.3	Count rate measurement	137
5.5.3.1	Discriminator level dependence of the dark count rate	137
5.5.3.2	Bias current dependence of the dark count rate	138
5.5.3.3	Count rate in presence of laser illumination	142
5.6	Conclusion	143

The different SSPD models presented in chapter 2 pointed the key role played by the vortices, both in the observation of the dark counts and in the single photon detection mechanisms. In the following chapter, we will focus on the vortex behavior in the different regimes of the IV curve prior to the switching.

In chapter 4, we mentioned briefly the vortex signatures in the different voltage regimes as the bias current is sweeping up. At first, a low voltage regime appears from the superconducting state above I_c . The temperature dependence of the critical current was explained by the δ_1 pinning model based on the electron mean free path fluctuations. Section 5.2 will analyse the low voltage branch to confirm the role of the pinning in the framework of the flux creep theory. In the same voltage range, we will study the effect of an external RF source causing the appearance of Shapiro-like steps. An additional behavior will arise: the coherent vortex motion. It will be presented in section 5.3. Then, the IV curves will be further analysed in the intermediate voltage range corresponding to the flux flow regime in section 5.4. We will show that the voltage arises from a thermally activated vortex motion in the presence of vortex interactions. The chapter will be completed by the detection and the counting of voltage pulses generated by fluctuations in section 5.5. Prior to going into the details of the experiments and their corresponding models, we give a brief introduction of the vortex behavior into superconductors.

This chapter is dedicated to the typical YBCO nanowires with a 30 nm thickness and a 500 nm length. For consistency and comparative purposes, all the devices presented in this chapter belongs to the sample CS15. They all present a sharp RT transition with an almost untouched T_{c0} and $\rho(100\text{K}) \approx 300 \mu\Omega\cdot\text{cm}$. Similar results have been obtained in other samples both qualitatively and quantitatively.

5.1 Introduction

In a type-II superconductor, under the application of an external magnetic field H , the vortices nucleate once H overpasses the first critical field H_{c1} . Flux lines parallel to the magnetic field penetrate the material to balance H and maintain superconductivity. They correspond to the so-called vortices. As each vortex carries a flux quantum, the number of vortices is simply proportional to H . In this respect, the vortex density linearly increases with the magnetic field. The supercurrents circulating around each flux line lead to a repulsive magnetic interaction between the vortices on a distance about λ_L . On the contrary, at short distances about ξ , the vortices are attracted to each other until their core almost merge together. In order to minimize the total interaction energy, the vortices tend to form a triangular lattice in the plane perpendicular to the magnetic field. Figure 5.1 show such a lattice imaged with a scanning tunneling microscope picture depicted in (a) and a corresponding schematic of the triangular vortex lattice.

Strictly speaking, the previous assertion holds only for an isotropic defect free superconductor at zero temperature. In the presence of inhomogeneities, such as a hole, the superconducting order parameter is locally suppressed. It becomes energetically favorable for the vortex core to locate at the hole position. This mechanism, called core or vortex pinning, tends to trap the vortices in a pinning potential of energy E_p . The defect positions are usually not controlled, they result in a random potential map. But, it is possible to engineer artificial defects in a superconductor in order to modify the vortex lattice. As an example, Harada *et al.* [259] have patterned holes in a Nb thin film acting as defects. The vortices tend to occupy the artificial defects, but they cannot occupy all of them due to the vortex-vortex interaction resulting in a different vortex lattice. Figure 5.1(c) shows a Lorenz micrograph of vortex lattice in a square array configuration as schematized by fig. 5.1(d). As a consequence, due to the competition between vortex-vortex interaction

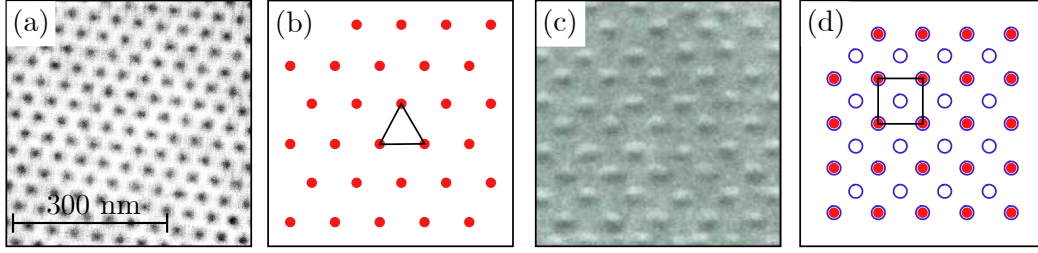


Figure 5.1 – (a) Scanning tunneling microscope image of a triangular Abrikosov vortex lattice generated by a 1 T magnetic field at 1.8 K in a NbSe₂ sample. (b) Schematics of the triangular vortex lattice observed in (a). Red dots represent the vortices and the black triangle contour correspond to a unit cell of the vortex lattice. (c) Lorentz micrograph of a vortex configuration in a square array of artificial defects. (d) Schematics of the artificial vortex lattice observed in (c). Red dots represent the vortices, blue open circles depict the artificial defects, and the black square contour is one unit cell of the vortex lattice. (a) Adapted from Hess *et al.* [258]. (b-d) Adapted and inspired from Harada *et al.* [259].

and vortex pinning, the ideal hexagonal flux lattice is perturbed [260].

Now, if temperature is non-zero, the vortex configuration is also disturbed due to the thermal fluctuations. The flux lines move around their original lattice sites. If the thermal energy $k_B T$ is smaller than E_p , the vortices are stuck onto the pinning sites provided that the pinning site density is important enough to receive all the vortices. In the opposite case of $k_B T > E_p$, the vortices are free to move and they dissipate energy *via* the Lorentz force. They may potentially merge together if $k_B T$ is sufficiently high.

From the discussion above, three energy scales emerge: the thermal energy, the pinning energy, and the vortex-vortex interaction energy. The competition between them rules the final vortex arrangement. Since we only consider a constant static magnetic field, the flux structure is almost static, but it evolves with time due to the thermal fluctuations.

Similarly, when a bias current is applied along a superconducting wire, a magnetic field is induced and the vortices nucleate at the wire edges. In this case, the vortex lattice also interacts with the current. The vortices are set in motion perpendicularly to the current thanks to the Lorentz force. Thus the vortex lattice becomes dynamical. By considering a superconducting wire with a thickness smaller than its width $d < w$, the vortices are expected to be perpendicular to the thin film plane.¹ In this configuration, the vortices are nucleated on one side and they move across the width. Eventually, if both the thermal energy and the Lorentz force F_L are low enough, they get pinned by the defects. As soon as $k_B T > E_p$ or $F_L > F_p$ where F_p is the pinning force, the vortices escape from their pinning sites and they continue on their way toward the opposite wire edge. Therefore the vortex velocity and hence the vortex crossing time both depend on the above mentioned energy scales. In addition, the vortex-vortex interaction adds for close enough vortices. This may modify the overall vortex dynamics.

In summary, the key ingredients to understand vortex dynamics are temperature, pinning through defects, Lorentz force, and vortex-vortex interaction. The study of the flux structure under the application of an external magnetic field and bias current results then in a rich physics which has been extensively studied. A complete study is out of scope of this manuscript, the reader interested in a more precised description should consult the reviews of Blatter *et al.* [261] or Cohen and Jensen [260].

¹Rigorously this assertion is valid for an s-wave superconductor with an isotropic order parameter. In the case of a d-wave superconductor, such as YBCO, the vortices are aligned along the *c*-axis.

5.2 The flux creep regime

In this section, we study the appearance of the low voltage drop in the YBCO nanowire IV curves when the critical current is overpassed. We have shown in chapter 4 that the temperature dependence of the critical current suggests that it is limited by the vortex pinning. In order to further develop this interpretation we will now use the flux creep model proposed by Bernstein *et al.* [53] to describe the low voltage range of the IV curves in YBCO microbridges.

5.2.1 Theory

Anderson and Kim developed the flux creep theory [52] to account for the resistance appearance in a superconductor due to the vortex motion. Bernstein *et al.* [53] have applied the flux creep theory to YBCO microbridges. In their model, they consider isolated vortices and a strong pinning that limit the vortex motion. In this framework, the Lorentz force is thermally assisted to overcome the pinning force such that the vortices can jump from one pinning site to another. In the case of a wire of length l , the vortices are generated at the edges of the nanowire. As they cross the wire they create a voltage drop V written as:

$$V = n_v l v_\varphi \Phi_0 \quad (5.1)$$

where v_φ is the average vortex velocity and n_v is the surface vortex density. If there is no external magnetic field and if we consider that the diffusion is responsible of the vortex motion, the vortex density along the edges for $I > I_c$ is expressed as:

$$n_v \left(x = \frac{w}{2} \right) = \frac{\mu_0 (I - I_c)}{2\Phi_0 d} \quad (5.2)$$

According to the original Anderson and Kim flux creep model [52], the vortex velocity writes:

$$v_\varphi = 2\omega_0 \delta_p \exp \left(-\frac{E_p}{k_B T} \right) \sinh \left(\frac{I \delta_p \Phi_0}{w k_B T} \right) \quad (5.3)$$

where ω_0 is the thermal activation attempt frequency, δ_p is the jump width between pinning sites, E_p is the pinning energy, and $W_L = I \delta_p \Phi_0 / w$ is the work done by the Lorentz force when a vortex jumps out of a pinning site. From eq. (5.3), we clearly see that both the Lorentz force and the thermal fluctuations come into play to move the vortices out of the pinning sites. By combining eqs. (5.1) to (5.3) altogether, we finally obtain the current dependence of the voltage as:

$$V = (I - I_c) \frac{\mu_0 l \omega_0 \delta_p}{d} \exp \left(-\frac{E_p}{k_B T} \right) \sinh \left(\frac{I \delta_p \Phi_0}{w k_B T} \right) \quad (5.4)$$

Fixing ω_0 to experimental values [54, 262], using the wire dimensions, and retrieving the critical current from IV curves, the only fitting parameters are pinning properties, namely E_p and δ_p . They characterize the flux creep regime when the pinning affects the vortex motion. In this respect, it is possible to fit IV data with eq. (5.4) with only two fitting parameters.

5.2.2 Current-voltage curve fitting

In the following subsection, we present the analysis procedure to interpret the IV curves according to the flux creep regime of the device C8, a 500 nm long 200 nm wide 30 nm thick YBCO nanowire. We use a set of IV curves measured with no external magnetic field

at different temperatures. In such conditions, only the induced magnetic field resulting from the bias current I has to be considered such that eq. (5.2) is valid.

Moreover, in this regime, the vortices should be isolated. Thus, we can estimate the vortex surface density to verify that the vortices are not interacting with each other. For a current difference $|I - I_c| = 0.1$ mA and a 30 nm thick superconducting film, from eq. (5.2) we obtain that $n_v(w/2) = 1$ vortex. μm^{-2} which corresponds to a vortex-vortex spacing of about 1 μm . In thin films, the flux lines interact together at a distance set by the Pearl length $\Lambda(T)$ defined by eq. (2.18). Considering a typical London penetration length at 0 K of 150 nm, we estimate that $\Lambda_0 = 1.5$ μm which is approximately the vortex distance. Hence, for a current difference of about 0.1 mA, it is expected that the vortices start interacting with each other and the isolated vortex hypothesis does not longer hold. It limits the application of the flux creep model toward the low current values nearby the critical current. As a conclusion, the model assumptions are verified in our case as long as the current difference is not too high compared to 0.1 mA.

Figure 5.2 shows the IV curves measured at different temperatures described by the flux creep model. We perform a least squares fitting of the low voltage branch with eq. (5.4) using the lmfit python package. This specific module provides us a high-level control of the fitting procedure and computes numerous important statistical parameters. The attempt frequency is fixed to $\omega_0 = 10^{13}$ Hz as reported in the literature for YBCO nanobridges [54, 262], the critical current is extracted from the IV curves, so that E_p and δ_p are the only free parameters to adjust.

The model does not apply to the whole IV data set, the upper and lower boundaries have to be fixed in some way to fit properly the data. The lower current boundary I_{start} is naturally given by the value of the critical current estimated from the IV curve. On the contrary, the upper current boundary I_{stop} is the crossover point between the flux creep and the flux flow regime in which the vortices do no longer feel the pinning. The choice of the upper limit is rather problematic because there is not a clear separation between the two regimes. To overcome this problem, we use the Akaike information criteria (AIC) as a discriminator [263]. More specifically, we perform a least squares fitting on multiple data sets by varying both the critical current and the upper current limit. For each data

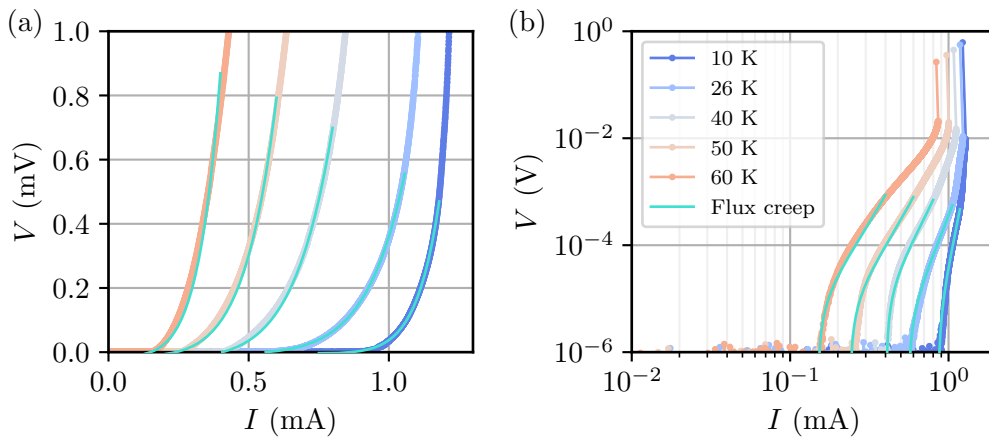


Figure 5.2 – IV curves of C8, a 500 nm long 200 nm wide 30 nm thick YBCO nanowire, at different temperatures linear and logarithmic scales respectively in (a) and (b). Data are fitted at low voltages near the critical current in the flux creep regime based on eq. (5.4). The AIC estimator has been used to select the data set which is best described by the model.

set, the AIC is computed *via* the `lmfit` module resulting in a two dimensional array whose dimensions is set by the size of I_c and I_{stop} . We then select the appropriate critical current giving a one dimensional array of AIC values. As the AIC described the information loss when data are described by a model, we choose the minimum value to set the upper current limit. The estimator takes into account both overfitting and underfitting as penalties. In other words, the minimum AIC gives a trade-off between having a small data set with respect to the fitting parameters number and a large data set which cannot be explain by the model. Using this method, we choose the data set with the minimum AIC which is best fitted by the model and the fitted parameters errors.

The IV curves along with their fitting curves presented in fig. 5.2 show that the flux creep model correctly describes the low voltage branches below 1 mV. If we have a closer look, for $T \geq 40$ K the model substantially deviates from the data. Surprisingly, we obtain a rather good fit with a current difference $|I - I_c|$ up to 0.5 mA. Hence, the model still works on a current range larger than 0.1 mA. The assumption of isolated vortices seems to hold in a greater extent than expected.

In addition, we also verify that lowering the upper current boundary leads to approximately the same value of the fitting parameters. Thus, we can reasonably claim that the model correctly catches the voltage behavior up to 0.5 mA. On the other hand, the choice of I_c affects significantly the value of the fitting parameters. In order to estimate the errors made on those parameters, we select a current range in which I_c should lie with a relative certainty and we perform a least squares fitting for the different I_c values. We obtain an array of E_p and δ_p values which are used to compute the corresponding standard deviations.

5.2.3 Temperature evolution of the pinning parameters

We now focus on the results of the fitting procedure that has just been presented. Figure 5.3 shows the temperature evolution of the optimized fitting parameters, namely the pinning energy in left panel and the jump width in the right panel. As temperature increases, E_p and δ_p are diverging respectively toward 0 and infinity with important relative errors. For this reason, we do not present the pinning parameters above 50 K since the fitting is no longer reliable, neither consistent. This fact confirms the deviation of the model observed in fig. 5.2 previously. As a comparison, we also add in the energy graphics the thermal energy $k_B T$ and the work done by the Lorentz force $W_L = I \delta_p \Phi_0 / w$ exerted on one vortex during its hopping from one pinning site to another.

If we first focus on the left panel, the pinning energy shows a dome shape peaked about 14 K with a maximum pinning energy of 7 meV. Above 14 K, E_p drops to zero and the same seems to happen below 14 K. Such a dome has already been observed by Bernstein *et al.* [53, 54] in YBCO microbridge for $T \geq 0.4T_c$, but they present two main discrepancies compared with our measurements. The dome has an opposite asymmetry as a function of temperature, meaning that the peak is observed near T_c in their case while we observe it at low temperatures far from T_c . In addition, the maximum pinning energy is one order of magnitude smaller in our case, suggesting that the pinning is weaker in our device.

It is worth noting that the thermal energy crosses the pinning energy about 30 K. For higher temperatures, the thermal motion alone is high enough to move the vortices out of their pinning sites without the need of the Lorentz force. It may explain quantitatively why the model failed to describe the data for $T > 40$ K. As temperature decreases, we expect that the pinning becomes dominant since the thermal motion is lessen while W_L should not change drastically as I_c reaches a plateau. It is indeed what we observe, E_p raises roughly linearly down to 14 K and W_L remains almost constant. But at lower temperatures, the pinning energy falls toward zero while we would expect a saturation of

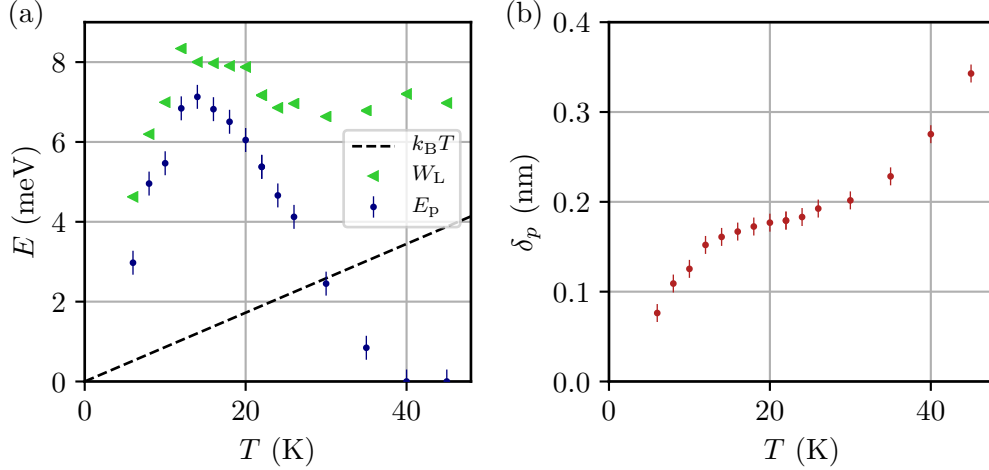


Figure 5.3 – (a) Temperature evolution of the pinning energy E_p along with the thermal energy and the work of the Lorentz force W_L . (b) Temperature evolution of the jump width δ_p . E_p and δ_p are the least squares fitting parameters of the IV curve using eq. (5.4) and the AIC analysis presented in section 5.2.2. The error bars correspond to the 95% interval confidence set by the choice of I_c .

E_p . Further investigations should be done to understand this behavior.

Figure 5.3(b) shows the temperature evolution of the vortex jump width. It may represent the pinning range² that is assumed to be equal to the average pinning sites distance. The temperature evolution follows the behavior observed in the literature [53, 54] that is δ_p shrinks when temperature decreases. This fact is rather intuitive, as the thermal motion is weaker the vortices are hopping to a smaller distance. They do not have enough energy to bypass several pinning sites as it could happen at higher temperatures. Moreover, our data quantitatively matches a data set presented by Pannetier *et al.* [54] at $T = 40$ K, which corresponds to a reduced temperature $t \approx 0.5$. Nevertheless, we found that the model is valid for the opposite temperature range. But, it is interesting to see that the jump width still decreases at lower temperatures in our case. Surprisingly, δ_p is rather small and corresponds roughly to the atomic distance which makes this value difficult to interpret.

As a conclusion, the flux creep model is relevant below 40 K in our case. For higher temperatures another mechanism should be used to better understand what governs the dissipation regime. The drop of the pinning energy at the lowest temperature near 5 K is not yet interpreted physically, but the temperature evolution of both E_p and δ_p from 14 K to 40 K is qualitatively coherent. Quantitatively, the pinning energy are rather low compare to the one in the literature. In contrast, the jump width is extremely small as observed in the literature [53, 54]. It suggests that the nanowire experiences a rather soft pinning which is easily bypassed thanks to the Lorentz force and the thermal motion. The IV analysis in the light of the flux creep theory has confirmed that the nanowire behavior is mostly governed by the vortex pinning near the critical current and below half- T_c .

²The pinning range might also be the vortex spacing or the separation of the pinning sites according to Bernstein *et al.* [53].

5.3 Radiofrequency synchronized vortex motion

Up to now, we interpreted the vortex presence as an established fact since YBCO is a type-II superconductor. This allowed us to investigate what controls the critical current. In this section, we report on the appearance of Shapiro-like steps in the IV curves of YBCO nanowire under an external RF source. We study the effect of temperature and RF power to get a better insight of the underlying mechanism. We ascribe the RF synchronization of the vortex motion as the origin of the current steps.

5.3.1 Observation of Shapiro-like steps

In order to apply an external RF signal, a home made RF log-log antenna is placed in the cryostat a few centimeters above the sample. The antenna is connected *via* a coaxial RF cable to a Anritsu MG3692C RF signal generator. The frequency can be tuned from 0.1 GHz up to 20 GHz, although in practice, we are limited by the antenna bandwidth. Analogously, the effective RF power transmitted to the device depends on both the coupling and the antenna radiation pattern. The total RF power transmission has not been calibrated, hence, we will use the Volt as an arbitrary unit given by the RF generator to describe the RF power linearly. Rigorously speaking, the RF power expressed in Volt corresponds to the square root of the RF power expressed in Watt. Thus, we will inaccurately expressed RF power in Volt.

The aim of the experiment is to observe the effect of an RF signal on the IV curves. For $T < T_c$, an increase of the RF power reduces the critical current which, at some point, might be completely suppressed. In addition, as the RF transmission depends strongly on the RF frequency, we have to find the best RF coupling between the RF generator and the device for each frequency. For this purpose, the temperature is set at 5 K such that the critical current is almost at its maximum and the device is current biased just above I_c . Then, we set an arbitrary RF power and scan the frequency in the whole available range while we measure continuously the voltage drop. With such a method, we identify the specific frequencies at which the RF coupling is the best and choose the operation frequencies accordingly.

The Shapiro steps appear at specific voltages given by:

$$V_n = \frac{nhf}{2e} \quad (5.5)$$

where $n \in \mathbb{N}$ is the current step index and f is the RF frequency. Hence, higher is the frequency larger the voltage spacing between successive steps. For this reason, it is more appropriate to use high frequency to have well separated steps. At first, we set $f = 18.32$ GHz to satisfy both criteria of high coupling and large voltage spacing.

We acquired several IV curves at different RF powers P_{rf} starting from no signal to completely suppressed I_c . Figure 5.4(a) shows different IV curves taken at $T = 50$ K and $f = 18.32$ GHz. To make the figure more readable, we have directly converted the voltage into the integer n representing the step index. In addition, fig. 5.4(b) displays the dynamic resistance³ $R_d = \partial V / \partial I$ as a function of n . It allows one to better distinguish the variation of the slope and therefore the current steps appearing as local minima.

As can be seen, starting from 0 V no step appears. As P_{rf} raises, we observe the appearance of the first step ($n = 1$) at $P_{\text{rf}} = 0.3$ V and the successive steps ($n > 1$) for $P_{\text{rf}} = 0.5$ V. At some point, the RF power completely removes the superconducting voltage branch, reducing the critical current to zero, while the current steps remain. In the IV

³We first performed a gaussian window filtering and then we derived numerically V with respect to I . With this procedure the derivative is less noisy at a cost of a shift of the minima toward higher voltages.

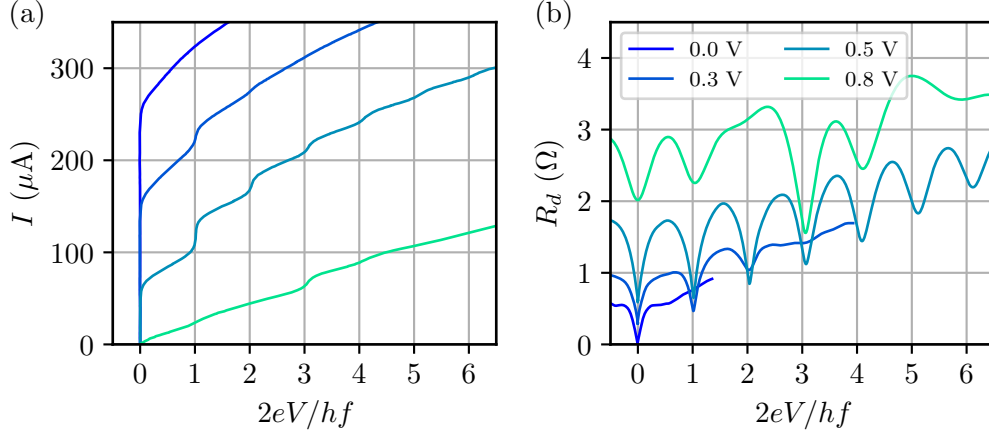


Figure 5.4 – (a) Current voltage characteristics and (b) dynamic resistance R_d as a function of voltage at 50 K showing Shapiro-like steps for C8: a 500 nm long 200 nm wide 30 nm thick YBCO nanowire. The voltage drop is converted into the step index n . An external RF signal at $f = 18.32$ GHz is applied at different powers presented in the legend.

curves, and mostly in the R_d graphic, we perceive a modulation of the current steps height: as P_{rf} raises from 0 V the first step ($n = 1$) starts increasing and reduces at higher power. We note that the different steps height modulation does not occur for the same RF power. For example, if we look at R_d data at $P_{\text{rf}} = 0.8$ V, for $n \in \{1, 3, 4\}$ the step seems to exist, while for $n \in \{2, 5, 6\}$ it completely disappears.

As we have seen in chapter 2, the observation of Shapiro steps cannot be unequivocally accounted for the presence of a Josephson junction, it can also be due to synchronized vortex motion. One way to discriminate between those effects is to measure the current phase relation of the device. As we will show in the following, numerous arguments tend to interpret the Shapiro-like steps observation as a microwave coherent vortex motion.

At first, we compare the YBCO nanowire presented in this chapter with the Josephson junction properties presented by Malnou *et al.* [56]. This JJ consists of two superconducting leads (S) separated by a nanometer scale barrier (S') whose T_c is reduced with respect to the bare YBCO film, abbreviated as (SS'S) junction. Table 5.1 summarizes the superconducting properties of both devices. Since they are both fabricated thanks to the O^+ ion irradiation technique on Ceraco YBCO thin films, the comparison is even more relevant to check the difference between pure Josephson behavior and synchronized vortex motion. The RT transition occurs about 86 K for both devices. While the JJ shows a second transition at $T_j = 66$ K, the nanowire transition goes sharply toward zero resistance. At least, there is no clear transition foot which might explains a weakened superconducting behavior such as in the case of the SS'S junction presented by Malnou *et al.* [56]. More strikingly, the nanowire has a critical current density two orders of magnitude higher than the JJ while the cross-section are reduced with respect to the former, and it is one order of magnitude smaller than the depairing current. With such a high j_c value it is more likely that the nanowire has a complete superconducting path. Besides, we have also measured IV curves under the application of an external magnetic field at 100 mK for similar YBCO nanowires. We have not observed any Fraunhofer modulation of the critical current up to 6.5 T, whereas in the case of a YBCO JJ the critical current should drop to zero about 50 μT Bergeal *et al.* [55]. As a partial conclusion, the nanowire does not behave like it is expected for a usual ion irradiated YBCO SS'S Josephson junction.

Based on the DC and RF superconducting characteristics, we favour the interpretation of the results as a synchronized vortex motion. In this picture, the nanowire also satisfies

Table 5.1 – Superconducting properties of two ion irradiated YBCO devices: a Josephson junction from Malnou *et al.* [56] and the nanowire presented in this section.

Device	d (nm)	w (μm)	l (nm)	T_c (K)	$j_c(50\text{ K})$ (MA.cm ⁻²)	$R_n(50\text{ K})$ (Ω)
JJ	70	2	20	86	0.07	1
Nanowire C8	30	0.2	500	86.1	5	< 0.1

the Josephson relations to some extent. Indeed, as a vortex carries a flux quantum, each vortex crossing the wire width produces a 2π -phase shift, which leads to a voltage drop proportional to Φ_0 . Thus, if we consider that vortices nucleate from one edge at a specific position along the wire at a frequency f the mean voltage drop along the wire V is expressed as [18]:

$$V = f\Phi_0 \quad (5.6)$$

Equation (5.6) is the voltage Josephson relation. Analytically, the external RF power can be treated as an AC current contribution at frequency f of the microwave source [18, 57]. In such a condition, the current Josephson relation is also satisfied. For those two reasons, we observe the same fingerprint in the IV curve. According to Likharev [18], in addition to the Lorentz force produced by the DC current, the RF external source generates an alternating Lorentz force moving the vortices back and forth across the wire at frequency f . In this respect, the vortex motion is synchronized with the RF frequency.

By contrast, the mathematical calculations and the experimental results are not identical for a superconducting nanowire and a JJ. In the case of JJs described by the voltage source RF model, the height of the successive current steps is given by Bessel functions of the first kind [185]. However this model does not always describe correctly the experimental observations. To counteract this problem, the RF contribution has been rather treated as a current source in the calculation. In this case, the current steps height has no longer analytical solutions: the two Josephson relations have to be solved numerically. The shape of the steps height modulation depends strongly on the Josephson frequency f_J set by the JJ characteristics, given by its normal resistance and its critical current. On the other hand, for coherent vortex motion, two models have been proposed [18, 57] to describe the phenomenon. They both model the RF contribution as an AC current source, but the current steps height cannot be computed analytically. Section 5.3.3 will present the modulation of the current steps height with the incident RF power for the studied YBCO nanowire.

5.3.2 Temperature dependence

In order to shed light on the appearance of Shapiro-like steps, we measured the IV curves for different RF powers and temperatures resulting in 2D maps. Figure 5.5 shows the evolution of the dynamic resistance with current and RF power for $f = 18.32$ GHz and for temperatures: 6 K, 20 K, 50 K, and 70 K. In the heatmap, black color corresponds to a vertical branch in the IV curve, corresponding to either the superconducting branch or the current steps. Whatever the temperature, it is always possible to suppress completely the supercurrent at a given RF power which varies with temperature following the I_c variation. For the ion irradiated YBCO JJ of Malnou *et al.* [56], the total suppression of I_c occurs only in the Josephson regime and not in the flux flow regime. Unless the YBCO nanowire is always in the Josephson regime, this is clearly inconsistent with the results on the YBCO nanowire.

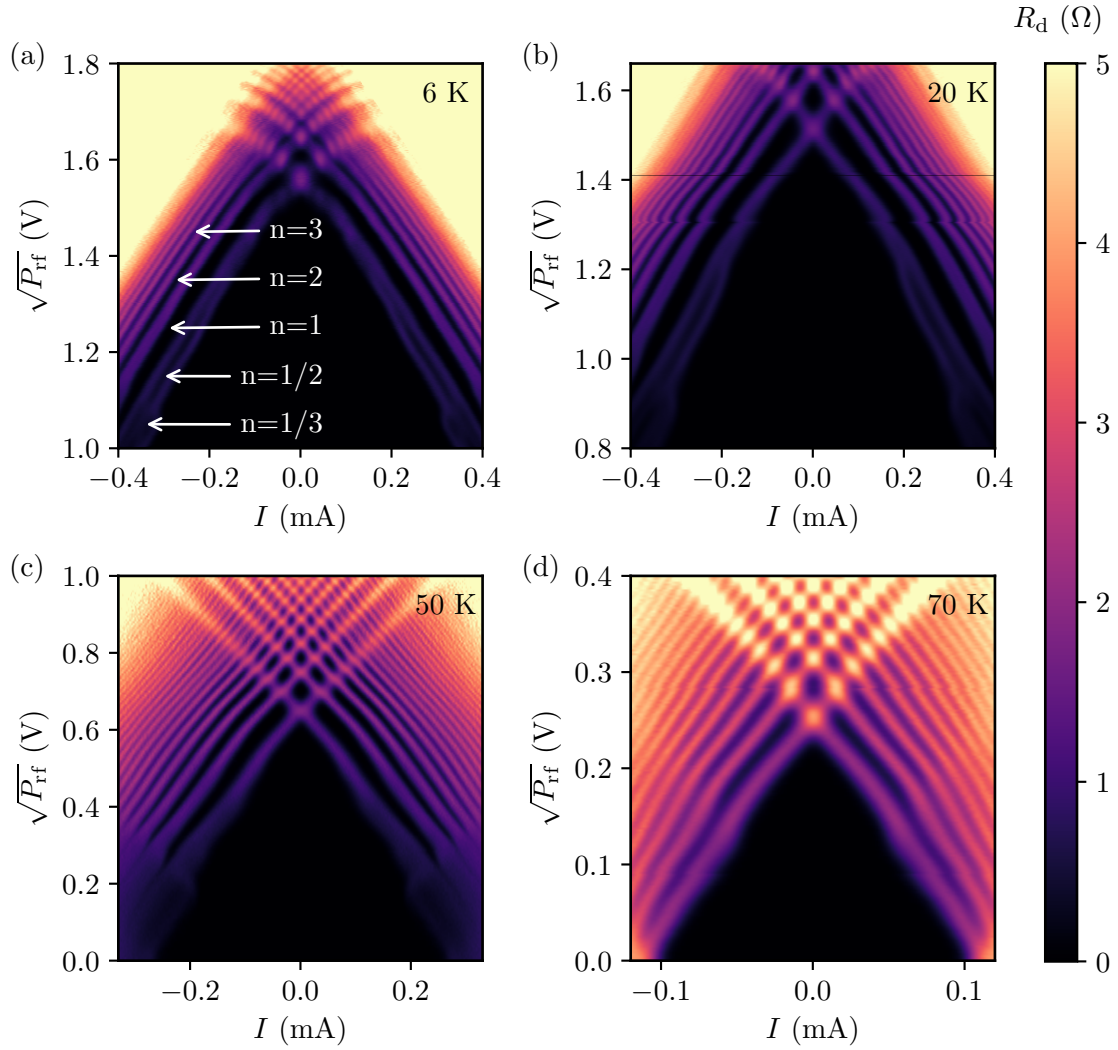


Figure 5.5 – Heat maps of the dynamic resistance under an RF illumination at $f = 18.32$ GHz as a function of bias current and the square root of RF power for C8: a 500 nm long 200 nm wide 30 nm thick YBCO nanowire. The temperatures in (a), (b), (c), and (d) are respectively 6 K, 20 K, 50 K, and 70 K. The white arrows in (a) indicate both integer and fractional order Shapiro-like steps.

As can be seen in fig. 5.5, the modulation of the current steps height with the RF power is evident. Following a black diagonal line, as the RF power increases the step appears necessarily at lower current up to the point it completely disappears and reappears for higher power. The separation between the black diagonal lines and upwards black diamonds corresponds to a total suppression of the current step.

We also see several successive current steps appearing for all temperatures. As temperature lessens, we observe a better contrast between the successive current steps probably due to a lower thermal blurring. It allows us to see more than 20 steps in panel (c) at 50 K. But as temperature decreases further, the dynamic resistance becomes so important that high order current steps fade away. We become limited to the observation of the first 6 steps at 6 K.

Finally, we observe fractional order current steps, as indicated by the white arrows in fig. 5.5(a) for $n = 1/2$ and $n = 1/3$. They appear only for $T \leq 50$ K prior to the first Shapiro step ($n = 1$) in fig. 5.5(a-c). At 50 K, we barely see a larger coloured line at low RF power, which then widens at lower temperatures in which a black line emerges inside the purple diagonal line. On the other hand, the fractional order step become evident at 6 K and 20 K, especially for $n = 1/2$. Nevertheless, for high enough RF power which depends on temperature, this feature vanishes. We will treat this observation in greater details in section 5.3.4 by providing a physical interpretation.

5.3.3 Current steps height modulation

For now on, we pursue the investigation of the current steps modulation with the RF power. The Shapiro-like current steps height is retrieved for the first fifth current steps including the critical current as $n = 0$. appendix C

Figure 5.6 displays the evolution of the current steps height as a function of RF power for different frequencies at 50 K. We observe that both I_c and the current steps height are modulated with the RF power. In panel (a), for $n = 0$, I_c decreases almost linearly with the square root of the RF power down to 0.65 V. For higher power, the critical current alternates from zero value with finite non-zero current. The local maximum decreases and the modulations are no longer observable. The current step at $n = 1$ appears for $\sqrt{P_{rf}} > 0.2$ V, and the following steps start to raise just after. They all slowly increase up to 0.7 V, afterwards they fall down and oscillate between zero current and non-zero finite values.

In addition, panels (b-d) display the current steps height at three different frequencies with a good RF power coupling: 18.32 GHz, 11.8 GHz, and 6.16 GHz.⁴ We observe Shapiro-like steps and the current steps height modulation with the RF power for those three frequencies. Quantitatively, the current steps height does not oscillate, neither vanish, at the same RF powers, and it does not have the same amplitude. Regardless of the frequency used, we observed qualitatively the same modulation pattern. It demonstrates that the phenomenon involved does not arise from a specific frequency of the system, it is unambiguously related to the microwave source frequency shone on the device.

In the case of JJs, the IV curve under microwave illumination can be simulated in the framework of the RCSJ model. The microwave radiation is accounted with an alternating current in the electrical equations. Using this model the amplitude of the current steps height modulation depends strongly on the JJ characteristic frequency given by:

$$f_J = \frac{I_c R_n}{\Phi_0} \quad (5.7)$$

⁴For frequencies of about 1 GHz, the system is too noisy with respect to the current steps voltage separation of a few μ V. For this reason, we could barely notice the first step at 961 MHz under specific condition of temperature and power, but the amplitude of the steps were too small for further analysis.

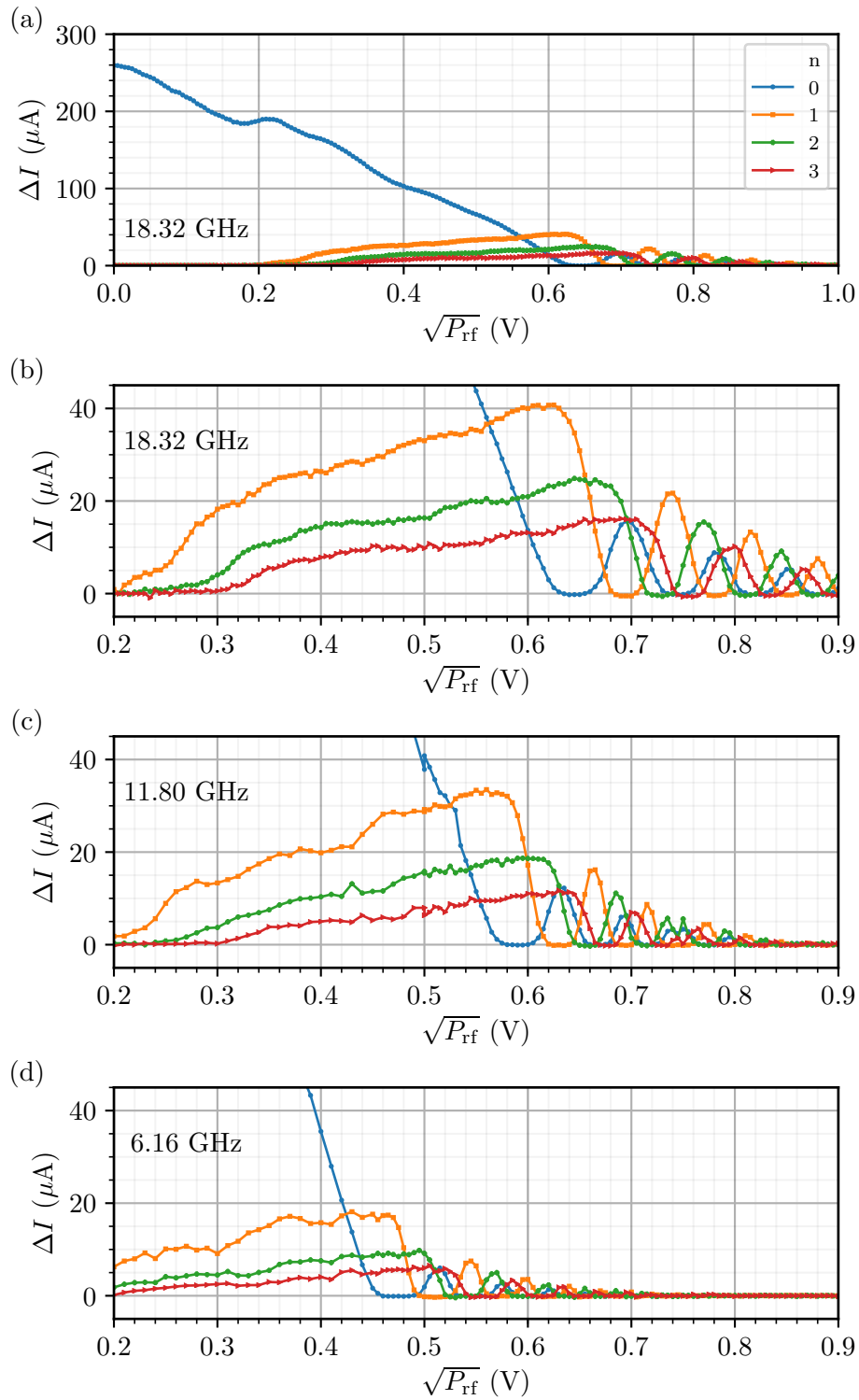


Figure 5.6 – Evolution of the current steps height ΔI of the IV curve as a function of RF power at 50 K for the three first steps. The RF illumination in panels (a), (b), (c), and (d) are respectively set at frequencies of 18.32 GHz, 18.32 GHz, 11.80 GHz and 6.16 GHz. The panels (a) and (b) represent the same data with different scales.

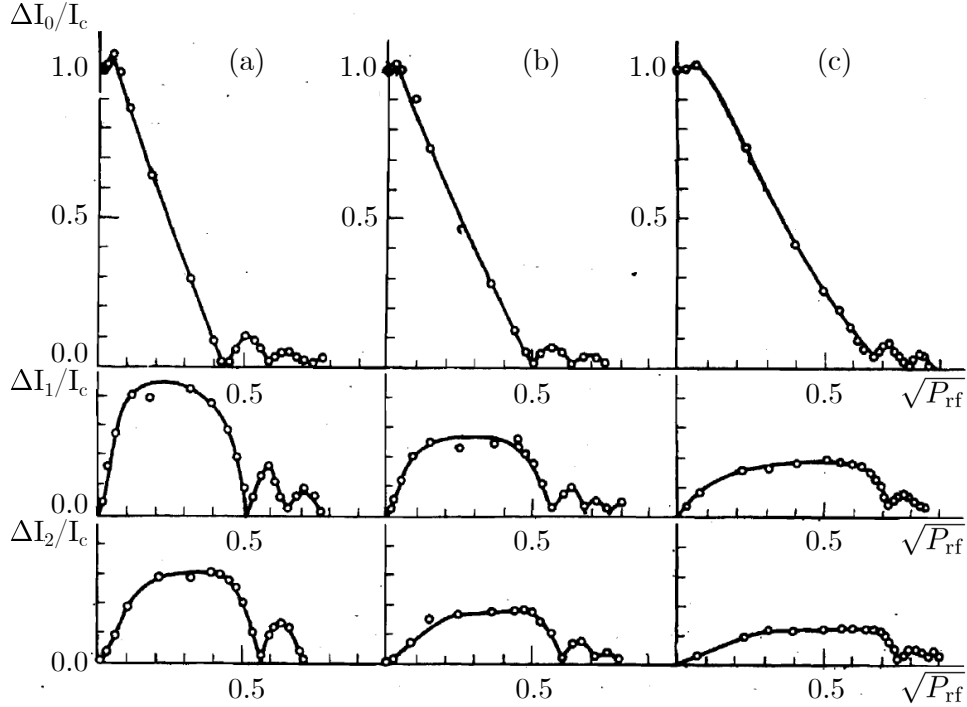


Figure 5.7 – Evolution of the critical current and the two first current steps heights as a function of the incident RF power of a tin bridge at temperatures (a) $0.975T_c$, (b) $0.91T_c$, and (c) $0.872T_c$. Adapted from Gubankov *et al.* [184].

where I_c is the critical current and R_n is the normal resistance. In particular, as f_J increases the maximum current steps height occurs at lower I_c . In the case of the YBCO nanowire, the maximum height of the first current step is almost 5 times smaller than the maximum critical current. If we want to account for this ratio between ΔI_1 and I_c obtained for the YBCO nanowire in the framework of the RCSJ model with a current source description, the simulations performed by Russer [264] estimate roughly that $f_J = 10f$ for $f = 18.32$ GHz. Knowing that $I_c = 0.26$ mA without microwave power, we estimate that $R_n = 1.5 \Omega$ within the RCSJ model. With such a model we obtain the same order of magnitude than the JJ presented in table 5.1. Hence, if we try to describe the nanowire as a JJ, the RCSJ model gives an inconsistent result.

In order to better describe the current steps height modulation, the set of differential equations of vortex motion proposed by Likharev [18] should be solved. Further investigations are required to get an adequate simulation based on the coherent vortex motion. Nevertheless, it is worth noting that we observe a similar RF power modulation of the current steps height than the one measured by Gubankov *et al.* in a tin bow-tie microbridge [184]. As can be seen in fig. 5.7(a) for $T = 0.975T_c$, the critical current rapidly drops when the incident RF power increases while the two first current steps heights raise up to reach a dome in a large RF power extent about 0.3 V. As in our case, when P_{rf} increases further, the critical current is first suppressed, then the first current step height becomes zero while I_c raises again and oscillates, and finally the suppression of the second current step height occurs. Afterwards, we observe the subsequent modulation of the current steps height and the critical current in a smaller extent in comparison with the current steps height. However, we stress that for lower temperatures, the current step never completely vanishes, the local minima are non zero. We have never observed such a fingerprint. According to Likharev [14], the Abrikosov vortices only exist for $w \gtrsim 4.41\xi$ and $l \gtrsim 3.49l$. The bridge presented in fig. 5.7 always satisfies $w \leq 4.41\xi$, but depending

on the temperature the bridge may satisfy either $l \leq 3.49\xi$ for $T = 0.975T_c$ in fig. 5.7(a) in which ΔI_i may be completely suppresses or $l \leq 3.49\xi$ for lower temperature in fig. 5.7(b-c) in which the local minima of ΔI_i are non zero.

5.3.4 Non-integer fractional steps

We briefly mentioned earlier the observation of non-integer fractional steps between $n = 0$ and $n = 1$ at temperature below 50 K. We could observe this behavior not only at different temperatures, but also at different frequencies. In order to better observe it, fig. 5.8 displays the IV curve and the corresponding dynamic resistance at 6 K for different RF powers. For RF powers equal to 0.8 V and 1.2 V, we distinguish a step appearing at $n = 1/2$, especially thanks to a local minimum in the $R_d V$ curves, as highlighted by arrows. For $\sqrt{P_{\text{rf}}} = 1$ V, two local minima emerge at position $n = 1/3$ and $n = 2/3$. In the heatmaps shown in fig. 5.5, we note that the fractional steps disappear for bias current below $I \approx 0.15$ mA.

Fractional Shapiro steps have already been observed in 2D JJ array [265, 266] and also in superconducting nanowires [267]. In quasi 1D superconducting nanowires, at high microwave powers and high frequencies, the fractional Shapiro steps are the signature of a multivalued current-phase relationship. In the case of superconducting bridge, the seminal work of Aslamazov and Larkin [57] gives the understanding of integer and fractional Shapiro steps as follow. When a vortex crosses a DC biased nanowire, the phase of the order parameter shifts by 2π . Far from the nanowire, the voltage is proportional to the rate of the phase change between the two sides of the nanowire such that:

$$V(t) = \frac{\hbar}{2e} \left(\frac{\partial\phi}{\partial t}(+\infty) - \frac{\partial\phi}{\partial t}(-\infty) \right) \quad (5.8)$$

If each vortex follows the preceding vortex with a frequency f_{vortex} , the phase switches by 2π each period $1/f_{\text{vortex}}$. It results in an alternating voltage along the nanowire. As soon as the number of vortices per unit of time increases for higher biased current, the interaction between vortices changes, and a kink should appear in the IV curve. Such an alternating voltage can be expanded in a Fourier series with voltage harmonics V_k related to the vortex velocity. When adding an RF signal at frequency f which is a multiple of the

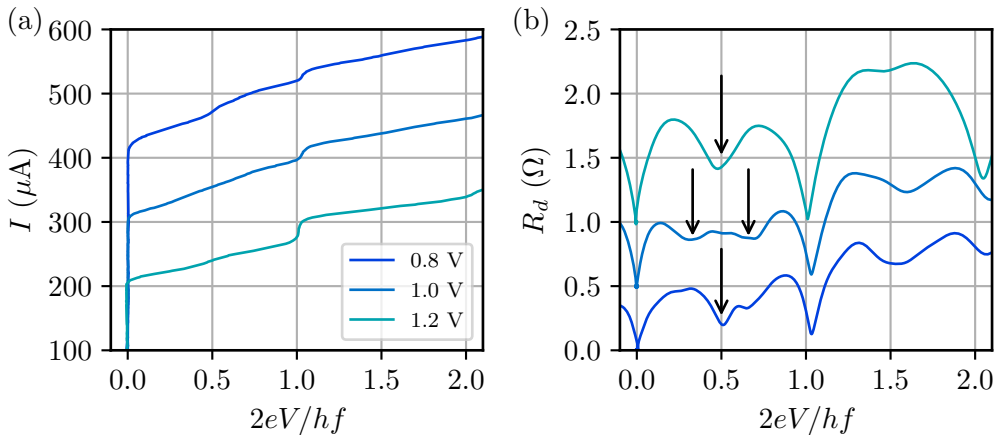


Figure 5.8 – (a) Current voltage characteristics and (b) dynamic resistance R_d as a function of voltage under an external RF illumination at $f = 18.32$ GHz for $T = 6$ K for C8, a 500 nm long 200 nm wide 30 nm thick YBCO nanowire. The voltage drop is converted into the step index n . Black arrows indicate the fractional order Shapiro-like steps.

vortex crossing frequency such that $f = qf_{\text{vortex}}$, the vortices are created after an equal time interval $\Delta t = q/f$. In other words, the vortices cross the nanowire at subharmonics of the RF signal. As a result, for one line of vortices, the mean voltage across the nanowire writes:

$$\bar{V} = \frac{1}{q} \frac{hf}{2e} \quad (5.9)$$

In the absence of inhomogeneities, a large number of vortices in the nanowire will tend to form an ordered spatial structure with k parallel lines of vortices with identical vortex frequency in each line. The total voltage along the nanowire is the sum of the voltages generated by each line of vortices such that:

$$\bar{V} = \sum \frac{1}{q} \int V dt = \frac{k}{q} \frac{hf}{2e} \quad (5.10)$$

If we consider only one vortex row ($k = 1$), the step for $n = 1/2$ ($q = 2$) corresponds to the vortex row synchronized to $f/2$, while $n = 1/3$ ($q = 3$) is a synchronization to $f/3$. If we consider two isolated vortex rows ($k = 2$) synchronized to $f/2$ ($q = 1$), the first Shapiro step will appear at $n = 1$ and for 3 isolated vortex rows synchronized to $f/3$, the first Shapiro step will appear at $n = 1$. Vortices have to be apart from $\Lambda \approx 2 \mu\text{m}$ not to interact with each other. Reminding that the nanowire is 500 nm long, the two rows are necessarily interacting. According to Fiory [268], the width of the Shapiro steps due to the synchronized vortex motion should be related to the fluctuations of the vortex velocity.

In order to illustrate the idea of synchronized vortex rows, fig. 5.9 presents magnetic imaging of both static and dynamical vortex configurations performed by Embon *et al.* [85]. While the current is smaller than the critical current, the vortex lattice is static, as depicted in fig. 5.9(a-b). But, as the bias current approaches the critical current, the vortices move due to the combination of thermal fluctuation with the Lorentz force: the vortex configuration fluctuates. As $I \gtrsim I_c$, the vortex configuration shown in fig. 5.9(c) becomes clearly dynamical as depicted by the solide yellow lines in the bridges. The vortices nucleate at the left bridge side at a single vortex entry point, as they move toward the opposite side they follow different paths splitting in several parallel rows at different bifurcation points. As bias current increases further, the first parallel rows may subsequently split as the original first row does. In this view, all the vortices nucleate at a single vortex entry point first but they follow several paths which form a tree of vortex rows which do not

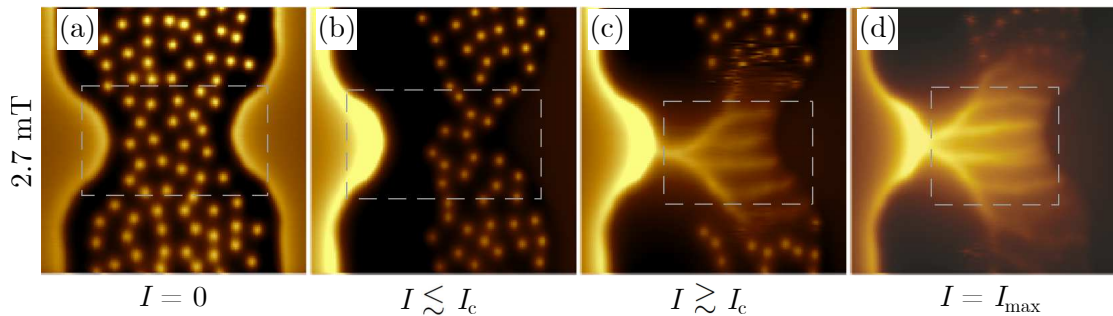


Figure 5.9 – Magnetic imaging of a Pb microbridge for $\mu_0 H = 2.7 \text{ mT}$ at 4.2 K and bias current such that: (a) $I = 0$, (b) $I \lesssim I_{\text{max}}$, (c) $I \gtrsim I_{\text{max}}$, and (d) $I = I_{\text{max}}$. Depending on the bias current, the vortex lattice form different vortex configuration, either static in (a-b) or dynamical (c-d). Each yellow point corresponds to one vortex, as vortices move the imaging generate a time averaging such that the yellow lines represent the vortex paths in the dynamical configuration. Adapted from Embon *et al.* [85].

merge after the bifurcation. For high current, the vortices may nucleate at different point along the bridge side.

According to Embon *et al.* [85], the physical interpretation is as follows. As fast vortices move to the right side, they suppress locally in time and space the superconducting order parameter in their wake which attract the subsequent vortices. It explains why the different rows follow the same path. But as the creation rate becomes higher than the crossing rate - due to an increase of the bias current - the vortices accumulate and push onto the neighboring vortices to the right side. In order to reach a stable state, newly entering vortex either speeds up following the same vortex channel, or follows a bifurcation in a subsequent vortex path. It results that the original vortex row split in multiple subsequent vortex rows. In our case, we interpret the fractional order Shapiro-like steps as the RF signal forces the vortex configuration to align the vortices in a specific number of parallel rows fixed at given voltage drop.

In summary, when an RF source at frequency f illuminates the YBCO nanowire, current steps appear in the IV curves. They are analogous to the Shapiro steps observed in JJs. The numerous measurements performed at different temperatures and RF frequencies along with the nanowire superconducting properties demonstrate that the device cannot be interpreted as a JJ, but rather it behaves like a superconducting nanowire. In this picture, the Josephson relations are verified thanks to the synchronized vortex motion at the RF frequency. The vortices are nucleating at one specific wire edge and their motion described a vortex row perpendicular to the DC bias current due to the Lorentz force, that is to say alongside the width. In this view, the appearance of non-integer fractional step is interpreted as a splitting of the original vortex row in multiple vortex rows. Further work is required to describe the data obtained with a coherent vortex motion model.

5.4 Thermally activated vortex motion

5.4.1 Voltage-current power law regime

We now focused our interest on the vortex motion in the low voltage branch for $V \leq 1$ mV, either in the flux creep regime or with a microwave synchronization. We are continuing the analysis of the IV characteristic in the intermediate voltage regime before that the switching voltage event occurs. In particular, we investigate the power law dependence of the voltage with respect to the current as:

$$V \propto I^n \tag{5.11}$$

We are interested in whether this regime can be ascribed to a thermally activated vortex motion (TAVM) or not. As proposed by different experimental studies [58, 59], it is expected that:

$$n(T) = 1 + \frac{\Phi_0^2}{8\pi^2\Lambda(T)k_B T} \tag{5.12}$$

where Φ_0 is the magnetic flux quantum and $\Lambda(T)$ is the Pearl penetration depth. Following the analysis performed by Tafuri *et al.* [59], if we consider a superconducting thin wire whose width w and thickness d are such that $\xi \ll d \ll w \ll \Lambda$, where ξ is the superconducting coherence length, Kogan [269] has shown that the vortex self-energy ϵ'_0

as a function of temperature at position x across the wire width writes⁵ as:

$$\epsilon'_0(T) = \epsilon_0(T) \ln \left(\frac{2w}{\pi\xi(T)} \sin \left(\frac{\pi x}{w} \right) \right), \quad \xi < x < w - \xi \quad (5.13a)$$

$$\epsilon_0(T) = \frac{\Phi_0^2}{8\pi^2\Lambda(T)} \quad (5.13b)$$

where $\epsilon_0(T)$ is the vortex self-energy in a superconducting infinite thin film. The additional prefactor in the right hand side of eq. (5.13a) corresponds to the correction for a narrow bridge with $w \ll \Lambda$. Equation (5.13a) is only valid at a distance larger than ξ from the edge, otherwise the expression fails as the vortex cannot exist. Indeed, the supercurrents cannot circulate around the normal vortex core if there is no superconducting part between its normal core and the wire edge. The temperature dependence of the penetration depth is given by the modified Gorter-Casimir law for YBCO expressed in eq. (4.21). Under such a condition, hereafter and in the following sections, the Pearl penetration depth writes:

$$\Lambda(T) = \Lambda_0 \left(1 - \left(\frac{T}{T_c} \right)^2 \right)^{-1} \quad (5.14a)$$

$$\Lambda_0 = \frac{2\lambda_0^2}{d} \quad (5.14b)$$

where λ_0 and Λ_0 are the London and Pearl magnetic penetration depths at 0 K respectively.

Now, if the device is biased with a uniform current I , the work done by the Lorentz force on the vortex subtracts to the vortex self-energy of eq. (5.13a). In this model, the bias current is high compared with I_c such that the Lorentz force prevails over the pinning force. Thus the latter is not considered. The resulting vortex energy $\epsilon(T, I)$ is:

$$\epsilon(T, I) = \epsilon_0(T) \ln \left(\frac{2w}{\pi\xi} \sin \left(\frac{\pi x}{w} \right) \right) - \epsilon_0(T) \frac{I}{I_0(T)} \frac{\pi x}{w}, \quad \xi < x < w - \xi \quad (5.15a)$$

$$I_0(T) = \frac{c\Phi_0}{8\pi\Lambda(T)} \quad (5.15b)$$

where I_0 is the characteristic current in ESU units. For the sake of clarity, we first model the data at 0 K. As the temperature dependence is only carried by ϵ_0 and I_0 through the Pearl penetration depth and therefore through the London penetration depth, the results are quite similar for $T < T_c/2$. For higher temperature, the results may change quantitatively, even though the energy barrier profile and the current dependence are qualitatively the same. For YBCO, $\lambda_0 \approx 200$ nm, we roughly estimate that $\Lambda_0 = 3 \mu\text{m}$ corresponding to $I_0 = 0.3$ mA. The characteristic current I_0 is about the same order of magnitude than the critical current approaching 1.2 mA at zero temperature.

Equation (5.15) represents the energy barrier to bypass for a vortex in order to cross the wire width. Figure 5.10(a) displays the numerical simulations of the energy barrier along the width for different normalized current I/I_0 in the case of YBCO. The energy has been normalized with respect to ϵ_0 . Here, we focus on the evolution with position and current values hiding the temperature dependence for a while. Obviously the energy profile is symmetric when $I = 0$. The maximum energy in the center at $x = 0.5$ is four times higher than ϵ_0 corresponding to a vortex free to move in a superconducting film. As bias current increases, the energy profile becomes asymmetric. The maximum energy lowers and the corresponding position goes toward the left wire edge as shown by the dash

⁵Here, eq. (5.13) is written in the electrostatic system of units (ESU). The appropriate factors for converting physical quantities from ESU into International System of Units (ISU) and vice-versa are picked in the NIST Guide to the SI.

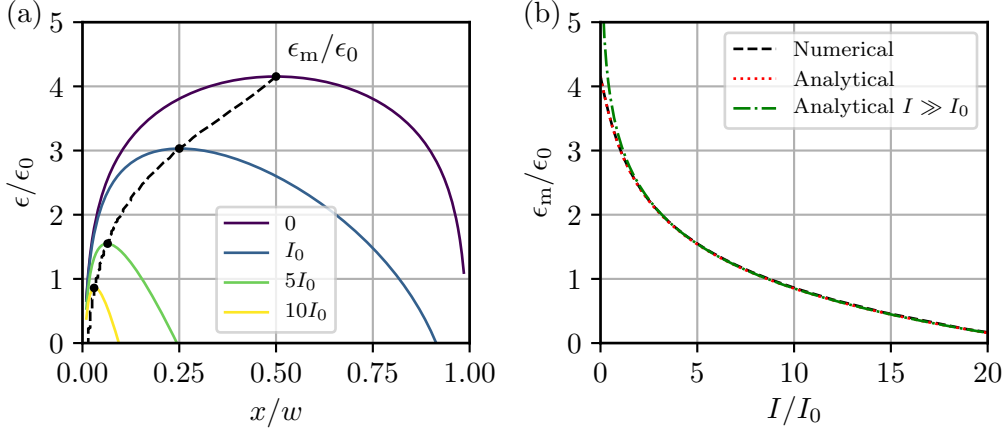


Figure 5.10 – (a) Vortex energy barrier along the width of a current biased superconducting wire for different bias currents displayed in the legend at 0 K. The black dotted line corresponds to the maximum energy ϵ_m estimated numerically for different bias currents. (b) Evolution of the normalized maximum energy as a function of the normalized bias current I/I_0 . Black dotted line corresponds to the numerical simulation from eq. (5.15), red dashed line is computed from eq. (5.16), and green dash dotted line is computed from eq. (5.17).

lines in fig. 5.10(a). If the current direction is reversed, the maximum energy position will be shifted to the opposite edge. Hence, it becomes easier for the vortex to cross the wire width thanks to the Lorentz force. Especially, the maximum energy $\epsilon_m(T, I)$ and its location $x_m(T, I)$ are analytically given by:

$$\epsilon_m(T, I) = \epsilon_0(T) \left[\ln \left(\frac{2w}{\pi\xi\sqrt{1 + (I/I_0(T))^2}} \right) - \frac{I}{I_0(T)} \arctan \left(\frac{I_0(T)}{I} \right) \right] \quad (5.16a)$$

$$x_m(T, I) = \frac{w}{\pi} \arctan \left(\frac{I_0(T)}{I} \right) \quad (5.16b)$$

Moreover, if we consider that $I \gg I_0$, eq. (5.16a) rewrites:

$$\epsilon_m(T, I) = \epsilon_0(T) \left(\ln \left(\frac{2wI_0(T)}{\pi\xi(T)I} \right) - 1 \right) \quad (5.17)$$

We obtain a simple analytical equation for the current dependence of ϵ_m . Nevertheless, the bias current in our YBCO nanowires do not satisfy the assumption that $I \gg I_0$.

Figure 5.10(b) shows the evolution of ϵ_m as a function of the normalized current at 0 K using different methods. At first, as the bias current increases we clearly see that the maximum energy reduces rapidly by one order of magnitude for $I \approx 15I_0$. In our case, the bias current lies between I_0 to $4I_0$ at most, therefore the energy barrier is never completely wiped out by the Lorentz force. The numerical and analytical simulations collapse on the same curve validating the consistency of the simulations. More surprisingly, the analytical simulation of eq. (5.17) for $I \gg I_0$ matches with the general analytical simulation, even for current of a few I_0 . Thus, the approximated equation with $I \gg I_0$ still holds on a larger current range than expected.

If the vortex barrier crossing is thermally activated, the voltage is proportional to

$\exp(-\epsilon_m/k_B T)$, that is to say:

$$V \propto \left(\frac{I}{I_d}\right)^m \quad (5.18a)$$

$$m(T) = \frac{\Phi_0^2}{8\pi^2 \Lambda(T) k_B T} \quad (5.18b)$$

$$I_d(T) = \frac{c\Phi_0 w}{4e\pi^2 \Lambda(T) \xi(T)} \quad (5.18c)$$

Equation (5.18a) needs an additional prefactor proportional to the current to ascribe for the high temperature limit when Λ diverges. At the end, $V \propto I^n$ as previously announced by eq. (5.12) with the exponent $n = m + 1$. Hence, if the voltage drop arises from a thermally activated vortex motion, it should follow a power law dependence in current. The latter is essentially controlled by the magnetic penetration depth.

5.4.2 Current-voltage curve fitting with the original model

Figure 5.11(a) presents a set of IV curves at different temperatures. The IV curves are almost linear in log-log scale for $10 \mu\text{V} < V < 10 \text{ mV}$ which is in favour of a power law relation described by eq. (5.11). As temperature raises, the regime described by the TAVM phenomenon extends to a different voltage and current ranges. For each IV curve we face the same fitting problem presented in section 5.2.2: choosing correctly the data range to fit the data. We employ the same technique based on the AIC method presented in section 5.2.2 to choose the data range. Therefore, at a given temperature we fit the IV curve with a least squares method for several possible data ranges and we select the data range with the lowest AIC value. Figure 5.11(a) shows the resulting fitting curves with eq. (5.11) that best describe the data.

Figure 5.11(b) displays the evolution of the parameter n retrieved from the IV power law curves fitting at different temperatures. We first note that n monotonically increases as temperature lowers. This is expected from eq. (5.12) since $\Lambda(t) \propto (1-t^2)^{-1}$ (eq. (5.14)), it follows that $m \propto (1-t^2)/t$ diverges at low temperatures and tends toward 0 near T_c .⁶

⁶Here again we use the reduced temperature notation $t = T/T_c$.

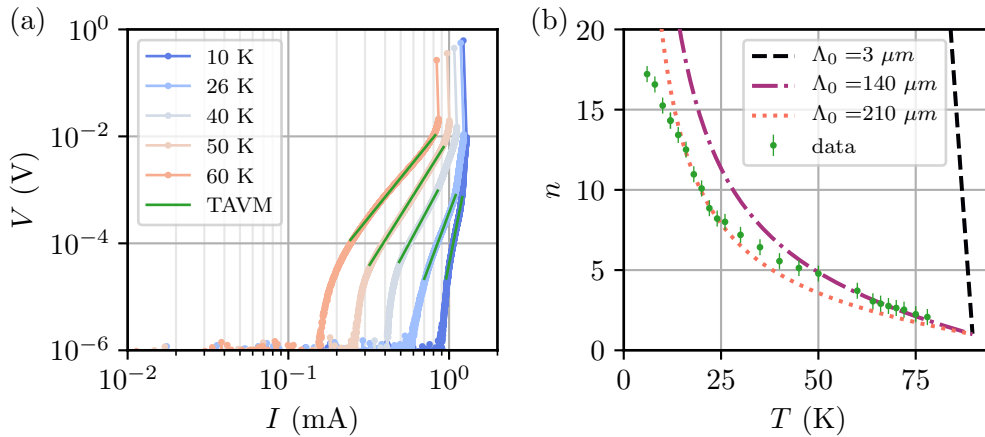


Figure 5.11 – (a) IV curves at different temperatures of C8, a 500 nm long 200 nm wide 30 nm thick YBCO nanowire. The solid green lines are least squares fitting with a power law model. (b) Evolution of the exponent n as a function of temperature along with the TAVM model for different Pearl penetration length at 0 K.

In order to test the quantitative validity of the TAVM model, we plot in fig. 5.11(b) the exponent n estimated thanks to eq. (5.12) for three different Λ_0 values: $3 \mu\text{m}$, $140 \mu\text{m}$, and $210 \mu\text{m}$. Based on the expected value $\Lambda_0 = 3 \mu\text{m}$ there is a clear discrepancy between the model and the exponent n . Though it is possible to approximately match the data in the high temperature range by using $\Lambda_0 = 140 \mu\text{m}$, but the model does not follow the data down to low temperatures. Even if Λ_0 is raised we cannot fully account for the whole temperature dependency with the TAVM expression of n expressed in eq. (5.12). In order to describe correctly the data we need a Pearl penetration length two orders of magnitude higher than expected.

Besides, if we try to reconcile the extracted parameter Λ_0 by using different physical parameters, it is unlikely that we succeed in settling the inconsistency. There is only three physical parameters to tune according to eq. (5.12): temperature, the thickness, and the London magnetic penetration depth. The first is measured precisely at 0.1 K precision hence it is not questionable; d might potentially varies by a few nanometers resulting in approximately 10% variation; λ_0 might be possibly larger but certainly not higher than 500 nm . Thus even in the worst scenario $\Lambda_0 = 25 \mu\text{m}$ which is still one order of magnitude smaller than the value expected by the model. Though the thermally activated vortex motion model fails to describe quantitatively our IV curves while it is in reasonable agreement qualitatively. In order to address the problem, we need a lower Λ_0 value or equivalently a higher vortex energy.

5.4.3 Including the vortex-vortex interaction

In the original TAVM model, two hypothesis are questionable for the studied YBCO nanowire. At first, we suppose that $I \gg I_0$ whereas we estimated that $I_0 = 0.3 \text{ mA}$. Though, the condition $I > I_0$ is always verified, but the current never exceeds I_0 by more than one order of magnitude. We have seen that it is not a stringent requirement, though it cannot explain the important inconsistency. Secondly, we implicitly supposed that vortices are isolated and do not interact with each other. As mentioned previously in section 5.2.2, this assumption is not verified for current larger than I_c by 0.1 mA , which is precisely the case here. Thus, we should consider the vortex-vortex interaction.

In order to include the vortex-vortex interaction, we need the interaction energy, but also the vortex layout in the plane perpendicular to the thickness. Kogan [60] has demonstrated that for two vortices at positions (x_1, y_1) and (x_2, y_2) the interaction energy ϵ_{int} is:

$$\epsilon_{\text{int}}(T) = \epsilon_0(T) \ln \left(\frac{\cosh(\pi(y_1 - y_2)/w) - \cos(\pi(x_1 + x_2)/w)}{\cosh(\pi(y_1 - y_2)/w) - \cos(\pi(x_1 - x_2)/w)} \right) \quad (5.19)$$

In the section 5.3, we concluded that the vortices nucleate at one point along the edge and that their coherent synchronized motion forms one or several rows parallel to the width. For this reason, we assume that vortices are aligned along the width such that $y_1 = y_2$. In this way eq. (5.19) simplifies to:

$$\epsilon_{\text{int}}(T) = \frac{\epsilon_0(T)}{2} \ln \left(\frac{\sin(\pi(x_1 + x_2)/2w)}{\sin(\pi(x_1 - x_2)/2w)} \right) \quad (5.20)$$

In addition, we change the problem variables according to the standpoint of the first vortex at position $x_1 = x$ and by placing the second vortex at position $x_2 = x + x_0$ with x_0 being simply the vortices spacing distance. With such a substitution eq. (5.20) rewrites:

$$\epsilon_{\text{int}}(T) = \frac{\epsilon_0(T)}{2} \ln \left(\frac{\sin(\pi(2x + x_0)/2w)}{\sin(\pi x_0/2w)} \right) \quad (5.21)$$

So far, the system contained one vortex and we derived its total energy. From now on, in a simplistic view, we consider a chain of vortices equally spaced by x_0 and we compute the

total energy of a new vortex entering in the nanowire. The k -th vortex interacting with the vortex of interest adds an interaction energy $\epsilon_{\text{int},k}$:

$$\epsilon_{\text{int},k}(T) = \frac{\epsilon_0(T)}{2} \ln \left(\frac{\sin(\pi(2x + kx_0)/2w)}{\sin(\pi kx_0/2w)} \right) \quad (5.22)$$

Overall, the vortex energy ϵ' interacting with its neighboring vortices is given by:

$$\epsilon'(T, I) = \epsilon(T, I) + \sum_{k=1}^N \epsilon_{\text{int},k}(T) \quad (5.23a)$$

$$N = \left\lfloor \frac{x_0}{w - \xi} \right\rfloor \quad (5.23b)$$

where N is the total number of interacting vortices with the vortex considered. For a given vortex spacing x_0 , by deriving eq. (5.23a) with respect to the position x to find the maximum energy, we have to solve the following equation:

$$\frac{I}{I_0} = \cotan \left(\frac{\pi x}{w} \right) + \sum_{k=1}^N \cotan \left(\frac{\pi(2x + kx_0)}{2w} \right) \quad (5.24)$$

This time, the maximum energy position cannot be derived analytically as before. To circumvent the problem, we compute eq. (5.23a) numerically for a given vortex spacing x_0 and a bias current, and then we retrieve the maximum energy ϵ'_m . Figure 5.12 shows the corresponding numerical simulations for $I = I_0$ and different x_0 at 0 K along with the previous simulation presented in fig. 5.10 without interaction labeled as 'none'. When vortex-vortex interaction is included and as vortices are getting closer, *i.e.* x_0 increases, we note that the maximum energy position shifts slightly toward the width center but it remains globally the same. By contrast, the maximum energy is varying significantly when vortices become closer. For $x_0 = 8$ nm the maximum energy is almost four times higher than the case without interaction, and it is one order of magnitude higher for the smaller vortex spacing: $x_0 = 4$ nm. For $x_0 = 64$ nm the energy profile is almost unchanged with

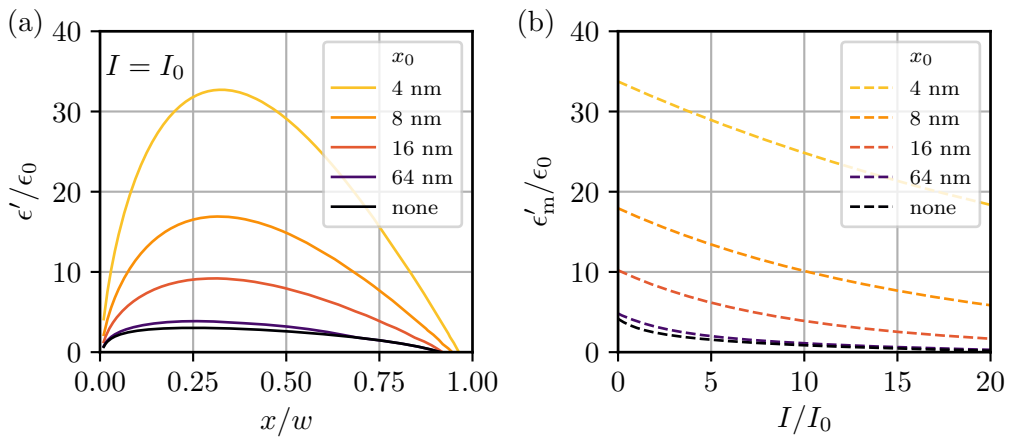


Figure 5.12 – (a) Simulation of the vortex energy barrier along the width of a current biased superconducting wire for different vortex spacing x_0 at $I = I_0$. (b) Evolution of the corresponding maximum energy as a function of the normalized bias current I/I_0 estimated numerically. The energies are normalized to the characteristic vortex energy ϵ_0 and the position of the studied vortex is normalized to the wire width w .

respect to the one without interaction.⁷ Thus, according to the numerical simulations in fig. 5.12, the vortex-vortex interaction becomes relevant for vortex spacing about 64 nm rather than a few microns estimated at first.

Following the same reasoning than before, if the vortex motion is thermally activated the voltage is now proportional to $\exp(-\epsilon'_m/k_B T)$. Though IV curve can be modelled by the expression below with V_0 a characteristic voltage including the attempt frequency:

$$V = V_0 \exp\left(-\frac{\epsilon'_m(T, I)}{k_B T}\right) \quad (5.25)$$

5.4.4 Current-voltage curve fitting with vortex-vortex interaction

We use the same set of IV curves than before and we simulate them thanks to eq. (5.25). We set reasonable superconducting parameters $\lambda_0 = 200$ nm, $T_c = 86.1$ K, and the wire dimensions as $d = 30$ nm and $w = 200$ nm. The only adjustable parameters are the vortex spacing x_0 and the characteristic voltage V_0 . Figure 5.13 displays the IV curves at different temperatures with the simulation based on the modified TAVM model including the vortex-vortex interactions. In log-log scale V_0 corresponds to a vertical offset, while the vortex spacing controls the curve slope. As vortices get closer, the vortex energy raises and consequently the slope decreases. By tuning the two adjustable parameters we succeed in describing the IV curves in the same data range than before for the whole temperature range. However, the simulations become incoherent for $T > 70$ K and $T < 10$ K. In the former case the vortex spacing is smaller than 2ξ though vortices interpenetrate together. At low temperatures the simulated vortex energy is too high compared with the data, even without interactions. The model does not longer correctly describe the experimental observations, another mechanism has to be considered. For the intermediate temperatures the simulation are in agreement with both data and physical sense. In particular, we use consistent physical parameters to perform the numerical simulations.

We carry out the simulation of the IV curves for all the different temperatures by choosing the current range that correctly describes the data and we estimate the vortex spacing x_0 . Figure 5.14(a) shows the temperature evolution of x_0 . Starting from a closely packed vortex layout with $x_0 \approx 4$ nm at 70 K, as temperature decreases the vortices spread

⁷For $x_0 = 128$ nm the energy profile collapses with the curve without interactions.

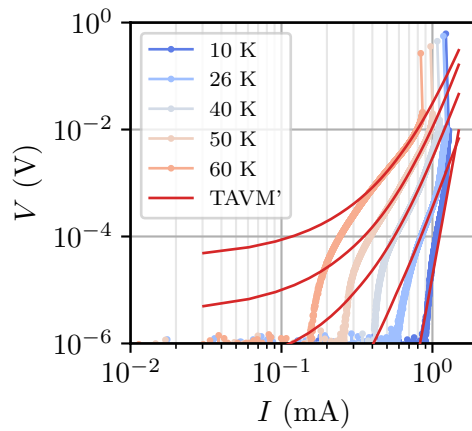


Figure 5.13 – IV curves (dotted line) at different temperatures of C8, a 500 nm long 200 nm wide 30 nm thick YBCO nanowire. The solid red lines are simulation based on the TAVM model including vortex-vortex interaction.

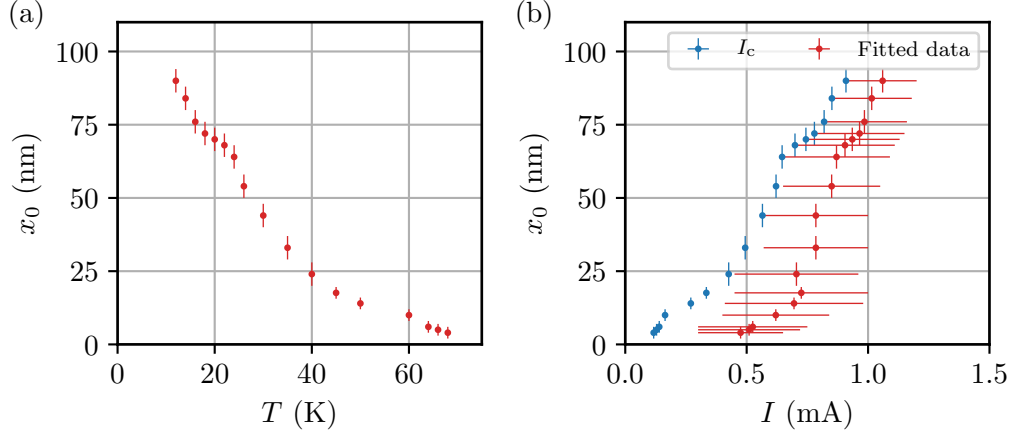


Figure 5.14 – (a) Estimate of the vortex-vortex inter spacing x_0 as a function of temperature in the framework of the TAVM including vortex-vortex interaction. (b) Estimated vortex spacing as a function of the experimental critical current retrieved from the IV curves (blue) and the bias current at which the simulations match with the IV curves (red). For the latter, the horizontal error bars correspond to the bias current range which is well described by the TAVM model with vortex-vortex interaction.

to almost no interaction about 10 K. Thus, the vortex surface density n_v diminishes when the thermal activation is weaker. Naively, we would expect that the ratio $\epsilon'_m/k_B T$ should be higher at low temperatures, thus vortices would have more difficulties in crossing the barrier. As it would create a bottleneck in the vortex motion, thus vortices should be closer, all other things being equal. Such an argument would be in clear contradiction with our observations.

In the case of a lateral vortex row the vortex surface density is proportional to the vortex spacing: $n_v \propto 1/x_0$. Equation (5.2) in section 5.2.1 shows that $n_v \propto (I - I_c)$, that is, the bias current value with respect to the critical current sets n_v . Thus I is probably a better parameter to explain the vortex spacing evolution. We plot in Figure 5.14(b) both the evolution of x_0 as a function of the critical current retrieved from the experimental IV curves, and as a function of bias current at which the simulations match with the IV curves. For a given voltage drop in the IV curve, high temperatures correspond to a low bias current, while at low temperatures the bias current raises, the curve slope is thus inverted compared with fig. 5.14(a). For small vortex spacing, the fitted data range moves away from the critical current; while they are getting closer and eventually touch for large x_0 values. Now, the observation is in qualitative agreement with the previous expectation from eq. (5.2): n_v is larger when the difference $I - I_c$ increases.

In addition, another simplistic model allows one to understand such a dependence. The Lorentz force raises linearly with the bias current. If we consider that it is the predominant force: $v_\varphi \propto I$ where v_φ is the average vortex velocity. So the higher is the bias current the faster move the vortices. Considering that the vortex time-of-flight writes $\tau_0 = w/v_\varphi$, we simply have $\tau_0 \propto 1/I$ that shortens linearly with I . A more rigorous calculation done by Bulaevskii *et al.* [27] showed indeed that the time-of-flight is inversely proportional to the bias current (see eq. (43)). If we consider the average vortex nucleation rate per unit of time R_{vn} and the vortex number in the wire N_v , the time evolution of N_v writes:

$$\frac{dN_v}{dt} = R_{vn} - \frac{N_v}{\tau_0} \quad (5.26)$$

The first term of the right hand side corresponds to the vortex creation, while the second

term represents the vortex annihilation when vortex crosses the whole width w . In the stationary limit ($t \rightarrow \infty$) the solution of eq. (5.26) is:

$$N_v = \tau_0 R_{vn} \quad (5.27)$$

If we suppose that R_{vn} is not varying with respect to temperature and current: $N_v \propto 1/I$. As the vortex number in the chain writes simply $N_v = w/x_0$, the vortex spacing should be proportional to the bias current. This very simple model allows us to understand intuitively why the vortex spacing is higher at low temperatures at which bias current is higher and close to the critical current.

As a conclusion, the intermediate voltage regime in the IV curve after the flux creep behavior is interpreted as a thermally activated vortex motion regime. Vortices cross an energy barrier reduced by the bias current and assisted by the thermal motion. Their crossing generates an average voltage drop. In the case of isolated vortices, if we try to simulate the data with the model, we obtained inconsistent physical value for the London penetration depth. It cannot be reasonably explained by invoking different physical quantities. We included the vortex-vortex interaction energy, and then we simulated the IV curves numerically with only two adjustable parameters. The physical quantities λ_0 and x_0 required to describe the experimental IV curves are now coherent. The evolution of the vortex spacing as a function of the bias current is also physically consistent. In the picture depicted in this section, the vortex crossing seems to be the bottleneck process since we need to include the vortex-vortex interaction. In other words, one vortex is nucleating at one edge and moves along the wire width before the previous one annihilates at the opposite edge.

5.5 Voltage pulse detection

Up to now, we have interpreted the appearance of the DC voltage drop as a consequence of the vortex motion. Transport measurement probes the average effect resulting from the vortices crossing the wire. In this section, we perform voltage pulse detection measurements to probe single vortex crossing. As described by Bulaevskii *et al.* [27] the vortex crossing of a superconducting thin nanowire generates a voltage pulse. In particular, this phenomenon explains partly the dark count rate observed in SSPDs near their critical current. Therefore the section interests are twofold: observing voltage pulses and measuring the corresponding count rates.

5.5.1 Experimental setup

For the purpose of single photon detection, we built up a voltage pulse detection and counting setup as presented in fig. 5.15. The nanowire is placed in the cold plate of the cryostat and connected to the input of a bias tee fixed inside the cryostat. In order to current bias the nanowire, a Yokogawa GS200 current source goes to a 1.9 MHz low-pass filter and feeds the DC part of a Marki BT-0040 bias tee. The filter limits the input noise from the current source.⁸ The output AC part of the bias tee collects the generated voltage pulse. It is connected to a high-pass filter and amplified with a gain G_{in} using a LNF-LNC1_12A cryogenic low noise amplifier fixed onto the 3 K plate of the cryostat. The voltage pulse goes out of the cryostat through a high-pass filter. Then, the signal is amplified using a MITEQ AFS3-00100200-09-CR-4 amplifier with a gain G_{out} . At the end the voltage pulse is either acquired thanks to a Lecroy Wavepro 950 oscilloscope or counted thanks to a SR400 gated photon counter.

⁸Particularly, the Yokogawa GS200 current source produces a noise peak at 80 MHz.

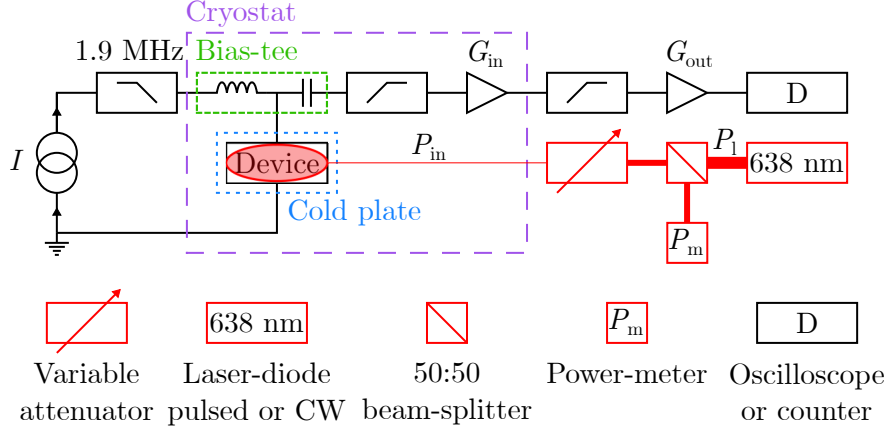


Figure 5.15 – Voltage pulse detection and counting setup. The device is biased at a constant current I through the DC part (inductor) of a bias tee, while the fast RF response is collected through the AC part (capacitor) of the bias tee. The latter signal is filtered, amplified, and connected either to an oscilloscope or to a pulse counter depending on the needs. A laser-diode monochromatic light goes through a (50:50) beam splitter, an attenuator, and finally to the device. The other end of the beam splitter allows one to perform real-time measurement of the average power going to the device.

In addition to the electrical setup, we also mounted a fiber coupled optical path. As depicted by Hadfield in [138], this setup allows us to prove the single photon detection. The device is illuminated by a Picoquant LDH-D-C-640 monochromatic ($\lambda = 638$ nm) picosecond laser diode head controlled by a Picoquant PDL 800-D pulsed diode laser driver. The latter allows one to control the illumination mode, either pulsed or continuous wave (CW), the pulse repetition frequency, and the laser power P_l . The laser beam goes through a (50:50) beam splitter, one part goes to a S151C Thorlabs power meter to measure $P_m = P_l/2$ while the other branch is attenuated. The latter is connected to a vacuum feedthrough with optical fibers going down to the device, illuminating it with a power P_{in} . The optical fiber end is placed at about 5 mm from the device such that the beam diameter is focused on a few millimeters with a radius $r_B \approx 2$ mm. Prior to cooling down the cryostat, we calibrate the optical path by measuring P_m and P_{in} for a given attenuation and various P_l . With such a configuration it is possible to estimate the laser power going to the device while the voltage count rate is measured.

The setup described in fig. 5.15 has been developed first in the 4 K Optidry cryostat previously presented in section 4.1 without the MITEQ low noise cryogenic amplifier placed inside the cryostat. We first observed voltage pulse generated by YBCO nanowires from different samples, both CS and JS type at 5 K. But at that time the peak signal to noise ratio was too important to perform quality measurements of the voltage pulse count rate. In order to limit the voltage noise affecting both the pulse detection and the pulse counting we have performed the measurements depicted in this section in a dilution fridge down to 60 mK. It allowed us to benefit from the additional low noise amplifier and also to cool down at lower temperatures limiting the thermal noise. At the end, the RF output signal from the bias tee is amplified with a gain up to 70 dB with a 3 dB bandwidth of 130 MHz - 1.0 GHz.

5.5.2 Voltage pulse observation

In this section, we study the YBCO nanowire A3 whose dimensions are 150 nm in width, 500 nm in length, and 30 nm in thickness from the same chip as device C8. Globally,

A3 and C8 both display the same characteristics in terms of RT curves and IV curves as presented in table 5.2. In particular, they have a sharp RT transition, they both show reproducible voltage switches in the volt range with a large hysteresis, and similar superconducting parameters.

The nanowire A3 is stuck with silver paste on a sample holder and then wire bounded to the microwave transmission line of a PCB. The device is then connected *via* an SMA RF connector to the input of the bias tee. In such a configuration, the transport measurement characterization of the nanowire can only be done thanks to 2 probes, but we can properly carry the voltage pulse into the RF detection system.

Figure 5.16 shows the IV curve measured at 60 mK with two probes through the DC part of the bias tee. The 35.5Ω resistance in series with the device due to the wire bounds and cables has been subtracted for a better comparison with previous data sets.⁹ We observe the same behavior than for device C8. The critical current is high with $I_c = 741 \mu\text{A}$ corresponding to 13% of the depairing critical current. Once $I > I_c$, a first dissipation regime appears, then the voltage switches abruptly for current higher than $I_s = 789 \mu\text{A}$ with a 0.7 V voltage switch. When the current is ramped down, we observe an important hysteresis due to the Joule heating with a current amplitude of $250 \mu\text{A}$ between I_s and I_r .

At very low temperature, we still observe a dissipation branch. Following our previous interpretations in section 5.4 and section 5.2, it is most likely involving vortex motion. In this temperature range, thermal energy drops making vortex quantum tunnelling a possible mechanism accounting for voltage dissipation, as proposed by Tafuri *et al.* [59] in the case of ultra thin superconducting wire.

⁹The resistance is estimated thanks to the IV curve slope in the superconducting branch.

Table 5.2 – Nanowire superconducting properties summary

Device	d (nm)	l (nm)	w (nm)	T_c (K)	T_{cm} (K)	$\rho(100 \text{ K})$ $\mu\Omega.\text{cm}$	$j_c(5 \text{ K})$ $\text{MA}.\text{cm}^{-2}$
C8	30	500	200	86.1	89.6	297	16
A3	30	500	150	83.1	88.9	334	17

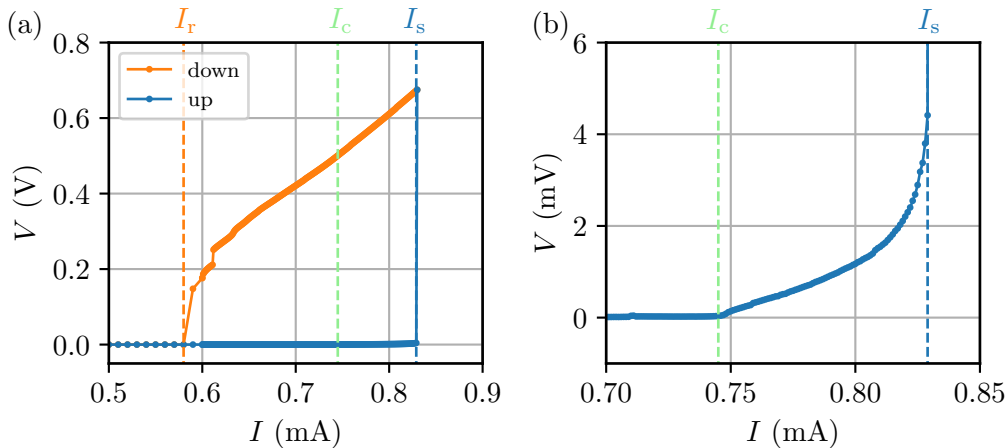


Figure 5.16 – IV characteristic of A3, a 150 nm wide 500 nm long 30 nm thick YBCO nanowire at 60 mK. It corresponds to the device studied in section 5.5. The two panels represent the same data with different scales.

In SSPD, the device is current biased near the critical current such that it remains in the superconducting state. Voltage pulses might be generated without illumination, they are considered as dark counts or false positives. Ejrnaes *et al.* [64] were the first, and the only ones, to observe dark count pulses in YBCO nanowires. Their nanowire dimensions are slightly smaller than the nanowire presented in this thesis in all directions with a 80 nm in length, a 65 nm in width, and a 10 nm in thickness. In terms of superconducting properties, $T_{c0} = 78$ K is a little lowered due to the thinner film, but $j_c = 34$ MA.cm⁻² is rather close to the depairing current. The device exhibits a hysteretic IV curve, but as the wire switches directly to the normal state without any dissipation branch for $I > I_c$, the experimental critical and switching current are identical. At 3 K, the appearance of vortex dissipation in a stable regime is prohibited. Indeed, the phonons are frozen resulting in low thermal conduction which drives the device directly to the resistive state. Thus, they only observed voltage pulses for current below I_c as usually in SSPD.

In the opposite case of Ejrnaes *et al.*, our YBCO nanowire has a voltage drop before the voltage switch. We observe identical voltage pulses nearby the critical current, both above and below I_c at 60 mK and 3 K. When $I < 710$ μ A, we do not observe any voltage pulses with the oscilloscope for a duration of about a dozens of minutes. However, as bias current approaches the critical current, voltage pulses appear. More and more voltage pulses occur as bias current increases further. Figure 5.17 shows the voltage pulses acquired with the oscilloscope in AC mode at 60 mK for two different bias currents I . The upper panel represents a single waveform acquisition with a signal to noise ratio

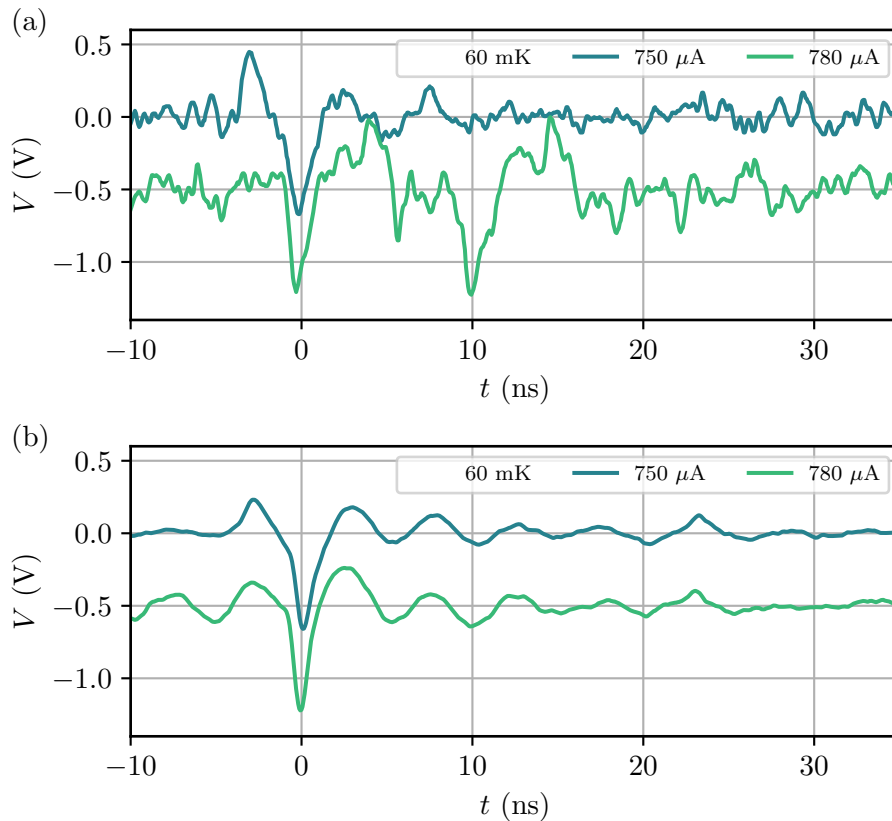


Figure 5.17 – (a) Raw waveforms acquired at two distinct bias currents. (b) Average waveforms on 100 oscilloscope acquisitions at two distinct bias currents. In both panels the waveform at 780 μ A is offset by -0.5 V for convenience purpose. The data are obtained on A3, a 500 nm long 150 nm wide 30 nm thick YBCO nanowire.

about 10. For $I = 750 \mu\text{A} \approx I_c$, one voltage pulse is observed, while for $I = 780 \mu\text{A} > I_c$, we note the appearance of another similar voltage pulse in the time windows. Thus, we expect a higher pulse count rate for the second bias current.

We perform an averaging of the waveform over 100 traces in the lower panel of fig. 5.17 in order to better observe the voltage pulse shape. Obviously, for $I = 780 \mu\text{A}$, the averaging method cancels out the second pulse observed in fig. 5.17(a) since there is no time correlation between the two pulses. Particularly, we see the after pulsing oscillations due to the RF impedance mismatch, and both voltage pulses have globally the same form and time duration of a few ns. Unfortunately, the rise time and fall time are limited by the 1 GHz bandwidth of the RF setup. We cannot retrieve quantitative information on the voltage pulse except that the characteristic time is smaller than 1 ns. Further work should be done to improve the impedance matching on the chip, and to raise the upper cutoff frequency. With such improvements the signal to noise ratio could be enhanced for analyzing in greater details the voltage pulse timing.

5.5.3 Count rate measurement

We are now interested in counting the voltage pulse events occurring in the nanowire. To do so, an analog counter collects the voltage pulse satisfying two specific requirements: the signal edge and the discriminator level V_d . The former might be either rising or falling, while the latter parameter sets the voltage threshold for which the voltage pulse is counted. During a time window of duration $T_i = 1$ s, each time that the signal fulfills those conditions the counter is incremented by 1. Thus the minimum non-zero count rate corresponds to 1 Hz. We then retrieve the total counts number N_c and we compute the detection count rate as $R_t = N_c/T_i$. However, the pulse counter cannot distinguish between two pulses less than 5 ns delayed in time. Hence, the instrument is limited to a counting rate of 200 MHz at most. Additionally the discriminator level should lie in the voltage range $[-300 \text{ mV} ; 300 \text{ mV}]$.

5.5.3.1 Discriminator level dependence of the dark count rate

We set a rising edge counting method. In order to choose correctly the discriminator level V_d , we performed a counting rate experiment making a scan of V_d for different bias currents at 60 mK. It provides complementary information to the voltage pulse measurement and allows us to check that the counting experiment is consistent with voltage pulse acquisition in section 5.5.2. Figure 5.18 shows the evolution of the dark count rate R_d as a function of discriminator level for various bias currents both below and above $I_c = 741 \mu\text{A}$.

For the two lowest bias currents set in the experiment, $0 \mu\text{A}$ and $700 \mu\text{A}$, the data collapse onto the same curve. It can be modelled by a gaussian function represented by the white dashed lines centered at 0 V with an amplitude of 100 MHz and $\sigma = 5$ mV. We attributed this specific form to a gaussian electronic noise. It confirms the oscilloscope observations that there is no voltage pulse for bias currents below $700 \mu\text{A}$.

As bias current raises, the data curve deviates from the gaussian dome. Especially at $730 \mu\text{A}$, in addition to the gaussian curve about 0 V, we observe a gentler slope going to zero counts for both negative and positive V_d . It suggests that other counts than the voltage noise are contributing to R_d . This effect becomes even more important for higher currents with R_d growing for all the discriminator levels except at 0 V.

For $I > 780 \mu\text{A}$, the count rate in addition to the gaussian dome falls down, until the curve can be once again modelled by a gaussian function as represented by the black dashed line. This time, for $I = 815 \mu\text{A}$ the gaussian amplitude is still about 100 MHz but $\sigma = 29$ mV. It suggests that we are only measuring noise for the higher bias current tested. Indeed, in this current range the oscilloscope waveform becomes a lot noisier and

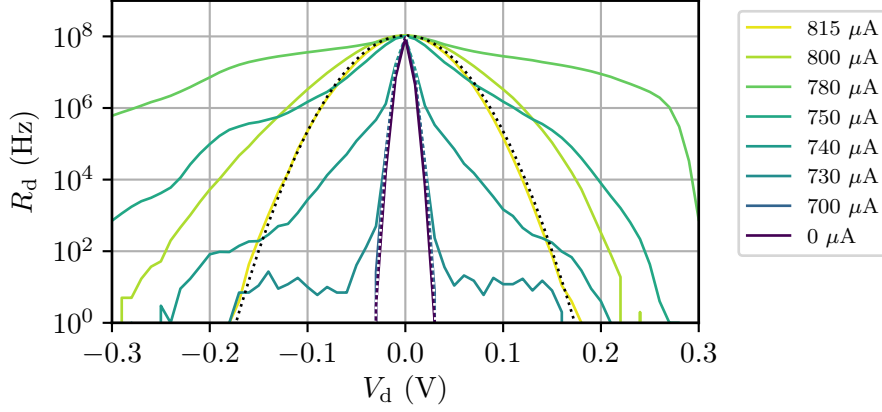


Figure 5.18 – Evolution of the count rate R_d as a function of discriminator level V_d for several bias currents displayed in the legend at 60 mK without illumination. The solid lines represent the measurement data, while the dashed lines are simulated gaussian functions for $I = 0$ A in white and for $I = 815 \mu\text{A}$ in black. The data are obtained on A3, a 500 nm long 150 nm wide 30 nm thick YBCO nanowire.

the voltage pulses are hardly distinguishable. For these reasons, we consider that the measured count rates for $I > 780 \mu\text{A}$ were irrelevant.

We also notice that the asymmetry of the curve becomes more pronounced for intermediate currents about $780 \mu\text{A}$. If we start from $V_d=0$ V and we increase its absolute value, the count rate lowers more rapidly for positive V_d value rather than negative one. This fact comes from the negative value of the voltage pulse. Thus we expect more counts for a negative discriminator level.

We scanned the discriminator level to check the consistency of the pulse counting experiment with the oscilloscope observation. Particularly, we observe the voltage pulses for, $710 \mu\text{A} < I < 780 \mu\text{A}$, while for the other bias currents we are measuring a gaussian noise behavior. The asymmetry of the curve corresponds to the asymmetry of the voltage pulse waveform.

5.5.3.2 Bias current dependence of the dark count rate

In order to characterize an SSPD, the dark count and photon count rates are measured at various bias currents to choose it adequately by mitigating the effect of false positive counts with respect to the true counts. These experiments are also relevant to explore both the origin of the hotspot mechanism and the dark counts. To study the evolution of the count rate as a function of the bias current, we set $V_d = -0.15$ V such that we limit the noise contribution and we measure enough counts. For the following experiments, the counting time window is repeated over 40 times to estimate both the average and the standard deviation for each bias current.

Figure 5.19 shows the evolution of the dark count rate as a function of the normalized bias current I/I_c at 60 mK and 3 K in logarithmic-linear (log-lin) scale. As we saw previously, the count rate increases dramatically when the current raises: from a few Hz to more than 10 MHz. In fig. 5.19(a) at 60 mK and for $I < 0.975I_c$, we observe an important relative errors: the count rate is not well defined. As soon as $I \geq 725 \mu\text{A}$ corresponding to $0.975I_c$, the count rate increases linearly in log-lin scale suggesting an exponential dependence with respect to the normalized current. For $I \approx I_c$, we observe a slope breaking. Above the critical current, the slope increases first and then lowers for

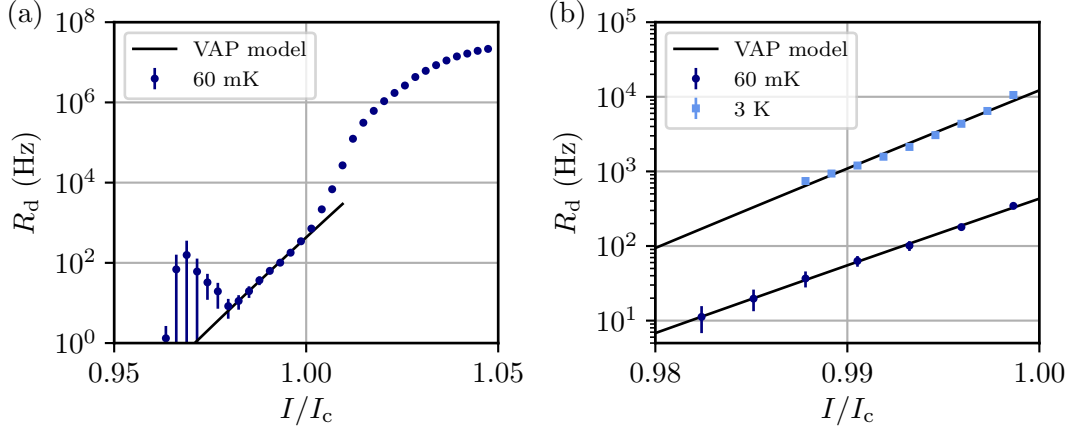


Figure 5.19 – (a) Evolution of the dark count rate as a function of the normalized bias current I/I_c at 60 mK. (b) Evolution of the dark count rate as a function of the normalized bias current I/I_c at 60 mK and 3 K. The black lines are least squares fitting curves using the VAP unbinding rate below I_c given by eq. (5.29). The error bars correspond to 95% confidence intervals.

higher current values.

Different theoretical models may account for dark count rate experiments in SSPDs. If we ascribed the dark count either to single vortex crossing or VAP unbinding, the overall growth of the count rate is intuitive. Indeed, as bias current raises, the Lorentz force increases and the energy barrier lowers accordingly. Hence the vortex crossing events are more likely to happen resulting in a count rate increase. As an example, Bartolf *et al.* [61] have performed simulations of the fluctuation rate of a NbN SSPD according to several dark count models, as depicted in fig. 5.20(a). In the case of YBCO nanowires, Ejrnaes *et al.* [64] have measured the dark count rate in YBCO nanowires as shown in fig. 5.20(b). They have modelled their measurements with a thermally activated vortex-antivortex pair unbinding process, as proposed earlier in NbN SSPD [61–63]. In this model, the vortex-antivortex forming the pairs in the superconducting nanowire are forced to be separated owing to the Lorentz force exerted on opposite directions for the vortex and antivortex. During their motion across the wire, they generate one voltage pulse. Its characteristic time is about one picosecond to one nanosecond depending on the crossing distance and the vortex velocity. Then the vortices and antivortices annihilate to the opposite wire edges.

By combining the vortex-antivortex magnetic attraction with the Lorentz force, Mooij has shown theoretically that the VAP separation $r = 2.6\xi I_c/I$ minimizes the binding energy [270]. According to Bartolf *et al.* [61], the corresponding minimum VAP binding energy writes:

$$U_{\text{VAP}}(T, I) = \frac{A(T)}{\varepsilon} \left[\ln \left(\frac{2.6I_c}{I} \right) - 1 + \frac{I}{2.6I_c} \right] \quad (5.28a)$$

$$A(T) = \frac{\Phi_0^2}{\pi\mu_0\Lambda(T)} \quad (5.28b)$$

where $A(T)$ is the vortex-antivortex interaction constant and ε is the VAP polarizability. In eq. (5.28), we have intentionally omitted the current dependence of the magnetic penetration depth proposed by Bartolf *et al.* [61] since it only increases the penetration depth by 13% at most for $I = I_c$. If temperature is sufficiently high, the VAP may be thermally

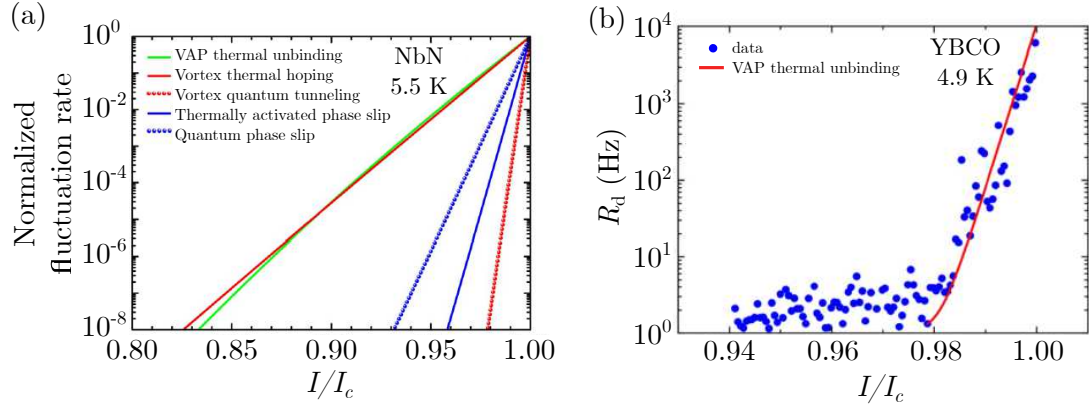


Figure 5.20 – (a) Simulation of the normalized fluctuation rate as a function of the normalized current I/I_c of a NbN nanowire according to different dark count mechanism. Adapted from Bartolf *et al.* [61]. (b) Dark count rate evolution with respect to the normalized bias current I/I_c of YBCO nanowire at 4.9 K. The data are fitted with the VAP thermal unbinding model. Adapted from Ejrnaes *et al.* [64].

unbound, and the corresponding VAP count rate is given by:

$$\Gamma_{\text{VAP}}(T, I) = \Gamma_{\text{VAP}}^0 \exp\left(-\frac{U_{\text{VAP}}(T, I)}{k_B T}\right) \quad (5.29)$$

where Γ_{VAP}^0 is the attempt frequency.

Following the analysis of Ejrnaes *et al.* [64], we performed a least squares fitting of the dark count rate at 60 mK below the critical current using eqs. (5.28) and (5.29) with $A(T)/\varepsilon$ and Γ_{VAP}^0 as fitting parameters. Figure 5.19 shows that the VAP model fitting curve accounts for the dark count rate measurement. Since U_{VAP} is roughly proportional to the normalized current I/I_c , the VAP rate Γ_{VAP} depends exponentially on the current as noted before, which results in a linear current dependence in log-lin scale. More unexpectedly, the fit provides $A(T)/\varepsilon = 1.8 \pm 0.08$ meV which is two orders of magnitude smaller than the value of 0.13 eV reported in [64].

According to eq. (5.28b), if we consider that $\lambda_0 = 200$ nm and $d = 30$ nm, we estimate that $A(T = 60 \text{ mK}) = 2.5$ eV. Such a value is three orders of magnitude higher than what we found for the fitting parameter $A(T)/\varepsilon = 1.8$ meV corresponding to $\varepsilon \approx 1000$. In addition, the VAP polarizability represents how the VAP stretches out, in other words, how the vortex and the antivortex are separated from each other on a distance l_{VAP} . Thus, a rough estimate of the vortex polarizability writes $\varepsilon \approx l_{\text{VAP}}/\xi$ which gives $l_{\text{VAP}} \approx 2 \mu\text{m}$. The estimate of the vortex-antivortex length equals roughly the Pearl magnetic penetration depth below which vortices interact with each other electromagnetically. But, the simulations of the vortex interaction energy in section 5.4 have shown that the vortex interaction becomes relevant below 100 nm. It results that such a VAP is unlikely to exist, all the more so because the wire width is about a few hundreds of nanometer. At last, for $I \approx I_c$, the VAP approaches the minimum separation with $\varepsilon \approx 1$ [61] which is in clear contradiction with our estimate based on the fitting parameter. Moreover, the VAP state is based on the Berezinsky Kostertlitz Thouless model [271, 272] in which VAP binding occurs below the BKT temperature in 2D superconducting film. Despite the fact that the BKT transition has been widely studied in YBCO thin films and single crystals, there is no consensus among the scientific community on its existence [58, 273–276]. Therefore, such an interpretation may be not relevant for the ion irradiated YBCO nanowires.

Additionally, we stress that the measurements presented in fig. 5.19(a) have been performed at 60 mK in the sub kelvin regime in which thermal activation may be irrelevant.

For $T < T_c/2$, Λ is approximately constant with respect to temperature as shown by the measurement of the kinetic inductance as function of the temperature presented in chapter 4. Both vortex-antivortex interaction constant $A(T)$ (eq. (5.28b)) and vortex characteristic energy ϵ_0 (eq. (5.13)) are temperature dependent through Λ . We conclude that they are also constant with respect to temperature for $T < T_c/2$. In eq. (5.29), below half T_c , the only temperature dependence lies in thermal energy $k_B T$. Thus, in the case of a thermally activated process, the slope of the dark count in log-lin scale of fig. 5.19 is inversely proportional to temperature. In order to test the latter assertion, we have also measured the dark count rate as a function of the normalized bias current at 3 K, as shown in Figure 5.19(b). It allows us to compare the dark count rate measurement at two different temperatures varying by two orders of magnitude. In fig. 5.19(b), the two slopes in log-lin at 60 mK and 3 K are almost identical. The measurements are in contradiction with an inverse relationship between the temperature and the slope. We have also performed a least squares fitting according to the thermally activated VAP unbinding for 3 K. In particular, the least squares fitting method estimates that $A/\epsilon = 0.10 \pm 0.009$ eV which is now very similar to the value of .13 eV reported by Ejrnaes *et al.*. But if we estimate the parameter $A(T)/\epsilon k_B T$ for 3 K and 60 mK we obtain $3.9 \times 10^2 \pm 0.3 \times 10^2$ and $3.3 \times 10^2 \pm 0.1 \times 10^2$ respectively. While temperature is varying by a factor 50 and $A(T)$ is almost the same - because Λ is independent of temperature - the slope of the curve is almost unchanged. This observation discredits the thermal activation process itself in the dark count rate observed in the irradiated YBCO nanowires.

As we presented previously in section 2.3.4.1, different mechanisms have been proposed as the dark count origin in SSPD: the phase slip, the single vortex crossing, and the VAP unbinding. They can be either activated thermally or through quantum tunnelling. We have questioned the dark count rate fitting based on thermal VAP unbinding because the activation process seems to be temperature independent, but also because the estimated VAP polarizability is physically inconsistent. The phase slip event is unlikely to happen since both width and thickness are larger than ξ by one order of magnitude at least [16]. A rigorous calculation performed by Bulaevskii *et al.* [27] shows that the phase slip rate is actually very low. On the other hand, we have shown throughout this manuscript that vortex dynamics is responsible of the voltage dissipation in the IV curves. Having discarded the thermal VAP unbinding and the phase slip processes, the vortex hopping is the last mechanism to look at, activated either by thermal motion or *via* quantum tunneling

At first, for large enough current, Bulaevskii *et al.* [27] have shown that the energy barrier for single vortex crossing is roughly half the VAP binding energy barrier. With such a consideration, it is likely that the thermal single vortex hopping will give the same quantitative discrepancy with respect to the temperature dependence than for the thermal VAP unbinding. The simulations performed by Nasti *et al.* [63] and Bartolf *et al.* [61] support the Bulaevskii reasoning. Indeed, the thermal vortex hopping count rate has globally the same normalized current dependence than the thermal VAP unbinding rate as shown by fig. 5.20(a). These arguments disfavor the thermally activated single vortex hopping as the origin of dark count.

Therefore, the vortex quantum tunnelling is the last model to consider. We have seen in section 5.4 that the thermally activated vortex motion model failed to account for the experimental IV curves below 10 K. Nonetheless, the voltage dissipation branch and the vortices are still present as pointed by the Shapiro-like steps observed at 6 K in section 5.3. Further work is needed to model the data using the single vortex crossing model through quantum tunnelling. It will help to validate this physical interpretation.

5.5.3.3 Count rate in presence of laser illumination

Finally, we have tested the possibility of single photon detection in the YBCO nanowire. We repeated the count rate measurement in presence of a continuous laser illumination at 635 nm with the maximum input power available: $P_{\text{in}} = 0.35$ mW. As we see in fig. 5.21, the corresponding count rate in red follows exactly the dark count rate in black: the laser illumination has no influence on R_t . However, when the laser is turned on, the thermometer fixed on the sample holder is heating up. At least, the laser beam goes down to the sample. So, does YBCO superconducting nanowire can detect single photons? At first, it does not seem to be the case. As we saw in chapter 2 there is no predictive and quantitative model embracing all the experimental observations of conventional SSPD like the NbN ones. Though, it is even more difficult to convincingly predict the feasibility of YBCO based SSPD. Thus, the theoretical models do not answer the question, no more than the count rate measurement under illumination presented hereinabove in fig. 5.21. Even so, several other reasons may explain why the laser illumination has no influence on the count rate. They might be related either to the detection setup or to the device itself.

If we focus on the optical setup, the incident photon rate on the nanowire writes:

$$R_i = \frac{P_{\text{in}} \lambda_i}{hc} \frac{wd}{\pi r_B^2} \quad (5.30)$$

where λ_i is the laser wavelength, c is the speed of light, and h the Planck constant. In the right hand side of eq. (5.30), the first term represents the ratio of the incident power at the optical fiber end over the photon energy, while the second term is the aspect ratio of the nanowire over the beam covering area. Since we are studying a 500 nm long wire, the latter ratio is rather small compared with a nanomeander. By considering the wire dimensions and the laser characteristics we estimate that $R_i = 7 \cdot 10^6$ photon.s⁻¹. Though, if each photon had generated a pulse, we would have measured a count rate of 7 MHz. As long as $R_t \geq 0.1 R_d$, the contribution of the photon counts is out of the error bars. Thus, a high count rate $R_t = 7$ MHz could have been measured by the setup and be significantly observable in fig. 5.15. This condition is fulfilled up to $I \approx 1.03 I_c$.

However if we also consider the absorption coefficient α , the total absorbed photon rate writes $R_a = \alpha R_i$. It depends strongly on the laser wavelength and the material thickness. It characterizes the light coupling with the superconducting device. Now, the

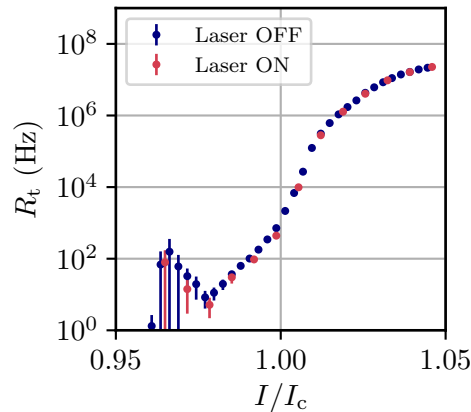


Figure 5.21 – Evolution of the total count rate R_t as a function of the normalized bias current I/I_c at 60 mK for $V_d = -150$ mV without illumination (Laser OFF) and with laser illumination at $P_{\text{in}} = 0.35$ mW (Laser ON). The error bars correspond to 95% confidence interval.

photon count rate can be a lot smaller if the superconducting thin film absorbed only a few photons among the incident photons. Thus, poor light coupling could also explain that we do not observe any influence of the laser. Furthermore, there is no specific patterning for light coupling such as an optical cavity structure [133, 277]. The optical coupling is not optimized. We also stress that we checked with an AFM that there was no remaining resist left after the nanofabrication processes. Thus, it is likely that the optical coupling is poor. Further work could improve it drastically thanks to an optical cavity.

Another approach is to question the superconducting nanowire itself. The YBCO nanowires cross-section studied in this thesis are still large compare to the dimensions of the usual SSPDs. The width is globally of the same order of magnitude about a hundred nanometers. But it is not a stringent parameter as it is possible to detect single photon with micron wide NbN SSPD [278]. As noticed previously in chapter 2, as long as the device presents high quality superconducting properties, the intrinsic detection efficiency could approach unity. In contrast the thickness of 30 nm is rather large. The thin films used in SSPD are generally sub-10 nm thick whatever the material. But comparisons are odious since the material properties are different. According to chapter 2, it is possible that the nanowire cross-section might be not sufficiently small to generate a normal core along the whole thickness. Hence, the subsequent processes of diffusive core spreading and/or vortex assisted detection are inappropriate. This is why the mastering of high-quality YBCO thin film deposition and nanofabrication become crucial to have a chance of detecting single photons.

5.6 Conclusion

In this chapter, we have performed transport and optical experiments in ion irradiated YBCO nanowires in order to probe the vortex dynamics. The measurements have been interpreted in the light of different theoretical models based on vortex motion. How much imperfect those interpretations may be However imperfect those interpretations may be, they provide an overall consistent view of the voltage dissipation generated by the vortex motion both in IV curves and voltage pulse measurements. First, they are linked by the fact that they always arise from a vortex crossing an energy barrier. Depending on various physical parameters - such as temperature, bias current, or RF power - the relevant energy barrier changes and different physical mechanisms are involved.

At first, the low voltage branch of the IV curves is mainly described by a flux creep regime. The vortices are hopping from a pinning site to another *via* Lorentz force and thermal motion. The model is in good agreement with experimental data for temperature below half T_c . It provides further argument for considering pinning as the parameter setting the critical current.

The application of an external RF power demonstrates the appearance of Shapiro-like current steps. We compare the nanowire with a YBCO irradiated Josephson junction. Quantitatively, the results obtained on YBCO nanowires are significantly different than those of a JJ especially as we observe this effect in a wide temperature range. A number of elements are suggesting that the YBCO is not a Josephson junction, but rather a superconducting nanowire experiencing RF synchronized vortex motion. This interpretation leads to the fact that a vortex row is necessarily forming alongside the wire width. The appearance of half-integer step at low temperatures presumes that additional vortex rows open.

We described the intermediate dissipative voltage regime between the flux creep and the voltage switch. In this case, the pinning is no longer relevant because the Lorentz force is sufficiently high. The vortices overpass an energy barrier thanks to thermal activation.

In order to get consistent results, we include the vortex-vortex interaction in an equally spaced vortex row. The model successfully described the IV curve in a large temperature range for $10\text{ K} < T < 70\text{ K}$.

Having all these elements in mind, we conclude that the vortex motion shed light on the dissipative voltage regime prior to the voltage switch. As vortices also play a key role to understand the dark count rate and the single photon detection in SSPD, we performed voltage pulsed detection experiments. As reported earlier by Ejrnaes *et al.* [64], we observed voltage pulses in YBCO nanowires as well. We measure both the dark count rate and the photon count rate as a function of the normalized bias current. The laser illumination has no effect on the count rate. It does not help to prove single photon detection, but it is rather unfavorable in our YBCO nanowire since we have only $0.1\ \mu\text{m}^2$ detection area without a specific optical coupling. However, the study of false positive counts is very instructive. Especially, the fact that the slope of the dark count rate almost does not change with temperature disclaims the interpretation of a thermally activated process. Another mechanism has to be considered to explain this observation. As it does not depend on the temperatures separated by a factor 50, the single vortex quantum tunnelling might be a potential process to look at.

As a summary, the different experiments performed in this chapter improve the understanding of the ion irradiated high-quality YBCO nanowires according to the vortex dynamics. Even though the single photon detection in the devices has not been yet proven, it is still reasonable to believe in its feasibility. Particularly, the dark count experiments are very encouraging. The work presented in this chapter gives a general understanding of the physics involved in high quality YBCO nanowires.

Chapter 6

Voltage switch in YBCO nanowires

Contents

6.1	Switching mechanisms in superconducting devices	146
6.1.1	Vortex instability in superconducting wires	147
6.1.2	Phase dynamics in Josephson junctions	150
6.1.3	Phase slip in one dimensional superconducting wires	151
6.1.4	The Fulton-Dunkelberger transformation	153
6.2	Statistical moments	154
6.2.1	Definition	155
6.2.2	The Kurkijärvi-Garg model	156
6.2.3	Universality of the high order moments	159
6.3	Acquisition of the current distributions	160
6.3.1	Fast current-voltage curve measurement	160
6.3.2	Numerical analysis	162
6.3.3	Dealing with outliers	164
6.4	Estimate of the statistical moments	166
6.4.1	Evolution with temperature	166
6.4.2	Comparison with other devices	168
6.4.3	Evolution with external parameters	170
6.5	Voltage switch triggered by a vortex instability	171
6.5.1	Fingerprint of the Larkin-Ovchinnikov instability	171
6.5.2	The alternative model of Kunchur	173
6.5.3	Concluding remarks	176
6.6	Switching current distributions	177
6.6.1	Observation of multimodal distribution	177
6.6.2	Modelling of the histograms	179
6.6.3	Relation with the vortex instability	180
6.7	Conclusion	181

Thus far, in chapter 4 we examined the hysteresis appearance as the current bypasses the minimal healing current, while in chapter 5 we focused our attention on the nanowire behavior in the dissipative voltage branch prior to the switching current. The latter is related to the vortex motion in the mixed state, while the former is due to the thermal properties in the normal state. The transition from the mixed state to the normal state is characterized by a significant voltage switch at the switching current.

In standard SSPDs, the dissipative regime does not exist: the wire goes directly from the pure superconducting state to the normal state. By studying the switching current distribution (SCD) in NbN superconducting nanowires, Murphy *et al.* [65] attributes the switching event to phase slip processes like in 1D superconducting nanowires [70, 72, 267, 279, 280]. Such switching current statistics have also been widely studied in Josephson junctions [66, 68, 69, 76, 281–288]. In this case, it is caused by a phase escape out of the washboard potential according to the RCSJ model. For both cases, the switching event can be either thermally activated or due to quantum tunnelling. As previously explained in chapter 2 and in chapter 5, neither of the two interpretations should apply in the case of the YBCO nanowires studied in this thesis. The dimensions are too large for a phase slip to occur and the superconducting nanowire properties, such as the critical current density or the critical temperature, are so high that the devices are unlikely to be a Josephson junction. Voltage switches have also been studied in YBCO microbridges. In this case, it arises from a vortex instability that triggers the device to the normal state. In order to clarify the underlying physical phenomenon, the present chapter is devoted to the study of the voltage switch in YBCO irradiated nanowires.

At first, we will give a brief description of different physical mechanisms related to the voltage switch. We are mostly interested in the ones arising from the vortex instabilities in superconducting wire. Nevertheless, we also present the models for 1D superconducting nanowire and Josephson junction respectively. Then, we will define the different statistical moments presented in this chapter along with their expected evolution in specific cases. In order to acquire a large data set of switching currents we developed a specific experimental setup along with a numerical analysis procedure. We will then present the evolution of the statistical moments with different set of parameters and compare them with the model expectations for JJs and 1D superconducting nanowire. We will further investigate the voltage switch in the framework of a voltage instability with measurements under the application of an external magnetic field. Finally, we will gather various information introduced in this chapter to interpret the SCDs. Those different measurements will give a better insight of the voltage switch origin in our YBCO nanowires.

6.1 Switching mechanisms in superconducting devices

The voltage switch behavior has been reported in a wide range of superconducting devices such as Josephson junctions [66–69], 1D superconducting nanowires [70–72], and HTS nanowire [39, 73–75]. We are mainly interested in the latter description since it involves vortex dynamics compatible with the previous vortex motion interpretations presented in chapter 5. Besides, considerable scientific researches have studied the switching statistics of JJs and 1D superconducting nanowire, both experimentally and theoretically. It is of particular interest to introduce the corresponding physical phenomena for each device type though. It provides a good comparison too distinguish between the different switching mechanisms.

6.1.1 Vortex instability in superconducting wires

In the presence of an electric field, the non-linear effects arising from the non-equilibrium quasiparticle distribution have been predicted by Larkin and Ovchinnikov in 1974 [83]. The Larkin-Ovchinnikov (LO) mechanism schematized in fig. 6.1(a) is the following. In a biased current superconducting film, the vortices move under the Lorentz Force. This creates an electric field across the vortex core. The quasiparticles which are trapped in the core, because of the surrounding gap, start moving and gain more energy. At the edge of the vortex, the Andreev reflection create a hole, which is in turn accelerated under the same electric field. Such a process repeats at each edge of the vortex core until the energy of the quasiparticles becomes higher than the gap. Then, the quasiparticles escape out of the vortex and diffuse around. As a consequence, the volume of the vortex core shrinks and a homogeneous out of equilibrium density of quasiparticles surrounds the vortex.

In the framework of LO theory, the vortex velocity v_φ raises as it feels a lower viscous damping η_φ expressed as:

$$\eta_\varphi = \frac{\eta_{\varphi 0}}{1 + \left(\frac{v_\varphi}{v_\varphi^*}\right)^2} \quad (6.1)$$

where $\eta_{\varphi 0}$ is the damping coefficient of a motionless vortex and v_φ^* is the critical velocity. As v_φ approaches v_φ^* , the damping monotonically decreases and the system becomes strongly non-linear. Thus, the voltage drop increases rapidly as the current raises in the IV curve and the device switches to a different state when $v_\varphi = v_\varphi^*$. This manifests itself in an abrupt voltage switch in the current-biased IV characteristic at the switching point denoted as (I_s, V_s) . According to the LO theory, the switching velocity v_φ^* writes:

$$v_\varphi^* = \sqrt{\frac{D_{\text{qp}}}{\pi\tau_{\text{in}}}} \left[14\zeta(3) \left(1 - \frac{T}{T_c}\right) \right]^{1/4} \quad (6.2a)$$

$$D_{\text{qp}} = \frac{v_F l_0}{3} \quad (6.2b)$$

where D_{qp} is the quasiparticles diffusion constant given by eq. (6.2b), v_F is the Fermi velocity, l_0 is the electronic mean free path, τ_{in} is the inelastic scattering time of quasiparticles, and ζ is the Riemann zeta function. From eq. (6.2), as the sample is considered

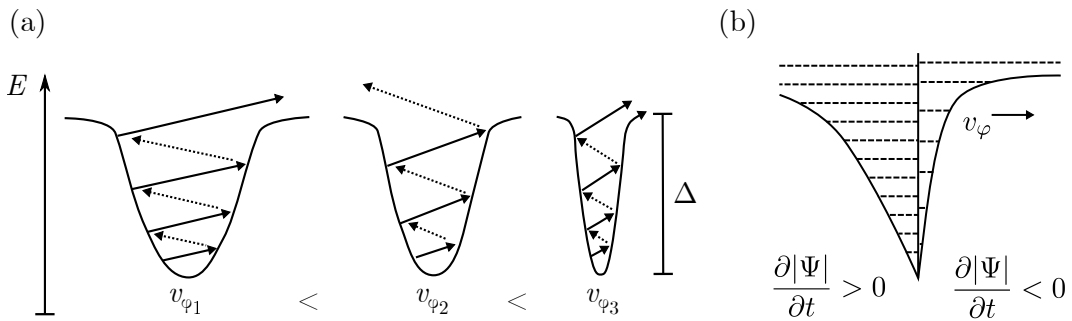


Figure 6.1 – (a) The electric field accelerates the quasiparticles in the vortex core that reflect on the vortex core edges. The quasiparticles gain sufficient energy to go out of the vortex core potential resulting in a vortex core shrinkage. Adapted from Doettinger *et al.* [289]. (b) Asymmetric vortex potential considered by Vodolazov *et al.* to include the vortex deformation along behind the vortex motion wake. Adapted from Vodolazov *et al.* [290].

into the flux flow regime the corresponding switching voltage V_s is expressed as:

$$V_s = v_\varphi^* \mu_0 H l \quad (6.3)$$

where l is the sample length and H is the external magnetic field. Thus, by varying H and measuring V_s at the abrupt voltage switch, it is possible to estimate the critical velocity v_φ^* using eq. (6.3). It follows that the inelastic scattering time may be estimated using eq. (6.2).

Experimentally, the LO instability has been observed in various superconducting thin films such that $w > \Lambda_0$ [73, 77–81]. This electronic instability has two main fingerprints: IV curves without hysteresis below the switching point, and a constant critical velocity as a function of a low external magnetic field compared to H_{c2} [78]. To confirm the latter characteristic, the IV curve is measured while an external magnetic field is applied and the switching velocity is estimated using eq. (6.3) [73, 77, 84]. The absence of hysteresis below the switching point allows one to rule out any phenomenon related to a thermal runaway effect. Indeed, the LO instability is mainly driven by the high Lorentz force exerted at high current rather than by temperature or external magnetic field effect.

Figure 6.2 shows typical experimental curves of a YBCO bridge interpreted in the framework of the LO instability. In fig. 6.2(a), we see that starting from $T = 89.5$ K the curve is continuous. As temperature lowers, the switch is triggered at lower voltage and the dissipative voltage range is reduced accordingly. If the same experiment is performed at different applied magnetic fields rather than different temperatures, a similar behavior is observed. The voltage switch is reduced while H is raised and it is completely suppressed for high enough magnetic field. Figure 6.2(b) shows the critical velocity extracted from the IV curves as a function of the magnetic field. Whatever the temperature, v_φ^* is constant as a function of H .

Since the experiments measure average transport properties, they do not provide any information about the vortex configuration near the instability. In order to give insights of such a configuration, Vodolazov and Peeters [290] performed TDGL calculations in a superconducting slab. They studied the evolution of the order parameter at different working point of the IV characteristic, with and without external magnetic field, as depicted in fig. 6.3. In the model proposed by Vodolazov and Peeters, the vortex moves with a velocity v_φ , the quasiparticles distribution in its core evolves with a time $\tau_\varphi \sim \xi/v_\varphi$. If τ_φ becomes smaller than the quasiparticles relaxation time, it results in a non homogeneous

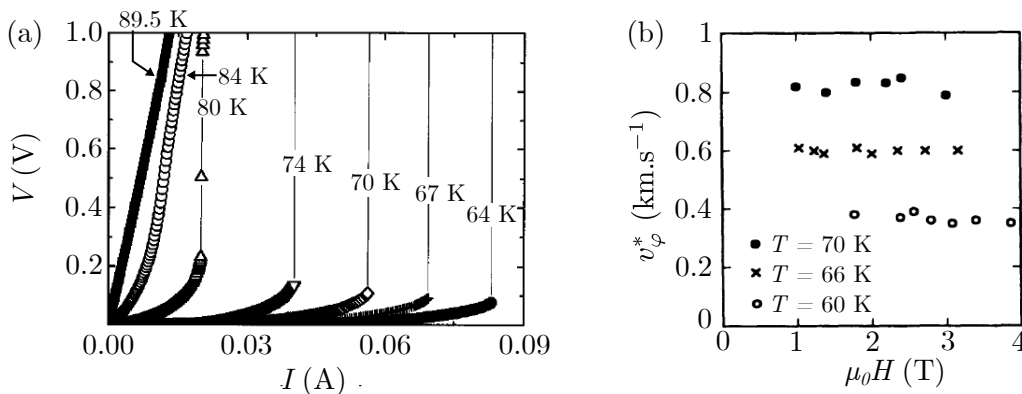


Figure 6.2 – (a) IV characteristic of a $5 \mu\text{m}$ wide $100 \mu\text{m}$ long YBCO bridge on a 250 nm thick film deposited on $\text{CeO}_2/\text{Al}_2\text{O}_3$ substrate measured at different temperatures. Adapted from Xiao *et al.* [75]. (b) Critical flux flow velocity as a function of an external perpendicular magnetic field of a YBCO bridge. Adapted from Doettinger *et al.* [73].

distribution of the quasiparticles out of equilibrium. In particular, the quasiparticles behind the vortex do not go back to equilibrium as fast as the quasiparticles in front of the vortex. They included such a behavior as an asymmetric vortex core becomes along the vortex motion wake, as depicted in fig. 6.1(b). In fig. 6.3(a), for small bias current in the dissipative voltage branch (1), the vortices form a dynamical triangular lattice. As current is swept up the vortex lattice is significantly deformed (2). The vortices tend to form vortex rows with both slow and fast velocities (3), keeping the vortex density constant in the system. For higher current, the latter configuration is no longer stable, the vortex rows merged together leading to a lower number of fast vortex rows (4). The fast vortex rows are called quasi-phase slip lines since the vortices are so fast that the quasiparticles have no time to relax back to equilibrium between two subsequent vortices. While the superconducting slab goes from state (3) to (4), we notice an abrupt voltage switch. If the simulation is performed with $H = 0$, the vortex density is smaller, but a similar fingerprint is observed in fig. 6.3(b). In addition to the vortex nucleation at the left side, antivortices are nucleating at the opposite edge and move in the opposite direction from right to left. The vortices and antivortices annihilate in the middle of the slab with an increasing rate as the current raises. As in the previous case in presence of a magnetic field, we observe a vortex configuration transition from the state (2) to (3) in which the quasi-phase slip lines. These simulations demonstrate that there is a substantial transformation of the vortex arrangement from a triangular lattice to a set of parallel fast vortex rows. The transition is accompanied by an abrupt voltage switch in the IV curve of a superconducting slab.

The theoretical and experimental work presented in this section supports the idea that the acceleration of vortices at high bias current leads to an instability of the vortex configuration. It results in a runaway process responsible for a voltage switch. However, little

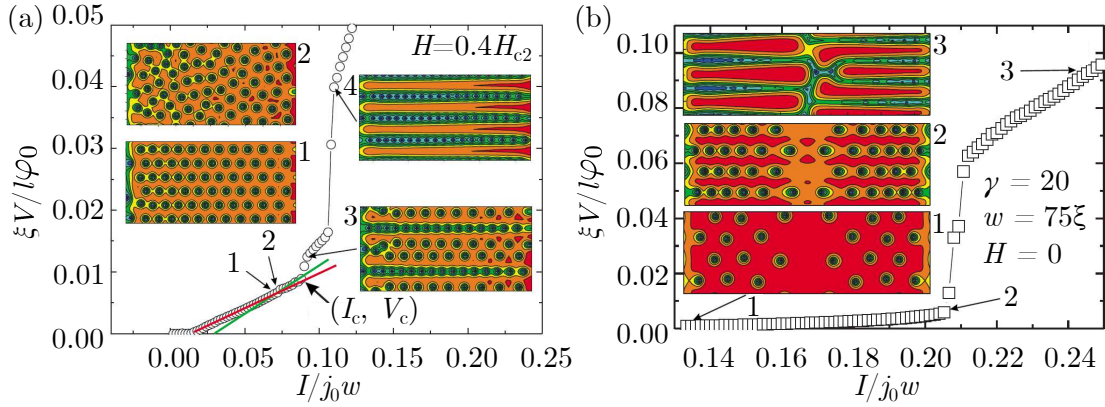


Figure 6.3 – (a) IV curve of a superconducting slab under the application of an external magnetic field H . As I increases, (1) the initial triangular vortex configuration becomes distorted (2). (3) At sufficiently high current, the vortex configuration rearranges itself with a coexistence of fast vortex rows (green blue lines) and slow vortex rows (vortex core separated by orange). (4) After the voltage switch, the slow vortex rows disappear, while the fast vortex rows form quasi-phase slip lines. Adapted from Vodolazov *et al.* [290]. (b) IV curve of a superconducting slab without magnetic field. (1) Vortices and antivortices nucleate at the left and right edge respectively, and they move toward opposite edges compared to their nucleation edge. (2) As current raises prior to the voltage switch, they form parallel rows and annihilate at the middle of the bridge. (3) When the current bypasses the switching point, vortices and antivortices accelerate further and form parallel quasi-phase slip lines. Adapted from Vodolazov *et al.* [290]. The insets represent snapshots of the superconducting order parameter at specific bias currents I labelled by numbers.

is known about the switching event statistics in superconducting nanowire experiencing vortex motion. In this respect, it is of particular interest to perform statistical study of the switching event to gain further insight into the mechanism involved. Such a statistical work has been treated extensively in JJs and 1D superconducting nanowires. That is why it is relevant to introduce the reported results in such devices to compare the voltage switches in our nanowire with the existing models. Hereinbelow, we will briefly introduce the main physical interpretations along with their theoretical models.

6.1.2 Phase dynamics in Josephson junctions

The phase dynamics in underdamped Josephson junctions has arisen considerable theoretical and experimental interest in both LTSs [68, 282–285] and HTSs [69, 286–288], with the aim to see a macroscopic quantum tunnelling (MQT) effect [76, 281, 291]. The phase difference across an underdamped JJ is a macroscopic metastable system. Its dynamics is analogous to the one of a particle in a tilted washboard potential as schematized in fig. 6.4. If the temperature is sufficiently high, the phase particle trapped in a local minimum escape toward a lower energy state thanks to thermal activation (TA). Additionally, if the damping is low enough $Q \gg 1$, the phase particle keeps running to the successive local minima.

The particle motion triggers a voltage switch to a resistive state corresponding to a switching event in the IV curve. The SCD measurements have turned to be an usual method to investigate the phase dynamics in such a system. At low temperature, the thermal fluctuations are so small that the quantum tunnelling rate becomes predominant with respect to the TA rate: this is the MQT process. In the same spirit, the MQT also generates a running state and a voltage switch. But unlike the TA mechanism, the MQT is independent of temperature.

Depending on the temperature range, either MQT or TA phase escape is dominant. In order to determine the crossover temperature T_q separating the two regimes, it is necessary to know the corresponding switching rate. According to Kramers theory [292] followed by Büttiker *et al.* [293], the TA switching rate Γ_{TA} in a JJ writes:

$$\Gamma_{TA} = a_t \frac{\omega_p}{2\pi} \exp\left(-\frac{\Delta U}{k_B T}\right) \quad (6.4)$$

where ω_p is the plasma frequency of the particle oscillating at the bottom of the well and $a_t \approx 1$ is a corrective term. Knowing the energy barrier ΔU to overcome, it is possible to

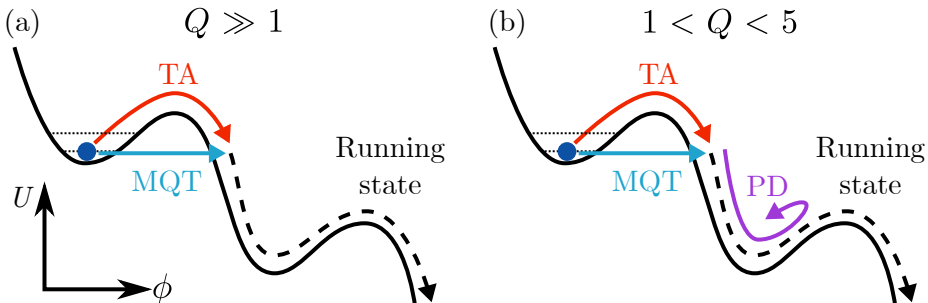


Figure 6.4 – Evolution of the phase of a JJ in a tilted washboard potential. (a) For low dissipation $Q \gg 1$, the phase particle undergoes a transition to a lower energy state *via* thermal activation (TA) or macroscopic quantum tunnelling (MQT). (b) For moderately damped JJ $1 < Q < 5$, the phase particle is likely to be retrapped in a subsequent local minima due to the phase diffusion (PD) process. Adapted from Massarotti *et al.* [291].

determine ω_p and thus the exact formula of eq. (6.4).¹ In the case of the MQT switching for a JJ, the calculation performed by Caldeira and Leggett [294] gives the MQT switching rate Γ_{MQT} as:

$$\Gamma_{\text{MQT}} = a_q \frac{\omega_p}{2\pi} \exp\left(-\frac{7.2\Delta U}{\hbar\omega_p} \left(1 + \frac{0.87}{Q}\right)\right) \quad (6.5)$$

As before, the terms a_q and ω_p can be computed to determine the exact switching rate of the JJ. By equating eqs. (6.4) and (6.5), it is possible to infer the crossover temperature at which the thermal and quantum fluctuations are equal. Therefore, it becomes more convenient to write eq. (6.5) as:

$$\Gamma_{\text{MQT}} = \frac{\omega_p}{2\pi} \exp\left(-\frac{\Delta U}{k_B T_{\text{es}}}\right) \quad (6.6)$$

where T_{es} is the effective escape temperature such that $\Gamma_{\text{MQT}} = \Gamma_{\text{TA}}$. Now, we clearly see that both MQT and TA are equivalent mathematically speaking. The only difference is that T_{es} in eq. (6.6) is temperature independent, while eq. (6.4) depends on temperature.

In the case of moderately damped JJ - typically for $1 < Q < 5$ - an additional process has to be accounted: the phase diffusion (PD) or retrapping event [291, 295–298]. When the phase particle is running through the washboard potential, it diffuses and loses its energy accordingly. It results in a retrapping of the particle in one of the subsequent local minimum as depicted in fig. 6.4(b). Afterwards, it may eventually escape another time *via* TA or MQT process. Under such conditions, the retrapping rate has to be considered to fully account for the experiments.

The phase escape dynamics is intrinsically stochastic since it is triggered by the fluctuations. For this purpose, its statistics has been studied to gain further information of the SCD. We will treat this aspect along with the 1D superconducting nanowire which exhibits a similar behavior and can be treated in an analogous way.

6.1.3 Phase slip in one dimensional superconducting wires

For 1D superconducting nanowires, the switching behavior arises from a phase slip event [70, 72, 280, 299]. It might be either a single phase slip [70, 279] or multiple phase slips (MPS) [70, 279, 300]. In addition, it is worth noting that Pekker *et al.* [279] have related the low number of MPS in NbTiN SSPD to the low dark count rate. Therefore, the study of the phase slip is also of interest to understand the properties of the SSPD.

As presented previously in chapter 2, the phase slip occurs when the superconducting order parameter change by 2π between two distinct current carrying states. They are separated by the free-energy barrier at zero bias current $\Delta F(T)$ written as:

$$\Delta F(T) = \frac{\sqrt{6}\hbar I_d(T)}{2e} \quad (6.7)$$

where I_d is the theoretical depairing critical current without fluctuations. When fluctuations become sufficiently high, the energy barrier separating the two distinct states might be crossed. It results in a dissipative state which is responsible for the appearance of a resistance below T_c prior to the superconducting normal transition. As temperature decreases with respect to T_c the fluctuations are not sufficient to trigger a phase slip event. If the superconducting wire is current biased near I_d the energy barrier might be sufficiently lowered such that phase slips occur. The free-energy barrier in presence of a bias current writes:

$$\Delta F(T, I) = \frac{\sqrt{6}\hbar I_d(T)}{2e} \left(1 - \left(\frac{I}{I_d(T)}\right)^{5/4}\right) \quad (6.8)$$

¹The exact expressions can be found in the following articles [283, 293].

In eq. (6.8), we clearly see that ΔF decreases as I approaches I_d . Therefore, even at temperatures far from T_c , it is possible to trigger a phase slip. As in the case of JJ, it might be triggered by thermal or quantum fluctuations. Knowing the energy barrier profile, it is possible to derive the phase slip rate in both cases. In particular, the thermally activated phase slip (TAPS) rate $\Gamma_{\text{TAPS}}(T, I)$ writes:

$$\Gamma_{\text{TAPS}}(T, I) = \frac{\Omega_{\text{TAPS}}(T)}{2\pi} \exp\left(-\frac{\Delta F(T, I)}{k_B T}\right) \quad (6.9)$$

where $\Omega_{\text{TAPS}}(T)$ is the attempt frequency. Similarly, for quantum fluctuations, we can associate an effective quantum temperature T_q such that the quantum phase slip (QPS) rate $\Gamma_{\text{QPS}}(T, I)$ is expressed as:

$$\Gamma_{\text{QPS}}(T, I) = \frac{\Omega_{\text{QPS}}(T)}{2\pi} \exp\left(-\frac{\Delta F(T, I)}{k_B T_q}\right) \quad (6.10)$$

where $\Omega_{\text{QPS}}(T)$ is the corresponding attempt frequency. Like for JJs, by equating eqs. (6.9) and (6.10) it is possible to derive the crossover temperature between the quantum and the thermal regimes.

Whatever the fluctuations, the origin of the switching voltage in 1D superconducting nanowires is the same. When a phase slip occurs, heat is generated in the wire which raises locally the temperature. The phase slip rate, whether $\Gamma_{\text{TAPS}}(T, I)$ or $\Gamma_{\text{QPS}}(T, I)$, increases accordingly as long as the wire is hotter. If another phase slip happens prior to complete cooling, the phase slip rate will raise again, and so on and so forth. The appearance of successive phase slips before cooling generates a thermal runaway and turns the wire into a normal state: it generates a voltage switch.

Simulations performed in Sahu PhD thesis [70] support this interpretation, as depicted in fig. 6.5(a). When a few number of phase slips - typically 1 to 3 - happens almost at the same time, temperature raises of about 0.1 K. If the phase slip number increases or if the phase slips occur closer in time, temperature abruptly goes up and the device switches to the normal state fig. 6.5(b). Since the fluctuations trigger the switching event, the voltage switch in 1D superconducting nanowires is inherently a stochastic process like the one

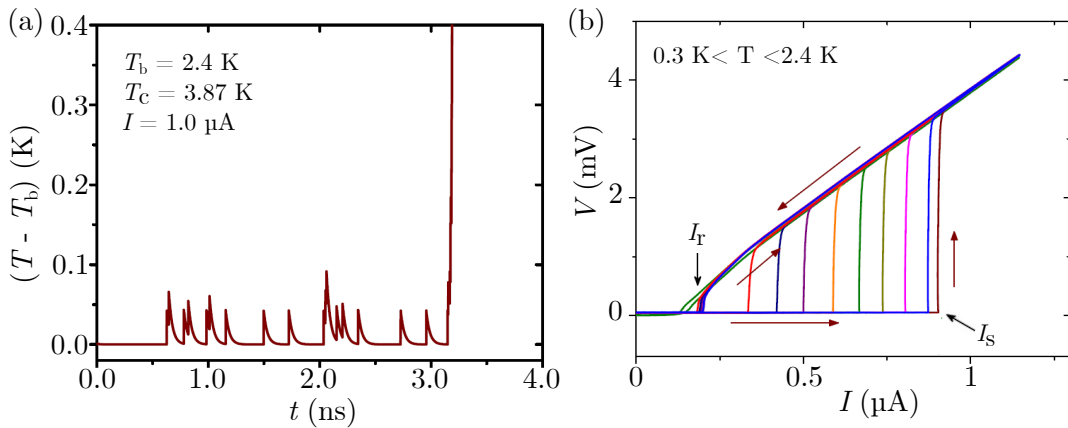


Figure 6.5 – (a) Simulation of thermal pulses in a 1D superconducting nanowire caused by phase slip events. If successive phase slip events occur close enough in time, the temperature overpasses T_c and the wire switches to the normal state. (b) IV curves at different temperatures measured in a MoGe 1D superconducting nanowire. The black arrows with I_s and I_r denote the switching and retrapping current respectively. Adapted from Sahu PhD Thesis [70].

for JJs. For this reason, the phase slip cascade may be triggered at different switching currents I_s near the depairing critical current. On the contrary, if the fluctuations are removed, the wire would switch at the same deterministic switching current each time the experiment is repeated. That is why the switching event is usually studied in terms of switching current statistics. This aspect will be covered in greater details afterwards in sections 6.1.4 and 6.2.

Experimentally, the voltage switch is observed in the IV curve like the one presented in fig. 6.5(b). If the current is swept up from the zero voltage superconducting branch, at some point the nanowire switches abruptly to the normal Joule heating state at the switching current I_s . When the current is swept down, the wire goes back to the superconducting state always at the same retrapping current value I_r whatever the temperature. It results in an important hysteresis in the IV characteristic. This is quite similar to what we observe in the irradiated YBCO nanowires, though we also stress that there are substantial differences. The dissipative voltage regime in the superconducting state is more pronounced, and the retrapping current evolves largely with temperature. Nevertheless, this fact cannot discriminate whether the voltage switch is generated by a phase slip or a vortex instability.

In order to distinguish the origin, we will present in section 6.1.4 how we can relate the phase slip rate introduced previously with the SCD. We will then present in section 6.2.2 the main results expected according to the Kurkijärvi-Garg theory which encompasses the voltage switch statistics in both JJs and 1D superconducting nanowires. They will serve as guidelines to understand the switching mechanism in the irradiated YBCO nanowires.

6.1.4 The Fulton-Dunkelberger transformation

Experimentally, it is difficult to have a direct access to the switching rate and to test the corresponding models described previously in this section. Fulton and Dunkelberger [67] proposed an alternative way to obtain the switching rate as follows. They measured several times the switching current I_s by repeating the IV curve acquisition. Then, they estimated the probability density function of the SCD in the form of a discrete histogram. Thanks to the use of the eponym Fulton-Dunkelberger (FD) transformation, they converted the SCD into the switching rate. Using this technique they studied the evolution of the switching rate with various parameters. The switching rate is more fundamental since it does not depend on the way the current is swept in the IV curve acquisition.

We consider the discrete SCD, as $p(I_k)$ being the probability that the device switches in the interval $[I_k - \Delta I/2, I_k + \Delta I/2]$ with ΔI being the current bin size. If we measure experimentally N times the IV curves, all other things being equal, the probability $p(I_k)$ is simply estimated as:

$$p(I_k) = \frac{N_k}{N} \quad (6.11)$$

where N_k is the number of IV curves that have switches in the interval $[I_k - \Delta I/2, I_k + \Delta I/2]$. It follows that the FD transformation used to convert $p(I_k)$ in the switching rate Γ_s writes:

$$\Gamma_s(I_k) = \frac{\nu_I}{\Delta I} \ln \left(\frac{\sum_{j=k}^m p(I_j)}{\sum_{i=k+1}^m p(I_i)} \right) \quad (6.12)$$

where $\nu_I = dI/dt$ is the current sweep rate, ΔI is the current bin size of the histogram, and m corresponds to the bin index with the highest I_s value.

Figure 6.6 shows typical SCD measurements performed by Aref *et al.* [280] in a MoGe 1D superconducting nanowire along with the corresponding switching rates calculated

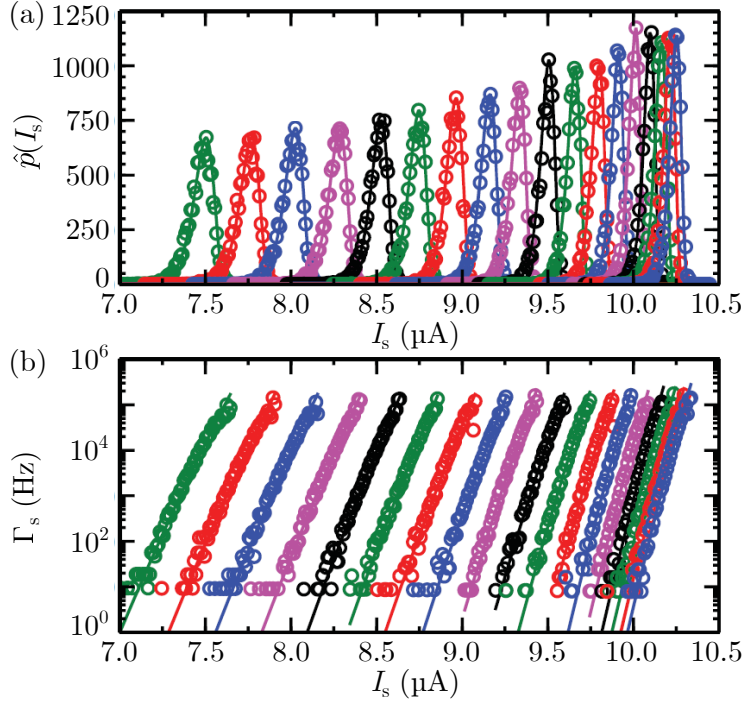


Figure 6.6 – (a) Measurements of the SCDs at different temperatures in a MoGe 1D superconducting nanowire. The switching current probability $\hat{p}(I_s)$ corresponds to the counts, thus the SCD is not normalized to unity. (b) Switching rate derived from the SCD in (a) thanks to the FD transformation. Circles represent data points while solid lines are fitting curves according to the generalized Kurkijärvi-Garg (KG) model with $b = 3/2$. Such a model will be presented in section 6.2.2. Adapted from Aref *et al.* [280].

following the FD transformation given by eq. (6.12). As temperature lowers, the SCD goes toward higher I_s value and narrows. As SCD is converted into the switching rate Γ_s , Aref *et al.* fitted the switching rate with the PS switching rate formula given in section 6.1.3 as presented by solid lines. Therefore, they have verified that the theoretical current dependence of Γ_s correctly accounts for the experiment.

Up to now we introduced the main physical ingredients to feed our reflection on the vortex instability and the switching behavior in both JJs and 1D superconducting nanowires. There is no such a development for superconducting nanowire experiencing LO instability. Though, we will verify whether the models developed in the case of JJs and 1D superconducting nanowires apply for a voltage switch arising from a vortex instability in nanowires.

6.2 Statistical moments

In the previous section we only saw the SCD interpreted in terms of a switching rate thanks to the FD transformation. In order to push forward the statistical analysis, we introduce in this section statistical moments of interest. Their expression will be used later on to present the expected evolution of such moments in the known cases of the JJs and the phase slips in 1D superconducting nanowire. It will be another guidelines to interpret the SCDs in the ion irradiated YBCO nanowire.

6.2.1 Definition

The statistical moments are parameters characterizing any distribution of a random variable X . In our case, X is either the switching or the retrapping current. We limit ourselves to the first four moments commonly used: the expected value, the standard deviation, the skewness, and the kurtosis. We consider a discrete random variable X with probabilities $\{p_i\}$ associated to finite values $\{X_i\}$ with $\sum p_i = 1$. The first order statistical moment is the theoretical expected value of X denoted as $\mathbb{E}[X]$ and written as:

$$\mathbb{E}[X] = \sum_{i=1}^n p_i X_i \quad (6.13)$$

Experimentally, we do not have access to the probabilities. In order to estimate the expected value, we repeat the experiment n times to obtain a sample $\{X_i\}$ of the overall population X . Then the estimator of $\mathbb{E}[X]$, namely the arithmetic mean or average specified as \bar{X} , is simply given by:

$$\bar{X} = \sum_{i=1}^n \frac{X_i}{n} \quad (6.14)$$

In addition, we introduce the k^{th} central moment denoted as $\mu_k(X)$ and expressed as:

$$\mu_k(X) = \mathbb{E} \left[(X - \mathbb{E}[X])^k \right] \quad (6.15)$$

where k is the moment order. In contrast to the first statistical moment, it is centered with respect to the expected value of X .

The second order central moment is the variance μ_2 . But it is more useful to define the standard deviation as $\sigma = \sqrt{\mu_2}$. Using eq. (6.15), it simply writes:

$$\sigma(X) = \sqrt{\mathbb{E} \left[(X - \mathbb{E}[X])^2 \right]} \quad (6.16)$$

It characterizes how much the values are spread apart from the expected value. In order to estimate the standard deviation, we use the unbiased estimator² of the standard deviation $\hat{\sigma}$ written as³:

$$\hat{\sigma}(X) = \sqrt{\frac{1}{n-1} \sum_{i=1}^n (X_i - \bar{X})^2} \quad (6.17)$$

In order to define the high-order moments⁴, such as the skewness and the kurtosis, we introduce the k^{th} standardized moment as:

$$\gamma_k(X) = \frac{\mu_k}{\sigma^k} = \mathbb{E} \left[\left(\frac{X - \mathbb{E}[X]}{\sigma} \right)^k \right] \quad (6.18)$$

It follows that the skewness and the kurtosis correspond respectively to the 3rd and 4th standardized moments, respectively denoted as γ_3 and γ_4 . They are estimated in the same spirit as the standard deviation in eq. (6.17):

$$\hat{\gamma}_3(X) = \frac{1}{n\hat{\sigma}^3} \sum_{i=1}^n (X_i - \bar{X})^3 \quad (6.19)$$

²For the biased estimator, $n-1$ is replaced by n in eq. (6.17). If $n = 10000$, the ratio between the biased and the unbiased standard deviation estimator is only 0.01%. Thus there is not a significant difference in this case.

³Aside from the mean, we put a caret symbol $\hat{}$ on the statistical parameter that corresponds to the estimate.

⁴In the manuscript, we define the high-order moments as the statistical moments whose corresponding moment order is equal or higher than 3.

$$\hat{\gamma}_4(X) = \frac{1}{n\hat{\sigma}^4} \sum_{i=1}^n (X_i - \bar{X})^4 \quad (6.20)$$

The skewness defines the distribution asymmetry. If the skewness is positive, the distribution has a longer right tail, it is considered a right skewed distribution. In the opposite case, if it is negative, the distribution has a longer left tail, it is considered a left skewed distribution. As an even order moment, the kurtosis is always positive. The kurtosis describes the distribution flatness compare to the normal distribution. In eq. (6.20), we use the Pearson's kurtosis definition. Thus, the estimate should be compared to the value 3 expected for the normal distribution. Table 6.1 summarizes the notations and the definitions previously introduced and used all along in the manuscript.

Table 6.1 – Summary of the first four statistical moments of a discrete random variable X with their corresponding estimate on a sample $\{X_i\}$.

Name	Order	Definition	Estimate
Mean	1	$\mathbb{E}[X] = \sum_{i=1}^n p_i X_i$	$\bar{X} = \sum_{i=1}^n \frac{X_i}{n}$
Standard deviation	2	$\sigma(X) = \sqrt{\mathbb{E}[(X - \mathbb{E}[X])^2]}$	$\hat{\sigma}(X) = \sqrt{\frac{1}{n-1} \sum_{i=1}^n (X_i - \bar{X})^2}$
Skewness	3	$\gamma_3(X) = \mathbb{E}\left[\left(\frac{X - \mathbb{E}[X]}{\sigma}\right)^3\right]$	$\hat{\gamma}_3(X) = \frac{1}{n\hat{\sigma}^3} \sum_{i=1}^n (X_i - \bar{X})^3$
Kurtosis	4	$\gamma_4(X) = \mathbb{E}\left[\left(\frac{X - \mathbb{E}[X]}{\sigma}\right)^4\right]$	$\hat{\gamma}_4(X) = \frac{1}{n\hat{\sigma}^4} \sum_{i=1}^n (X_i - \bar{X})^4$

As a last remark, we stress that the high-order moments, typically the skewness and the kurtosis, are less robust against noise. Especially, as they are central moments with respect to the expected mean value taken to the power of their moment order, any data point apart from the distribution will affect dramatically their estimate. Furthermore, to obtain a statistical moment estimate with a good precision, higher is the moment order, larger the total data points. In this respect we need to perform more than 10 000 acquisitions to properly estimate the skewness and the kurtosis.

Now, we will present how they evolve with respect to temperature. Our concern is mainly focused on the statistical moments of order higher than 1.

6.2.2 The Kurkijärvi-Garg model

For the moment, we have focused on the second central moment by studying how the standard deviation evolves with respect to temperature. Kurkijärvi has first developed a model to account for the thermal fluctuations in JJs [66] based on the RCSJ model. Garg has extended further this theory [76] for various damping values in JJs with thermal and quantum fluctuations. In this respect, the Kurkijärvi-Garg (KG) theory covers a wide range of process (QPS, MQT, TAPS) in various of superconducting devices (JJs, 1D superconducting nanowires). Thus, it provides a unified description of the effects of thermal and quantum escape from a metastable state. In the framework of the KG model, the switching rate can be written as a function of the reduced current $\varepsilon = 1 - I/I_c$ as:

$$\Gamma = A\varepsilon^{a+b-1} \exp(-B\varepsilon^b) \quad (6.21)$$

The parameters a, b, A, B depend on the process types - quantum or thermal - and on the damping in the device. Generally speaking, a and b are fractional power laws about unity, while the parameters A and B are associated to the energy potential involved. For each specific case, the four parameters can be estimated once fluctuation is set and the energy barrier is known. As a concrete example for the thermal escape of a low damped JJ, the energy barrier is described by the tilted washboard potential. It follows that $A, B \propto U_c/k_B T$ with U_c being a characteristic energy, $a = 1$, and $b = 3/2$. Therefore, it is possible to model the switching rate data using eq. (6.21).

If we are only interested in the statistical moments, it is possible to compute approximately the expressions of the mean and the standard deviation of the switching current [65, 280, 299] without loss of generality as:

$$\bar{I}_s = I_c \left(1 - u^{-1/b} \kappa^{1/b} \right) \quad (6.22a)$$

$$\hat{\sigma}(I_s) = \frac{\pi I_c}{\sqrt{6b}} u^{-1/b} \kappa^{(1-1/b)} \quad (6.22b)$$

where $u = U_c(T)/k_B T_{\text{es}}$ is the reduced energy barrier. If the process is thermally activated, the escape temperature T_{es} is simply T , while in the quantum tunnelling case, it represents an effective temperature T_q . In addition, $\kappa = \ln(\Omega t_\sigma)$ where Ω is the attempt frequency and t_σ is the sweeping time during the sweeping up to the switching. The variation of κ is usually supposed irrelevant due to the logarithm function, it follows from eq. (6.22b) that the dependence of $\hat{\sigma}(I_s)$ is:

$$\hat{\sigma}(I_s) \propto I_c(T) U_c(T)^{-1/b} T_{\text{es}}^{1/b} \quad (6.23)$$

omitting the constant term $\pi/\sqrt{6b}$. We obtain a general expression for the dependence of the SCD standard deviation with respect to the characteristic energy U_c and the critical current. Now, it becomes necessary to assume a specific energy potential to obtain the evolution of $\hat{\sigma}(I_s)$ with respect to temperature. For a phase escape in JJs or a PS in a 1D superconducting nanowire, the exact calculation gives $U_c(T) \propto I_c(T)$ [65, 280, 299] without any other temperature dependence. In such a case eq. (6.23) can be written as:

$$\hat{\sigma}(I_s) \propto I_c(T)^{1-1/b} T_{\text{es}}^{1/b} \quad (6.24)$$

Therefore, we obtain a general expression encompassing the switching statistics for both JJs and PS in 1D superconducting nanowire. Table 6.2 summarises some specific cases of the switching statistical results in the framework of the KG theory. Thus, it is possible to determine which switching mechanism is involved in a superconducting device by studying the evolution of $\hat{\sigma}(I_s)$ with respect to temperature. Especially, if there is a crossover temperature T_{cr} between quantum and thermal regimes, we should obtain approximately: $T_{\text{cr}} \approx T_q$. For $T > T_{\text{cr}}$, the switching is dominated by the TA process and strongly depends on temperature, while for lower temperature the standard deviation reaches a plateau since the quantum process does not depend on temperature. This is a strong signature of the

Table 6.2 – Summary of the typical SCD properties of different superconducting devices in the framework of the generalized KG theory.

Device	Fluctuation	Process	T_{es}	b	$\hat{\sigma}(I_s)$
JJ	Thermal	TA phase escape	T	3/2	$\propto I_c(T)^{1/3} T^{2/3}$
1D wire	Thermal	TAPS	T	5/4	$\propto I_c(T)^{1/5} T^{4/5}$
1D wire	Quantum	QPS	T_q	5/4	$\propto I_c(T)^{1/5}$

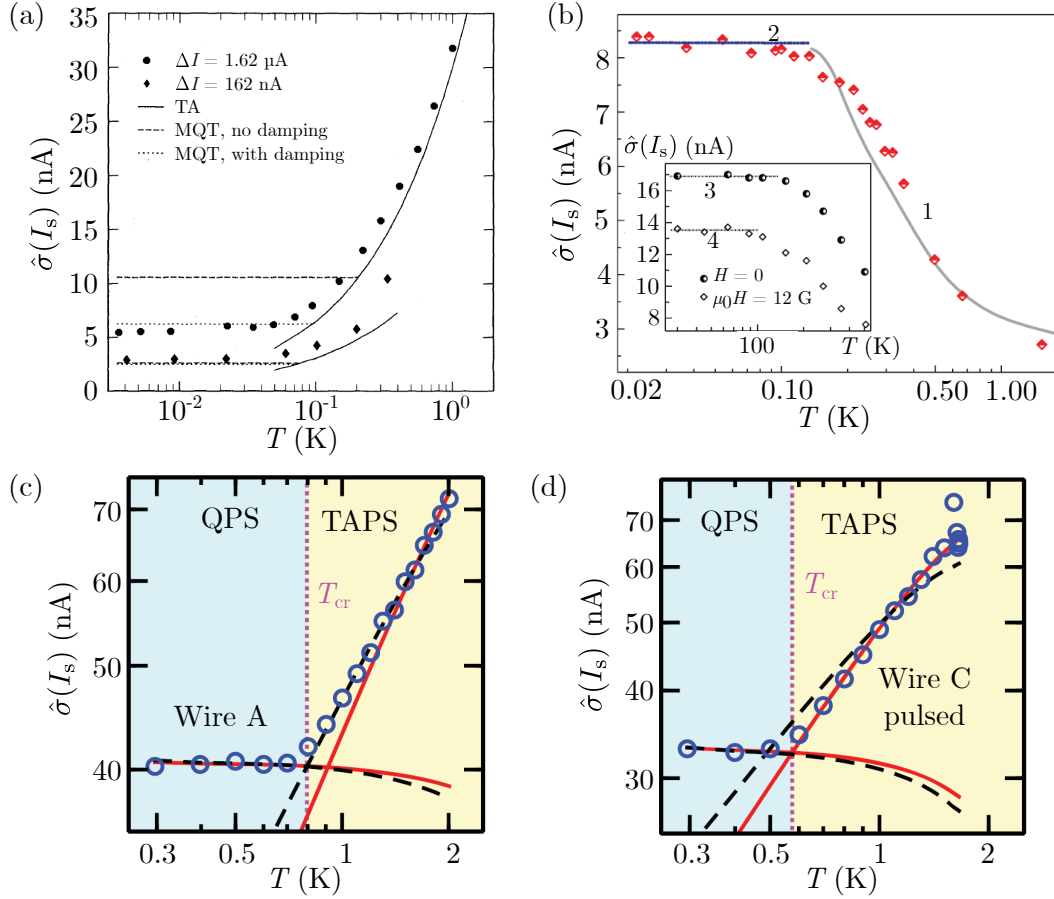


Figure 6.7 – Evolution of the switching current standard deviation as a function of temperature for different superconducting devices. (a) Study of two underdamped ($Q \approx 70$) Nb JJs along with the theoretical predictions according to TA and MQT processes. Adapted from Voss *et al.* [282]. (b) Study of a moderately damped ($Q = 1.3$) YBCO JJ with the Monte Carlo simulations (light grey solid) and the saturation of σ at low temperature. Adapted from Massarotti *et al.* [291]. (c-d) Study of two MoGe 1D superconducting nanowires experiencing voltage switch. The solid red line and dashed black line are fitting lines according to the KG model for $b = 5/4$ and $b = 3/2$ respectively. The dashed line separates the QPS regime at low temperatures from the TAPS regime at high temperatures. Adapted from Aref *et al.* [280].

appearance of the QPS or the MQT respectively in a JJ or a 1D superconducting nanowire, in particular if the switching current is still increasing.

To illustrate this point, fig. 6.7 shows some typical evolution of $\hat{\sigma}(I_s)$ as a function of temperature obtained in both JJs and 1D superconducting nanowires respectively in upper and lower panels. The measurements are presented along with their corresponding fitting model according to the KG theory with the appropriate parameters. In all the figures, we clearly see a transition between two regimes. For low temperatures, the standard deviation saturates at a constant value, while it evolves as a power law for temperature above T_{cr} with a factor 2 to 5 with respect to the saturation plateau. $T_{cr} \approx 100 \text{ mK}$ for the JJs in fig. 6.7(a,b), while $T_{cr} \approx 700 \text{ mK}$ for the MoGe 1D superconducting nanowire in fig. 6.7(c,d). We stress that the transition from thermal to quantum fluctuations driven process is usually observed in sub-K temperature regime.

The standard deviation of the JJs in fig. 6.7(a) exhibits a typical evolution of an underdamped junction with a $b = 3/2$ power law dependence. Starting from high temperatures,

while temperature decreases, $\hat{\sigma}(I_s)$ continuously lowers and then saturates. Surprisingly the 1D superconducting MoGe wire presented in fig. 6.7(c) follows a similar behavior with again a $b = 3/2$ power law dependence (dashed black line). However, for the 1D superconducting MoGe wire shown in fig. 6.7(d), we observe the expected result with a KG model using $b = 5/4$. At last, fig. 6.7(d) corresponds to a moderately damped YBCO JJ. In this case, the phase diffusion is responsible for the opposite slope of $\hat{\sigma}(I_s)$. The power b is not specified, but the Monte-Carlo simulation (grey line) considering the retrapping process account roughly for the experiment.

The KG model presented in this section have proven its worth, it has been verified experimentally in several different systems. One main fingerprint is the transition between a QT and a TA mechanism. While the former is temperature independent, the latter is described by a power law dependence with respect to temperature and critical current.

6.2.3 Universality of the high order moments

In addition to the standard deviation, Murphy *et al.* have also studied the evolution of the high order moments in both 1D MoGe superconducting nanowires and graphene junctions. Figure 6.8 shows the temperature evolution of the high order moments for the MoGe wire. It demonstrates experimentally that whatever the temperature and the device, the skewness and the kurtosis are grossly constant within the experimental uncertainty having $\hat{\gamma}_3 = -1.14$ and $\hat{\gamma}_4 = 5.4$. This typical result is exactly the same for the JJ. Both skewness and kurtosis are universal for JJs and 1D superconducting nanowires. Strikingly, it applies even if the MoGe wire goes from a TAPS regime to a QPS regime at lower temperatures.

Generally speaking, it tells that the form of the SCD remains the same whatever the other parameters. As the skewness is negative the SCD is always left skewed, meaning that the premature voltage switches are more prone to occur below the mean switching current value. Since the kurtosis is higher than 3, it is expected that the tail extremities of the SCDs are more pronounced than a normal gaussian distribution.

In order to corroborate their experimental results, Murphy *et al.* [72] also performed numerical simulations and derived an analytical model. The simulations are based on an Arrhenius activation law to account for both quantum and thermal process. The corresponding simulations confirm the experiment as shown by the solid lines in fig. 6.8. In addition, they extended the KG model presented previously in section 6.2.2 to explain the universality of the high order moments. By deriving the expressions of the high

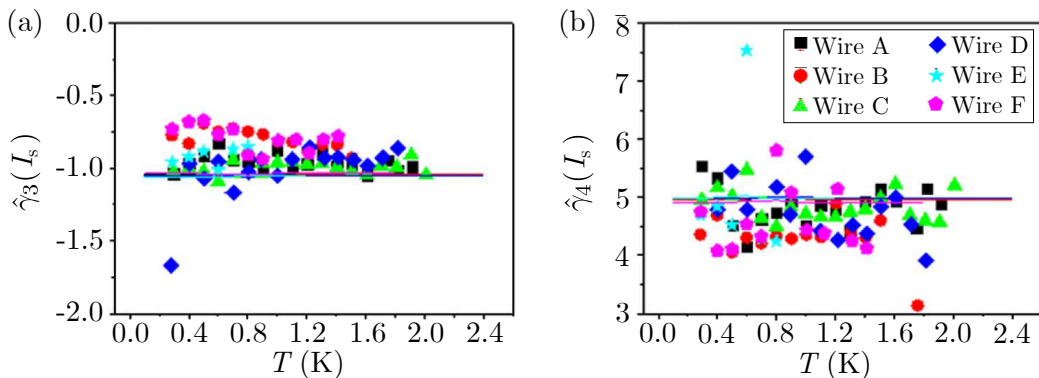


Figure 6.8 – Temperature evolution of (a) the skewness and (b) the kurtosis for different MoGe 1D superconducting nanowires. The skewness and the kurtosis are respectively equal to -1.14 and 5.4 whatever the temperature according to the extended KG model. Adapted from Murphy *et al.* [72].

order statistical moments based on eq. (6.21), they demonstrated analytically that they are current independent at first order approximation. The skewness and the kurtosis are respectively given by $\gamma_3 \approx -1.139$ and $\gamma_4 \approx 5$.

The measurements combined with the simulations and the analytical model provide strong arguments to demonstrate the universality of the high order moments in the studied superconducting devices. Besides, we draw the attention to the fact that any external noise might dramatically affects the results. In particular, additional simulations performed by Murphy *et al.* [72] showed that an external gaussian noise blurs the universal values of the high order moments. As the external noise standard deviation raises, the skewness and the kurtosis tends toward the values of a normal distribution, that is $\hat{\gamma}_3 = 0$ and $\hat{\gamma}_4 = 3$.

6.3 Acquisition of the current distributions

In the previous sections we introduced the theoretical background, the notations, and the usual features of switching statistics in different superconducting devices. Now, we focus on the data acquisition and the corresponding numerical analysis performed in this thesis to obtain the SCD of the irradiated YBCO nanowires.

6.3.1 Fast current-voltage curve measurement

We presented in chapter 4 how we measure the DC IV curves up to now. In order to estimate the high order statistical moments up to the order 4, we need to gather a lot of IV curves, typically $N = 10000$ acquisitions. Let's consider a typical YBCO nanowires whose switching current is slightly smaller than 1 mA at low temperature. To estimate the statistics moments, we need a current resolution of about $0.1 \mu\text{A}$. If the current is incremented by $\delta I = 0.1 \mu\text{A}$ each $\delta t = 0.1$ s from 0 A up to 1 mA, the IV curve is acquired in a time $T_i = 10^3 \text{s} \approx 17$ min. To gather 10 000 acquisitions, the experiment will lasts 116 days. It is clearly not a good way to acquire the IV curves to estimate the statistical parameters for only one set of external parameters. Especially, we need to study the evolution with respect to temperature to check whether there is a crossover between different regimes and if the high order moments are universal.

To counteract this problem, different experimental method may be used to meet the requirements of a reasonable time acquisition and a precise measurements of the current. Roughly speaking, if we consider a IV curve time acquisition T_i , the switching current I_s sets the sweep current as $\nu_I \approx I_s/T_i$. However, the current precision δI should be set to correctly estimate $\hat{\sigma}(I_s)$, that is to say: $\delta I < \hat{\sigma}(I_s)$. Table 6.3 summarises the typical current parameters used for different types of superconducting devices while measuring the SCD. The last line corresponds to the requirements for the irradiated YBCO nanowires fabricated and measured in this thesis. As noted previously, when I_s becomes larger, it is necessary to raise the sweep current ν_I , while $\hat{\sigma}(I_s)$ is usually higher.

Table 6.3 – Summary of the sweep current ramp parameters required for measuring the SCDs of different superconducting devices compared with our requirements.

Device	Material	I_s (μA)	ν_I ($\text{mA}\cdot\text{s}^{-1}$)	$\hat{\sigma}(I_s)$ (nA)	ΔI (nA)	Ref
1D wire	MoGe	1	0.1	10	3	[301]
HTS JJ	YBCO	1	0.02	10	1	[291]
LTS JJ	Nb-Nb _x O _y -Pb	100	2	5000	40	[68]
HTS wire	YBCO	1000	4	1000	40	This work

A common experimental setup is to build an AC current source using an AC voltage source feeding a set of two resistors: one large resistor compare to the device resistor for limiting the current, and another one for reading the current [65, 67, 70]. It is nothing less than the four probes lock-in measurement setup presented previously in chapter 4. Both voltages across the device and the current reading resistor are then connected to a fast voltage data acquisition (DAQ) card plug to a computer to obtain the IV curve. Usually, the maximum current is about 1-100 μA and the device switches from the superconducting zero voltage branch to the resistive branch. In our case, the YBCO nanowires exhibit a first dissipative regime with $R_d \approx 10 \text{ k}\Omega$ and the maximum current necessary to trigger the voltage switch is larger than 1 mA. With such characteristics, we need at least a 10 V AC voltage source. In addition, as the device resistor varies with the voltage, the current will not be directly proportional to the voltage set by the source, thus it is mandatory to measure the voltage drop with an additional resistor. In this case, the current resolution of 10 nA in combination with a maximum current of 1 mA is difficult to achieve.

For all these reasons, we have better to use a dedicated current ramp source and to measure the voltage using an oscilloscope. Figure 6.9 depicts the experimental setup that we use to perform fast IV curve acquisitions with a high current amplitude up to 2 mA and a low current resolution about 10 nA at best. The device is connected to a Yokogawa GS200 current source. It generates a linear current ramp between a low current boundary I_L and a high current boundary I_H in a time $T_i = 0.1 \text{ s}$. The current sweep rate ν_I is then simply given by:

$$\nu_I = \frac{I_H - I_L}{T_i} \quad (6.25)$$

As long as we are assured that the source delivers the proper signal, we do no longer need to bother of the current reading, it is directly infer *a posteriori* using the parameters I_L , I_H , and T_i . The resulting voltage drop across the device is then amplified and a Lecroy Wavepro 950 oscilloscope acquires the voltage waveform afterwards. The oscilloscope acquisition triggers on the current source clock such that it is synchronized with the current ramp. With such a procedure, knowing that the current ramp starts at the initial time $t = 0 \text{ s}$, we ensure that we estimate correctly the current ramp evolution through time.

Figure 6.10 shows a typical voltage waveform of a YBCO superconducting nanowire measured with the experimental setup depicted in fig. 6.9. The current source applies successive current ramps alternating between positive $+\delta I$ and negative $-\delta I$ current increment in a time T_i . The combination of two successive current ramps constitutes one complete IV characteristic in which we observe both the voltage switching event and the retrapping event. Here, 5 IV curves are acquired in one waveform in 1 s, thus 10 000 acquisitions will last only 33 min. It is definitely a more reasonable experiment duration to estimate the SCD.

Knowing that the oscilloscope sample rate is $f_s = 100 \text{ kS}\cdot\text{s}^{-1}$, the current resolution is

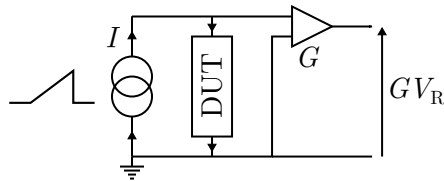


Figure 6.9 – Electrical circuit for fast IV curve acquisition. The device is connected to a current ramp source, while the voltage drop across the device is amplified and acquired with an oscilloscope.

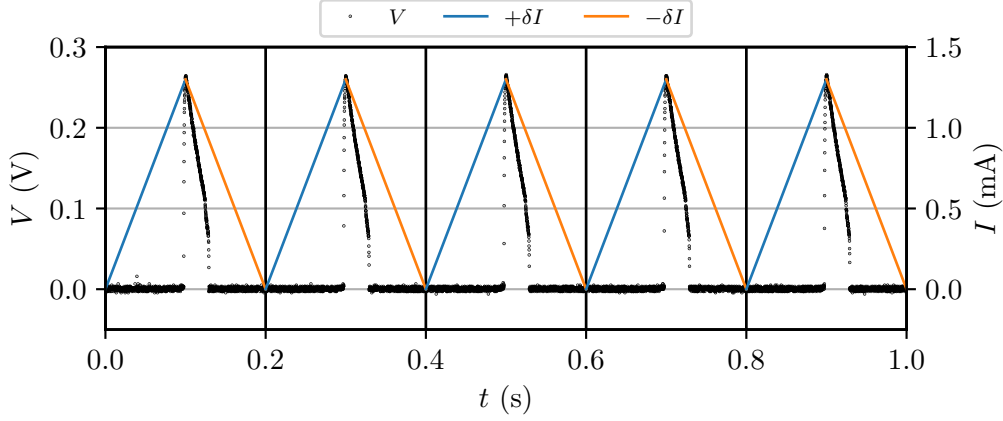


Figure 6.10 – Voltage waveform data across a YBCO superconducting nanowire (black dot) while the current is successively swept up (blue line) and down (orange line) with a current increment $+\delta I$ and $-\delta I$ respectively at 20 K.

simply given by:

$$\delta I = \frac{\nu_I}{f_s} \quad (6.26)$$

In fig. 6.10, the parameters are such that $T_i = 0.1$ s and $I_L = 0$ mA to $I_H = 1.3$ mA. According to eqs. (6.25) and (6.26), for the voltage waveform presented in fig. 6.10 we obtain a sweep rate $\nu_I = 13$ mA.s⁻¹ and a current resolution $\delta I = 130$ nA. We finally meet the experimental requirements to perform fast *IV* acquisitions and therefore estimate the SCDs.

6.3.2 Numerical analysis

The voltage waveform presented in fig. 6.10 is divided in five subsets for further analysis, each one corresponding to an *IV* curve. From the subset showed in fig. 6.11(a) the *IV* curve is reconstructed in fig. 6.11(b) by inferring the current ramp. We get back the typical *IV* curve that we observe in the experimental DC setup. As the current is swept positively, the voltage switches abruptly from a low voltage dissipative branch to a resistive state governed by the Joule heating.

In order to retrieve the switching and the returning currents, we set numerical thresholds denoted respectively as V_{th}^+ and V_{th}^- such that they lie in the voltage switch range as depicted in fig. 6.11(b). While the current is swept up ($+\delta I$) starting from I_L , the first data point with a voltage higher than V_{th}^+ is tagged as the switching data point.⁵ In the opposite case, when the current is swept down ($-\delta I$) starting from I_H , the returning current is the first data point whose voltage is lower than V_{th}^- . Therefore, for each *IV* curve we collect one data point for both I_s and I_r .

The numerical threshold procedure is not free from errors. As seen in fig. 6.11, the red circle shows a voltage data point higher than the sweep up threshold prior to the switching event. Numerically it will be tagged as the switching current while it is rather clear that it is not since no large switching occurs: it is a serious outlier. We do our best to avoid such an outlier due to the voltage noise by setting an appropriate voltage threshold. Nevertheless, it has to be mitigated to register the voltage switch as soon as it occurs.

We performed the switching measurements and the numerical analysis on C8, a 500 nm

⁵We have also considered to use a numerical derivative, but the method is less robust than the threshold method described in the text.

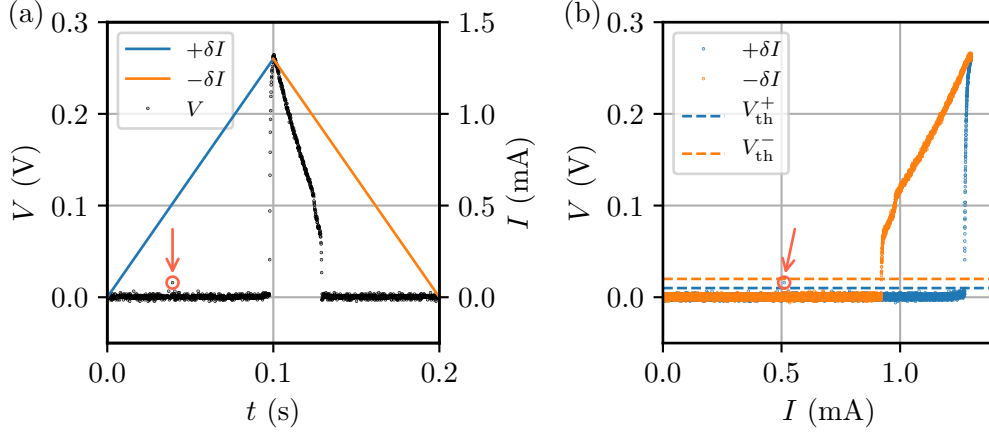


Figure 6.11 – (a) Voltage waveform data across a YBCO superconducting nanowire (black dot) while the current is swept up (blue line) and down (orange line) with a current increment $+\delta I$ and $-\delta I$ respectively. (b) Corresponding reconstructed IV curve based on the inference of the current ramp values. A numerical threshold is set for both the switching current I_s and the retrapping current I_r respectively denoted as V_{th}^+ (blue dashed line) and V_{th}^- (orange dashed line) to retrieve their corresponding values. The red circle annotated with an arrow raises awareness about the presence of data points above V_{th}^+ prior to the switching event due to the voltage noise.

long 200 nm wide irradiated YBCO nanowire patterned on the 30 nm thin film sample CS15. It has been partly studied in chapter 5, in this way all the physical findings properties previously remain valid. We first measure the switching statistics more than 10000 times for temperatures at which the hysteresis exists, that is from 5 K up to 72 K, and therefore we retrieve the switching data points.⁶ While we retrieved the switching current data set numerically as depicted herein, we also extracted the returning current data set at the same time. Our interest is twofold: confirm that the returning current is a deterministic process ruled by the YBCO thermal properties, and thus validate the data set of both switching statistic measurements and the numerical analysis.

Figure 6.12 shows the temperature evolution of the estimated mean and standard deviation of the switching and the returning currents. In left panel, we observe exactly the same trend than the one in chapter 4 using the standard DC IV measurement setup. Both I_s and I_r are decreasing as T raises and the hysteresis collapses about 72 K. On the other hand, the estimate of the standard deviation for both data sets are completely erratic. As we noticed earlier in fig. 6.11, the outliers may still be present after setting the numerical threshold. According to table 6.1, the central moments are estimated using the sum of $(X_i - \bar{X})^k$ with k the moment order. Thus, if one specific data point X_j is greatly away from the mean value \bar{X} , the outlier will affect dramatically the estimate of the central moments. In particular, higher is the moment order k , larger the effect of the outlier. Therefore, the data set needs to be treated further to remove the outlier data points.

⁶In this respect, we stress that we studied the C8 device in many aspects. Especially, the nanowire has been subjected to several millions of current sweeps and as many voltage switch without any damaging after several vacuum cyclings in the cryostat. It proves once again that the irradiated YBCO nanowires are robust in a great extent.

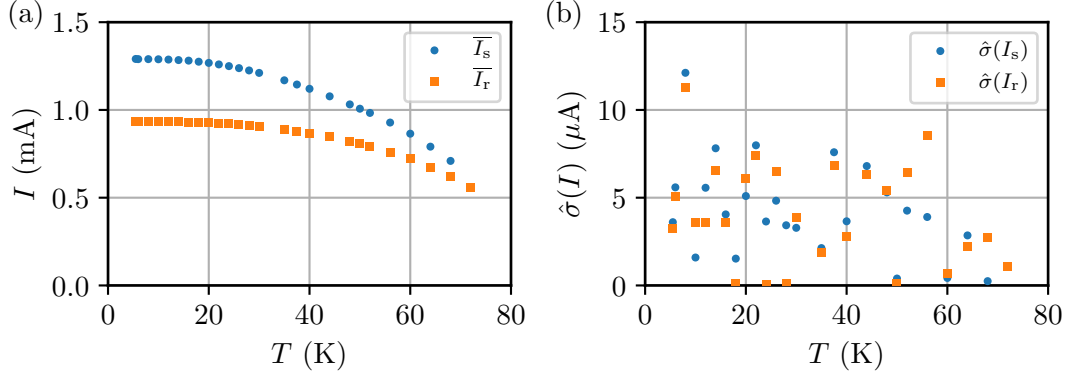


Figure 6.12 – (a) Temperature evolution of the raw switching current average value \bar{I}_s and the retrapping current average value \bar{I}_r . (b) Temperature evolution of the raw switching current standard deviation $\hat{\sigma}(I_s)$ and the retrapping current standard deviation $\hat{\sigma}(I_r)$. The data are obtained on C8, a 500 nm long 200 nm wide 30 nm thick YBCO nanowire.

6.3.3 Dealing with outliers

By definition, an outlier $X_j \in \{X_i\}$ is a data point which significantly deviates from the overall sample $\{X_i\}$. Statistical methods are specifically defined to identify and treat outliers in a data set. In our case, we do not know the total expected number of outliers, though the most appropriate technique is the generalized extremely studentized deviate (ESD) test originally proposed by Rosner [302]. It only requires to assume an approximately normal SCD.

The generalized ESD test determines what is the number of outliers r in the data set. A test statistic coefficient R_k is computed for the raw data set $\{X_i\}$. The observation X_j which is the most away from the mean is removed from the raw data set and the coefficient R_{k+1} is recomputed on the new data set. This operation is repeated as long as we think there are outliers. In practice we fix it to $r_{\max} = 500$, even if the outliers number is less than 500 it ensures that we tag all of them. For each R_k corresponds a critical value λ_k set by the total number of data points n and the significance level α at which the test is rejected. We typically use $\alpha = 0.01$ representing a risk of 1% that the data point is not an outlier. The highest index k such that $R_k > \lambda_k$ corresponds to the total number of outliers found in the raw data set.⁷

Returning to our case, we performed a generalized ESD test on both the switching and the returning current data sets independently. We removed the r outliers from the raw data sets and obtained the treated data sets with $n - r$ data points. We name accordingly the ESD data sets. We stress that r is different for I_s and I_r though. In order to see how the generalized ESD test treatment affects the estimate of the statistical moments fig. 6.13 shows the results with and without the test. We plot in fig. 6.13(a) all the switching current observations as a function of the observation index i_{subset} . The detected outliers have been tagged with a red circle in (a-b). Additionally, the evolution of the mean switching current \bar{I}_s and the switching current standard deviation $\hat{\sigma}(I_s)$ are represented respectively in fig. 6.13(b) and fig. 6.13(c) with and without the generalized ESD test respectively mentioned as Raw and ESD. If we first look at \bar{I}_s in fig. 6.13(b), both the raw and the ESD data sets are converging toward the same value about 1.279 mA. But, if we inspect the upper panel, we notice several outliers lying largely away from the cloud of points about 1.3 mA. Especially, the outliers followed by a red arrow affect seriously

⁷A more detailed overview and methods for dealing with outliers can be found in the NIST/SEMATECH e-Handbook of Statistical Methods or in the article of Aguinis *et al.* [303].

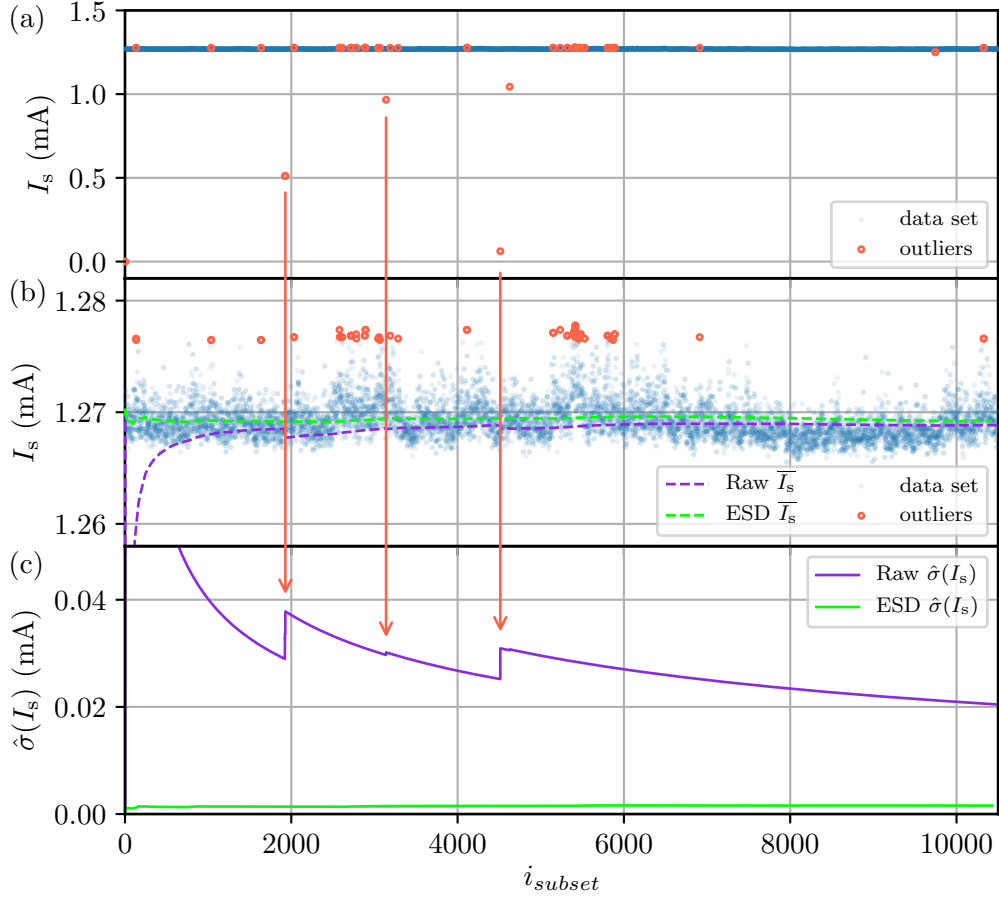


Figure 6.13 – (a-b) The switching current data points as a function of the observation index i_{subset} . The outliers according to the generalized ESD test with a 1% significance level are highlighted with a red circle. (b) The estimate of the switching current mean value on the raw data set and on the ESD data set are respectively represented by a dashed purple line and a dashed green line. (d) Evolution of the switching current standard deviation on the raw data set and on the ESD data set are respectively represented by a solid purple line and a solid green dashed line.

the estimate of the standard deviation for the raw data set presented in the lower panel. Indeed, we observe spike in the raw $\hat{\sigma}(I_s)$ for those outliers. After summing the outliers, the estimate of the standard deviation decays slowly toward smaller values in the long run. But even after 10 000 observations, there is one order of magnitude ratio between the estimate with the raw data set compared to the ESD data set. It becomes clear that the outliers have completely ruined the estimate of the second central moment.

We performed the ESD treatment for all the different temperatures and estimated the standard deviation accordingly. The statistical results with and without the generalized ESD treatment, for both I_s and I_r , are shown in fig. 6.14. At this time we observe a distinct evolution of $\hat{\sigma}(I_s)$ with respect to temperature, while $\hat{\sigma}(I_r)$ is rather constant for all the measured temperatures. Therefore, there is undoubtedly no timing jitter problem in the electronic system since $\hat{\sigma}(I_r)$ is flat and near the current resolution set by the oscilloscope capability, while $\hat{\sigma}(I_s)$ varies by one order of magnitude. The two standard deviations are almost the same at high temperatures at approximately $0.1 \mu\text{A}$. As temperature lowers, $\hat{\sigma}(I_s)$ increases and reaches a plateau about 1.5 mA for $T < 20 \text{ K}$, even if $\hat{\sigma}(I_s)$ saturates at low temperatures like for the quantum tunnelling process in JJs or PS. Nevertheless,

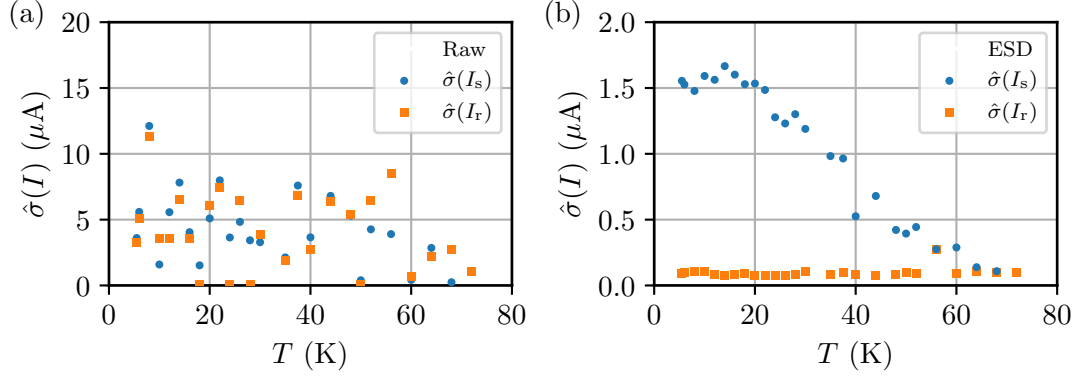


Figure 6.14 – Temperature evolution of the switching current standard deviation $\hat{\sigma}(I_s)$ and the retrapping current standard deviation $\hat{\sigma}(I_r)$ data sets for the 500 nm long 200 nm wide YBCO nanowire C8. (a) Estimate on the raw data set. (b) Estimate on the treated ESD data set free from outliers with a 1% significance level according to the generalized ESD test.

the standard deviation saturates at 20 K, which is 1 to 2 orders of magnitude higher than the cases presented in section 6.2.2. Therefore, we should be cautious. The experimental results will be studied in a greater extend in the next section.

In conclusion, we presented in this section how we performed the fast IV characteristic acquisitions in a reasonable time with a sufficient current precision: typically 10 000 observations in 30 min for one set of external parameters. In order to remove the outliers, we performed a generalized ESD test at a 1% significance level. We demonstrated that such a statistical method enhances significantly the estimates and enables to observe a temperature evolution of $\hat{\sigma}(I_s)$.

6.4 Estimate of the statistical moments

In the following section, we study the evolution of the fourth first statistical moments presented in table 6.1. We have performed the experiment with a current sweep ramp $\nu_I = 4 \text{ mA}\cdot\text{s}^{-1}$ along with the numerical treatment introduced in section 6.3 with a 1% significance level for all the data sets presented thereafter. Before proceeding, we stress that we have paid attention to the heating effects during the application of the current ramp. At first, the sweep rate is so fast that the temperature reading on the thermometer is constant. But mostly, as the current is swept up and down prior to the switching current there is no hysteresis. Both up and down curves are matching, it demonstrates that there is no significant heating effect before the switching event.

6.4.1 Evolution with temperature

At first, we focus our attention on the temperature dependence as it is the usual fluctuation origin in the framework of the KG theory introduced in section 6.2.2. Figure 6.15(a) and (b) show the temperature evolution of the mean and the standard deviation respectively of both switching and retrapping current. As temperature decreases, both \bar{I}_s and \bar{I}_r increase with a more rapid raising than for the switching case. On the contrary, $\hat{\sigma}(I_r)$ is temperature independent, but as temperature diminishes $\hat{\sigma}(I_s)$ raises and saturates below 20 K. We noticed that this behavior is typical of a moderately damped JJs in presence of the phase diffusion retrapping like the results of YBCO JJs reported by Massarotti *et al.* [291]

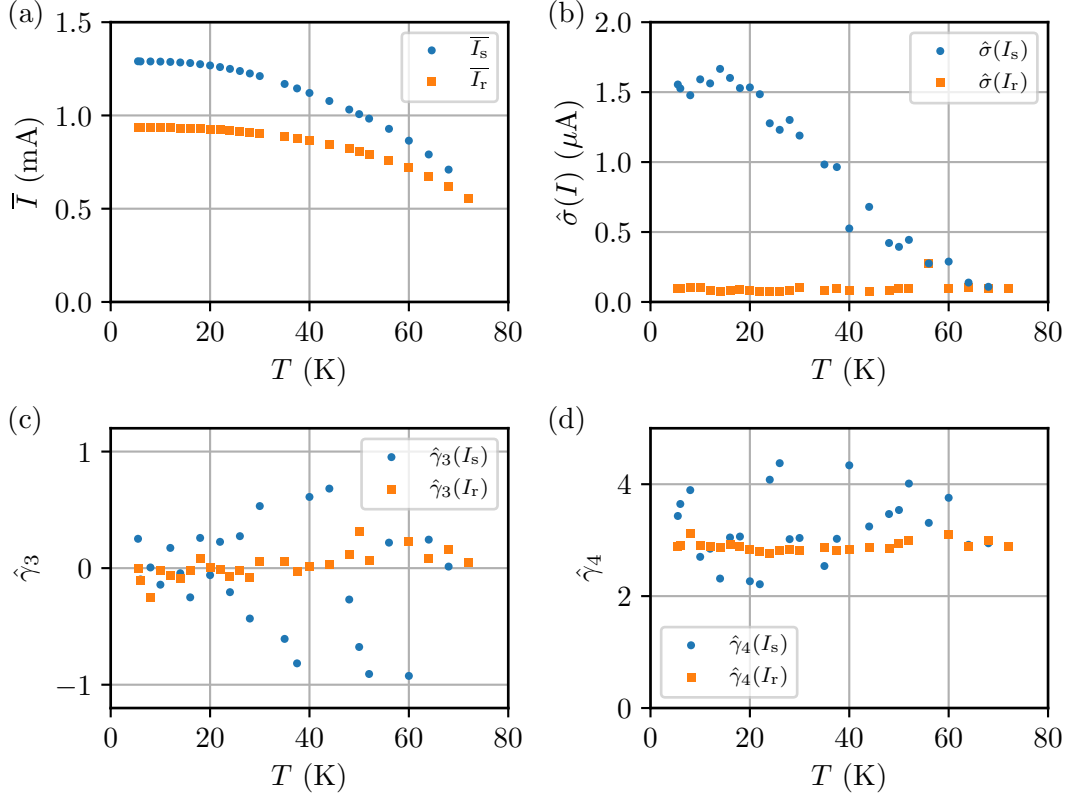


Figure 6.15 – Temperature evolution of the statistical moments of the switching and returning current in C8, 500 nm long 200 nm wide YBCO nanowire: (a) mean value, (b) standard deviation, (c) skewness, and (d) kurtosis. (a) and (b) correspond to the same figures presented respectively in figs. 6.13 and 6.14.

presented in section 6.2.2. But this similarity stops here since there is no evidence of a JJ behavior in the irradiated YBCO nanowires. By comparing the temperature evolution of \bar{I}_s and $\hat{\sigma}(I_s)$, it is difficult to tell whether the standard deviation is driven by the mean switching current value or by temperature. We cannot claim that there is a transition from a thermal to a quantum regime. A different data representation will be considered to raise the ambiguity in sections 6.4.2 and 6.4.3.

Figure 6.15(c,d) correspond to the high order moments, respectively the skewness and the kurtosis estimated for I_s and I_r . It is worth noting that for the returning current I_r , $\hat{\gamma}_3(I_r) \approx 0$ and $\hat{\gamma}_4(I_r) \approx 3$ which is characteristic of a normal distribution. It demonstrates that the returning event is temperature independent and completely deterministic as stated in chapter 4. Therefore, the returning standard deviation is governed by the intrinsic noise of the experimental setup. We attribute it to the timing jitter of the overall electronic system. It constitutes an important consistency check to verify that the experimental setup effectively measures the current statistics.

In contrast, there is no apparent trend for the high order moments of the switching current, their value are erratic with respect to temperature. As temperature decreases, they are largely apart from the values of a normal distribution and they alternate above and below them. First and foremost, it should be noted that the high order moments are not distributed about the universal values expected by the extended KG theory [72]: $\gamma_3 \approx -1.139$ and $\gamma_4 \approx 5$. This is the first clear indication that the switching mechanism in the YBCO irradiated nanowire is not in agreement with the classical KG theory. In addition, the skewness spreading indicates that the asymmetry of the SCD changes without

a specific correlation with temperature. Definitely, it is necessary to look more into the details of the data sets, especially by presenting the current switching distribution. This aspect will be covered later in section 6.6. For the moment we pursue our study of the switching current standard deviation evolution. Even though, there are several indications pointing toward the fact that the SCD is not exactly normal, the generalised ESD test remains valid in a reasonable extent and the estimate of $\hat{\sigma}(I_s)$ is still a relevant parameter.

As a conclusion, the returning current distribution confirms the reliability of the current statistic acquisition by presenting the statistical moments relative to a normal distribution. The returning current standard deviation reaches the current resolution of the experimental setup. In contrast, the switching current data sets are more complex. Their high order moments do not follow the universal KG model, but they rather vary erratically with respect to temperature.

6.4.2 Comparison with other devices

For the purpose of ensuring the reliability of the temperature evolution of $\hat{\sigma}(I_s)$ found previously, we present additional data sets on two other different nanowires with similar dimensions. The relevant characteristics of the devices are summarised in table 6.4. They are all 500 nm long nanowires patterned on a 30 nm thick YBCO superconducting films and exhibit similar critical current densities above the healing current such that we observe a large hysteresis with a voltage switch. The devices C8 and C6 belong to the same sample CS15, while C11 is patterned on the sample CS3. But both samples CS3 and CS15 have the same stack of layers and are patterned using the same nanofabrication recipes. We measured the switching and returning current distributions of C11 in the same temperature range than C8. We also measured the ones of C6 but only at 0.5 K in the dilution fridge.

The results for the three devices are depicted in fig. 6.16 in which we plotted the mean value and the standard deviation with respect to temperature. We observe a similar evolution of both $\hat{\sigma}(I_s)$ and $\hat{\sigma}(I_r)$ for C8 and C11. As temperature decreases there is an enlarging hysteresis, $\hat{\sigma}(I_r)$ is at the same constant level while $\hat{\sigma}(I_s)$ raises by one order of magnitude. Therefore, we notice the same trend for two different devices patterned on two different samples. It demonstrates the reproducibility of the switching and returning statistics measurements. In the case of C6 at 0.5 K, the estimate of the mean and the standard deviation give approximately the same values than C8 and C11 in the low temperature regime for both returning and SCDs. We conclude that there is no substantial change of the standard deviation for temperature down to 0.5 K, it still saturates about the same order of magnitude. It is worth noting that those three devices behave similarly while they have been measured in different cryostats. It consolidates the idea that the trend of the statistical moments are not due to systematic errors, but they rather have a physical origin.

Furthermore, in fig. 6.16, $\overline{I_s}$ and $\hat{\sigma}(I_s)$ have a similar temperature evolution. Thus, it

Table 6.4 – Summary of the superconducting properties acquired on YBCO nanowires patterned on 30 nm thin films of CS types. Measurements on C6 have only been performed about 0.5 K.

Sample	Device	l (nm)	w (nm)	j_c (MA.cm ⁻²)
CS3	C11	500	126	26 @ 5 K
CS15	C8	500	200	12 @ 5 K
CS15	C6	500	176	16 @ 0.5 K

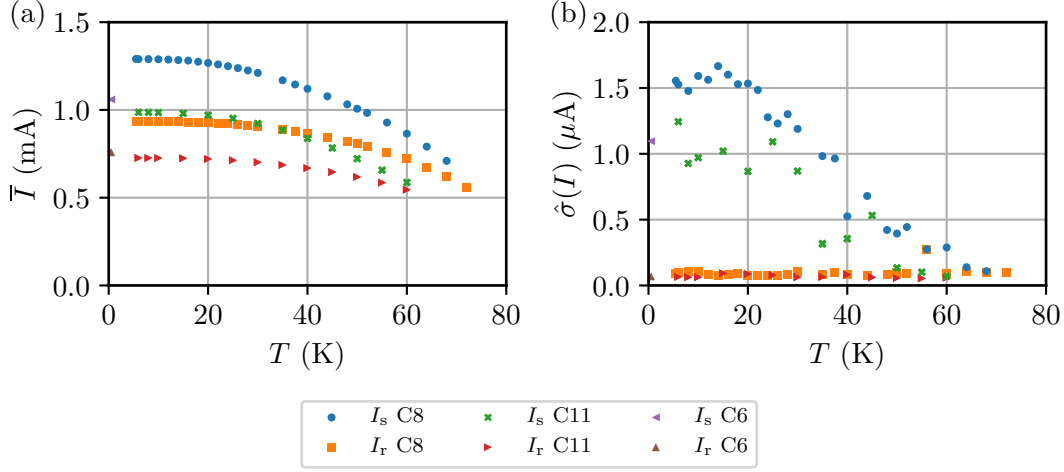


Figure 6.16 – Temperature evolution of (a) the mean value and (b) the standard deviation of the switching and the returning current for different devices belonging to different samples.

is not clear whether $\hat{\sigma}(I_s)$ correlates with temperature or with the switching current, as they are the two relevant parameters in the generalized KG model. In order to clarify this point, fig. 6.17 presents the same evolution of $\hat{\sigma}(I_s)$ as a function of \bar{I}_s for both devices C8 and C11. We notice roughly a power-law dependence between the two first statistical moments. The data are fitted with a least squares method according to:

$$\hat{\sigma}(I_s) \propto \bar{I}_s^{1/b} \quad (6.27)$$

It corresponds to the KG model without the direct temperature dependence, only the switching current dependence remains. For the YBCO nanowires C8 and C11, we obtained respectively $b = 4.8 \pm 0.3$ and $5.5b = \pm 1.0$, suggesting a strong dependence with a power $b \approx 5$. This is unexpected in comparison with the KG model in which $b = 3/2$ or $b = 5/4$. More surprisingly, with eq. (6.27), the direct temperature dependence completely vanishes suggesting that it is not a relevant parameter for the switching mechanism as opposed to

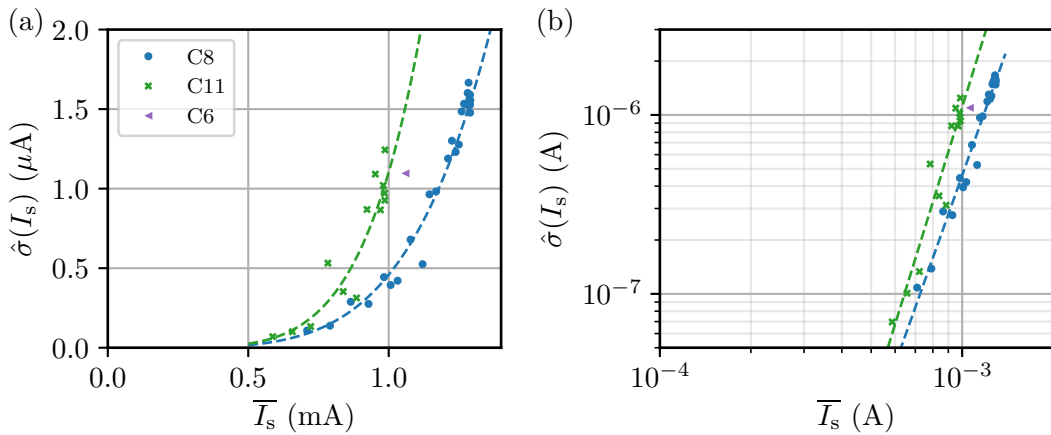


Figure 6.17 – Evolution of the switching current standard deviation with respect to the switching current (a) in linear and (b) logarithmic scale. The dashed lines are power law least squares fittings according to eq. (6.27).

the case of PS in 1D superconducting nanowire and the JJs.

6.4.3 Evolution with external parameters

In order to confirm the idea that the switching current mean value sets its standard deviation, we performed additional experiments by varying two other distinct parameters which modifies \bar{I}_s indirectly.

We study the SCDs under the application of an external RF signal for C8. It is performed for an RF frequency of 18.32 GHz at both 6 K and 50 K. In this case, as we saw previously in section 5.3, the RF power reduces the critical current. As previously mentioned, we emphasize that this reduction is not resulting from a heating of the sample. If it was the case, all the sample holder should be heated and it would be reflected in an increase of the temperature measured by the thermometer. For the temperatures and the RF powers that have been set, the latter effect has not been observed. Nonetheless, one might argue that the phonon bath is decoupled from the electronic bath, resulting in a different temperature for the phonons and the electrons. That is, the temperature measured by the thermometer is different than the temperature of the electrons in the nanowire. Since the electron-phonon coupling is proportional to T^5 , the decoupling of the electron bath from the phonon bath occurs at sub-K temperatures.

In addition, we also studied the influence of an external magnetic field perpendicular to the film for C11 at 0.5 K. Here, the magnetic field reduces the vortex entry energy barrier, therefore the critical current diminishes accordingly.

Having these elements in mind, we retrieved the switching current data sets for C8 and C11 as a function of the RF power P_{rf} and the external magnetic field H respectively. For both cases, the critical current is reduced without noticeable heating effects. Thus, the superconducting nanowires enter in the flux flow regime with a smaller current, and the switching current is modified accordingly. Then we plot the evolution of $\hat{\sigma}(I_s)$ as a function of \bar{I}_s in fig. 6.18.

For C8 presented in fig. 6.18(a), we superimposed the data for different temperatures without RF signal, and the data with different RF powers at 6 K and 50 K. Without RF illumination, for a 50% variation in \bar{I}_s , $\hat{\sigma}(I_s)$ is modified by one order of magnitude. As

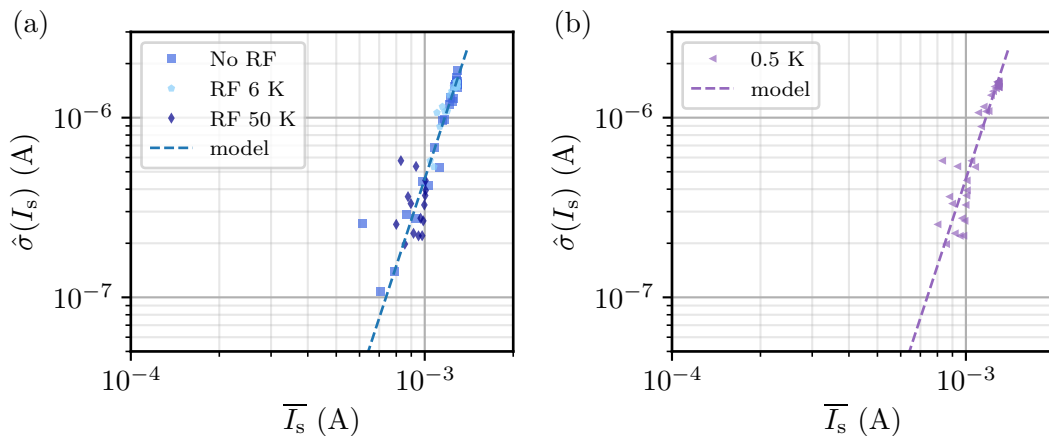


Figure 6.18 – Evolution of the standard deviation as a function of the mean value of the switching current. (a) The data sets are measured in C8 without RF while varying temperature, with an 18.32 GHz RF signal while varying the incident RF power at 6 K and 50 K. (b) The data set is measured in C11 at 0.5 K while varying the external magnetic field in the direction perpendicular to the chip.

the RF power raises, both $\hat{\sigma}(I_s)$ and \bar{I}_s are reduced for the two temperatures. The voltage switch is less pronounced at 50 K and \bar{I}_s is reduced by 20% only though. At 6 K without an external RF source, the voltage switch is larger and $\bar{I}_s = 1.3$ mA. In this case, while varying the RF power \bar{I}_s is also reduced by about 20% with respect to the value without RF. For both temperatures, it results in a noticeable variation of $\hat{\sigma}(I_s)$ by a factor 3 at maximum thanks to the high power $b \approx 5$ in eq. (6.27). This is coherent since a 20% variation in the mean corresponds to a change by a factor $0.8^5 \approx 0.33$ in the standard deviation. Indeed, the three different data sets - without RF at different temperatures and with a RF power at 6 K and 50 K - collapse all together on the same dashed line in log-log scale. This observation represents the fact that the two additional data sets are following the same power law presented previously with $b \approx 5$. Whereas there is no heating effect when the RF signal is turned on, we demonstrate that the RF power has the same effect than temperature on the two first statistical moments. Especially, the mean value and the standard deviation have the same power law dependence. We conclude that the main contribution to $\hat{\sigma}(I_s)$ is governed by the switching current mean value rather than temperature or incident RF power.

Another argument supporting this conclusion comes from the SCDs acquisitions performed while sweeping the external magnetic fields H for C11, as shown in fig. 6.18(b). The switching current mean value varies about 30% while its standard deviation changes by a factor 6. The data points are distributed along the dashed line representing a power law relation with $b = 5$. Here again, $\hat{\sigma}(I_s)$ and \bar{I}_s have the same relationship whatever the external magnetic field.

As a conclusion, the temperature evolution of the first fourth statistical moments for the switching current data sets is not in agreement with the extended KG theory. Especially the skewness and the kurtosis are not universal. The high order moments suggest to look in more details the histograms. Additionally, we observed the saturation of the switching current standard deviation as the mean value raises in three distinct devices. This dependence is observed irrespective of three external parameters affecting the switching current mean value: the temperature, the incident RF power, and the external magnetic field. Another approach must be taken in order to shed light on the switching event in YBCO superconducting nanowire.

6.5 Voltage switch triggered by a vortex instability

Now that we excluded the KG model to interpret our results, we focus our attention toward the vortex instability presented at first. We will show the typical experimental results accounting for the vortex instability in the irradiated YBCO nanowires. It will give us additional clues to investigate the SCDs afterwards.

6.5.1 Fingerprint of the Larkin-Ovchinnikov instability

In the framework of the Larkin-Ovchinnikov instability, the evolution of the voltage switch has been widely studied as a function of temperature and the external magnetic field near T_c . In YBCO microbridges, the low temperature range is usually difficult to access since a high bias current generates a significant Joule heating in the device. Here, the YBCO wires are only 30 nm thick and about 150 nm wide, therefore the bias current and the heating are limited. It becomes possible to investigate the switching in a wider range of parameters, especially at low temperature.

Figure 6.19 shows typical IV curves evolution with respect to temperature and the external magnetic field at 100 mK in the left and right panel respectively. In fig. 6.19(a),

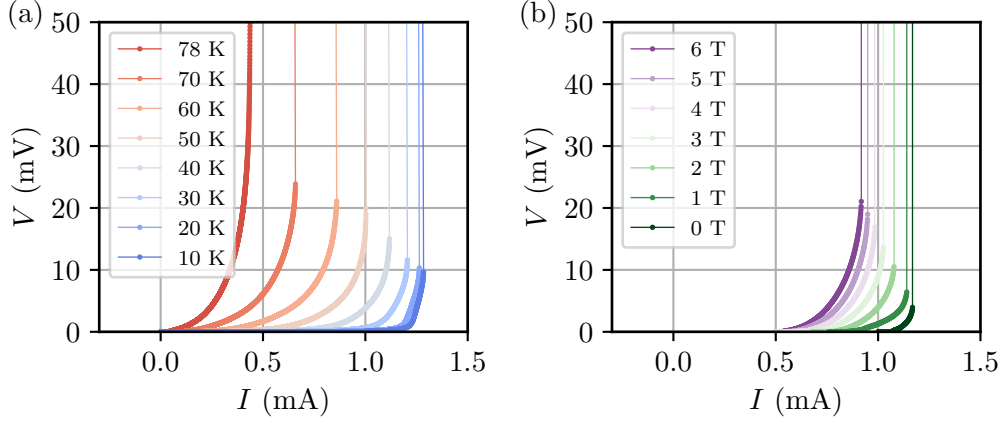


Figure 6.19 – (a) IV curves showing the voltage switch at different temperatures for C8 without magnetic field. (b) IV curves showing the voltage switch at different external magnetic fields for C6 at $T = 100$ mK.

starting from $T = 78$ K near T_c , as the current is swept up there is a continuous increase of the voltage drop. While for $T < 75$ K a clear voltage switch appears. As temperature lowers, the switching current raises and the voltage switch is triggered at a lower switching voltage V_s . We observe a similar trend in fig. 6.19(b) while the external magnetic field changes. When H raises from 0 T to 6 T at 100 mK, the voltage switch increases while the switching current diminishes. But this time, we cannot completely suppress the voltage switch as before in the case of $T = 78$ K. Besides, it is worth noting that the critical current is not fully suppressed at 6 T and there is no Fraunhofer critical current diffraction pattern as observed in YBCO JJs about 5 mT. It provides another strong argument that the YBCO nanowires presented here cannot be interpreted as JJs. Overall, the IV measurements are in qualitative agreement with the experiments performed earlier in YBCO microbridges [73, 75, 84].

If we go into further details, the LO instability occurs when the vortex velocity reaches the critical velocity v_φ^* . Experimentally, it is estimated thanks to the IV curves in presence of an external magnetic field H as follows:

$$v_\varphi^* = \frac{V_s}{\mu_0 l H} \quad (6.28)$$

where V_s is the switching voltage in the flux flow regime. According to the original LO model, the critical velocity is independent of H for low enough magnetic field in comparison to the upper critical field. In the YBCO case, $B_{c2} \approx 120$ T [304, 305], thus this condition is satisfied as long as $\mu_0 H \leq 8$ T. We show in fig. 6.20 the evolution of the critical velocity as a function of the external magnetic field for two different 500 nm long YBCO nanowires patterned on the same 30 nm thick YBCO sample CS15. C6 is 176 nm wide, while C4 is only 150 nm wide, they are both evolving in an identical way with H . In fig. 6.20(a), v_φ^* is almost independent of the external magnetic field for $\mu_0 H > 1$ T, while at small magnetic fields it depends strongly on H .

In comparison to the previous studies in YBCO microbridges [73, 84], we obtained a similar evolution of v_φ^* with respect to the external magnetic field for $\mu_0 H > 1$ T, but not in the same ranges of temperature and magnetic field. In the literature, the phenomenon occurs for $T > 50$ K, while here we observe it at $T = 100$ mK. This is quite surprising since the LO theory is valid for $T \approx T_c$. At low magnetic field, Klein *et al.* [77] have reported both theoretically and experimentally that $v_\varphi^* \propto \sqrt{H}$. In our case, fig. 6.20(b)

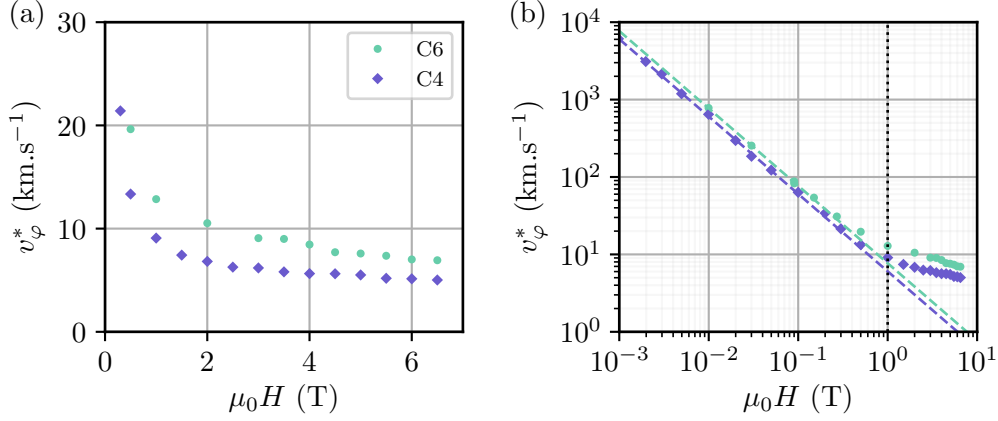


Figure 6.20 – Evolution of the estimated critical velocity v_φ^* using eq. (6.28) for two different 500 nm long 30 nm thick YBCO nanowires at 0.5 K in (a) linear and (b) logarithmic scale.

shows an inverse relationship between v_φ^* and H . We fitted both data sets below 1 T using a least squares method with an inverse relation $v_\varphi^* = \alpha/H$. The dashed lines representing the fitted curves match each data sets. It strongly suggests that the YBCO nanowires are not correctly described by the LO theory in the temperature range studied above.

6.5.2 The alternative model of Kunchur

For $T = 100$ mK, the quasiparticles properties are different in comparison with the properties near T_c . At low temperatures, the phonons are frozen. It results in a longer electron-phonon interaction time, while the electron-electron interaction time is temperature independent. Thus, the quasiparticles constituting the vortices cannot release their excess energy *via* phonons: the electron bath is decoupled from the phonon bath. Therefore, the electronic temperature T_e is higher than the phonon temperature T_p such that $T_e > T_p \gtrsim T$. According to Kunchur [82] the electron-phonon decoupling leads to a different mechanism than the LO instability previously described. Instead of a vortex core shrinkage due to the quasiparticles escaping from the core, the vortex core expands due to the quasiparticles generation enhancement. While, the LO instability and the Kunchur model affect differently the vortices, they both result in a viscosity loss leading to an instability triggering a voltage switch. However, the magnetic field dependence of the switching parameters - such as the switching voltage or the switching current - differs depending on the model. Table 6.5 recapitulates the magnetic field dependencies expected from the different theoretical models.

In the model of Kunchur [82], the non-linear IV curve prior to the switching at temperature T in presence of an external magnetic field H writes:

$$I - I_{c0} \approx \frac{w d H_{c2}(T) V}{H \rho_n(T) L} \sqrt{f(x)} \quad (6.29)$$

where L is the voltage drop extension along the nanowire, $x = 0.0245V^2/V_s^2$, and $f(x) \simeq 1 - 0.4386x - 1.539x^2 + 40.381x^3 - 345.217x^4$. Here, V_s is the switching voltage at the instability point. It corresponds to an infinite slope in the IV curves presented by Kunchur, as depicted in fig. 6.21(a).

In order to test the Kunchur model, we perform a least squares fitting of the IV data sets under external magnetic fields presented previously for C6 in fig. 6.19 using eq. (6.29). Since $H_{c2}(T)$, $\rho_n(T)$, and L are correlated parameters, we can only use one of them as a

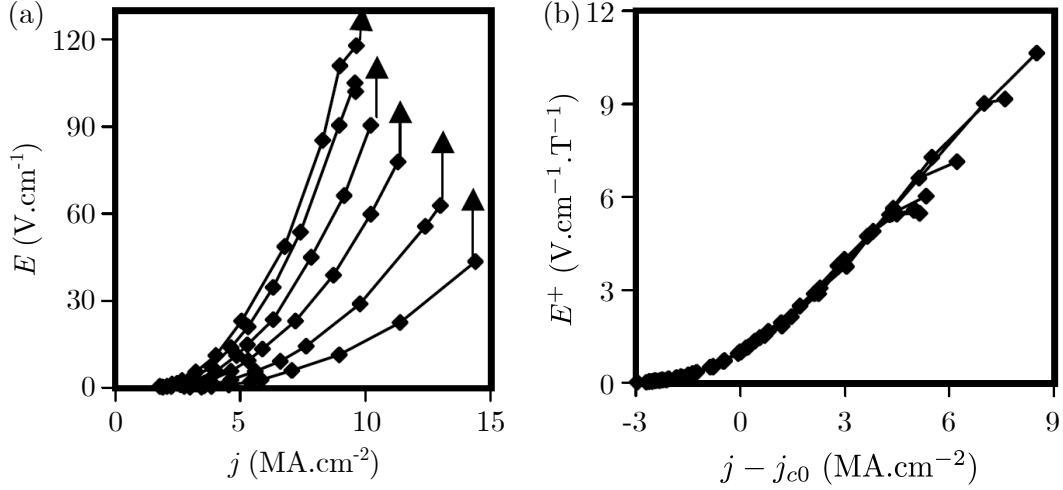


Figure 6.21 – (a) Current voltage curve at 20 K and different external magnetic fields $\mu_0 H$ equal to 3 T, 5 T, 8 T, 11 T, and 15.8 T from right to left. The arrows highlight the voltage switch. (b) Data from (a) are rescaled with eq. (6.30) as a function of the current density subtracted by the critical current density measured from the IV curve. Adapted from Kunchur [82].

fitting parameter. We stress that L does not correspond to the device length but rather to the vortices extension since they are the source of the voltage drop extension. To estimate an order of magnitude, we propose to fix $\mu_0 H_{c2}(T) = 120$ T for $T \approx 0$ K and $\rho_n(T) = 300 \mu\Omega.cm$ measured at $T = 100$ K, while I_c , V_s , and L are adjusting parameters. Let's note that any change of the parameters $H_{c2}(T)$ or $\rho_n(T)$ will modified linearly the length L . Thus we can infer how the three correlated parameters are evolving with respect to each others since $H_{c2}(T) \propto \rho_n(T)L$ all other things being equal.

Figure 6.22(a) shows the IV data along with the best fit curves in plain red lines. The fitting procedure has been performed only on a voltage range near the instability, if a wider voltage range is used the model deviates from the data sets. The Kunchur model accurately accounts for the experiments for all the different external magnetic fields applied. As the bias current raises the slope gets steeper up to the point it is almost infinite at the instability point for $V = V_s$. The dashed red lines are the extension of the best fit curves. Their intersection with the abscissa correspond to the critical current necessary to correctly fit the data. Though, it is worth noting that the critical current used to fit the data does not match the experimental value, it always over estimates it. It may be explained by the fact that a different vortex mechanism comes into play at lower voltages

Table 6.5 – Relationships of the switching parameters with respect to the external magnetic field $\mu_0 H$. The (–) symbol means that it is independent of H , while the (\times) symbol means that the relationship is not specified.

Model	Temperature range	E_s or V_s	v_φ^*	I_s	ρ^*	Reference
LO instability Low field	$T \approx T_c$	$\propto H\sqrt{H}$	$\propto \sqrt{H}$	\times	\times	[73, 75, 83]
LO instability High field	$T \approx T_c$	$\propto H$	–	\times	\times	[73, 75, 77]
Kunchur	$T < T_c/2$	$\propto \sqrt{H}$	$\propto 1/\sqrt{H}$	$\propto 1/\sqrt{H}$	$\propto H$	[82]

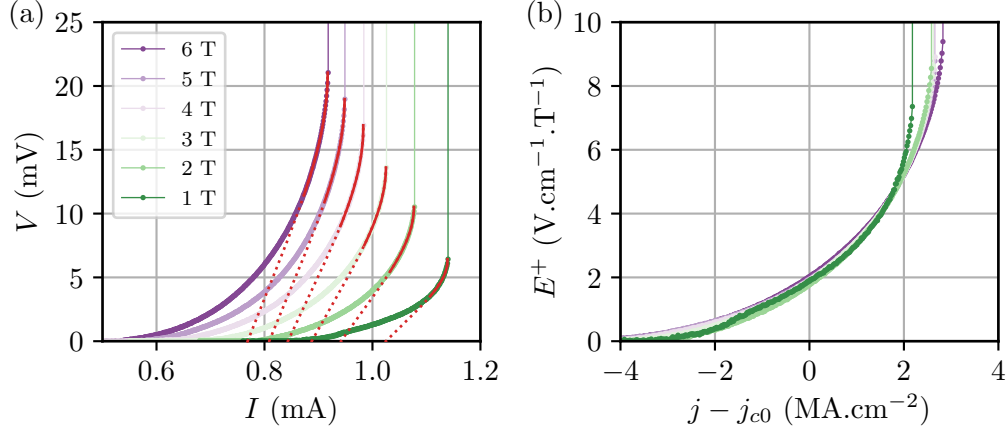


Figure 6.22 – (a) IV curves for different external magnetic fields of C6, a 500 nm long 176 nm wide superconducting nanowire patterned on a 30 nm thick YBCO film. The plain red lines are least squares fittings according to the Kunchur model, while the dotted red lines are the extension of the fitted curves to lower voltages. Their intersections with the abscissa corresponds to the fitting parameters I_{c0} . (b) The same IV curves with a scaling for voltage according to eq. (6.30) and current by subtracting j_{c0} , the current density corresponding to I_{c0} .

as we saw previously in chapter 5.

As regards the voltage drop extension obtained from the fitting, $L \approx 5 \mu\text{m}$. It slightly decreases with the external magnetic field with a total variation of $5 \mu\text{m}$ between $\mu_0 H = 1 \text{ T}$ and $\mu_0 H = 6 \text{ T}$. We note that L corresponds to the vortex electromagnetic extension $2\Lambda_0 \approx 5.4 \mu\text{m}$. This is serendipity what we expected. The qualitative agreement of the fitting is good. In the experiment $T = 100 \text{ mK}$, it follows that the normal resistivity is definitely smaller than its value taken at 100 K while the upper critical field is almost unchanged. According to eq. (6.29) it should result in a longer L value. It suggests that either the vortex electromagnetic length is larger near the instability, or several vortex rows are superimposed in parallel which extends the electromagnetic length *de facto*.

Following Kunchur [82], fig. 6.22(b) shows the same IV data that rescaled in voltage using the equation below:

$$E^+ = \frac{E}{\mu_0 H} \sqrt{f \left(0.0245 \frac{V^2}{V_s^2} \right)} \quad (6.30)$$

while the current density is simply centered on the fitted critical current density value j_{c0} . All our data curves are collapsing on the same master curve like the ones of Kunchur depicted in fig. 6.21(b). In addition, both set of rescaled IV curves have the same order of magnitude for both E^+ and $j - j_{c0}$, whether in our case or Kunchur case. Nevertheless, the curvature approaching the instability point in our data is rather different than Kunchur. In fig. 6.21, we observe that the master curve with the rescaling becomes concave, while in our case the curvature remains convex with and without the scaling, as shown in fig. 6.22.

In order to continue the comparison with Kunchur results we also plot in fig. 6.23 two characteristic parameters of the Kunchur model: the critical velocity v_φ^* given by eq. (6.28) and the critical resistivity ρ^* written as:

$$\rho^* = \frac{V_s}{L j_s} \quad (6.31)$$

The main interest is to compare the magnetic field dependence of such parameters with

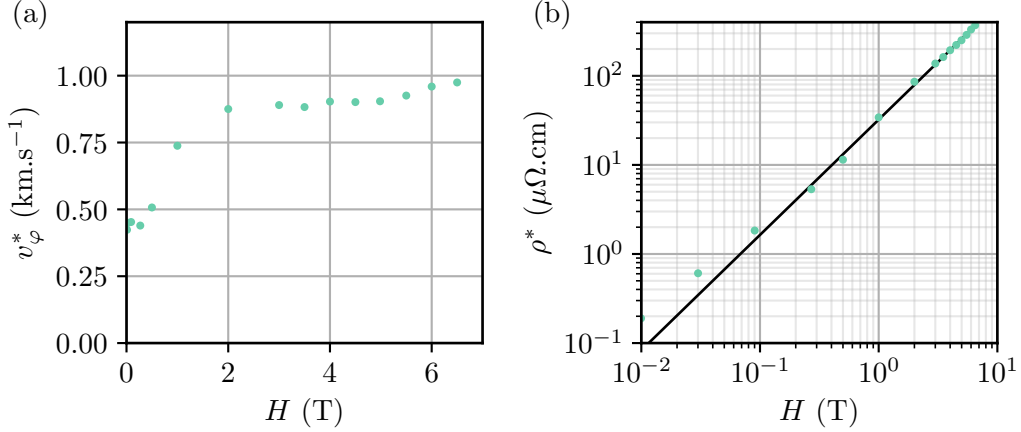


Figure 6.23 – Evolution of the fitting parameters extracted using the Kunchur model as a function of the external magnetic field: (a) the critical velocity v_φ^* and (b) the critical resistivity $\rho^* = V_s/Lj_s$.

the expected dependencies by the model knowing that $v_\varphi^* \propto 1/\sqrt{H}$ and $\rho^* \propto H$ as summed up in table 6.5.

In fig. 6.23(a), starting from low magnetic field values, the critical velocity rapidly increases and it almost saturates above 2 T. In fig. 6.23(b), we observe that the critical resistivity raises monotonically with a power law behavior represented by the plain black line with a power value of 1.3. Thus, we clearly see that the magnetic field evolution of both fitting parameters are not in accordance with the magnetic dependencies predicted by Kunchur. The discrepancy may stem from different effects. First, in contrast to Kunchur, the self-field induced by the current is not negligible in our case. Second, in the fitting procedure the magnetic field dependence lies in the electromagnetic length L keeping the upper critical field and the normal resistivity constant. It is not necessary the case as the magnetoresistance affects the ρ_n value, which changes the estimate of L , and thus modify the values of both v_φ^* and ρ^* . Therefore, the magnetic field evolution of the critical parameters characterizing the instability needs further analysis.

6.5.3 Concluding remarks

Both LO and Kunchur models describe a similar vortex instability, but in a different temperature regime. While the former occurs near T_c with a vortex core shrinkage, the latter applies at low temperatures below $T_c/2$ while the vortex core expands. They both lead to a vortex instability that triggers a drastic voltage switch in the IV characteristic. In our case, the Kunchur model accounts well for the IV experiments near the instability point, but the magnetic field dependence is still unclear. Despite this aspect, the interpretation of the switching mechanism in the light of a vortex instability is more convincing than the interpretation given by the KG model.

In this section, we have only studied the effect of the magnetic field on the instability point at 100 mK. In order to provide additional arguments in favor of the vortex instability interpretation, it could be of particular interest to perform similar experiments for different temperatures. It could provide a crossover temperature between the LO instability and the Kunchur one. Additionally, we could also speculate that this crossover temperature may be related to the crossover temperature observed in section 6.4 in which the standard deviation of the switching current grows as temperature lowers.

Be that as it may, up to now the main conclusion is that the voltage switch is triggered

by a vortex instability. In the KG model the voltage switch is driven by the fluctuations, whether thermal or quantal, thus it is a purely stochastic mechanism. The voltage switch follows a Poisson distribution law as an event is independent of the previous event. In contrast, the switching mechanism triggered by the vortex instability is inherently chaotic: a strong non linearity in the vortex dynamics generates a vortex instability. In this respect, the voltage switch is deterministic: it occurs when the vortex velocity bypasses the critical vortex velocity. But a little change of the initial conditions may lead to a different switching point due to the strong non linearity.

6.6 Switching current distributions

In section 6.4 we deliberately set the switching current histograms aside from the analysis. We only studied the statistical moments characterizing globally the SCD to make the comparison easier in light of the KG model. We concluded that the KG theory does not account for the experiments in the YBCO irradiated nanowires. Several arguments show that the vortex instability is the origin of the voltage switch in our devices. Now that we better identified the voltage switch origin, we come back at the analysis of the switching current histograms with regard to the vortex instability.

6.6.1 Observation of multimodal distribution

Figure 6.24 shows the switching current histograms of the ESD data sets presented previously in section 6.4.1 at different temperatures for C8, the device whose properties is resumed in table 6.4. The switching current histograms are binned with $\Delta I = 40$ nA, centered on the expected mean value \bar{I}_s , and normalized to unity. Such a procedure facilitates the comparison between histograms at different temperatures on the same scale. Obviously, we observe qualitatively the same behavior depicted by the fourth first statistical moments shown in fig. 6.15. Starting from 68 K the histogram is narrowly peaked. While temperature decreases, the histograms widen and necessarily their amplitude diminishes as they are normalized. The distribution widening continues down to the lowest temperature at 6 K. This observation reflects the fact that the standard deviation of the switching current $\hat{\sigma}(I_s)$ increases while temperature lowers.

There was a significant loss of information when we studied the statistical moments at first. Now, the most striking feature is that we observed multimodal switching current histograms. Instead of having one single peak the estimated distribution may be bimodal or even trimodal for low enough temperatures. The transition between the unimodal and the multimodal histograms occurs about 40 K, at least within the peak resolution limit. For higher temperatures the principal peak is asymmetric (44 K, 50 K), and it is not possible to distinguish another satellite peak. Additionally, we notice that the mode with higher weighting, *i.e.* with the larger area under the curve, may be alternatively on the left side (30 K), on the right side (35 K), or within the center (6 K). The histograms may be alternatively left skewed, right skewed, or almost symmetric depending on temperature but without correlation with it. This observation explains why the evolution of the skewness was erratic. We cannot conclude anything about the kurtosis because the histogram is multimodal while it usually characterizes how flat is the distribution compared to a unimodal normal distribution. Previously, we consider that as temperature diminishes the standard deviation increases because of the widening of the SCD. In fact, the unimodal distribution splits up in two distinct modes for $T \approx 40$ K and they move away of each other as temperature decreases further.

While the switching current histograms are rather intriguing, two major observations emerge: when temperature diminishes the SCD widens and it becomes multimodal. We

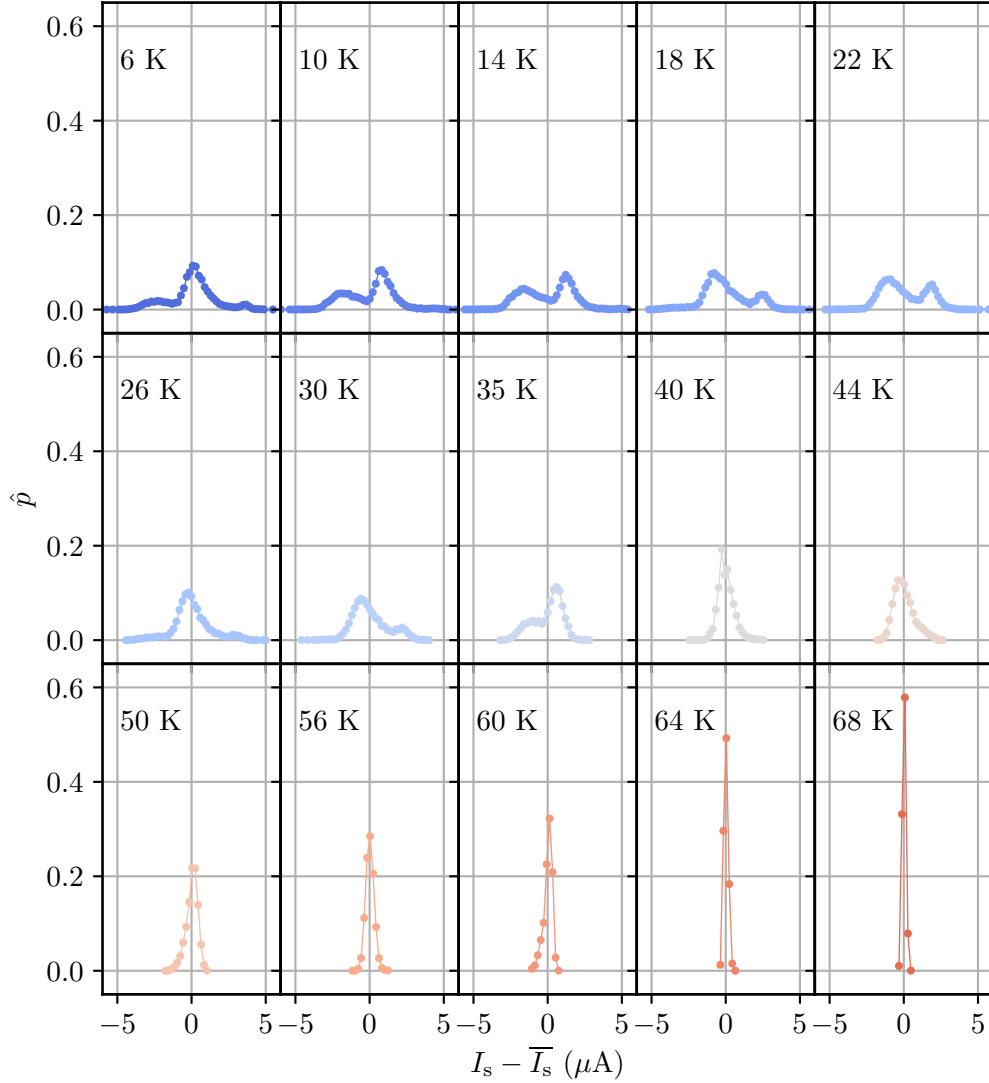


Figure 6.24 – Histograms of the switching current centered on the mean switching current value \bar{I}_s at different temperatures for the nanowire C8 (see table 6.4 for further details).

have seen those features in several devices of different samples whose superconducting properties are similar (cf section 6.4.2). The widening of the SCD at low temperatures have been also noticed by Rouco *et al.* [74] in YBCO nanowires. They attributed the voltage switch to a vortex instability but they do not provide physical interpretation of the SCD widening. We also stress that multimodal SCDs have been observed by Lyatti *et al.* in YBCO nanowires [306]. In contrast to Rouco *et al.* and this work, they interpret the voltage switch as a phase slip dynamics in a washboard potential. In this framework, they argued that the multimodal SCD is the proof of an energy level quantization. As there is no convincing evidences that a phase slip process occurs in the YBCO nanowires, neither that it behaves like a JJ, we do not support this interpretation in this thesis. However, we conclude that the two experimental features are systematically observed at low temperatures for several devices by different research groups: they are reproducible.

6.6.2 Modelling of the histograms

In order to gain further insights into the switching dynamics we model the SCDs presented in fig. 6.24 by a linear combination of gaussian functions. It allows us to see how the SCDs is evolving with temperature and how the weightings are distributed between the different modes of the SCDs. We consider a gaussian function written as:

$$g(x) = ae^{-\frac{(x-m)^2}{2s^2}} \quad (6.32)$$

where a is the amplitude, m is the mean value, and s is the standard deviation of the gaussian function. We stress that the parameters are not the estimate of the statistical moments. They correspond to the parameters of a gaussian function that will be fitted with a least squares fitting. For $T \geq 40$ K, the histogram is fitted with only one gaussian function g_0 using a_0 , m_0 , and s_0 as fitting parameters. In the case of $T < 40$ K, the histogram is at least bimodal, thus it is fitted with a sum of two gaussian function g_1 and g_2 whose fitting parameters are a_1 , m_1 , s_1 , a_2 , m_2 , and s_2 . Here above, the indexes 1 and 2 correspond to the modes with the lower and the upper mean values respectively: $m_1 < m_2$. We also mentioned the appearance of a third mode at low temperatures. Since its amplitude is small and for the sake of simplicity, we ignore it in the following analysis in order to focus on the two major modes of the SCDs.

Figure 6.25 shows some of the switching current histograms fitted by the linear combination of gaussian functions: two for (a,b) and one for (c).⁸ As a first approach, the multimodal gaussian function catches the main features of the SCDs without losing the multimodal information as it was the case when the statistical moments were estimated.

Figure 6.26 shows the temperature evolution of the fitting parameters s and a respectively in (a) and (b). The last fitting parameter m has not been represented incidentally. Since the histograms have been centered with respect to the mean value \bar{I}_s estimated on each data set, the mean values m_i taken solely are meaningless.⁹ Starting at high temperature, we observe in fig. 6.26(a) that s_0 is raising while temperature lessens down to

⁸Even if some histogram modes may deviate from the normal distribution, considering another type of probability density function won't give much additional information at the moment.

⁹Even if we decentered them, the mean values $m_i + I_s$ collapse almost on the same curve which also corresponds to the estimated mean value \bar{I}_s because m_i are about a few μA while $I_s \approx 1 \mu\text{A}$. The only

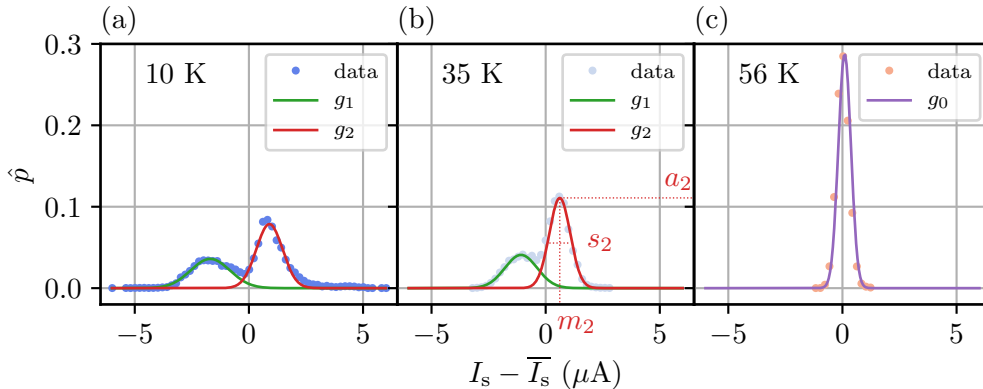


Figure 6.25 – Histograms of the switching current centered on the mean switching current value \bar{I}_s for three temperatures. In (a,b,c), the solid lines are least squares fitting curves of the SCDs. In (c), the dotted red lines highlight the fitting parameters of one gaussian function. In (a) and (b), the SCD is fitted with a sum of two gaussian functions, while in (c), the SCD is fitted with a single gaussian function. The data are obtained on C8.

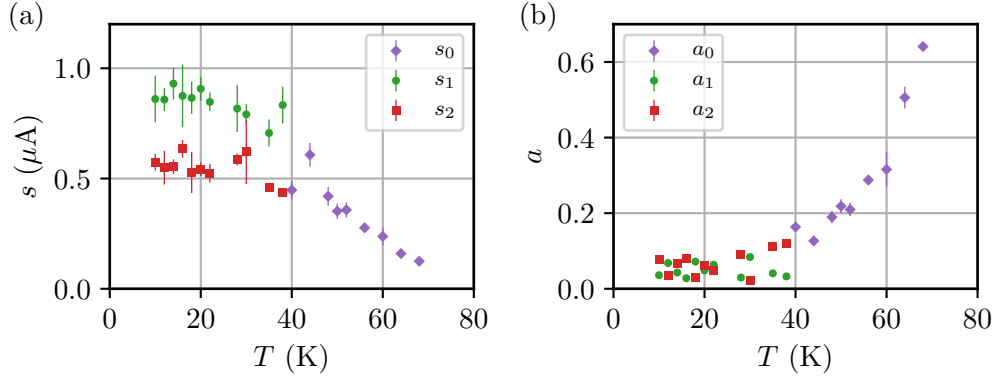


Figure 6.26 – Temperature evolution of (a) the standard deviation and (b) the amplitude of the gaussian fits performed on the switching current histograms. Index 0 corresponds to the gaussian function of a unimodal SCD, while indices 1 and 2 are respectively the lower and the upper gaussian function of a bimodal SCD.

40 K. For lower temperatures, the two other standard deviations s_1 and s_2 are saturating about $0.9 \mu\text{A}$ and $0.5 \mu\text{A}$ respectively. Therefore, the origin of the distribution broadening observed in $\hat{\sigma}(I_s)$ at low temperatures is twofold: first, the appearance of a multimodal distribution, and second, a widening of the two modes compared to the unimodal distribution observed at high temperatures. In addition, it is worth noting that the first mode in the bimodal SCD is always wider than the second one: $s_1 > s_2$. Now, if we look at fig. 6.26(b), we see that the amplitudes drop as temperature decreases. Since the SCDs have been normalized to unity and that the standard deviation raises at low temperatures, the mean values should necessarily decrease in order to preserve the same total area under the curve. However, the amplitudes of the bimodal SCDs do not exhibit a specific trend: there is no correlation of the peak amplitude with respect to its position - lower or upper - neither to temperature.

6.6.3 Relation with the vortex instability

Now that we presented numerous observations on the switching current statistic, we outline a physical interpretation to account for the experiments. Hereinbelow the reasoning is only qualitative and based on the vortex instability, whether in the framework of the LO or the Kunchur models. Prior to the voltage switch and under current biasing the superconducting nanowires exhibit a complex dynamical vortex configuration. At any time vortices nucleate at one edge, they are moving to the opposite edge, and they eventually annihilate. They may potentially form vortex rows as the simulations performed by Vodolazov and Peeters [290] or as the fractional order Shapiro steps observed experimentally in chapter 5. When the current raises the vortices speed up, it leads to an instability in which the vortex configuration rearranges itself rapidly and triggers the voltage switch.

One interpretation may be related to the number of parallel vortex rows opening as the current raises. In chapter 5, we observed that under an RF illumination at 6 K and 20 K fractional current steps appear in the IV curves. They have been associated to a different number of vortex rows synchronized by the RF frequency. For $n = 1/2$ and $n = 1/3$, we understand it as 2 and 3 vortex rows respectively. In the same spirit, the number of modes may be attributed to the number of parallel vortex rows opening. In this case, the first

relevant information lies in the difference $m_2 - m_1$ for the multimodal histograms. It tells how far the two modes are separated apart.

mode is wider than the second mode because there are probably more different current configurations that may trigger the voltage switch. As the first mode is bypassed, the current is higher which results in a narrower number of current configurations inside the nanowire that generates an instability.

Besides, according to the experiments shown in section 6.4, the triggering of the switch is not driven by thermal fluctuations as the mean value sets the standard deviation of the switching current. On the other hand, the non linearity arising from the instability make the system chaotic. In this respect, if the initial conditions of the vortex configuration are slightly modified, the appearance of the voltage switch may change notably. This argument supports the idea that the different modes observed in the multimodal histograms are related to different vortex configurations that trigger the voltage switch. After one IV acquisition, it is likely that the subsequent acquisition is not exactly in the same initial condition. As an example the vortices do not nucleate exactly at the same position or different vortex rows configuration are formed. It results in a different current path into the nanowire, then a different switching current, and thus several modes in the SCD. In other words, each mode in the SCD corresponds to a dynamical vortex configuration prior to the voltage switch.

When the nanowire is engaged in a specific vortex configuration, it may possibly go to another vortex configuration provided that it is still in the dissipative branch and that some energy is supplied. For high temperatures, it is likely that the thermal motion enables the nanowire to go from one configuration to another such that the lowest energy configuration will certainly trigger the event. In other words, the thermal fluctuations blur out the multimodal aspect by averaging the initial conditions. At lower temperatures, the vortex configuration may not necessarily be interchanged with another thanks to the thermal activation. Once the device is stuck in a specific configuration, the switching will occur at its corresponding switching current value without the opportunity to engage in another vortex configuration. With this interpretation, we explain the transition from a unimodal SCD to a multimodal SCD at low temperatures. However, it does not tell much why the SCD modes widen at low temperatures. The answer must probably lie in the correlation of the mean value with the standard deviation of the switching current. It might be interesting to correlate the fitting parameters of the multimodal gaussian function with the switching current mean value as we performed in section 6.4.3. It could tell if they are also set by \bar{I}_s only.

As a last remark, we interpret inherently the voltage switch as a chaotic behavior, that is the results is deterministic but very sensitive with respect to the initial conditions. In the case of the KG model, the results is purely stochastic in the sense that it is driven by the fluctuations. It could be of relevance to apply mathematical methodology, such as symbolic technique [86] or permutation spectrum test [87] - on both the returning and the switching current data sets. Depending on the patterns found in the data sets, these methods discriminate the data set governed by a chaotic or a stochastic dynamics. It would give a supporting argument toward the chaotic behavior, and thus the vortex instability rather than a fluctuation driven process.

6.7 Conclusion

In this chapter, we studied in details the voltage switch mechanism in the irradiated YBCO nanowires. At first we introduced the different theoretical models that describe a voltage switch in different superconducting devices. A fast IV acquisitions setup has been implemented to gather large switching current data sets. The statistical moments and the distribution of the switching current have been treated and retrieved thanks to a

combination of numerical analysis. Numerous experiments have been carried out to study the influence of several external parameters on the switching mechanism.

Afterwards, we compared the experiments with the different theoretical models. The generalized KG theory describes the origin of a voltage switch as PSs in 1D superconducting nanowires or as a phase particle escape in underdamped JJs. The mechanism is driven by the quantum and the thermal fluctuations. It results in the appearance of a sub-K crossover temperature between the two regimes, a specific evolution of the switching current standard deviation, and universal high order statistical moments. None of these features have been observed in the YBCO nanowires. On the other hand, the voltage switch in the IV curves measured on different devices, temperatures, and magnetic fields are very similar to the measurements performed on YBCO microbridges by other research groups. In this case, the switching mechanism is attributed to a vortex instability due to the enhancement of the vortex velocity according to the LO theory and the model of Kunchur. We successfully modelled the IV curves prior to the switch in the case of the application of a magnetic field. While the magnetic field dependence is not fully understood at present, the different experiments presented in this chapter and in chapter 5 are providing arguments in favor of the vortex instability. In this framework, the appearance of the multimodal distribution at low temperatures is interpreted as different dynamical vortex configurations. This feature is not observed at high temperatures because the thermal motion always activates the same dynamical vortex configuration. This aspect explains why the standard deviation enlarges significantly by one order of magnitude when temperature lowers.

Further theoretical work is necessary to account quantitatively for the experimental observations, let it be for the evolution of the statistical moments or the multimodal distributions. In addition, the measurements performed under the application of an external magnetic field should be extended to a wider temperature range. It could better describe the voltage switch in the framework of the LO instability and the Kunchur model. The use of mathematical methods could also discriminate whether the dynamics is stochastic or chaotic.

Conclusion

The whole research work of this thesis was driven by the potential of detecting single photon in YBCO superconducting nanowires. SSPDs based on LTS have proven their worth, especially in quantum communication, thanks to their high performances. But SSPD will remain a high technology niche because of its low operation temperature about a few kelvin. In this context, a HTS material like YBCO could make a big difference. If the operation temperature could gain one order of magnitude, SSPD could open to several new fields of application. In addition, SSPD mechanism has not been fully elucidated yet, as it is the case for superconductivity in YBCO. This is a great opportunity to investigate the peculiar physical phenomenon of superconductivity at low dimensions in presence of light-matter interaction. Because there is no theoretical consensus whether YBCO based SSPD could exist or not, this work presents a real scientific and experimental challenge.

Patterning long superconducting nanowires on high quality YBCO thin films is not an easy task. Indeed, both oxygen diffusion and disorder damage the material. We circumvented this problem by exploiting the latter effect with the ion irradiation technique. The ions introduce defects along their path into YBCO and turn the material into an insulator. By the means of electronic beam lithography and Monte-Carlo simulations, we developed an innovative and flexible fabrication workflow in which the YBCO thin nanowires are always embedded in an insulating matrix. Transports measurements demonstrated that our fabrication process is suitable to pattern robust YBCO superconducting devices in a reproducible and effective manner. Especially, we succeeded in making hundreds of micron long meander with 100 nm in width, and also shorter 100 nm wide nanowires. Both types of devices exhibit almost undamaged global superconducting properties with respect to the pristine films, representing a major breakthrough.

On the other hand, only the shorter nanowires present high critical current density of about 10% compared to the theoretical depairing current density, which is mandatory to develop and sustain a hotspot according to theoretical models. The consequences of such properties on the current voltage characteristics are twofold: first a large voltage switch about 1 V appears, and second, the characteristic becomes hysteretic. The thermal model developed by Skocpol, Beasley, and Tinkham accounts for the appearance of a hysteresis. It represents an opportunity to access the thermal properties of the YBCO nanowires. On the contrary, the voltage switch is not ruled by thermal properties, but rather by vortex instability. The complete physical picture is not fully understood, but several arguments point toward a chaotic process rather than a stochastic one as it is usually the case in metastable system driven by fluctuations. Further measurements within an external magnetic field and in a larger temperature range are required to clarify the mechanism at play.

We investigated thoroughly the different voltage dissipation regimes appearing between the superconducting branch and the voltage switch. The voltage drop is dominated by vortices crossing the nanowire width that is described as an energy barrier. Depending on external parameters, like bias current, temperature, and incident RF power, the vortex dynamics varies substantially. For current near the critical current, vortices hop between

pinning sites thanks to thermal motion and Lorentz force. As current increases further, pinning energy becomes too weak in comparison with the work done by Lorentz force, and the crossing energy barrier lessens. The vortices are also thermally activated to cross the energy barrier. In this picture, we introduced the vortex-vortex interaction in order to quantitatively account for the voltage dissipation. In presence of an incident RF power, we observed integer and fractional Shapiro like current steps: it revealed synchronized vortex motion. Altogether, the experiments along with their corresponding models prove that the vortex dynamics is one key ingredient to understand the physics of YBCO superconducting nanowires.

Finally, we measured experimentally the dark and photon count rates arising from voltage pulses in YBCO nanowires. We interpreted the dark count rate within the theoretical models proposed for SSPD. We obtained qualitative agreement using the VAP unbinding model. Nonetheless, this interpretation is physically inconsistent for numerous reasons. Among the other possible models, only the single vortex quantum tunneling seems reasonable within the temperature range that we probed. This study requires additional investigation both in terms of analysis and experiments to corroborate the latter mechanism. Regarding the single photon detection, we did not observe any influence of the laser light on the dark count. Several reasons may explain this fact. In particular the surface detection of the nanowire is very small, and we did not use state of the art light coupling: both leads to poor light coupling. It is also possible that the cross-section of the superconducting nanowires are still too important, or that the critical current density is not sufficiently high. Nevertheless, the count rate experiments are very encouraging, especially as dark count has already been observed in YBCO nanowires by another group. We made our contribution to stretch the limits of technology and knowledge aiming to achieve single photon detection in YBCO.

Appendix A

Fabrication recipes of irradiated YBCO nanowires

Contents

A.1 Step 1: PMMA resist	186
A.1.1 Spin-coating	186
A.1.2 Electronic beam lithography	186
A.1.3 Development	187
A.2 Step 1: S1805B resist	187
A.2.1 Spin-coating	187
A.2.2 Laser lithography	188
A.2.3 Development	188
A.3 Step 2: Ar⁺ ion beam etching	188
A.4 Step 3: Au deposition	188
A.5 Step 4: ma-N2405 resist	189
A.5.1 Spin-coating	189
A.5.2 Electronic beam lithography	189
A.5.3 Development	190
A.5.4 Lift-off	191

The following appendix presents the different fabrication recipes to design YBCO thin film nanodevices. The fabrication parameters have been optimized carefully in order not to damage the superconducting properties. Depending on the desired samples, specific steps are followed.

To design the Au electrodes, we perform either an EBL using a positive 500 nm thick PMMA resist as described in appendix A.1, or a laser beam lithography with a positive 500 nm thick S1805B resist as summarized in appendix A.2. As far as the dimensions are larger than 10 μm , the processes are both suitable. Steps 2 and 3 explain how we contact the YBCO thin film with gold electrodes using an Ar^+ IBE as presented in appendix A.3 and a Ti/Au deposition as described in appendix A.4. During steps 4 and 5, we fabricate the YBCO electrodes and the nanodevices. We pattern a resist mask of negative 500 nm thick ma-N 2405 resist using a two steps EBL as introduced in appendix A.5. It is designed to protect specific areas of the sample during the O^+ ion irradiation which follows. For specific samples, we terminate the nanofabrication with a He^+ FIB patterning on micron size YBCO bridges.

A.1 Step 1: PMMA resist

A.1.1 Spin-coating

We deposit a 500 nm thick PMMA positive photoresist at clean room facility of ENS Paris as follows:

- Clean 1 min in acetone at 50 °C with low-power ultrasound (3).
- Clean 1 min in isopropanol (IPA) at 50 °C with low-power ultrasound (3).
- Optical microscope observation.
- Repeat the first steps in case of dusts.
- Bake 1 min at 90 °C for dehydration.
- Spin-coat PMMA at 4000/4000/30 s.
- Bake 5 min at 120 °C.

A.1.2 Electronic beam lithography

We perform the EBL with an SEM FEG-SEM Magellan FEI at ESPCI Paris to pattern the resist mask by following the successive steps below:

- Adjust the working distance to 5 mm, and link the column depth: link-Z.
- Measure the currents on the Faraday's cup at the currents used during the EBL.
- Align the upper sample boundary horizontally: xT-align feature.
- Position the flags at three distinct corners of the sample as it is a 10 mm side square.
- Make burn spots at 20 kV and 13 pA in immersion mode in the center of the sample such that they do not super impose with the future nanostructures.
- Adjust the stigmatism and the focus on the burn spots. Under optimal conditions, burn spots are circular of 35 nm in diameter.
- Adjust the stigmatism and the focus on the burn spots at 20 kV and 26 nA.

- Proceed to the write-field alignments at a magnification of 600X with a $100 \mu\text{m}^2$ writing field (600x, $100 \mu\text{m}$) by lowering progressively the size of the window.
- Add a zoom factor 1.005.¹
- Run the EBL
 - Step: $0.1 \mu\text{m}$
 - $I = 26 \text{ nA}$ at 20 kV
 - writing-field: $100 \mu\text{m}$
 - Magnification: $600\times$
 - Dose: $250 \mu\text{C.cm}^{-2}$

The EBL lasts between 1 h and 7 h depending on the total written area. We compute the expected duration time and compare it to the previous similar EBLs in order to control the layout and avoid of committing errors in settings. If the duration time is considerably different, a special care have to be taken to consistently check the parameter settings.

A.1.3 Development

When the PMMA is exposed to an electronic beam, as a positive resist, the exposed PMMA is removed during the development. We perform the development either at the clean room facility of ENS Paris or Université Paris Diderot as follows:

- Develop 2 min in MIBK:IPA (1:3).
- Rinse 10 s in IPA.

A.2 Step 1: S1805B resist

A.2.1 Spin-coating

We deposit a 500 nm thick S1805B positive photoresist at the clean room facility of Collège de France or Paris Diderot as follows:

- Clean 1 min in acetone at $50 \text{ }^\circ\text{C}$ with low-power ultrasound (3).
- Clean 1 min in IPA at $50 \text{ }^\circ\text{C}$ with low-power ultrasound (3).
- Optical microscope observation.
- Repeat the first steps in case of dusts.
- Bake 1 min at $90 \text{ }^\circ\text{C}$ for dehydration.
- Spin-coat LOR5B at 4000/4000/60 s for large undercuts.
- Bake 5 min at $110 \text{ }^\circ\text{C}$.
- Spin-coat S1805B at 4000/4000/75 s.
- Bake 1 min at $110 \text{ }^\circ\text{C}$.

¹Increasing the zoom factor creates a small overlap between the structures allowing us to avoid gaps between different write-fields.

A.2.2 Laser lithography

We pattern the resist layer with a PhotonSteer LW450C laser lithographic system either at clean room facility of ENS Paris or Collège de France. Since there is no need for precise alignments at first step we only adjust the horizontality manually.

- Align the lower sample boundary horizontally.
- Adjust the focus with lens 3 at the center of the sample.
- Set the focus at three different points apart from each other.
- Run the laser lithography with the following parameters:
 - Lens: 2
 - D-step: 2
 - Dose: 250 mJ.cm⁻²

The lithography lasts around 10 min depending on the total written area.

A.2.3 Development

As a positive photoresist, resist is removed when it is exposed to the laser beam during the development. We develop the resist mask either at the clean room facility of Collège de France or the one of Université Paris Diderot as follows:

- Develop 30 s in MIP319.
- Rinse 10 s in deionized water.

A.3 Step 2: Ar⁺ ion beam etching

We perform the etching process at clean room facility of Université Paris Diderot using a Plassys MEB 550S as follows:

- Place the sample in the center of the sample holder, tilt it at 10° and rotate it at 10°/s.
- Wait for a pressure below 1.10⁻³ mbar.
- Turn on the high voltage at 78 mA, 500 V, and -50 V.
- Etch during adequate time knowing that the etching rate for Au is 20 nm.min⁻¹, while for CeO₂ is 7 nm.min⁻¹.

A.4 Step 3: Au deposition

We deposit an Au layer at clean room facility of Université Paris Diderot using a Plassys MEB 550S with the following steps:

- Place the sample in the Plassys machine and rotate the holder at 10°/s.
- Wait for a pressure below 1.10⁻⁶ mbar.
- Apply 20 mA to the Ti target and wait for 2 min.

- Deposit 0.5 nm at 0.02 nm.s⁻¹.
- Wait 5 min for the cool down of the crucible.
- Apply 50 mA to the Ti target and wait for 2 min.
- Deposit 200 nm at 0.3 nm.s⁻¹.
- Lift-off at 60 °C with 5 s flash of ultrasound at low power, in acetone or SVC14 depending on the resist used in step 1, respectively PMMA or S1805.
- Rinse in IPA.
- Optical microscope observation.
- Repeat the two previous steps if resist is not completely lifted.

A.5 Step 4: ma-N2405 resist

In order to avoid unwanted polymerization due to UV light exposure, spin-coating and development processes are done in optical room where the UV light is filtered. Until development we do not expose the samples to natural light. We deposit the resist at the clean room facility of ENS Paris or Université Paris Diderot as follows:

A.5.1 Spin-coating

- Clean 1 min in acetone at 50 °C with low-power ultrasound (3).
- Clean 1 min in IPA at 50 °C with low-power ultrasound (3).
- Optical microscope observation.
- Repeat the first steps in case of dusts.
- Bake 1 min at 90 °C for dehydration.
- Spin-coat Ti' at 3000/3000/30 s for promoting adhesion.
- Wait 10 s.
- Spin-coat ma-N 2405 at 3000/3000/30 s.
- Bake 3 min at 90 °C.

A.5.2 Electronic beam lithography

We perform the EBLs with a SEM FEG-SEM Magellan FEI at ESPCI Paris. During the lithography, we make sure not to take picture of the area of interest which will contain the devices, neither with classical camera nor SEM, whatever the exposure time. We have to locate the sample at its edges and then place the flags thanks to the Raith e-line pattern generator facility.

- Adjust the working distance to 5 mm, and link the column depth: link-Z.
- Measure the electronic beam current on the Faraday's cup at the currents used for the lithography: 13 pA in Immersion mode, and 26 nA in field-free mode.
- Align the upper sample boundary horizontally: xT-align feature.

- Position the flags at three distinct corners of the sample as it is a 10 mm side square.
- Position flags on three distinct Au marks apart from a few millimeters.
- Make burn spots at 20 kV and 13 pA in immersion mode in the center of the sample such that they do not super impose with the design structures.
- Adjust the stigmatism and the focus on the burn spots.
- Proceed to the write-field alignments at magnification $2400\times$ and a $25\ \mu\text{m}^2$ -writing field ($2400\times$, $25\ \mu\text{m}$) by lowering progressively the size of the window.
- Add a zoom factor 1.005 to get a small overlap of the structure and avoid gaps.
- Run the EBL with the following parameters:
 - Step: 2 nm
 - $I = 13\ \text{pA}$ at 20 kV in immersion mode
 - writing-field: $25\ \mu\text{m}$
 - Magnification: $2400\times$
 - Dose: $200\ \mu\text{C.cm}^{-2}$
- Center the ETD picture on a burn spot.
- Adjust the stigmatism and the focus on one burn spot at low current in field-free mode.
- Adjust the stigmatism and the focus on one burn spot at 20 kV and 26 nA in field-free mode without moving the sample holder.
- Proceed to the write-field alignments at a magnification of $600\times$ with a $100\ \mu\text{m}^2$ -writing field ($600\times$, $100\ \mu\text{m}$) by lowering progressively the size of the window.²
- Add a zoom factor 1.005.
- Run the EBL with the following parameters:
 - Step: $0.1\ \mu\text{m}$
 - $I = 26\ \text{nA}$ at 20 kV
 - writing-field: $25\ \mu\text{m}$
 - Magnification: $600\times$
 - Dose: $210\ \mu\text{C.cm}^{-2}$

A.5.3 Development

- Develop 1 min 30 s in AZ MIF 726.
- Rinse 10 s in deionized water.

²This method allows us to align precisely the low-current and high-current layers by compensating the beam-shift with the write-field alignment procedure. It gives better results than placing flags once more between the two EBLs.

A.5.4 Lift-off

- 1 min O₂ stripping with optical control.
- Lift-off 10 min in acetone at 50 °C with short 10 s ultrasound (US 3) shots.
- Rinse in IPA.
- Optical microscope observation.
- Repeat all the steps until the resist goes out of the sample.

Appendix B

Sample characteristics

Table B.1 – Sample characteristics

Origin	Name	Substrate	Seed layer	YBCO thickness	Capping layer
Ceraco	N	Sapphire	40 nm CeO ₂	12 nm	8 nm CeO ₂
				15 nm	
				20 nm	
				30 nm	
Ceraco	CS	Sapphire	40 nm CeO ₂	10 nm	8 nm CeO ₂ (5 mm ϕ) 20 nm Au
				20 nm	
				30 nm	
Briatico	T	STO	6 nm PBCO	5 nm	4 nm PBCO
				10 nm	
				20 nm	
				30 nm	
Briatico	JS	STO	4 nm CeO ₂	10 nm	4 nm CeO ₂ (5 mm ϕ) 20 nm Au
				30 nm	

Appendix C

Estimate of the Shapiro-like current steps height

Figure C.1 shows the numerical analysis procedure to estimate the current steps height based on the IV characteristic. The IV data are fitted with a linear function below and above the n^{th} step of interest on a limited range. The two linear fits are extrapolated at the voltage step position set by eq. (5.5) giving two points. The difference between those two points gives an estimate of the current step height ΔI_n .

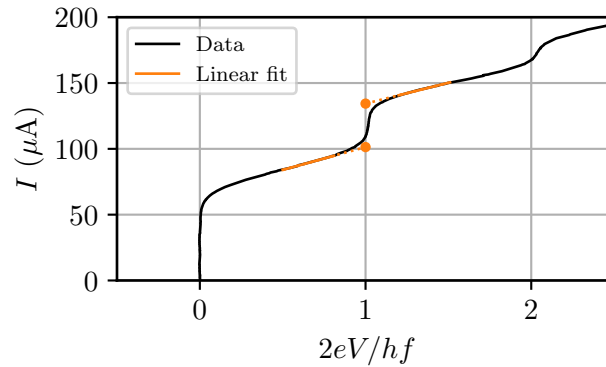


Figure C.1 – IV curve presenting the first Shapiro step at $f = 18.32$ GHz and $T = 50$ K of C8. The data (black line) are fitted with a linear model (solid orange line) below and above the appearance of the first step $n = 1$. The extrapolation of the linear fit at $n = 1$ (orange dotted line) gives an estimate of the current step height by measuring the current difference of the two orange points.

Bibliography

- [1] G. N. Gol'tsman, O. Okunev, G. Chulkova, A. Lipatov, A. Semenov, K. Smirnov, B. Voronov, A. Dzardanov, C. Williams, and R. Sobolewski, "Picosecond superconducting single-photon optical detector," *Applied Physics Letters*, vol. 79, no. 6, pp. 705–707, Aug. 2001. [Online]. Available: <http://aip.scitation.org/doi/10.1063/1.1388868>
- [2] G. Gol'tsman, O. Okunev, G. Chulkova, A. Lipatov, A. Dzardanov, K. Smirnov, A. Semenov, B. Voronov, C. Williams, and R. Sobolewski, "Fabrication and properties of an ultrafast NbN hot-electron single-photon detector," *IEEE Transactions on Applied Superconductivity*, vol. 11, no. 1, pp. 574–577, Mar. 2001. [Online]. Available: <http://ieeexplore.ieee.org/document/919410/>
- [3] H. Shibata, H. Takesue, T. Honjo, T. Akazaki, and Y. Tokura, "Single-photon detection using magnesium diboride superconducting nanowires," *Applied Physics Letters*, vol. 97, no. 212504, pp. 1–3, Nov. 2010. [Online]. Available: <http://aip.scitation.org/doi/10.1063/1.3518723>
- [4] F. Marsili, V. B. Verma, J. A. Stern, S. Harrington, A. E. Lita, T. Gerrits, I. Vayshenker, B. Baek, M. D. Shaw, R. P. Mirin, and S. W. Nam, "Detecting single infrared photons with 93% system efficiency," *Nature Photonics*, vol. 7, no. 3, pp. 210–214, Mar. 2013. [Online]. Available: <http://www.nature.com/articles/nphoton.2013.13>
- [5] H. Kamerlingh-Onnes, "Disappearance of the Electrical Resistance of Mercury at Helium Temperatures," *Proceedings Koninklijke Akademie van Wetenschappen te Amsterdam*, vol. 14, pp. 113–115, 1911.
- [6] F. London and H. London, "The electromagnetic equations of the supraconductor," *Proceedings of the Royal Society A*, vol. 149, no. 866, pp. 71–88, Mar. 1935. [Online]. Available: <https://doi.org/10.1098/rspa.1935.0048>
- [7] H. London, "Phase-equilibrium of supraconductors in a magnetic field," *Proceedings of the Royal Society A*, vol. 152, no. 877, pp. 650–663, Nov. 1935. [Online]. Available: <https://doi.org/10.1098/rspa.1935.0212>
- [8] L. Landau, "On the theory of superconductivity," in *Collected Papers of L.D. Landau*. Elsevier, 1965, pp. 546–568. [Online]. Available: <https://linkinghub.elsevier.com/retrieve/pii/B978008010586450078X>
- [9] J. Bardeen, L. N. Cooper, and J. R. Schrieffer, "Theory of Superconductivity," *Physical Review*, vol. 108, no. 5, pp. 1175–1204, Dec. 1957. [Online]. Available: <https://link.aps.org/doi/10.1103/PhysRev.108.1175>
- [10] R. Arpaia, D. Golubev, R. Baghdadi, R. Ciancio, G. Dražić, P. Orgiani, D. Montemurro, T. Bauch, and F. Lombardi, "Transport properties of

ultrathin $\text{YBa}_2\text{Cu}_3\text{O}_{7-\delta}$ nanowires: A route to single-photon detection,” *Physical Review B*, vol. 96, no. 6, Aug. 2017. [Online]. Available: <https://link.aps.org/doi/10.1103/PhysRevB.96.064525>

- [11] L. V. Shubnikov, V. I. Khotkevich, Y. D. Shepelev, and Y. N. Ryabinkin, “Magnetic properties and critical currents of superconducting alloys,” *Soviet Journal of Experimental and Theoretical Physics*, vol. 7, pp. 221–237, 1937.
- [12] A. Abrikosov, “On the Magnetic Properties of Superconductors of the Second Group,” *Soviet Physics Journal of Experimental and Theoretical Physics*, vol. 5, no. 6, pp. 1174–1182, Dec. 1957.
- [13] B. D. Josephson, “Possible new effects in superconductive tunnelling,” *Physics Letters*, vol. 1, no. 7, pp. 251–253, Jul. 1962.
- [14] K. K. Likharev, “Superconducting weak links,” *Reviews of Modern Physics*, vol. 51, no. 1, pp. 101–159, Jan. 1979. [Online]. Available: <https://link.aps.org/doi/10.1103/RevModPhys.51.101>
- [15] P. Anderson and A. Dayem, “Radio-frequency effects in superconducting thin film bridges,” *Physical Review Letters*, vol. 13, no. 6, pp. 195–197, Aug. 1964.
- [16] W. A. Little, “Decay of persistent currents in small superconductors,” *Physical Review*, vol. 156, no. 2, pp. 396–403, Apr. 1967.
- [17] W. J. Skocpol, M. R. Beasley, and M. Tinkham, “Phase-slip centers and nonequilibrium processes in superconducting tin microbridges,” *Journal of Low Temperature Physics*, vol. 16, no. 1-2, pp. 145–167, Jul. 1974. [Online]. Available: <http://link.springer.com/10.1007/BF00655865>
- [18] K. K. Likharev, “Vortex motion and the Josephson effect in superconducting thin bridges,” *Soviet Physics Journal of Experimental and Theoretical Physics*, vol. 34, pp. 906–912, Oct. 1971.
- [19] A. Andronov, I. Gordion, V. Kurin, I. Nefedov, and I. Shereshevsky, “Kinematic vortices and phase slip lines in the dynamics of the resistive state of narrow superconductive thin film channels,” *Physica C: Superconductivity and its Applications*, vol. 213, no. 1-2, pp. 193–199, Aug. 1993. [Online]. Available: <https://linkinghub.elsevier.com/retrieve/pii/092145349390777N>
- [20] S. Shapiro, “Josephson currents in superconducting tunneling: The effect of microwaves and other observations,” *Physical Review Letters*, vol. 11, no. 2, pp. 80–82, Jul. 1963.
- [21] A. Rothwarf and B. N. Taylor, “Measurement of Recombination Lifetimes in Superconductors,” *Physical Review Letters*, vol. 19, no. 1, pp. 27–30, Jul. 1967. [Online]. Available: <https://link.aps.org/doi/10.1103/PhysRevLett.19.27>
- [22] A. D. Semenov, R. S. Nebosis, Y. P. Gousev, M. A. Heusinger, and K. F. Renk, “Analysis of the nonequilibrium photoresponse of superconducting films to pulsed radiation by use of a two-temperature model,” *Physical Review B*, vol. 52, no. 1, pp. 581–590, Jul. 1995. [Online]. Available: <https://link.aps.org/doi/10.1103/PhysRevB.52.581>

- [23] A. D. Semenov, G. N. Gol'tsman, and A. Korneev, "Quantum detection by current carrying superconducting film," *Physica C: Superconductivity and its Applications*, vol. 351, no. 4, pp. 349–356, Apr. 2001. [Online]. Available: [https://doi.org/10.1016/S0921-4534\(00\)01637-3](https://doi.org/10.1016/S0921-4534(00)01637-3)
- [24] A. Semenov, A. Engel, H.-W. Hübers, K. Il'in, and M. Siegel, "Spectral cut-off in the efficiency of the resistive state formation caused by absorption of a single-photon in current-carrying superconducting nano-strips," *The European Physical Journal B*, vol. 47, no. 4, pp. 495–501, Oct. 2005. [Online]. Available: <http://www.springerlink.com/index/10.1140/epjb/e2005-00351-8>
- [25] A. Engel, J. Lonsky, X. Zhang, and A. Schilling, "Detection Mechanism in SNSPD: Numerical Results of a Conceptually Simple, Yet Powerful Detection Model," *IEEE Transactions on Applied Superconductivity*, vol. 25, no. 3, pp. 1–7, Jun. 2015. [Online]. Available: <http://ieeexplore.ieee.org/document/6960053/>
- [26] M. Hofherr, D. Rall, K. Ilin, M. Siegel, A. Semenov, H.-W. Hübers, and N. A. Gippius, "Intrinsic detection efficiency of superconducting nanowire single-photon detectors with different thicknesses," *Journal of Applied Physics*, vol. 108, no. 014507, pp. 1–9, Jul. 2010. [Online]. Available: <http://aip.scitation.org/doi/10.1063/1.3437043>
- [27] L. N. Bulaevskii, M. J. Graf, C. D. Batista, and V. G. Kogan, "Vortex-induced dissipation in narrow current-biased thin-film superconducting strips," *Physical Review B*, vol. 83, no. 144526, pp. 1–9, Apr. 2011. [Online]. Available: <https://link.aps.org/doi/10.1103/PhysRevB.83.144526>
- [28] L. N. Bulaevskii, M. J. Graf, and V. G. Kogan, "Vortex-assisted photon counts and their magnetic field dependence in single-photon superconducting detectors," *Physical Review B*, vol. 85, no. 014505, pp. 1–10, Jan. 2012. [Online]. Available: <https://link.aps.org/doi/10.1103/PhysRevB.85.014505>
- [29] A. Engel and A. Schilling, "Numerical analysis of detection-mechanism models of superconducting nanowire single-photon detector," *Journal of Applied Physics*, vol. 114, no. 214501, pp. 1–12, Dec. 2013. [Online]. Available: <http://aip.scitation.org/doi/10.1063/1.4836878>
- [30] A. N. Zotova and D. Y. Vodolazov, "Intrinsic detection efficiency of superconducting nanowire single photon detector in the modified hot spot model," *Superconductor Science and Technology*, vol. 27, no. 12, pp. 1–9, Oct. 2014. [Online]. Available: <http://stacks.iop.org/0953-2048/27/i=12/a=125001?key=crossref.5c0ae8accd40ab6d15cefd52f298f0eb>
- [31] D. Y. Vodolazov, "Current dependence of the red boundary of superconducting single-photon detectors in the modified hot-spot model," *Physical Review B*, vol. 90, no. 054515, pp. 1–5, Aug. 2014. [Online]. Available: <https://link.aps.org/doi/10.1103/PhysRevB.90.054515>
- [32] H. Assink, "Critical currents in submicron YBa₂Cu₃O₇ lines," *IEEE Transactions on Applied Superconductivity*, vol. 3, no. 1, pp. 2983–2985, Mar. 1993.
- [33] S. Nawaz, T. Bauch, and F. Lombardi, "Transport Properties of YBCO Nanowires," *IEEE Transactions on Applied Superconductivity*, vol. 21, no. 3, pp. 164–167, Jun. 2011. [Online]. Available: <http://ieeexplore.ieee.org/document/5710674/>

- [34] P. Larsson, B. Nilsson, and Z. G. Ivanov, "Fabrication and transport measurements of $\text{YBa}_2\text{Cu}_3\text{O}_{7-x}$ nanostructures," *Journal of Vacuum Science & Technology B, Nanotechnology and Microelectronics: Materials, Processing, Measurement, and Phenomena*, vol. 18, no. 1, pp. 25–31, Jan. 2000.
- [35] G. Papari, F. Carillo, D. Stornaiuolo, L. Longobardi, F. Beltram, and F. Tafuri, "High critical current density and scaling of phase-slip processes in YBaCuO nanowires," *Superconductor Science and Technology*, vol. 25, no. 035011, pp. 1–5, Jan. 2012. [Online]. Available: <http://stacks.iop.org/0953-2048/25/i=3/a=035011?key=crossref.31f397f03f3792641cb290624fb4906f>
- [36] R. Arpaia, S. Nawaz, F. Lombardi, and T. Bauch, "Improved nanopatterning for YBCO nanowires approaching the depairing current," *IEEE Transactions on Applied Superconductivity*, vol. 23, no. 3, pp. 1–5, Jun. 2013.
- [37] R. Arpaia, M. Ejrnaes, L. Parlato, R. Cristiano, M. Arzeo, T. Bauch, S. Nawaz, F. Tafuri, G. P. Pepe, and F. Lombardi, "Highly homogeneous YBCO/LSMO nanowires for photoresponse experiments," *Superconductor Science and Technology*, vol. 27, no. 4, pp. 1–9, Mar. 2014.
- [38] G. Papari, F. Carillo, D. Stornaiuolo, D. Massarotti, L. Longobardi, F. Beltram, and F. Tafuri, "Dynamics of vortex matter in YBCO sub-micron bridges," *Physica C: Superconductivity and its Applications*, vol. 506, pp. 188–194, Nov. 2014. [Online]. Available: <https://linkinghub.elsevier.com/retrieve/pii/S0921453414001968>
- [39] S. K. H. Lam, A. Bendavid, and J. Du, "Hot spot formation in focused-ion-beam-fabricated $\text{YBa}_2\text{Cu}_3\text{O}_{7-x}$ nanobridges with high critical current densities," *Nanotechnology*, vol. 30, no. 32, pp. 1–8, May 2019. [Online]. Available: <https://iopscience.iop.org/article/10.1088/1361-6528/ab1971>
- [40] A. Sharafiev, M. Malnou, C. Feuillet-Palma, C. Ulysse, T. Wolf, F. Couëdo, P. Febvre, J. Lesueur, and N. Bergeal, "HTS Josephson junctions arrays for high-frequency mixing," *Superconductor Science and Technology*, vol. 31, no. 3, p. 035003, Jan. 2018. [Online]. Available: <http://stacks.iop.org/0953-2048/31/i=3/a=035003?key=crossref.1d4121712a479a302f18c5af12ba14ab>
- [41] S. Ouanani, J. Kermorvant, C. Ulysse, M. Malnou, Y. Lemaître, B. Marcilhac, C. Feuillet-Palma, N. Bergeal, D. Crété, and J. Lesueur, "High- T_c superconducting quantum interference filters (SQIFs) made by ion irradiation," *Superconductor Science and Technology*, vol. 29, no. 9, p. 094002, Jul. 2016. [Online]. Available: <http://stacks.iop.org/0953-2048/29/i=9/a=094002?key=crossref.494af18107217d97950b85c89af4bffd>
- [42] F. Couëdo, E. Recoba Pawlowski, J. Kermorvant, J. Trastoy, D. Crété, Y. Lemaître, B. Marcilhac, C. Ulysse, C. Feuillet-Palma, N. Bergeal, and J. Lesueur, "High- T_c superconducting detector for highly-sensitive microwave magnetometry," *Applied Physics Letters*, vol. 114, no. 19, p. 192602, May 2019. [Online]. Available: <http://aip.scitation.org/doi/10.1063/1.5090175>
- [43] J. Lesueur, L. Dumoulin, S. Quillet, and J. Radcliffe, "Ion-beam induced metal insulator transition in YBCO films," *Journal of Alloys and Compounds*, vol. 195, pp. 527–530, May 1993. [Online]. Available: <http://linkinghub.elsevier.com/retrieve/pii/092583889390792L>

- [44] L. Bégon-Lours, “Ferroelectric Field-Effects in High-Tc Superconducting Devices,” Ph.D. dissertation, UPMC, Jan. 2017.
- [45] W. J. Skocpol, M. R. Beasley, and M. Tinkham, “Selfheating hotspots in superconducting thin film microbridges,” *Journal of Applied Physics*, vol. 45, no. 9, pp. 4054–4066, Sep. 1974. [Online]. Available: <http://aip.scitation.org/doi/10.1063/1.1663912>
- [46] R. Griessen, Wen Hai-hu, A. J. J. van Dalen, B. Dam, J. Rector, H. G. Schnack, S. Libbrecht, E. Osquiguil, and Y. Bruynseraede, “Evidence for mean free path fluctuation induced pinning in YBa₂Cu₃O₇ and YBa₂Cu₄O₈ films,” *Physical Review Letters*, vol. 72, no. 12, pp. 1910–1913, Mar. 1994. [Online]. Available: <https://link.aps.org/doi/10.1103/PhysRevLett.72.1910>
- [47] H. Greenhouse, “Design of Planar Rectangular Microelectronic Inductors,” *IEEE Transactions on Parths, Hybrids, and Packaging*, vol. 10, no. 2, pp. 101–109, Jun. 1974.
- [48] M. Tinkham, *Introduction to superconductivity*, 2nd ed., 1996.
- [49] W. Rauch, E. Gornik, G. Sölkner, A. A. Valenzuela, F. Fox, and H. Behner, “Microwave properties of YBa₂Cu₃O_{7-x} thin films studied with coplanar transmission line resonators,” *Journal of Applied Physics*, vol. 73, no. 4, pp. 1866–1872, Feb. 1993. [Online]. Available: <http://aip.scitation.org/doi/10.1063/1.353173>
- [50] J. Johansson, K. Cedergren, T. Bauch, and F. Lombardi, “Properties of inductance and magnetic penetration depth in (103)-oriented YBa₂Cu₃O_{7-δ} thin films,” *Physical Review B*, vol. 79, no. 214513, pp. 1–6, Jun. 2009. [Online]. Available: <https://link.aps.org/doi/10.1103/PhysRevB.79.214513>
- [51] T. Wolf, N. Bergeal, J. Lesueur, C. J. Fourie, G. Faini, C. Ulysse, and P. Febvre, “YBCO Josephson Junctions and Striplines for RSFQ Circuits Made by Ion Irradiation,” *IEEE Transactions on Applied Superconductivity*, vol. 23, no. 2, pp. 1101205–1101205, Apr. 2013. [Online]. Available: <http://ieeexplore.ieee.org/document/6466450/>
- [52] P. W. Anderson and Y. B. Kim, “Hard Superconductivity: Theory of the Motion of Abrikosov Flux Lines,” *Reviews of Modern Physics*, vol. 36, no. 1, pp. 39–43, Jan. 1964. [Online]. Available: <https://link.aps.org/doi/10.1103/RevModPhys.36.39>
- [53] P. Bernstein, C. Picard, M. Pannetier, P. Lecoeur, J. F. Hamet, T. D. Doan, J. P. Contour, M. Drouet, and F. X. Regi, “Current–voltage characterization of the vortex motion in YBa₂Cu₃O_{7-δ} microbridges and the implications on the development of superconducting flux flow transistors,” *Journal of Applied Physics*, vol. 82, no. 10, pp. 5030–5038, Nov. 1997. [Online]. Available: <http://aip.scitation.org/doi/10.1063/1.366374>
- [54] M. Pannetier, P. Lecoeur, P. Bernstein, T. D. Doan, and J. F. Hamet, “Characterization of pinning and vortex motion in thin superconducting microbridges,” *Physical Review B*, vol. 62, no. 22, pp. 15162–15171, Dec. 2000. [Online]. Available: <https://link.aps.org/doi/10.1103/PhysRevB.62.15162>
- [55] N. Bergeal, X. Grison, J. Lesueur, G. Faini, M. Aprili, and J. P. Contour, “High-quality planar high-Tc Josephson junctions,” *Applied Physics Letters*, vol. 87, no. 102502, pp. 1–3, Aug. 2005. [Online]. Available: <http://aip.scitation.org/doi/10.1063/1.2037206>

- [56] M. Malnou, C. Feuillet-Palma, C. Ulysse, G. Faini, P. Febvre, M. Sirena, L. Olanier, J. Lesueur, and N. Bergeal, “High- T_c superconducting Josephson mixers for terahertz heterodyne detection,” *Journal of Applied Physics*, vol. 116, no. 074505, pp. 1–11, Aug. 2014. [Online]. Available: <http://aip.scitation.org/doi/10.1063/1.4892940>
- [57] L. G. Aslamazov and A. I. Larkin, “Josephson effect in wide superconducting bridges,” *Soviet Physics Journal of Experimental and Theoretical Physics*, vol. 41, no. 2, pp. 381–386, Feb. 1975.
- [58] J. M. Repaci, C. Kwon, Q. Li, X. Jiang, T. Venkatesan, R. E. G. Iii, C. J. Lobb, and R. S. Newrock, “Absence of a Kosterlitz-Thouless transition in ultrathin YBCO films,” *Physical Review B*, vol. 54, no. 14, pp. R9674–R9677, Oct. 1996.
- [59] F. Tafuri, J. Kirtley, D. Born, D. Stornaiuolo, P. Medaglia, P. Orgiani, G. Balestrino, and V. G. Kogan, “Dissipation in ultra-thin current-carrying superconducting bridges; evidence for quantum tunneling of Pearl vortices,” *Europhysics Letters*, vol. 73, no. 6, pp. 948–954, Mar. 2006.
- [60] V. G. Kogan, “Interaction of vortices in thin superconducting films and the Berezinskii-Kosterlitz-Thouless transition,” *Physical Review B*, vol. 75, no. 064514, pp. 1–5, Feb. 1994. [Online]. Available: <https://link.aps.org/doi/10.1103/PhysRevB.75.064514>
- [61] H. Bartolf, A. Engel, A. Schilling, K. Il’in, M. Siegel, H.-W. Hübers, and A. Semenov, “Current-assisted thermally activated flux liberation in ultrathin nanopatterned NbN superconducting meander structures,” *Physical Review B*, vol. 81, no. 024502, pp. 1–12, Jan. 2010. [Online]. Available: <https://link.aps.org/doi/10.1103/PhysRevB.81.024502>
- [62] T. Yamashita, S. Miki, K. Makise, W. Qiu, H. Terai, M. Fujiwara, M. Sasaki, and Z. Wang, “Origin of intrinsic dark count in superconducting nanowire single-photon detectors,” *Applied Physics Letters*, vol. 99, no. 161105, pp. 1–3, Oct. 2011. [Online]. Available: <http://aip.scitation.org/doi/10.1063/1.3652908>
- [63] U. Nasti, L. Parlato, M. Ejrnaes, R. Cristiano, T. Taino, H. Myoren, R. Sobolewski, and G. Pepe, “Thermal fluctuations in superconductor/ferromagnet nanostripes,” *Physical Review B*, vol. 92, no. 014501, pp. 1–6, Jul. 2015. [Online]. Available: <https://link.aps.org/doi/10.1103/PhysRevB.92.014501>
- [64] M. Ejrnaes, L. Parlato, R. Arpaia, T. Bauch, F. Lombardi, R. Cristiano, F. Tafuri, and G. P. Pepe, “Observation of dark pulses in 10 nm thick YBCO nanostrips presenting hysteretic current voltage characteristics,” *Superconductor Science and Technology*, vol. 30, no. 12LT02, pp. 1–6, Nov. 2017. [Online]. Available: <http://stacks.iop.org/0953-2048/30/i=12/a=12LT02?key=crossref.10f7bf79dabff3103021e4d8d1af7d8e>
- [65] A. Murphy, A. Semenov, A. Korneev, Y. Korneeva, G. Gol’tsman, and A. Bezryadin, “Three Temperature Regimes in Superconducting Photon Detectors: Quantum, Thermal and Multiple Phase-Slips as Generators of Dark Counts,” *Scientific Reports*, vol. 5, no. 10174, pp. 1–10, May 2015. [Online]. Available: <http://www.nature.com/articles/srep10174>
- [66] J. Kurkijärvi, “Intrinsic fluctuations in a superconducting ring closed with a Josephson junction,” *Physical Review B*, vol. 6, no. 3, pp. 832–835, Aug. 1972. [Online]. Available: <https://journals.aps.org/prb/abstract/10.1103/PhysRevB.6.832>

- [67] T. A. Fulton and L. N. Dunkleberger, “Lifetime of the zero-voltage state in Josephson tunnel junctions,” *Physical Review B*, vol. 9, no. 11, pp. 4760–4768, Jun. 1974. [Online]. Available: <https://link.aps.org/doi/10.1103/PhysRevB.9.4760>
- [68] P. Silvestrini, O. Liengme, and K. E. Gray, “Current distributions of thermal switching in extremely underdamped Josephson junctions,” *Physical Review B*, vol. 37, no. 4, pp. 1525–1531, Feb. 1988. [Online]. Available: <https://link.aps.org/doi/10.1103/PhysRevB.37.1525>
- [69] T. Bauch, F. Lombardi, F. Tafuri, A. Barone, G. Rotoli, P. Delsing, and T. Claeson, “Macroscopic Quantum Tunneling in d-Wave YBCO Josephson Junctions,” *Physical Review Letters*, vol. 94, no. 087003, pp. 1–4, Mar. 2005. [Online]. Available: <https://link.aps.org/doi/10.1103/PhysRevLett.94.087003>
- [70] M. Sahu, “Switching current distribution of superconducting nanowires: evidence of quantum phase slip events,” Ph.D. dissertation, Urbana-Champaign, 2009.
- [71] M.-H. Bae, R. C. Dinsmore, M. Sahu, and A. Bezryadin, “Stochastic and deterministic phase slippage in quasi-one-dimensional superconducting nanowires exposed to microwaves,” *New Journal of Physics*, vol. 14, no. 043014, pp. 1–15, Apr. 2012. [Online]. Available: <http://stacks.iop.org/1367-2630/14/i=4/a=043014?key=crossref.6ce2e7d3078691af484a96b16562d10c>
- [72] A. Murphy, P. Weinberg, T. Aref, U. C. Coskun, V. Vakaryuk, A. Levchenko, and A. Bezryadin, “Universal Features of Counting Statistics of Thermal and Quantum Phase Slips in Nanosize Superconducting Circuits,” *Physical Review Letters*, vol. 110, no. 247001, pp. 1–5, Jun. 2013. [Online]. Available: <https://link.aps.org/doi/10.1103/PhysRevLett.110.247001>
- [73] S. G. Doettinger, R. P. Huebener, R. Gerdemann, A. Kühle, S. Anders, T. G. Träuble, and J. C. Villégier, “Electronic Instability at High Flux-Flow Velocities in High- T_c Superconducting Films,” *Physical Review Letters*, vol. 73, no. 12, pp. 1691–1694, Sep. 1994. [Online]. Available: <https://link.aps.org/doi/10.1103/PhysRevLett.73.1691>
- [74] V. Rouco, D. Massarotti, D. Stornaiuolo, G. Papari, X. Obradors, T. Puig, F. Tafuri, and A. Palau, “Vortex Lattice Instabilities in YBa₂Cu₃O_{7-x} Nanowires,” *Materials*, vol. 11, no. 211, pp. 1–10, Jan. 2018. [Online]. Available: <http://www.mdpi.com/1996-1944/11/2/211>
- [75] Z. L. Xiao and P. Ziemann, “Vortex dynamics in YBa₂Cu₃O₇ superconducting films: Experimental evidence for an instability in the vortex system at high current densities,” *Physical Review B*, vol. 53, no. 22, pp. 1–7, Jun. 1996.
- [76] A. Garg, “Escape-field distribution for escape from a metastable potential well subject to a steadily increasing bias field,” *Physical Review B*, vol. 51, no. 21, pp. 15 592–15 595, Jun. 1995. [Online]. Available: <https://link.aps.org/doi/10.1103/PhysRevB.51.15592>
- [77] W. Klein, R. P. Huebener, S. Gauss, and J. Parisi, “Nonlinearity in the flux-flow behavior of thin-film superconductors,” *Journal of Low Temperature Physics*, vol. 61, no. 5-6, pp. 413–432, Dec. 1985. [Online]. Available: <http://link.springer.com/10.1007/BF00683694>

- [78] S. G. Doettinger, S. Kittelberger, R. P. Huebener, and C. C. Tsuei, “Quasiparticle energy relaxation in the cuprate superconductors,” *Physical Review B*, vol. 56, no. 21, pp. 14 157–14 162, Dec. 1997. [Online]. Available: <https://link.aps.org/doi/10.1103/PhysRevB.56.14157>
- [79] Z. L. Xiao, P. V.-d. Haan, G. Jakob, T. Kluge, P. Haibach, H. Adrian, and E. Y. Andrei, “Flux-flow instability and its anisotropy in Bi₂Sr₂CaCu₂O_{8-δ} superconducting films,” *Physical Review B*, vol. 59, no. 2, p. 10, Jan. 1999.
- [80] E. Andersson, R. Arpaia, E. Tralbaldo, T. Bauch, and F. Lombardi, “Fabrication and electrical transport characterization of high quality underdoped YBa₂Cu₃O_{7-δ} nanowires,” *arXiv:1910.11062 [cond-mat.supr-con]*, Oct. 2019. [Online]. Available: <https://arxiv.org/abs/1910.11062>
- [81] G. Grimaldi, A. Leo, F. Avitabile, N. Martucciello, A. Galluzzi, M. Polichetti, S. Pace, and A. Nigro, “Vortex lattice instability at the nanoscale in a parallel magnetic field,” *Nanotechnology*, vol. 30, no. 424001, pp. 1–8, Jul. 2019. [Online]. Available: <https://iopscience.iop.org/article/10.1088/1361-6528/ab3314>
- [82] M. N. Kunchur, “Unstable Flux Flow due to Heated Electrons in Superconducting Films,” *Physical Review Letters*, vol. 89, no. 137005, pp. 1–4, Sep. 2002. [Online]. Available: <https://link.aps.org/doi/10.1103/PhysRevLett.89.137005>
- [83] A. I. Larkin and Y. N. Ovchinnikov, “Nonlinear conductivity of superconductors in the mixed state,” *Soviet Physics Journal of Experimental and Theoretical Physics*, vol. 41, no. 5, pp. 960–965, May 1976.
- [84] S. Doettinger, R. Huebener, and A. Kühle, “Electronic instability during vortex motion in cuprate superconductors Regime of low and high magnetic fields,” *Physica C*, vol. 251, no. 3-4, pp. 285–289, Sep. 1995. [Online]. Available: <https://linkinghub.elsevier.com/retrieve/pii/0921453495004114>
- [85] L. Embon, Y. Anahory, L. Jelić, E. O. Lachman, Y. Myasoedov, M. E. Huber, G. P. Mikitik, A. V. Silhanek, M. V. Milošević, A. Gurevich, and E. Zeldov, “Imaging of super-fast dynamics and flow instabilities of superconducting vortices,” *Nature Communications*, vol. 8, no. 85, pp. 1–10, Dec. 2017. [Online]. Available: <http://www.nature.com/articles/s41467-017-00089-3>
- [86] Z. Yang and G. Zhao, “Application of symbolic techniques in detecting determinism in time series,” in *Proceedings of the 20th annual international conference of the IEEE Engineering in Medicine and Biology Society. Vol. 20 Biomedical Engineering Towards the Year 2000 and Beyond*, vol. 5, Nov. 1998, pp. 2670–2673.
- [87] C. W. Kulp and L. Zunino, “Discriminating chaotic and stochastic dynamics through the permutation spectrum test,” *Chaos: An Interdisciplinary Journal of Nonlinear Science*, vol. 24, no. 033116, pp. 1–9, Sep. 2014. [Online]. Available: <http://aip.scitation.org/doi/10.1063/1.4891179>
- [88] F. Bacon, *Bacon’s essays and Wisdom of the Ancients*, 1701. [Online]. Available: <http://www.gutenberg.org/files/56463/56463-h/56463-h.htm>
- [89] R. Hanbury Brown and R. Twiss, “A test of a new type of stellar interferometer on Sirius,” *Nature*, vol. 178, no. 4541, pp. 1046–1049, Nov. 1956.

- [90] G. Goldhaber, W. B. Fowler, S. Goldhaber, T. F. Hoang, T. E. Kalogeropoulos, and W. M. Powell, "Pion-Pion Correlations in Antiproton Annihilation Events," *Physical Review Letters*, vol. 3, no. 4, pp. 181–183, Aug. 1959. [Online]. Available: <https://link.aps.org/doi/10.1103/PhysRevLett.3.181>
- [91] E. Reiger, S. Dorenbos, V. Zwiller, A. Korneev, G. Chulkova, I. Milostnaya, O. Minaeva, G. Gol'tsman, J. Kitaygorsky, D. Pan, W. Slysz, A. Jukna, and R. Sobolewski, "Spectroscopy With Nanostructured Superconducting Single Photon Detectors," *IEEE Journal of Selected Topics in Quantum Electronics*, vol. 13, no. 4, pp. 934–943, Jul. 2007. [Online]. Available: <http://ieeexplore.ieee.org/document/4303051/>
- [92] C. J. Chunnillall, I. P. Degiovanni, S. Kück, I. Müller, and A. G. Sinclair, "Metrology of single-photon sources and detectors: a review," *Optical Engineering*, vol. 53, no. 8, pp. 081910–1–17, Jul. 2014. [Online]. Available: <http://opticalengineering.spiedigitallibrary.org/article.aspx?doi=10.1117/1.OE.53.8.081910>
- [93] Y. Hochberg, I. Charaev, S.-W. Nam, V. Verma, M. Colangelo, and K. K. Berggren, "Detecting Dark Matter with Superconducting Nanowires," *Physical Review Letters*, vol. 123, no. 15, pp. 1–7, Oct. 2019.
- [94] The BIG Bell Test Collaboration, "Challenging local realism with human choices," *Nature*, vol. 557, no. 7704, pp. 212–216, May 2018. [Online]. Available: <http://www.nature.com/articles/s41586-018-0085-3>
- [95] Q.-C. Sun, Y.-L. Mao, S.-J. Chen, W. Zhang, Y.-F. Jiang, Y.-B. Zhang, W.-J. Zhang, S. Miki, T. Yamashita, H. Terai, X. Jiang, T.-Y. Chen, L.-X. You, X.-F. Chen, Z. Wang, J.-Y. Fan, Q. Zhang, and J.-W. Pan, "Quantum teleportation with independent sources and prior entanglement distribution over a network," *Nature Photonics*, vol. 10, no. 10, pp. 671–675, Oct. 2016. [Online]. Available: <http://www.nature.com/articles/nphoton.2016.179>
- [96] H. Zhou, Y.-H. He, C.-L. Lü, L.-X. You, Z.-H. Li, G. Wu, W.-J. Zhang, L. Zhang, X.-Y. Liu, X.-Y. Yang, and Z. Wang, "Photon-counting chirped amplitude modulation lidar system using superconducting nanowire single-photon detector at 1550-nm wavelength," *Chinese Physics B*, vol. 27, no. 1, pp. 1–5, Jan. 2018. [Online]. Available: <http://stacks.iop.org/1674-1056/27/i=1/a=018501?key=crossref.c076a96d1f2e4b54bbdda59130dab37a>
- [97] S. Chan, A. Halimi, F. Zhu, I. Gyongy, R. K. Henderson, R. Bowman, S. McLaughlin, G. S. Buller, and J. Leach, "Long-range depth imaging using a single-photon detector array and non-local data fusion," *Scientific Reports*, vol. 9, no. 8075, pp. 1–10, May 2019. [Online]. Available: <http://www.nature.com/articles/s41598-019-44316-x>
- [98] J. Tachella, Y. Altmann, N. Mellado, A. McCarthy, R. Tobin, G. S. Buller, J.-Y. Tournieret, and S. McLaughlin, "Real-time 3D reconstruction from single-photon lidar data using plug-and-play point cloud denoisers," *Nature Communications*, vol. 10, no. 4984, pp. 1–6, Nov. 2019. [Online]. Available: <http://www.nature.com/articles/s41467-019-12943-7>
- [99] J. Yin, Y. Cao, Y.-H. Li, S.-K. Liao, L. Zhang, J.-G. Ren, W.-Q. Cai, W.-Y. Liu, B. Li, H. Dai, G.-B. Li, Q.-M. Lu, Y.-H. Gong, Y. Xu, S.-L. Li, F.-Z. Li, Y.-Y. Yin, Z.-Q. Jiang, M. Li, J.-J. Jia, G. Ren, D. He, Y.-L. Zhou, X.-X. Zhang, N. Wang, X. Chang, Z.-C. Zhu, N.-L. Liu, Y.-A. Chen, C.-Y. Lu, R. Shu, C.-Z.

- Peng, J.-Y. Wang, and J.-W. Pan, "Satellite-based entanglement distribution over 1200 kilometers," *Science*, vol. 356, no. 6343, pp. 1140–1144, Jun. 2017. [Online]. Available: <http://www.sciencemag.org/lookup/doi/10.1126/science.aan3211>
- [100] P. W. Shor, "Polynomial-Time Algorithms for Prime Factorization and Discrete Logarithms on a Quantum Computer," *SIAM Journal on Computing*, vol. 26, no. 5, pp. 1484–1509, Oct. 1997, arXiv: quant-ph/9508027. [Online]. Available: <http://arxiv.org/abs/quant-ph/9508027>
- [101] C. Gidney and M. Ekerå, "How to factor 2048 bit RSA integers in 8 hours using 20 million noisy qubits," *arXiv:1905.09749 [quant-ph]*, Dec. 2019. [Online]. Available: <http://arxiv.org/abs/1905.09749>
- [102] C. Bennett and G. Brassard, "Quantum cryptography: public key distribution and coin tossing," in *Proc. IEEE International Conf. Computers, Systems and Signal Processing*, vol. 1, Bangalore, India, Dec. 1984, pp. 175–179. [Online]. Available: <https://researcher.watson.ibm.com/researcher/files/us-bennetc/BB84highest.pdf>
- [103] H. Ko, B.-S. Choi, J.-S. Choe, K.-J. Kim, J.-H. Kim, and C. J. Youn, "Critical side channel effects in random bit generation with multiple semiconductor lasers in a polarization-based quantum key distribution system," *Optics Express*, vol. 25, no. 17, pp. 20 045–20 055, Aug. 2017. [Online]. Available: <https://www.osapublishing.org/abstract.cfm?URI=oe-25-17-20045>
- [104] L. You, J. Quan, Y. Wang, Y. Ma, X. Yang, Y. Liu, H. Li, J. Li, J. Wang, J. Liang, Z. Wang, and X. Xie, "Superconducting nanowire single photon detection system for space applications," *Optics Express*, vol. 26, no. 3, pp. 2965–2971, Feb. 2018. [Online]. Available: <https://www.osapublishing.org/abstract.cfm?URI=oe-26-3-2965>
- [105] A. M. Pawlikowska, A. Halimi, R. A. Lamb, and G. S. Buller, "Single-photon three-dimensional imaging at up to 10 kilometers range," *Optics Express*, vol. 25, no. 10, pp. 11 919–11 931, May 2017. [Online]. Available: <https://www.osapublishing.org/abstract.cfm?URI=oe-25-10-11919>
- [106] C. M. Natarajan, M. G. Tanner, and R. H. Hadfield, "Superconducting nanowire single-photon detectors: physics and applications," *Superconductor Science and Technology*, vol. 25, no. 6, pp. 1–16, Apr. 2012. [Online]. Available: <http://stacks.iop.org/0953-2048/25/i=6/a=063001?key=crossref.1c2cb0f1672747cf1557fd0396786328>
- [107] L. Stevens, R. Jonckheere, E. Froyen, S. Decoutere, and D. Lanneer, "Determination of the proximity parameters in electron beam lithography using doughnut-structures," *Microelectronic Engineering*, vol. 5, no. 1-4, pp. 141–150, Dec. 1986. [Online]. Available: <http://linkinghub.elsevier.com/retrieve/pii/0167931786900407>
- [108] S. Jahanmirinejad and A. Fiore, "Proposal for a superconducting photon number resolving detector with large dynamic range," *Optics Express*, vol. 20, no. 5, p. 5017, Feb. 2012. [Online]. Available: <https://www.osapublishing.org/oe/abstract.cfm?uri=oe-20-5-5017>
- [109] F. Mattioli, Z. Zhou, A. Gaggero, R. Gaudio, S. Jahanmirinejad, D. Sahin, F. Marsili, R. Leoni, and A. Fiore, "Photon-number-resolving superconducting nanowire detectors," *Superconductor Science and Technology*, vol. 28, no. 104001, pp. 1–15, Aug. 2015. [Online]. Available: <http://stacks.iop.org/0953-2048/28/i=10/a=104001?key=crossref.61f03aa29c629d75c70170cecb60e0bf>

- [110] F. Marsili, “Single-Photon and Photon-Number-Resolving Detectors Based on Superconducting Nanowires,” Ph.D. dissertation, EPFL, 2009.
- [111] M. J. Fitch, B. C. Jacobs, T. B. Pittman, and J. D. Franson, “Photon-number resolution using time-multiplexed single-photon detectors,” *Physical Review A*, vol. 68, no. 043814, pp. 1–6, Oct. 2003. [Online]. Available: <https://link.aps.org/doi/10.1103/PhysRevA.68.043814>
- [112] D. Achilles, C. Silberhorn, C. Sliwa, K. Banaszek, I. A. Walmsley, M. J. Fitch, B. C. Jacobs, T. B. Pittman, and J. D. Franson, “Photon-number-resolving detection using time-multiplexing,” *Journal of Modern Optics*, vol. 51, no. 9-10, pp. 1499–1515, Jun. 2004. [Online]. Available: <https://www.tandfonline.com/doi/full/10.1080/09500340408235288>
- [113] Hamamatsu, “Photomultiplier tubes and assemblies.” [Online]. Available: https://www.hamamatsu.com/resources/pdf/etd/High_energy_PMT_TPMZ0003E.pdf
- [114] —, “Photomultiplier tubes (PMTs) - About PMTs.” [Online]. Available: https://www.hamamatsu.com/eu/en/product/optical-sensors/pmt/about_pmts/index.html
- [115] M. Niigaki, T. Hirohata, T. Suzuki, H. Kan, and T. Hiruma, “Field-assisted photoemission from InP/InGaAsP photocathode with p/n junction,” *Applied Physics Letters*, vol. 71, no. 17, pp. 2493–2495, Oct. 1997. [Online]. Available: <http://aip.scitation.org/doi/10.1063/1.120098>
- [116] S. Cova, M. Ghioni, A. Lacaita, C. Samori, and F. Zappa, “Avalanche photodiodes and quenching circuits for single-photon detection,” *Applied Optics*, vol. 35, no. 12, pp. 1956–1976, Apr. 1996. [Online]. Available: <https://www.osapublishing.org/abstract.cfm?URI=ao-35-12-1956>
- [117] A. Spinelli, M. Ghioni, S. Cova, and L. Davis, “Avalanche detector with ultraclean response for time-resolved photon counting,” *IEEE Journal of Quantum Electronics*, vol. 34, no. 5, pp. 817–821, May 1998. [Online]. Available: <http://ieeexplore.ieee.org/document/668769/>
- [118] R. McIntyre, “On the avalanche initiation probability of avalanche diodes above the breakdown voltage,” *IEEE Transactions on Electron Devices*, vol. 20, no. 7, pp. 637–641, Jul. 1973. [Online]. Available: <http://ieeexplore.ieee.org/document/1477372/>
- [119] F. Guerrieri, S. Tisa, A. Tosi, and F. Zappa, “Two-Dimensional SPAD Imaging Camera for Photon Counting,” *IEEE Photonics Journal*, vol. 2, no. 5, pp. 759–774, Oct. 2010. [Online]. Available: <http://ieeexplore.ieee.org/document/5549868/>
- [120] C. Bruschini, H. Homulle, I. M. Antolovic, S. Burri, and E. Charbon, “Single-photon avalanche diode imagers in biophotonics: review and outlook,” *Light: Science & Applications*, vol. 8, no. 87, pp. 1–28, Sep. 2019. [Online]. Available: <http://www.nature.com/articles/s41377-019-0191-5>
- [121] Y. Mao, B.-X. Wang, C. Zhao, G. Wang, R. Wang, H. Wang, F. Zhou, J. Nie, Q. Chen, Y. Zhao, Q. Zhang, J. Zhang, T.-Y. Chen, and J.-W. Pan, “Integrating quantum key distribution with classical communications in backbone fiber network,” *Optics Express*, vol. 26, no. 5, pp. 6010–6020, Mar. 2018. [Online]. Available: <https://www.osapublishing.org/abstract.cfm?URI=oe-26-5-6010>

- [122] A. Pljonkin, K. Rumyantsev, and P. Singh, “Synchronization in Quantum Key Distribution Systems,” *Cryptography*, vol. 1, no. 18, pp. 1–9, Oct. 2017. [Online]. Available: <http://www.mdpi.com/2410-387X/1/3/18>
- [123] H. Kosaka, D. S. Rao, H. D. Robinson, P. Bandaru, K. Makita, and E. Yablonovitch, “Single photoelectron trapping, storage, and detection in a field effect transistor,” *Physical Review B*, vol. 67, no. 045104, pp. 1–5, Jan. 2003. [Online]. Available: <https://link.aps.org/doi/10.1103/PhysRevB.67.045104>
- [124] A. Migdall, S. Polyakov, J. Fan, and J. Bienfang, Eds., *Single-photon generation and detection: experimental methods in the physical sciences*, ser. Experimental methods in the physical sciences. Amsterdam ; Boston: Elsevier/AP, Academic Press is an imprint of Elsevier, 2013, no. volume 45, oCLC: ocn844308244.
- [125] Y.-L. Tang, H.-L. Yin, S.-J. Chen, Y. Liu, W.-J. Zhang, X. Jiang, L. Zhang, J. Wang, L.-X. You, J.-Y. Guan, D.-X. Yang, Z. Wang, H. Liang, Z. Zhang, N. Zhou, X. Ma, T.-Y. Chen, Q. Zhang, and J.-W. Pan, “Measurement-Device-Independent Quantum Key Distribution over 200 km,” *Physical Review Letters*, vol. 113, no. 190501, pp. 1–5, Nov. 2014. [Online]. Available: <https://link.aps.org/doi/10.1103/PhysRevLett.113.190501>
- [126] Y.-L. Tang, H.-L. Yin, Q. Zhao, H. Liu, X.-X. Sun, M.-Q. Huang, W.-J. Zhang, S.-J. Chen, L. Zhang, L.-X. You, Z. Wang, Y. Liu, C.-Y. Lu, X. Jiang, X. Ma, Q. Zhang, T.-Y. Chen, and J.-W. Pan, “Measurement-Device-Independent Quantum Key Distribution over Untrustful Metropolitan Network,” *Physical Review X*, vol. 6, no. 011024, pp. 1–8, Mar. 2016. [Online]. Available: <https://link.aps.org/doi/10.1103/PhysRevX.6.011024>
- [127] A. Boaron, G. Boso, D. Rusca, C. Vulliez, C. Autebert, M. Caloz, M. Perrenoud, G. Gras, F. Bussi eres, M.-J. Li, D. Nolan, A. Martin, and H. Zbinden, “Secure Quantum Key Distribution over 421 km of Optical Fiber,” *Physical Review Letters*, vol. 121, no. 190502, pp. 1–4, Nov. 2018. [Online]. Available: <https://link.aps.org/doi/10.1103/PhysRevLett.121.190502>
- [128] Y. Liu, X. Yuan, M.-H. Li, W. Zhang, Q. Zhao, J. Zhong, Y. Cao, Y.-H. Li, L.-K. Chen, H. Li, T. Peng, Y.-A. Chen, C.-Z. Peng, S.-C. Shi, Z. Wang, L. You, X. Ma, J. Fan, Q. Zhang, and J.-W. Pan, “High-Speed Device-Independent Quantum Random Number Generation without a Detection Loophole,” *Physical Review Letters*, vol. 120, no. 010503, pp. 1–6, Jan. 2018. [Online]. Available: <https://link.aps.org/doi/10.1103/PhysRevLett.120.010503>
- [129] M. Grein, E. Dauler, A. Kerman, M. Willis, B. Romkey, B. Robinson, D. Murphy, and D. Boroson, “A superconducting photon-counting receiver for optical communication from the Moon,” *SPIE Newsroom*, Jul. 2015. [Online]. Available: <http://www.spie.org/x114726.xml>
- [130] A. McCarthy, N. J. Krichel, N. R. Gemmell, X. Ren, M. G. Tanner, S. N. Dorenbos, V. Zwiller, R. H. Hadfield, and G. S. Buller, “Kilometer-range, high resolution depth imaging via 1560 nm wavelength single-photon detection,” *Optics Express*, vol. 21, no. 7, pp. 8904–8915, Apr. 2013. [Online]. Available: <https://www.osapublishing.org/abstract.cfm?URI=oe-21-7-8904>
- [131] S. Chen, D. Liu, W. Zhang, L. You, Y. He, W. Zhang, X. Yang, G. Wu, M. Ren, H. Zeng, Z. Wang, X. Xie, and M. Jiang, “Time-of-flight laser ranging and imaging

at 1550 nm using low-jitter superconducting nanowire single-photon detection system,” *Applied Optics*, vol. 52, no. 14, pp. 3241–3245, May 2013. [Online]. Available: <https://www.osapublishing.org/abstract.cfm?URI=ao-52-14-3241>

- [132] J. Huang, W. Zhang, L. You, C. Zhang, C. Lv, Y. Wang, X. Liu, H. Li, and Z. Wang, “High speed superconducting nanowire single-photon detector with nine interleaved nanowires,” *Superconductor Science and Technology*, vol. 31, no. 074001, pp. 1–7, May 2018. [Online]. Available: <http://stacks.iop.org/0953-2048/31/i=7/a=074001?key=crossref.4be3eace0d2b9c2cb669064c262817af>
- [133] K. M. Rosfjord, J. K. W. Yang, E. A. Dauler, A. J. Kerman, V. Anant, B. M. Voronov, G. N. Gol’tsman, and K. K. Berggren, “Nanowire single-photon detector with an integrated optical cavity and anti-reflection coating,” *Optics Express*, vol. 14, no. 2, pp. 527–534, Jan. 2006. [Online]. Available: <https://www.osapublishing.org/oe/abstract.cfm?uri=oe-14-2-527>
- [134] C. Schuck, W. H. P. Pernice, and H. X. Tang, “Waveguide integrated low noise NbTiN nanowire single-photon detectors with milli-Hz dark count rate,” *Scientific Reports*, vol. 3, no. 1893, pp. 1–10, May 2013. [Online]. Available: <http://www.nature.com/articles/srep01893>
- [135] S. Ferrari, C. Schuck, and W. Pernice, “Waveguide-integrated superconducting nanowire single-photon detectors,” *Nanophotonics*, vol. 7, no. 11, pp. 1725–1758, Oct. 2018. [Online]. Available: <http://www.degruyter.com/view/j/nanoph.2018.7.issue-11/nanoph-2018-0059/nanoph-2018-0059.xml>
- [136] M. Sidorova, A. Semenov, H.-W. Hübers, I. Charaev, A. Kuzmin, S. Doerner, and M. Siegel, “Physical mechanisms of timing jitter in photon detection by current-carrying superconducting nanowires,” *Physical Review B*, vol. 96, no. 184504, pp. 1–10, Nov. 2017. [Online]. Available: <https://link.aps.org/doi/10.1103/PhysRevB.96.184504>
- [137] B. A. Korzh, Q.-Y. Zhao, S. Frasca, J. P. Allmaras, T. M. Autry, E. A. Bersin, M. Colangelo, G. M. Crouch, A. E. Dane, T. Gerrits, F. Marsili, G. Moody, E. Ramirez, J. D. Rezac, M. J. Stevens, E. E. Wollman, D. Zhu, P. D. Hale, K. L. Silverman, R. P. Mirin, S. W. Nam, M. D. Shaw, and K. K. Berggren, “Demonstrating sub-3 ps temporal resolution in a superconducting nanowire single-photon detector,” *arXiv:1804.06839 [physics.ins-det]*, Apr. 2018. [Online]. Available: <https://arxiv.org/abs/1804.06839>
- [138] R. H. Hadfield, “Single-photon detectors for optical quantum information applications,” *Nature Photonics*, vol. 3, no. 12, pp. 696–705, Dec. 2009. [Online]. Available: <http://www.nature.com/articles/nphoton.2009.230>
- [139] M. D. Eisaman, J. Fan, A. Migdall, and S. V. Polyakov, “Invited Review Article: Single-photon sources and detectors,” *Review of Scientific Instruments*, vol. 82, no. 071101, pp. 1–25, Jul. 2011. [Online]. Available: <http://aip.scitation.org/doi/10.1063/1.3610677>
- [140] I. Holzman and Y. Ivry, “Superconducting Nanowires for Single Photon Detection: Progress, Challenges, and Opportunities,” *Advanced Quantum Technologies*, vol. 2, no. 1800058, pp. 1–28, Jan. 2019. [Online]. Available: <https://onlinelibrary.wiley.com/doi/abs/10.1002/qute.201800058>

- [141] L. Kubetsky, "Multiple Amplifier," *Proceedings of the IRE*, vol. 25, no. 4, pp. 421–433, Apr. 1937. [Online]. Available: <http://ieeexplore.ieee.org/document/1686374/>
- [142] W. E. Spicer and R. L. Bell, "The III-V photocathod: a major detector development," *Publications of the Astronomical Society of the Pacific*, vol. 84, no. 497, pp. 110–122, Feb. 1972. [Online]. Available: <http://www.jstor.org/stable/40675189>
- [143] K. Johnson, "High-speed photodiode signal enhancement at avalanche breakdown voltage," *IEEE Transactions on Electron Devices*, vol. 12, no. 2, pp. 55–63, Feb. 1965. [Online]. Available: <http://ieeexplore.ieee.org/document/1473917/>
- [144] B. Levine, C. Bethea, and J. Campbell, "Near room temperature 1.3 μm single-photon counting with a InGaAs avalanche photodiode," *Electronics Letters*, vol. 20, no. 14, pp. 596–598, Jul. 1984.
- [145] A. R. Dixon, Z. L. Yuan, J. F. Dynes, A. W. Sharpe, and A. J. Shields, "Gigahertz decoy quantum key distribution with 1 Mbit/s secure key rate," *Optics Express*, vol. 16, no. 23, pp. 18 790–18 797, Nov. 2008. [Online]. Available: <https://www.osapublishing.org/oe/abstract.cfm?uri=oe-16-23-18790>
- [146] S. Takeuchi, J. Kim, Y. Yamamoto, and H. H. Hogue, "Development of a high-quantum-efficiency single-photon counting system," *Applied Physics Letters*, vol. 74, no. 8, pp. 1063–1065, Feb. 1999. [Online]. Available: <http://aip.scitation.org/doi/10.1063/1.123482>
- [147] K. D. Irwin, "An application of electrothermal feedback for high resolution cryogenic particle detection," *Applied Physics Letters*, vol. 66, no. 15, pp. 1998–2000, Apr. 1995. [Online]. Available: <http://aip.scitation.org/doi/10.1063/1.113674>
- [148] A. E. Lita, A. J. Miller, and S. W. Nam, "Counting near-infrared single-photons with 95% efficiency," *Optics Express*, vol. 16, no. 5, pp. 3032–3040, Mar. 2008. [Online]. Available: <https://www.osapublishing.org/oe/abstract.cfm?uri=oe-16-5-3032>
- [149] D. Fukuda, R. Damayanthi, A. Yoshizawa, N. Zen, H. Takahashi, K. Amemiya, and M. Ohkubo, "Titanium Based Transition Edge Microcalorimeters for Optical Photon Measurements," *IEEE Transactions on Applied Superconductivity*, vol. 17, no. 2, pp. 259–262, Jun. 2007. [Online]. Available: <http://ieeexplore.ieee.org/document/4277398/>
- [150] D. Fukuda, G. Fujii, T. Numata, K. Amemiya, A. Yoshizawa, H. Tsuchida, H. Fujino, H. Ishii, T. Itatani, S. Inoue, and T. Zama, "Titanium-based transition-edge photon number resolving detector with 98% detection efficiency with index-matched small-gap fiber coupling," *Optics Express*, vol. 19, no. 2, pp. 870–875, Jan. 2011. [Online]. Available: <https://www.osapublishing.org/oe/abstract.cfm?uri=oe-19-2-870>
- [151] C. Zhang, W. Zhang, J. Huang, L. You, H. Li, C. Lv, T. Sugihara, M. Watanabe, H. Zhou, Z. Wang, and X. Xie, "NbN superconducting nanowire single-photon detector with an active area of 300 μm -in-diameter," *AIP Advances*, vol. 9, no. 075214, pp. 1–6, Jul. 2019. [Online]. Available: <http://aip.scitation.org/doi/10.1063/1.5095842>
- [152] S. N. Dorenbos, E. M. Reiger, U. Perinetti, V. Zwiller, T. Zijlstra, and T. M. Klapwijk, "Low noise superconducting single photon detectors on silicon," *Applied Physics Letters*, vol. 93, no. 131101, pp. 1–3, Sep. 2008. [Online]. Available: <http://aip.scitation.org/doi/10.1063/1.2990646>

- [153] I. Esmail Zadeh, J. W. N. Los, R. B. M. Gourgues, V. Steinmetz, G. Bulgarini, S. M. Dobrovolskiy, V. Zwiller, and S. N. Dorenbos, “Single-photon detectors combining high efficiency, high detection rates, and ultra-high timing resolution,” *APL Photonics*, vol. 2, no. 111301, pp. 1–7, Nov. 2017. [Online]. Available: <http://aip.scitation.org/doi/10.1063/1.5000001>
- [154] B. Baek, A. E. Lita, V. Verma, and S. W. Nam, “Superconducting a-WxSi1–x nanowire single-photon detector with saturated internal quantum efficiency from visible to 1850 nm,” *Applied Physics Letters*, vol. 98, no. 251105, pp. 1–3, Jun. 2011. [Online]. Available: <http://aip.scitation.org/doi/10.1063/1.3600793>
- [155] Y. P. Korneeva, M. Y. Mikhailov, Y. P. Pershin, N. N. Manova, A. V. Divochiy, Y. B. Vakhtomin, A. A. Korneev, K. V. Smirnov, A. G. Sivakov, A. Y. Devizenko, and G. N. Goltsman, “Superconducting single-photon detector made of MoSi film,” *Superconductor Science and Technology*, vol. 27, no. 095012, pp. 1–6, Aug. 2014. [Online]. Available: <http://stacks.iop.org/0953-2048/27/i=9/a=095012?key=crossref.d153e453b45ebc887196e2539a3ac044>
- [156] M. Caloz, M. Perrenoud, C. Autebert, B. Korzh, M. Weiss, C. Schönenberger, R. J. Warburton, H. Zbinden, and F. Bussi eres, “High-detection efficiency and low-timing jitter with amorphous superconducting nanowire single-photon detectors,” *Applied Physics Letters*, vol. 112, no. 061103, pp. 1–4, Feb. 2018. [Online]. Available: <http://aip.scitation.org/doi/10.1063/1.5010102>
- [157] T. Nguyen, M. Petach, M. Michaelian, J. Raab, and E. Tward, “Space Micro Pulse Tube Cooler,” in *International Cryocooler Conf.* Boulder, CO: S.D. Miller and R.G. Ross, Jr, 2011, pp. 97–101.
- [158] S. C. Group, “CNA-11 Indoor Air-Cooled Compressor Series.” [Online]. Available: <http://www.shicryogenics.com/products/compressors/cna-11-indoor-air-cooled-compressor-series/>
- [159] SCONTEL, “Superconducting Single Photon Detecting Systems (SSPD).” [Online]. Available: <http://www.scontel.ru/sspd/>
- [160] A. J. Annunziata, “Single-Photon Detection, Kinetic Inductance, and Non-Equilibrium Dynamics in Niobium and Niobium Nitride Superconducting Nanowires,” Ph.D. dissertation, Yale University, 2010.
- [161] K. S. Il’in, M. Lindgren, M. Currie, A. D. Semenov, G. N. Gol’tsman, R. Sobolewski, S. I. Cherednichenko, and E. M. Gershenzon, “Picosecond hot-electron energy relaxation in NbN superconducting photodetectors,” *Applied Physics Letters*, vol. 76, no. 19, pp. 2752–2754, May 2000. [Online]. Available: <http://aip.scitation.org/doi/10.1063/1.126480>
- [162] Y. Bugoslavsky, Y. Miyoshi, G. K. Perkins, A. V. Berenov, Z. Lockman, J. L. MacManus-Driscoll, L. F. Cohen, A. D. Caplin, H. Y. Zhai, M. P. Paranthaman, H. M. Christen, and M. Blamire, “Structure of the superconducting gap in MgB₂ from point-contact spectroscopy,” *Superconductor Science and Technology*, vol. 15, no. 4, pp. 526–532, Apr. 2002. [Online]. Available: <http://stacks.iop.org/0953-2048/15/i=4/a=308?key=crossref.c087e586a43f62440094fcc2704e6202>
- [163] M. Khafizov, “Photoresponse Mechanism of Superconducting MgB₂,” Ph.D. dissertation, University of Rochester, New-York, 2007.

- [164] Y. Dagan, R. Krupke, and G. Deutscher, “Determination of the superconducting gap in $\text{YBa}_2\text{Cu}_3\text{O}_{7-\delta}$ by tunneling experiments under magnetic fields,” *Physical Review B*, vol. 62, no. 1, pp. 146–149, Jul. 2000.
- [165] M. Lindgren, M. Currie, C. Williams, T. Y. Hsiang, P. M. Fauchet, R. Sobolewski, S. H. Moffat, R. A. Hughes, J. S. Preston, and F. A. Hegmann, “Intrinsic picosecond response times of Y–Ba–Cu–O superconducting photodetectors,” *Applied Physics Letters*, vol. 74, no. 6, pp. 853–855, Feb. 1999. [Online]. Available: <http://aip.scitation.org/doi/10.1063/1.123388>
- [166] J. Gavaler, “Superconductivity in Nb–Ge films above 22 K,” *Applied Physics Letters*, vol. 23, no. 8, pp. 480–482, Jul. 1973.
- [167] M. K. Wu, J. R. Ashburn, C. J. Torng, P. H. Hor, R. L. Meng, L. Gao, Z. J. Huang, Y. Q. Wang, and C. W. Chu, “Superconductivity at 93 K in a new mixed-phase Y–Ba–Cu–O compound system at ambient pressure,” *Physical Review Letters*, vol. 58, no. 9, pp. 908–910, Mar. 1987. [Online]. Available: <https://link.aps.org/doi/10.1103/PhysRevLett.58.908>
- [168] W. Meissner and R. Ochsenfeld, “Ein neuer Effekt bei Eintritt der Supraleitfähigkeit,” *Die Naturwissenschaften*, vol. 21, no. 44, pp. 787–788, Nov. 1933.
- [169] A. Mourachkine, *Room-temperature superconductivity*, ser. Literaturverz. S. 303 - 305. Cambridge: CISP, Cambridge Internat. Science Publ, 2004, oCLC: 249572629.
- [170] L. Gor’kov, “Microscopic derivation of the Ginzburg-Landau equations in the theory of superconductivity,” *Soviet Physics Journal of Experimental and Theoretical Physics*, vol. 36(9), no. 6, pp. 1364–1367, Dec. 1959.
- [171] E. Dagotto, “Correlated electrons in high-temperature superconductors,” *Reviews of Modern Physics*, vol. 66, no. 3, pp. 763–840, Jul. 1994. [Online]. Available: <https://link.aps.org/doi/10.1103/RevModPhys.66.763>
- [172] K. Krishana, J. M. Harris, and N. P. Ong, “Quasiparticle Mean Free Path in $\text{YBa}_2\text{Cu}_3\text{O}_7$ Measured by the Thermal Hall Conductivity,” *Physical Review Letters*, vol. 75, no. 19, pp. 3529–3532, Nov. 1995. [Online]. Available: <https://link.aps.org/doi/10.1103/PhysRevLett.75.3529>
- [173] W. H. Tang, C. Y. Ng, C. Y. Yau, and J. Gao, “Thickness dependence of superconductivity for $\text{YBa}_2\text{Cu}_3\text{O}_y$ ultra-thin films,” *Superconductor Science and Technology*, vol. 13, no. 5, pp. 580–583, May 2000. [Online]. Available: <http://stacks.iop.org/0953-2048/13/i=5/a=329?key=crossref.10a26c707f46841c9c3e52da2e9dd807>
- [174] F. S. Wells, A. V. Pan, X. R. Wang, S. A. Fedoseev, and H. Hilgenkamp, “Analysis of low-field isotropic vortex glass containing vortex groups in $\text{YBa}_2\text{Cu}_3\text{O}_{7-x}$ thin films visualized by scanning SQUID microscopy,” *Scientific Reports*, vol. 5, no. 8677, pp. 1–5, Mar. 2015. [Online]. Available: <http://www.nature.com/articles/srep08677>
- [175] J. Pearl, “Current distribution in superconducting films carrying quantized fluxoids,” *Applied Physics Letters*, vol. 5, no. 4, pp. 65–66, Aug. 1964. [Online]. Available: <http://aip.scitation.org/doi/10.1063/1.1754056>
- [176] J. Bednorz and K. Müller, “Possible High T_c Superconductivity in the Ba - La- Cu- O System,” *Z. Phys. B - Condensed Matter*, vol. 64, pp. 189–193, Apr. 1986.

- [177] K. Tomimoto, I. Terasaki, A. I. Rykov, T. Mimura, and S. Tajima, “Impurity effects on the superconducting coherence length in Zn- or Ni-doped YBa₂Cu₃O_{6.9} single crystals,” *Physical Review B*, vol. 60, no. 1, pp. 114–117, Jul. 1999. [Online]. Available: <https://link.aps.org/doi/10.1103/PhysRevB.60.114>
- [178] W. N. Hardy, D. A. Bonn, D. C. Morgan, R. Liang, and K. Zhang, “Precision measurements of the temperature dependence of λ in YBa₂Cu₃O_{6.95} : Strong evidence for nodes in the gap function,” *Physical Review Letters*, vol. 70, no. 25, pp. 3999–4002, Jun. 1993. [Online]. Available: <https://link.aps.org/doi/10.1103/PhysRevLett.70.3999>
- [179] H. Ding, M. R. Norman, J. C. Campuzano, M. Randeria, A. F. Bellman, T. Yokoya, T. Takahashi, T. Mochiku, and K. Kadowaki, “Angle-resolved photoemission spectroscopy study of the superconducting gap anisotropy in Bi₂Sr₂CaCu₂O_{8+x},” *Physical Review B*, vol. 54, no. 14, pp. R9678–R9681, Oct. 1996.
- [180] D. A. Wollman, D. J. Van Harlingen, W. C. Lee, D. M. Ginsberg, and A. J. Leggett, “Experimental determination of the superconducting pairing state in YBCO from the phase coherence of YBCO-Pb dc SQUIDs,” *Physical Review Letters*, vol. 71, no. 13, pp. 2134–2137, Sep. 1993. [Online]. Available: <https://link.aps.org/doi/10.1103/PhysRevLett.71.2134>
- [181] C. Tsuei, J. Kirtley, C. Chi, L. Yu-Jahnes, A. Gupta, and T. Shaw, “Pairing symmetry and flux quantization in a tricrystal superconducting ring of YBCO,” *Physical Review Letters*, vol. 73, no. 4, pp. 593–598, Aug. 1994.
- [182] P. Thoma, “Ultra-fast YBa₂Cu₃O_{7-x} direct detectors for the THz frequency range,” Ph.D. dissertation, KIT, 2013.
- [183] A. I. Larkin and Y. N. Ovchinnikov, “Nonlinear effects during the motion of vortices in superconductors,” *Soviet Physics Journal of Experimental and Theoretical Physics*, vol. 46, no. 1, pp. 155–162, Jul. 1977.
- [184] V. N. Gubankov, V. P. Koshelets, and G. A. Ovsyannikov, “Coherent effects in superconducting bridges of variable thickness,” *Soviet Physics Journal of Experimental and Theoretical Physics*, vol. 44, pp. 181–186, Jul. 1976.
- [185] C. C. Grimes and S. Shapiro, “Millimeter-Wave Mixing with Josephson Junctions,” *Physical Review*, vol. 169, no. 2, pp. 397–406, May 1968. [Online]. Available: <https://link.aps.org/doi/10.1103/PhysRev.169.397>
- [186] D. E. McCumber, “Effect of ac Impedance on dc Voltage-Current Characteristics of Superconductor Weak-Link Junctions,” *Journal of Applied Physics*, vol. 39, no. 7, pp. 3113–3118, Feb. 1968. [Online]. Available: <http://aip.scitation.org/doi/10.1063/1.1656743>
- [187] W. C. Stewart, “Current-Voltage characteristics of Josephson junctions,” *Applied Physics Letters*, vol. 12, no. 8, pp. 277–280, Jan. 1968.
- [188] G.-H. Lee, D. Jeong, J.-H. Choi, Y.-J. Doh, and H.-J. Lee, “Electrically Tunable Macroscopic Quantum Tunneling in a Graphene-Based Josephson Junction,” *Physical Review Letters*, vol. 107, no. 146605, pp. 1–4, Sep. 2011. [Online]. Available: <https://link.aps.org/doi/10.1103/PhysRevLett.107.146605>

- [189] S. L. Chu, A. T. Bollinger, and A. Bezryadin, “Phase slips in superconducting films with constrictions,” *Physical Review B*, vol. 70, no. 214506, pp. 1–6, Dec. 2004. [Online]. Available: <https://link.aps.org/doi/10.1103/PhysRevB.70.214506>
- [190] A. Bezryadin, “Quantum suppression of superconductivity in nanowires,” *Journal of Physics: Condensed Matter*, vol. 20, no. 043202, pp. 1–19, Jan. 2008. [Online]. Available: <http://stacks.iop.org/0953-8984/20/i=4/a=043202?key=crossref.b186278d662e01db8f0f3c85c19eafc7>
- [191] J. S. Langer and V. Ambegaokar, “Intrinsic resistive transition in narrow superconducting channels,” *Physical Review*, vol. 164, no. 2, pp. 498–510, Dec. 1967.
- [192] D. E. McCumber, “Intrinsic Resistive Transition in Thin Superconducting Wires Driven from Current Sources,” *Physical Review*, vol. 172, no. 2, pp. 427–429, Aug. 1968. [Online]. Available: <https://link.aps.org/doi/10.1103/PhysRev.172.427>
- [193] D. E. McCumber and B. I. Halperin, “Time scale of intrinsic resistive fluctuations in thin superconducting wires,” *Physical Review B*, vol. 1, no. 3, pp. 1054–1070, Feb. 1970.
- [194] C. N. Lau, N. Markovic, M. Bockrath, A. Bezryadin, and M. Tinkham, “Quantum Phase Slips in Superconducting Nanowires,” *Physical Review Letters*, vol. 87, no. 217003, pp. 1–4, Nov. 2001. [Online]. Available: <https://link.aps.org/doi/10.1103/PhysRevLett.87.217003>
- [195] A. Rogachev, A. T. Bollinger, and A. Bezryadin, “Influence of High Magnetic Fields on the Superconducting Transition of One-Dimensional Nb and MoGe Nanowires,” *Physical Review Letters*, vol. 94, no. 017004, pp. 1–4, Jan. 2005. [Online]. Available: <https://link.aps.org/doi/10.1103/PhysRevLett.94.017004>
- [196] M. Tinkham, “The electromagnetic properties of superconductors,” *Reviews of Modern Physics*, vol. 46, no. 4, pp. 587–596, Oct. 1974. [Online]. Available: <https://link.aps.org/doi/10.1103/RevModPhys.46.587>
- [197] J. Meyer, “Dissertation,” Ph.D. dissertation, University of Cologne, 1973.
- [198] K. K. Likharev and L. Iakobson, “Steady-state properties of superconducting bridges,” *Soviet Physics - Technical Physics*, vol. 20, no. 7, pp. 950–954, Jun. 1976.
- [199] A. G. Sivakov, A. M. Glukhov, A. N. Omelyanchouk, Y. Koval, P. Müller, and A. V. Ustinov, “Josephson Behavior of Phase-Slip Lines in Wide Superconducting Strips,” *Physical Review Letters*, vol. 91, no. 267001, pp. 1–4, Dec. 2003. [Online]. Available: <https://link.aps.org/doi/10.1103/PhysRevLett.91.267001>
- [200] G. Grimaldi, A. Leo, A. Nigro, S. Pace, C. Cirillo, and C. Attanasio, “Thickness dependence of vortex critical velocity in wide Nb films,” *Physica C: Superconductivity and its Applications*, vol. 468, no. 7-10, pp. 765–768, Apr. 2008. [Online]. Available: <https://linkinghub.elsevier.com/retrieve/pii/S0921453408001032>
- [201] A. A. Golubov, M. Y. Kupriyanov, and E. Il’ichev, “The current-phase relation in Josephson junctions,” *Reviews of Modern Physics*, vol. 76, no. 2, pp. 411–469, Apr. 2004. [Online]. Available: <https://link.aps.org/doi/10.1103/RevModPhys.76.411>
- [202] B. I. Ivlev, N. B. Kopnin, and I. A. Larkin, “Current-carrying states in superconducting channels with nonhomogeneities,” *Journal of Low Temperature Physics*, vol. 53, no. 1-2, pp. 153–176, Oct. 1983. [Online]. Available: <http://link.springer.com/10.1007/BF00685778>

- [203] R. C. Dinsmore, "Microwave response in superconducting nanowires," Ph.D. dissertation, Urbana-Champaign, 2009.
- [204] M. Nisenoff and S. Wolf, "Observation of a $\cos \varphi$ term in the current-phase relation for "Dayem"-type weak link contained in an rf-biased superconducting quantum interference device," *Physical Review B*, vol. 12, no. 5, pp. 1712–1714, Sep. 1975. [Online]. Available: <https://link.aps.org/doi/10.1103/PhysRevB.12.1712>
- [205] M. L. Della Rocca, M. Chauvin, B. Huard, H. Pothier, D. Esteve, and C. Urbina, "Measurement of the Current-Phase Relation of Superconducting Atomic Contacts," *Physical Review Letters*, vol. 99, no. 127005, pp. 1–4, Sep. 2007. [Online]. Available: <https://link.aps.org/doi/10.1103/PhysRevLett.99.127005>
- [206] A. M. Kadin, *Introduction to Superconducting Circuits*, 1999.
- [207] J. Ye and S. T. Cundiff, Eds., *Femtosecond Optical Frequency Comb: Principle, Operation, and Applications*. Boston: Kluwer Academic Publishers, 2005. [Online]. Available: <http://link.springer.com/10.1007/b102450>
- [208] A. D. Semenov, G. Gol'tsman, and R. Sobolewski, "Hot-electron effect in superconductors and its applications for radiation sensors," *Superconductor Science and Technology*, vol. 15, no. 4, pp. R1–R16, Mar. 2002.
- [209] M. Johnson, "Nonbolometric photoresponse of $\text{YBa}_2\text{Cu}_3\text{O}_{7-\delta}$ films," *Applied Physics Letters*, vol. 59, no. 11, pp. 1371–1373, Sep. 1991. [Online]. Available: <http://aip.scitation.org/doi/10.1063/1.105312>
- [210] A. Semenov, I. Goghidze, G. Gol'tsman, A. Sergeev, E. Aksaev, and E. Gershenzon, "Non-equilibrium quasiparticle response to radiation and bolometric effect in YBaCuO films," *IEEE Transactions on Applied Superconductivity*, vol. 3, no. 1, pp. 2132–2135, Mar. 1993. [Online]. Available: <http://ieeexplore.ieee.org/document/233923/>
- [211] A. Engel, J. J. Renema, K. Il'in, and A. Semenov, "Detection mechanism of superconducting nanowire single-photon detectors," *Superconductor Science and Technology*, vol. 28, no. 114003, pp. 1–22, Nov. 2015. [Online]. Available: <http://stacks.iop.org/0953-2048/28/i=11/a=114003?key=crossref.36d27875d9357de5eba8117decc5f54d>
- [212] R. Lusche, A. Semenov, K. Ilin, M. Siegel, Y. Korneeva, A. Trifonov, A. Korneev, G. Goltsman, D. Vodolazov, and H.-W. Hübers, "Effect of the wire width on the intrinsic detection efficiency of superconducting-nanowire single-photon detectors," *Journal of Applied Physics*, vol. 116, no. 043906, pp. 1–9, Jul. 2014. [Online]. Available: <http://aip.scitation.org/doi/10.1063/1.4891105>
- [213] A. Korneev, V. Matvienko, O. Minaeva, I. Milostnaya, I. Rubtsova, G. Chulkova, K. Smirnov, V. Voronov, G. Gol'tsman, W. Slysz, A. Pearlman, A. Verevkin, and R. Sobolewski, "Quantum Efficiency and Noise Equivalent Power of Nanostructured, NbN , Single-Photon Detectors in the Wavelength Range From Visible to Infrared," *IEEE Transactions on Applied Superconductivity*, vol. 15, no. 2, pp. 571–574, Jun. 2005. [Online]. Available: <http://ieeexplore.ieee.org/document/1439702/>
- [214] J. Renema, R. Gaudio, Q. Wang, Z. Zhou, A. Gaggero, F. Mattioli, R. Leoni, D. Sahin, M. de Dood, A. Fiore, and M. van Exter, "Experimental Test of Theories of the Detection Mechanism in a Nanowire Superconducting Single Photon

- Detector,” *Physical Review Letters*, vol. 112, no. 117604, pp. 1–5, Mar. 2014. [Online]. Available: <https://link.aps.org/doi/10.1103/PhysRevLett.112.117604>
- [215] J. J. Renema, G. Frucci, Z. Zhou, F. Mattioli, A. Gaggero, R. Leoni, M. J. A. de Dood, A. Fiore, and M. P. van Exter, “Universal response curve for nanowire superconducting single-photon detectors,” *Physical Review B*, vol. 87, no. 174526, pp. 1–7, May 2013. [Online]. Available: <https://link.aps.org/doi/10.1103/PhysRevB.87.174526>
- [216] R. Lusche, A. Semenov, Y. Korneeva, A. Trifonov, A. Korneev, G. Gol’tsman, and H.-W. Hübers, “Effect of magnetic field on the photon detection in thin superconducting meander structures,” *Physical Review B*, vol. 89, no. 104513, pp. 1–7, Mar. 2014. [Online]. Available: <https://link.aps.org/doi/10.1103/PhysRevB.89.104513>
- [217] A. M. Kadin and M. W. Johnson, “Nonequilibrium photon-induced hotspot: A new mechanism for photodetection in ultrathin metallic films,” *Applied Physics Letters*, vol. 69, no. 25, pp. 3938–3940, Dec. 1996. [Online]. Available: <http://aip.scitation.org/doi/10.1063/1.117576>
- [218] A. Semenov, A. Engel, K. Il’in, G. Gol’tsman, M. Siegel, and H.-W. Hübers, “Ultimate performance of a superconducting quantum detector,” *The European Physical Journal Applied Physics*, vol. 21, no. 3, pp. 171–178, Mar. 2003. [Online]. Available: <http://www.epjap.org/10.1051/epjap:2003009>
- [219] A. N. Zotova and D. Y. Vodolazov, “Photon detection by current-carrying superconducting film: A time-dependent Ginzburg-Landau approach,” *Physical Review B*, vol. 85, no. 024509, pp. 1–9, Jan. 2012. [Online]. Available: <https://link.aps.org/doi/10.1103/PhysRevB.85.024509>
- [220] D. Y. Vodolazov, Y. P. Korneeva, A. V. Semenov, A. A. Korneev, and G. N. Goltsman, “Vortex-assisted mechanism of photon counting in a superconducting nanowire single-photon detector revealed by external magnetic field,” *Physical Review B*, vol. 92, no. 104503, pp. 1–9, Sep. 2015. [Online]. Available: <https://link.aps.org/doi/10.1103/PhysRevB.92.104503>
- [221] D. Vodolazov, “Single-Photon Detection by a Dirty Current-Carrying Superconducting Strip Based on the Kinetic-Equation Approach,” *Physical Review Applied*, vol. 7, no. 034014, pp. 1–19, Mar. 2017. [Online]. Available: <https://link.aps.org/doi/10.1103/PhysRevApplied.7.034014>
- [222] H. Shibata, N. Kirigane, K. Fukao, D. Sakai, S. Karimoto, and H. Yamamoto, “Photoresponse of a $\text{La}_{1.85}\text{Sr}_{0.15}\text{CuO}_4$ nanostrip,” *Superconductor Science and Technology*, vol. 30, no. 074001, pp. 1–4, May 2017. [Online]. Available: <http://stacks.iop.org/0953-2048/30/i=7/a=074001?key=crossref.2367c718eabb271b1e14c1dc1225670c>
- [223] S. Charpentier, R. Arpaia, J. Gaudet, D. Matte, R. Baghdadi, T. Löfwander, D. Golubev, P. Fournier, T. Bauch, and F. Lombardi, “Hot spot formation in electron-doped PCCO nanobridges,” *Physical Review B*, vol. 94, no. 060503(R), pp. 1–5, Aug. 2016. [Online]. Available: <https://link.aps.org/doi/10.1103/PhysRevB.94.060503>
- [224] R. Arpaia, M. Arzeo, S. Nawaz, S. Charpentier, F. Lombardi, and T. Bauch, “Ultra low noise $\text{YBa}_2\text{Cu}_3\text{O}_{7-\delta}$ nano superconducting quantum interference devices

implementing nanowires,” *Applied Physics Letters*, vol. 104, no. 072603, pp. 1–4, Feb. 2014. [Online]. Available: <http://aip.scitation.org/doi/10.1063/1.4866277>

- [225] P. Amari, C. Feuillet-Palma, A. Jouan, F. Couëdo, N. Bourlet, E. Géron, M. Malnou, L. Méchin, A. Sharafiev, J. Lesueur, and N. Bergeal, “High-temperature superconducting nano-meanders made by ion irradiation,” *Superconductor Science and Technology*, vol. 31, no. 015019, pp. 1–6, Dec. 2018. [Online]. Available: <http://stacks.iop.org/0953-2048/31/i=1/a=015019?key=crossref.db8edf2d87395684e1f6c68f4a59dc0d>
- [226] M. Lyatti, M. A. Wolff, A. Savenko, M. Kruth, S. Ferrari, U. Poppe, W. Pernice, R. E. Dunin-Borkowski, and C. Schuck, “Experimental evidence for hotspot and phase-slip mechanisms of voltage switching in ultrathin $\text{YBa}_2\text{Cu}_3\text{O}_{7-x}$ nanowires,” *Physical Review B*, vol. 98, no. 054505, pp. 1–8, Aug. 2018. [Online]. Available: <https://link.aps.org/doi/10.1103/PhysRevB.98.054505>
- [227] R. Arpaia, M. Arzeo, R. Baghdadi, E. Trabaldo, F. Lombardi, and T. Bauch, “Improved noise performance of ultrathin YBCO Dayem bridge nanoSQUIDs,” *Superconductor Science and Technology*, vol. 30, no. 014008, pp. 1–6, Nov. 2017. [Online]. Available: <http://stacks.iop.org/0953-2048/30/i=1/a=014008?key=crossref.5f254e6f2edb6b288da3cd0c42773b7c>
- [228] N. Curtz, E. Koller, H. Zbinden, M. Decroux, L. Antognazza, . Fischer, and N. Gisin, “Patterning of ultrathin YBCO nanowires using a new focused-ion-beam process,” *Superconductor Science and Technology*, vol. 23, no. 4, pp. 1–6, Apr. 2010. [Online]. Available: <http://stacks.iop.org/0953-2048/23/i=4/a=045015?key=crossref.055232f83eeac52bfb30ed03a1583c8d>
- [229] M. Lyatti, A. Savenko, and U. Poppe, “Ultra-thin $\text{YBa}_2\text{Cu}_3\text{O}_{7-x}$ films with high critical current density,” *Superconductor Science and Technology*, vol. 29, no. 6, pp. 1–6, Jun. 2016. [Online]. Available: <http://stacks.iop.org/0953-2048/29/i=6/a=065017?key=crossref.dd63e5ee804d9ffa287ccb48c7e76196>
- [230] E. Y. Cho, “Focused Helium Beam Irradiated Josephson Junctions,” Ph.D. dissertation, UC San Diego, 2016.
- [231] E. Y. Cho, Y. W. Zhou, J. Y. Cho, and S. A. Cybart, “Superconducting nano Josephson junctions patterned with a focused helium ion beam,” *Applied Physics Letters*, vol. 113, no. 022604, pp. 1–4, Jul. 2018. [Online]. Available: <http://aip.scitation.org/doi/10.1063/1.5042105>
- [232] M. Malnou, “High-Tc Josephson mixers for Terahertz detection,” Ph.D. dissertation, UPMC, 2015.
- [233] R. P. Gupta and M. Gupta, “Order-disorder-driven change in hole concentration and superconductivity in $\text{YBa}_2\text{Cu}_3\text{O}_{6.5}$,” *Physical Review B*, vol. 44, no. 6, pp. 2739–2746, Aug. 1991.
- [234] A. A. Abrikosov and L. P. Gor’Kov, “On the problem of the Knight shift in superconductors,” *Soviet Physics Journal of Experimental and Theoretical Physics*, vol. 12, no. 2, pp. 337–339, Aug. 1960.
- [235] R. C. Jaeger, *Introduction to Microelectronic Fabrication*, 2nd ed., ser. Modular Series on Solid State Devices, 2001.

- [236] S. Sijbrandij, J. Notte, C. Sanford, and R. Hill, "Analysis of subsurface beam spread and its impact on the image resolution of the helium ion microscope," *Journal of Vacuum Science & Technology B, Nanotechnology and Microelectronics: Materials, Processing, Measurement, and Phenomena*, vol. 28, no. 6, pp. C6F6–C6F9, Nov. 2010. [Online]. Available: <http://avs.scitation.org/doi/10.1116/1.3497012>
- [237] D. Winston, B. M. Cord, B. Ming, D. C. Bell, W. F. DiNatale, L. A. Stern, A. E. Vladar, M. T. Postek, M. K. Mondol, J. K. W. Yang, and K. K. Berggren, "Scanning-helium-ion-beam lithography with hydrogen silsesquioxane resist," *Journal of Vacuum Science & Technology B: Microelectronics and Nanometer Structures*, vol. 27, no. 6, pp. 2702–2706, Dec. 2009. [Online]. Available: <http://scitation.aip.org/content/avs/journal/jvstb/27/6/10.1116/1.3250204>
- [238] J. F. Ziegler, "SRIM-2013, The stopping and range of ions in matter." [Online]. Available: <http://www.srim.org/SRIM/SRIM2011.htm>
- [239] S. A. Cybart, E. Y. Cho, T. J. Wong, B. H. Wehlin, M. K. Ma, C. Huynh, and R. C. Dynes, "Nano Josephson superconducting tunnel junctions in YBa₂Cu₃O_{7-δ} directly patterned with a focused helium ion beam," *Nature Nanotechnology*, vol. 10, no. 7, pp. 598–602, Jul. 2015. [Online]. Available: <http://www.nature.com/articles/nnano.2015.76>
- [240] "A method of measuring resistivity and hall coefficient on lamellae of arbitrary shape," *Philips Technical Review*, vol. 26, no. 8, pp. 220–224, 1958.
- [241] E. Y. Cho, H. Li, and S. A. Cybart, "Direct-Write Ion Beam Irradiated Josephson Junctions," *arXiv:1906.10328 [cond-mat.supr-con]*, Jun. 2019. [Online]. Available: <http://arxiv.org/abs/1906.10328>
- [242] R. P. Huebener, "Self-heating effects in thin-film type-I superconductors," *Journal of Applied Physics*, vol. 46, no. 11, pp. 4982–4985, 1975.
- [243] J. P. Maneval, K. Harrabi, F. Chibane, M. Rosticher, F. R. Ladan, and P. Mathieu, "Temperature Profile of Hotspots in Narrow Current-Biased Superconducting Strips," *IEEE Transactions on Applied Superconductivity*, vol. 23, no. 3, pp. 2 200 604–2 200 604, Jun. 2013. [Online]. Available: <http://ieeexplore.ieee.org/document/6389750/>
- [244] D. K. Liu, L. X. You, S. J. Chen, X. Y. Yang, Z. Wang, Y. L. Wang, X. M. Xie, and M. H. Jiang, "Electrical Characteristics of Superconducting Nanowire Single Photon Detector," *IEEE Transactions on Applied Superconductivity*, vol. 23, no. 3, pp. 2 200 804–2 200 804, Jun. 2013. [Online]. Available: <http://ieeexplore.ieee.org/document/6407837/>
- [245] D. Golubev, F. Lombardi, and T. Bauch, "Effect of heating on critical current of YBCO nanowires," *Physica C: Superconductivity and its Applications*, vol. 506, pp. 174–177, Nov. 2014. [Online]. Available: <https://linkinghub.elsevier.com/retrieve/pii/S0921453414001920>
- [246] A. Sergeev, A. Semenov, V. Trifonov, B. Karasik, G. Gol'tsman, and E. Gershenzon, "Heat transfer in YBaCuO thin film/sapphire substrate system," *Journal of Superconductivity*, vol. 7, no. 2, pp. 341–344, Apr. 1994. [Online]. Available: <http://link.springer.com/10.1007/BF00724565>

- [247] M. Nahum, S. Verghese, P. L. Richards, and K. Char, “Thermal boundary resistance for $\text{YBa}_2\text{Cu}_3\text{O}_{7-\delta}$ films,” *Applied Physics Letters*, vol. 59, no. 16, pp. 2034–2036, Oct. 1991. [Online]. Available: <http://aip.scitation.org/doi/10.1063/1.106123>
- [248] W. Little, “The transport of heat between dissimilar solids at low temperatures,” *Canadian Journal of Physics*, vol. 37, no. 3, pp. 334–349, Mar. 1959.
- [249] T. Klitsner and R. O. Pohl, “Phonon scattering at silicon crystal surfaces,” *Physical Review B*, vol. 36, no. 12, pp. 6551–6565, Oct. 1987. [Online]. Available: <https://link.aps.org/doi/10.1103/PhysRevB.36.6551>
- [250] S. Cohn, S. A. Wolf, T. Vanderah, V. Selvamanickam, and K. Salama, “Lattice thermal conductivity of $\text{YBa}_2\text{Cu}_3\text{O}_{7-x}$,” *Physica C*, vol. 192, no. 3-4, pp. 435–442, Mar. 1992.
- [251] R. C. Yu, M. B. Salamon, J. P. Lu, and W. C. Lee, “Thermal conductivity of an untwinned $\text{YBa}_2\text{Cu}_3\text{O}_{7-\delta}$ single crystal and a new interpretation of the superconducting state thermal transport,” *Physical Review Letters*, vol. 69, no. 9, pp. 1431–1434, Aug. 1992. [Online]. Available: <https://link.aps.org/doi/10.1103/PhysRevLett.69.1431>
- [252] M. Matsukawa, T. Mizukoshi, K. Noto, and Y. Shiohara, “In-plane and out-of-plane thermal conductivity of a large single crystal of $\text{YBa}_2\text{Cu}_3\text{O}_{7-x}$,” *Physical Review B*, vol. 53, no. 10, pp. R6034–R6037, Mar. 1996. [Online]. Available: <https://link.aps.org/doi/10.1103/PhysRevB.53.R6034>
- [253] J. Bardeen, “Critical fields and currents in superconductors,” *Reviews of Modern Physics*, vol. 34, no. 4, pp. 667–681, Oct. 1962.
- [254] M. N. Kunchur, “Evaluating Superconductors through Current Induced Depairing,” *Condensed Matter*, vol. 4, no. 54, Jun. 2019. [Online]. Available: <https://www.mdpi.com/2410-3896/4/2/54>
- [255] J. R. Clem and V. G. Kogan, “Kinetic impedance and depairing in thin and narrow superconducting films,” *Physical Review B*, vol. 86, no. 174521, pp. 1–16, Nov. 2012. [Online]. Available: <https://link.aps.org/doi/10.1103/PhysRevB.86.174521>
- [256] A. J. Annunziata, O. Quaranta, D. F. Santavicca, A. Casaburi, L. Frunzio, M. Ejrnaes, M. J. Rooks, R. Cristiano, S. Pagano, A. Frydman, and D. E. Prober, “Reset dynamics and latching in niobium superconducting nanowire single-photon detectors,” *Journal of Applied Physics*, vol. 108, no. 084507, pp. 1–7, Oct. 2010. [Online]. Available: <http://aip.scitation.org/doi/10.1063/1.3498809>
- [257] E. F. Talantsev, W. P. Crump, and J. L. Tallon, “Universal scaling of the self-field critical current in superconductors: from sub-nanometre to millimetre size,” *Scientific Reports*, vol. 7, no. 10010, pp. 1–15, Aug. 2017. [Online]. Available: <http://www.nature.com/articles/s41598-017-10226-z>
- [258] H. F. Hess, R. B. Robinson, R. C. Dynes, J. M. Valles, and J. V. Waszczak, “Scanning-Tunneling-Microscope Observation of the Abrikosov Flux Lattice and the Density of States near and inside a Fluxoid,” *Physical Review Letters*, vol. 62, no. 2, pp. 214–216, Jan. 1989. [Online]. Available: <https://link.aps.org/doi/10.1103/PhysRevLett.62.214>

- [259] K. Harada, O. Kamimura, H. Kasai, T. Matsuda, A. Tonomura, and V. V. Moshchalkov, “Direct observation of vortex dynamics in superconducting films with regular arrays of defects,” *Science*, vol. 274, no. 5290, pp. 1167–1170, Nov. 1996. [Online]. Available: <https://science.sciencemag.org/content/274/5290/1167/tab-pdf>
- [260] L. F. Cohen and H. J. Jensen, “Open questions in the magnetic behaviour of high-temperature superconductors,” *Reports on Progress in Physics*, vol. 60, no. 12, pp. 1581–1672, Dec. 1997. [Online]. Available: <http://stacks.iop.org/0034-4885/60/i=12/a=003?key=crossref.baa59bd17574a1da0485c372a00df984>
- [261] G. Blatter, M. V. Feigel'man, V. B. Geshkenbein, A. I. Larkin, and V. M. Vinokur, “Vortices in high-temperature superconductors,” *Reviews of Modern Physics*, vol. 66, no. 4, pp. 1125–1388, Oct. 1994. [Online]. Available: <https://link.aps.org/doi/10.1103/RevModPhys.66.1125>
- [262] M. J. M. E. de Nivelles, G. J. Gerritsma, and H. Rogalla, “Thermally activated coherent vortex motion in YBa₂Cu₃O_{7- δ} thin film microbridges,” *Physical Review Letters*, vol. 70, no. 10, pp. 1525–1528, Mar. 1993. [Online]. Available: <https://link.aps.org/doi/10.1103/PhysRevLett.70.1525>
- [263] H. Akaike, E. Parzen, K. Tanabe, and G. Kitagawa, *Selected papers of Hirotugu Akaike*. New York: Springer, 1998, oCLC: 37573269.
- [264] P. Russer, “Influence of Microwave Radiation on Current-Voltage Characteristic of Superconducting Weak Links,” *Journal of Applied Physics*, vol. 43, no. 3, p. 4, Apr. 1972.
- [265] S. P. Benz, M. S. Rzchowski, M. Tinkham, and C. J. Lobb, “Fractional giant Shapiro steps and spatially correlated phase motion in 2D Josephson arrays,” *Physical Review Letters*, vol. 64, no. 6, pp. 693–696, Feb. 1990. [Online]. Available: <https://link.aps.org/doi/10.1103/PhysRevLett.64.693>
- [266] D. Domínguez and J. V. José, “Giant Shapiro steps with screening currents,” *Physical Review Letters*, vol. 69, no. 3, pp. 514–517, Jul. 1992. [Online]. Available: <https://link.aps.org/doi/10.1103/PhysRevLett.69.514>
- [267] R. C. Dinsmore, M.-H. Bae, and A. Bezryadin, “Fractional order Shapiro steps in superconducting nanowires,” *Applied Physics Letters*, vol. 93, no. 192505, pp. 1–3, Nov. 2008. [Online]. Available: <http://aip.scitation.org/doi/10.1063/1.3012360>
- [268] A. T. Fiory, “Quantum Interference Effects of a Moving Vortex Lattice in Al Films,” *Physical Review Letters*, vol. 27, no. 8, pp. 501–503, Aug. 1971. [Online]. Available: <https://link.aps.org/doi/10.1103/PhysRevLett.27.501>
- [269] V. G. Kogan, “Pearl’s vortex near the film edge,” *Physical Review B*, vol. 49, no. 22, pp. 15 874–15 878, Jun. 1994. [Online]. Available: <https://link.aps.org/doi/10.1103/PhysRevB.49.15874>
- [270] J. E. Mooij, *Percolation, localization, and superconductivity.*, plenum press ed., ser. NATO ASI Series. Les Arcs: Springer-Verlag New York, Jul. 1983, vol. 109, oCLC: 922649889.

- [271] V. Berezinsky, “Destruction of Long-range Order in One-dimensional and Two-dimensional Systems Possessing a Continuous Symmetry Group. II. Quantum Systems,” *Soviet Physics Journal of Experimental and Theoretical Physics*, vol. 34, no. 3, pp. 610–616, Mar. 1972.
- [272] J. Kosterlitz and D. Thouless, “Ordering, metastability and phase transitions in two-dimensional systems,” *Journal of Physics C: Solid State Physics*, vol. 6, no. 7, pp. 1181–1203, Apr. 1973.
- [273] L. C. Davis, M. R. Beasley, and D. J. Scalapino, “Kosterlitz-Thouless transition in high- T_c superconductor films,” *Physical Review B*, vol. 42, no. 1, pp. 99–104, Jul. 1990. [Online]. Available: <https://link.aps.org/doi/10.1103/PhysRevB.42.99>
- [274] S. Artemenko and Y. Latyshev, “Two-dimensional behaviour of layered high T_c superconductors,” *Modern Physics Letter B*, vol. 6, no. 7, pp. 367–382, Mar. 1992. [Online]. Available: <https://www.worldscientific.com/doi/abs/10.1142/S0217984992000454>
- [275] V. Gasparov, G. Tsydynzhapov, I. Batov, and Q. Li, “Temperature and Frequency Dependence of Complex Conductance of Ultrathin $\text{YBa}_2\text{Cu}_3\text{O}_{7-x}$ Films: Observation of Vortex–Antivortex Pair Unbinding,” *Journal of Low Temperature Physics*, vol. 139, no. 1, pp. 49–63, Apr. 2005. [Online]. Available: <http://link.springer.com/10.1007/s10909-005-3911-6>
- [276] V. I. Nizhankovskiy and K. Rogacki, “BKT transition observed in magnetic and electric properties of $\text{YBa}_2\text{Cu}_3\text{O}_{7-\delta}$ single crystals,” *Physical Review B*, vol. 100, no. 104510, pp. 1–8, Sep. 2019. [Online]. Available: <https://link.aps.org/doi/10.1103/PhysRevB.100.104510>
- [277] I. Milostnaya, A. Korneev, I. Rubtsova, V. Seleznev, O. Minaeva, G. Chulkova, O. Okunev, B. Voronov, K. Smirnov, G. Gol’tsman, W. Slysz, M. Wegrzecki, M. Guziejewicz, J. Bar, M. Gorska, A. Pearlman, J. Kitaygorsky, A. Cross, and R. Sobolewski, “Superconducting single-photon detectors designed for operation at 1.55- μm telecommunication wavelength,” *Journal of Physics: Conference Series*, vol. 43, no. 1, pp. 1334–1337, Jun. 2006. [Online]. Available: <http://stacks.iop.org/1742-6596/43/i=1/a=326?key=crossref.760b6d68a935f3a4ee88b69c9a3e677f>
- [278] Y. Korneeva, D. Vodolazov, A. Semenov, I. Florya, N. Simonov, E. Baeva, A. Korneev, G. Goltsman, and T. Klapwijk, “Optical Single-Photon Detection in Micrometer-Scale NbN Bridges,” *Physical Review Applied*, vol. 9, no. 064037, pp. 1–13, Jun. 2018. [Online]. Available: <https://link.aps.org/doi/10.1103/PhysRevApplied.9.064037>
- [279] D. Pekker, N. Shah, M. Sahu, A. Bezryadin, and P. M. Goldbart, “Stochastic dynamics of phase-slip trains and superconductive-resistive switching in current-biased nanowires,” *Physical Review B*, vol. 80, no. 214525, pp. 1–17, Dec. 2009. [Online]. Available: <https://link.aps.org/doi/10.1103/PhysRevB.80.214525>
- [280] T. Aref, A. Levchenko, V. Vakaryuk, and A. Bezryadin, “Quantitative analysis of quantum phase slips in superconducting $\text{Mo}_76\text{Ge}_{24}$ nanowires revealed by switching-current statistics,” *Physical Review B*, vol. 86, no. 024507, pp. 1–7, Jul. 2012. [Online]. Available: <https://link.aps.org/doi/10.1103/PhysRevB.86.024507>
- [281] A. J. Leggett, “Macroscopic Quantum Systems and the Quantum Theory of Measurement,” *Progress of Theoretical Physics Supplement*, vol. 69, pp. 80–100,

Mar. 1980. [Online]. Available: <https://academic.oup.com/ptps/article/doi/10.1143/PTP.69.80/1896307>

- [282] R. F. Voss and R. A. Webb, “Macroscopic Quantum Tunneling in 1- μm Nb Josephson Junctions,” *Physical Review Letters*, vol. 47, no. 4, pp. 265–268, Jul. 1981. [Online]. Available: <https://link.aps.org/doi/10.1103/PhysRevLett.47.265>
- [283] M. H. Devoret, J. M. Martinis, and J. Clarke, “Measurements of Macroscopic Quantum Tunneling out of the Zero-Voltage State of a Current-Biased Josephson Junction,” *Physical Review Letters*, vol. 55, no. 18, pp. 1908–1911, Oct. 1985. [Online]. Available: <https://link.aps.org/doi/10.1103/PhysRevLett.55.1908>
- [284] A. N. Cleland, J. M. Martinis, and J. Clarke, “Measurement of the effect of moderate dissipation on macroscopic quantum tunneling,” *Physical Review B*, vol. 37, no. 10, pp. 5950–5953, Apr. 1988. [Online]. Available: <https://link.aps.org/doi/10.1103/PhysRevB.37.5950>
- [285] A. Wallraff, A. Lukashenko, J. Lisenfeld, A. Kemp, M. V. Fistul, Y. Koval, and A. V. Ustinov, “Quantum dynamics of a single vortex,” *Nature*, vol. 425, no. 6954, pp. 155–158, Sep. 2003. [Online]. Available: <http://www.nature.com/articles/nature01826>
- [286] K. Inomata, S. Sato, K. Nakajima, A. Tanaka, Y. Takano, H. B. Wang, M. Nagao, H. Hatano, and S. Kawabata, “Macroscopic Quantum Tunneling in a d -Wave High- T_C $\text{Bi}_2\text{Sr}_2\text{CaCu}_2\text{O}_{8+\delta}$ Superconductor,” *Physical Review Letters*, vol. 95, no. 107005, pp. 1–4, Sep. 2005. [Online]. Available: <https://link.aps.org/doi/10.1103/PhysRevLett.95.107005>
- [287] X. Y. Jin, J. Lisenfeld, Y. Koval, A. Lukashenko, A. V. Ustinov, and P. Müller, “Enhanced Macroscopic Quantum Tunneling in $\text{Bi}_2\text{Sr}_2\text{CaCu}_2\text{O}_{8+\delta}$ Intrinsic Josephson-Junction Stacks,” *Physical Review Letters*, vol. 96, no. 177003, pp. 1–4, May 2006. [Online]. Available: <https://link.aps.org/doi/10.1103/PhysRevLett.96.177003>
- [288] L. Longobardi, D. Massarotti, G. Rotoli, D. Stornaiuolo, G. Papari, A. Kawakami, G. Piero Pepe, A. Barone, and F. Tafuri, “Quantum crossover in moderately damped epitaxial NbN/MgO/NbN junctions with low critical current density,” *Applied Physics Letters*, vol. 99, no. 062510, pp. 1–3, Aug. 2011. [Online]. Available: <http://aip.scitation.org/doi/10.1063/1.3624471>
- [289] S. Doettinger, R. P. Huebener, and Y. N. Ovchinnikov, “Nonlinear Effects During Vortex Motion at High Velocities,” *Chinese Journal of Physics*, vol. 34, no. 2S, pp. 291–297, Apr. 1996. [Online]. Available: <http://www.airitilibrary.com/Publication/alDetailedMesh?docid=05779073-199604-201212030010-201212030010-291-297>
- [290] D. Y. Vodolazov and F. M. Peeters, “Rearrangement of the vortex lattice due to instabilities of vortex flow,” *Physical Review B*, vol. 76, no. 014521, pp. 1–9, Jul. 2007. [Online]. Available: <https://link.aps.org/doi/10.1103/PhysRevB.76.014521>
- [291] D. Massarotti, L. Longobardi, L. Galletti, D. Stornaiuolo, G. Rotoli, and F. Tafuri, “Macroscopic quantum tunneling and retrapping processes in moderately damped YBaCuO Josephson junctions,” *Low Temperature Physics*, vol. 39, no. 3, pp. 294–298, Mar. 2013. [Online]. Available: <http://aip.scitation.org/doi/10.1063/1.4795203>
- [292] H. Kramers, “Brownian motion in a field of force and the diffusion model of chemical reactions,” *Physica*, vol. 7, no. 4, pp. 284–304, Apr. 1940. [Online]. Available: <https://linkinghub.elsevier.com/retrieve/pii/S0031891440900982>

- [293] M. Büttiker, E. P. Harris, and R. Landauer, “Thermal activation in extremely underdamped Josephson-junction circuits,” *Physical Review B*, vol. 28, no. 3, pp. 1268–1275, Aug. 1983. [Online]. Available: <https://link.aps.org/doi/10.1103/PhysRevB.28.1268>
- [294] A. O. Caldeira and A. J. Leggett, “Influence of Dissipation on Quantum Tunneling in Macroscopic Systems,” *Physical Review Letters*, vol. 46, no. 4, pp. 211–214, Jan. 1981. [Online]. Available: <https://link.aps.org/doi/10.1103/PhysRevLett.46.211>
- [295] V. M. Krasnov, T. Bauch, S. Intiso, E. Hürfeld, T. Akazaki, H. Takayanagi, and P. Delsing, “Collapse of Thermal Activation in Moderately Damped Josephson Junctions,” *Physical Review Letters*, vol. 95, no. 157002, pp. 1–4, Oct. 2005. [Online]. Available: <https://link.aps.org/doi/10.1103/PhysRevLett.95.157002>
- [296] J. Männik, S. Li, W. Qiu, W. Chen, V. Patel, S. Han, and J. E. Lukens, “Crossover from Kramers to phase-diffusion switching in moderately damped Josephson junctions,” *Physical Review B*, vol. 71, no. 220509(R), pp. 1–4, Jun. 2005. [Online]. Available: <https://link.aps.org/doi/10.1103/PhysRevB.71.220509>
- [297] L. Longobardi, D. Massarotti, G. Rotoli, D. Stornaiuolo, G. Papari, A. Kawakami, G. P. Pepe, A. Barone, and F. Tafuri, “Thermal hopping and retrapping of a Brownian particle in the tilted periodic potential of a NbN/MgO/NbN Josephson junction,” *Physical Review B*, vol. 84, no. 184504, pp. 1–6, Nov. 2011. [Online]. Available: <https://link.aps.org/doi/10.1103/PhysRevB.84.184504>
- [298] D. Massarotti, L. Longobardi, L. Galletti, D. Stornaiuolo, D. Montemurro, G. Pepe, G. Rotoli, A. Barone, and F. Tafuri, “Escape dynamics in moderately damped Josephson junctions (Review Article),” *Low Temperature Physics*, vol. 38, no. 4, pp. 263–272, Apr. 2012. [Online]. Available: <http://aip.scitation.org/doi/10.1063/1.3699625>
- [299] A. Bezryadin, *Superconductivity in Nanowires - Fabrication and Quantum Transport*, 1st ed. Wiley, 2012. [Online]. Available: <https://onlinelibrary.wiley.com/doi/book/10.1002/9783527610501>
- [300] M. Ejrnaes, D. Salvoni, L. Parlato, D. Massarotti, R. Caruso, F. Tafuri, X. Y. Yang, L. X. You, Z. Wang, G. P. Pepe, and R. Cristiano, “Superconductor to resistive state switching by multiple fluctuation events in NbTiN nanostrips,” *Scientific Reports*, vol. 9, no. 8053, pp. 1–6, May 2019. [Online]. Available: <http://www.nature.com/articles/s41598-019-42736-3>
- [301] M. Sahu, M.-H. Bae, A. Rogachev, D. Pekker, T.-C. Wei, N. Shah, P. M. Goldbart, and A. Bezryadin, “Individual topological tunnelling events of a quantum field probed through their macroscopic consequences,” *Nature Physics*, vol. 5, no. 7, pp. 503–508, Jul. 2009. [Online]. Available: <http://www.nature.com/articles/nphys1276>
- [302] B. Rosner, “Percentage Points for a Generalized ESD Many-Outlier Procedure,” *Technometrics*, vol. 25, no. 2, pp. 165–172, May 1983. [Online]. Available: <http://www.tandfonline.com/doi/abs/10.1080/00401706.1983.10487848>
- [303] H. Aguinis, R. K. Gottfredson, and H. Joo, “Best-Practice Recommendations for Defining, Identifying, and Handling Outliers,” *Organizational Research Methods*, vol. 16, no. 2, pp. 270–301, Apr. 2013. [Online]. Available: <http://journals.sagepub.com/doi/10.1177/1094428112470848>

- [304] T. Sekitani, N. Miura, S. Ikeda, Y. Matsuda, and Y. Shiohara, “Upper critical field for optimally-doped $\text{YBa}_2\text{Cu}_3\text{O}_{7-\delta}$,” *Physica B: Condensed Matter*, vol. 346-347, pp. 319–324, Apr. 2004. [Online]. Available: <https://linkinghub.elsevier.com/retrieve/pii/S0921452604000894>
- [305] N. Miura, H. Nakagawa, T. Sekitani, M. Naito, H. Sato, and Y. Enomoto, “High-magnetic-field study of high-Tc cuprates,” *Physica B: Condensed Matter*, vol. 319, no. 1-4, pp. 310–320, Jul. 2002. [Online]. Available: <https://linkinghub.elsevier.com/retrieve/pii/S0921452602011341>
- [306] M. Lyatti, M. A. Wolff, I. Gundareva, M. Kruth, S. Ferrari, R. E. Dunin-Borkowski, and C. Schuck, “Energy-level quantization in $\text{YBa}_2\text{Cu}_3\text{O}_{7-x}$ phase-slip nanowires,” *arXiv:1903.00805 [cond-mat.supr-con]*, Apr. 2019. [Online]. Available: <https://arxiv.org/abs/1903.00805>

Sujet : Dynamique des vortex dans des nanofils supraconducteurs d'YBCO irradiés : vers la détection de photon unique

Résumé : Cette thèse étudie la possibilité de détecter un photon unique avec un supraconducteur à haute température. Pour cela, nous avons développé un procédé basé sur l'irradiation ionique de films minces d'YBCO pour fabriquer des nanofils supraconducteurs fiables grâce à une couche protectrice d'oxyde de cérium. Nous avons caractérisé des nanofils ayant au minimum une épaisseur de 12 nm et une largeur de 100 nm, et au maximum une longueur de 750 μm . Les courbes courant-tension des fils ayant de fortes densités de courant critique sont hystérétiques et présentent un saut de tension. La présence de l'hystérèse est dictée par les propriétés thermiques. Les mesures statistiques des courbes courant-tension en fonction de la température, du champ magnétique, et de la puissance micro-onde, montrent qu'une instabilité de vortex déclenche le saut de tension. Nous avons aussi analysé les régimes de tension dissipatifs en fonction de la température et de la puissance micro-onde. Le régime de basse tension est dominé par le piégeage des vortex. Pour des tensions plus grandes, les données sont décrites par le mouvement de vortex thermiquement activé avec des interactions de vortex. En présence de micro-onde, les nanofils présentent des marches de courant liées au mouvement cohérent de vortex. Les mesures de transport démontrent que le régime de tension dissipatif avant le saut de tension est gouverné par la dynamique des vortex. Enfin, nous avons étudié le taux de comptage des impulsions de tensions dans les nanofils à basses températures. Plusieurs arguments tendent à montrer que le taux de comptage noir est dû au passage de vortex par effet tunnel.

Mots clés : Supraconductivité, SSPD, YBCO, Dynamique des vortex, Nanofils, Distribution de courant d'échappement

Subject: Vortex dynamics in ion irradiated YBCO superconducting nanowires: toward single photon detection

Abstract: This thesis investigates the potential of high-temperature superconductor as single photon detector. To this end, we developed a fabrication workflow based on ion irradiation on YBCO thin films for patterning robust superconducting nanowires thanks to a cerium oxide protecting layer. We characterized superconducting YBCO nanowires, down to 12 nm in thickness and 100 nm in width, and up to 750 μm in length. The current voltage curves with high critical current density become hysteretic with a voltage switch. The thermal properties of the nanowire governs the hysteresis appearance. By measuring extensively the switching current statistics and the current voltage curves as a function of temperature, magnetic field, and incident microwave power, we concluded that vortex instabilities trigger the voltage switch. Additionally, we analyzed the dissipative voltage regimes in the current voltage characteristic with respect to temperature and incident microwave power. The low voltage branch is dominated by vortex pinning in the flux creep theory. At higher voltage, thermally activated vortex motion in presence of vortex interaction accounts for the experiments. If a microwave signal irradiates the nanowires, they exhibit integer and fractional Shapiro-like steps arising from a coherent vortex motion. Altogether, the transport measurement demonstrate that dissipation in ion irradiated nanowires is governed by vortex dynamics. At last, we study the count rates in YBCO nanowires at very low temperatures. Several arguments tend to show that the dark count arises from single vortex quantum tunneling.

Keywords: Superconductivity, SSPD, YBCO, Vortex dynamics, Nanowires, Switching current distribution